

Studies of Carbon Dioxide Methanation and Related Phenomena in Porous Catalysts



Ross Hubble

Department of Chemical Engineering and Biotechnology
University of Cambridge

A Dissertation submitted for the degree of Doctor of Philosophy
December 2018
Downing College

Summary of Studies of Carbon Dioxide Methanation and Related Phenomena in Porous Catalysts by Ross Hubble

This Dissertation investigates the kinetics of CO₂ methanation over nickel and cobalt catalysts. Methanation was studied for both Ni/γ-Al₂O₃ and Co/ZrO₂ catalysts, which were synthesised using an incipient wetness impregnation technique and subsequently characterised using analyses based on gas adsorption, XRD, TPR and thermogravimetry. Separately a CO hydrogenation reaction, the Fischer-Tropsch process, was modelled numerically to examine the influence of mass transfer in practical, commercial pellets of catalyst.

The kinetics of methanation was investigated for Ni/γ-Al₂O₃ over a wide range of reactant partial pressures using a gradientless, spinning-basket reactor operated in batch mode and in a laboratory-scale, continuous fixed-bed reactor. Langmuir-Hinshelwood kinetic models were developed to represent the observed kinetics in each reactor: these models were then compared. For the batch reactor, a rate expression based the dissociation of a chemisorbed CO intermediate being the rate-limiting step was found to be consistent with the experimental results. However, results from the fixed-bed suggested that the hydrogenation of an adsorbed C atom determined the rate of reaction. These differences in the kinetics on Ni/γ-Al₂O₃ between the fixed-bed and batch reactors suggest that a Langmuir approach using a single, rate-determining step may not be representative across all conversions.

The rate over the Co/ZrO₂ catalyst was characterised in the fixed-bed reactor over a range of reactant partial pressures at temperatures between 433 K and 503 K. The rate was observed to be dependent on hydrogen partial pressure and temperature, with the rate increasing with both. Previous research has reported a wide range of values of the apparent activation energy, with a study suggesting it was sensitive to pressure. Accordingly, the apparent activation energy was investigated for pressure sensitivity over a range of pressures between 5 and 15 barg: it was found to be constant. The values determined (~88-91±8 kJ/mol) were notably consistent with those reported for CO hydrogenation on cobalt. Kinetic schemes based on Langmuir-Hinshelwood and power law equations were evaluated, with the results best described by a reaction scheme based on the carbide pathway, with a rate-determining step of CH hydrogenation.

A reaction-diffusion model of the Fischer-Tropsch process in a 2-D hollow cylinder was developed and analysed across a range of Thiele moduli and the extents of error in both effectiveness factor and selectivity were quantified relative to one-dimensional sphere and slab analogues. The errors between 2-D and 1-D analogues were found to be most significant between Thiele moduli of ~0.25 and ~3. Hollow cylinder effectiveness factors were bounded

by those of sphere and slab above and below Thiele moduli of ~0.75 and ~1.15 respectively for the conditions examined, with the effectiveness factors exceeding those of both sphere and slab models between these moduli. A comparison of the hollow cylindrical pellets against spheres of equivalent volume demonstrated that hollow cylinders provided improved fixed-bed performance, with improved effectiveness factors and selectivities due to the lowered diffusion lengths of the hollow cylindrical geometry.

Preface

This dissertation is the result of my own work and includes nothing which is the outcome of work done in collaboration except as declared in the Preface and specified in the text.

It is not substantially the same as any that I have submitted, or, is being concurrently submitted for a degree or diploma or other qualification at the University of Cambridge or any other University or similar institution. I further state that no substantial part of my dissertation has already been submitted, or, is being concurrently submitted for any such degree, diploma or other qualification at the University of Cambridge or any other University or similar institution. It does not exceed the prescribed word limit for the relevant Degree Committee.

This dissertation contains approximately 61,300 words, excluding bibliography, and 75 figures.

Acknowledgements

I would like to thank Professor John S. Dennis for the opportunity to undertake this project, and for his advice and support which allowed me to complete this thesis. I am also grateful to Dr Stuart Scott and Dr Laura Torrente for their instruction and use of their experimental apparatus.

The experimental apparatus used within this dissertation at times provided significant challenges, and I would like to deeply thank the technical staff for their support in diagnosing and fixing equipment failures. The assistance provided by Wei-Yao Ma, John Gannon, Kevin Swann, Sebastien Cosnefroy, Peter Claxton, Chris Bawden, Andy Hubbard, Gary Chapman, and Lee Pratt was invaluable in solving the technical challenges throughout this project. I would also like to thank Zlatko Saracevic for his assistance with the BET equipment and my colleagues Martin and Ewa for their company and assistance in correctly using the TGA. I also wish to thank Felix, Wenting, Matthias, Kevin, Manny, Jin Yang, Paul, Ewa, Zach, PJ, Tamsin and Belen for their support during this Ph.D.

I am grateful to the EPSRC for providing funding for my studentship, Downing College for provision of conference travel grants and Alwyn Heong for their support of college hardship funds, without which I would not have been able to undertake this project.

Finally I would like to thank my parents for their love, patience and support, without which I would never have reached where I am today.

Abstract

This Dissertation investigates the kinetics of carbon dioxide methanation over nickel and cobalt catalysts. The methanation reaction is key in the generation of synthetic natural gas (SNG) and thus provides a means to substitute extracted natural gas with a fuel derived by the reaction of CO₂ and H₂, produced in turn from renewable energy sources, *e.g.* biomass. In addition to experimental investigations, numerical modelling was undertaken to examine the influence of mass transfer on the Fischer-Tropsch process in practical, commercial pellets of catalyst.

Methanation was studied for both Ni/ γ -Al₂O₃ and Co/ZrO₂ catalysts, which were synthesised using an incipient wetness impregnation technique and subsequently characterised using analyses based on gas adsorption, X-ray diffraction, temperature programmed reduction and thermogravimetry.

The kinetics of methanation were investigated for Ni/ γ -Al₂O₃ over a wide range of partial pressures of both products and reactants using both a gradientless, spinning-basket reactor operated in batch mode and in a laboratory-scale, continuous fixed-bed reactor. The rate and selectivity of the reaction were explored under batch conditions at temperatures 443 – 483 K and pressures up to 16 bar. Results were compared with the fixed-bed reactor, operating at the same temperatures and pressures. Langmuir-Hinshelwood kinetic models were developed to represent the observed kinetics in each type of reactor: these models were then compared. For the batch reactor, a rate expression based the dissociation of a chemisorbed CO intermediate being the rate-limiting step was found to be consistent with the experimental results. However, results from the fixed-bed suggested that the hydrogenation of an adsorbed C atom determined the rate of reaction. These differences in the kinetics on Ni/ γ -Al₂O₃ between the fixed-bed and batch reactors suggest that a Langmuir approach using a single, rate-determining step may not be representative across all conversions. The simplicity of the Langmuir-Hinshelwood approach was ascribed as a reason for the discrepancy and it was noted the quality of the fit of the Langmuir expression may be mathematical in basis rather than mechanistic.

The kinetics of methane formation over cobalt has received little previous research. In this Dissertation, the rate over the Co/ZrO₂ catalyst was characterised in the fixed-bed reactor over a range of reactant partial pressures at temperatures between 433 K and 503 K. The rate was observed to be dependent on hydrogen partial pressure and temperature, with the rate increasing with both. Previous research has reported a wide range of values of the apparent activation energy, with one study suggesting it was sensitive to pressure. Accordingly, the

apparent activation energy was investigated for pressure sensitivity over a range of pressures between 5 and 15 barg: it was found to be constant. The values determined ($\sim 88\text{--}91 \pm 8$ kJ/mol) were notably consistent with those reported over nickel catalysts, and those reported for CO hydrogenation on cobalt. Kinetic schemes based on Langmuir-Hinshelwood and power law equations were evaluated, with the results best described by a reaction scheme based on the carbide pathway, with a rate-determining step of CH hydrogenation.

A reaction-diffusion model of the Fischer-Tropsch process in a 2-D hollow cylinder was developed and analysed across a range of Thiele moduli and the extents of error in both effectiveness factor and selectivity were quantified relative to one-dimensional sphere and slab analogues. Two-dimensional modelling was found to be more accurate in representing industrial catalyst pellets. The errors between 2-D and 1-D analogues were found to be most significant between Thiele moduli of ~ 0.25 and ~ 3 . Hollow cylinder effectiveness factors were bounded by those of sphere and slab above and below Thiele moduli of ~ 0.75 and ~ 1.15 respectively for the conditions examined, with the effectiveness factors exceeding those of both sphere and slab models between these moduli. Concurrently, the chain growth parameters (α), and thus the selectivity to heavier hydrocarbons, between these values were lower than both those of sphere and slab geometry, and thus under these conditions hollow cylinders provided the greatest methane selectivity. The model was further evaluated against a simplified n^{th} order effectiveness factor model and found to differ over the Thiele range ~ 0.5 to ~ 1.5 . The greatest errors arose where the effectiveness factor exceeded 1. A comparison of the hollow cylindrical pellets against spheres of equivalent volume demonstrated that hollow cylinders provided improved fixed bed performance, with greater effectiveness factors and selectivities due to the lowered diffusion lengths of the hollow cylindrical geometry.

Overall, this research has indicated differences between the batch and fixed-bed kinetics for the CO_2 methanation reaction on a $\text{Ni}/\gamma\text{-Al}_2\text{O}_3$ catalyst, evaluated the kinetic behaviour of the reaction on Co/ZrO_2 , and determined the importance of shape in industrial scale hollow cylindrical Fischer-Tropsch pellets.

Table of Contents

1	Introduction	14
1.1	Background	14
1.2	Objectives and Structure	17
2	Experimental.....	19
2.1	Introduction.....	19
2.2	Determination of Kinetics under Transient Conditions	19
2.3	Gas Chromatography: Sample Analysis	24
2.3.1	Introduction	24
2.3.2	Quantitative Analysis of Chromatograms.....	28
2.4	Determination of Kinetics under Steady-State Conditions.....	32
2.4.1	Introduction	32
2.4.2	Description of the Apparatus	32
2.4.3	Product Analysis	36
2.4.4	Considerations in the Operation of a Fixed-Bed Reactor.....	36
2.4.5	Spatial Temperature Differences	37
2.5	Catalyst Particle Characterisation.....	38
2.5.1	Gas Adsorption Analysis	38
2.5.2	Thermogravimetric Analysis	38
2.5.3	X-Ray Diffraction.....	41
2.5.4	Temperature Programmed Reduction and Pulse Chemisorption Measurements	42
3	Synthesis and Characterisation of Supported Nickel and Cobalt catalysts	43
3.1	Introduction.....	43
3.2	Background	43
3.2.1	Method of Preparation	46
3.3	Experimental	51
3.3.1	Catalyst Selection	51
3.3.2	Preparation of the Nickel on Alumina Catalyst	52
3.3.3	Preparation of the Cobalt on Zirconia Catalyst	54
3.3.4	Physical and Chemical Characterisation of the Catalysts	55
3.4	Characterisation of the Ni/Al ₂ O ₃ Catalyst	57
3.4.1	Results: Gas Adsorption Analysis of the Ni/Al ₂ O ₃ Catalyst	57
3.4.2	Results: Thermogravimetric Analysis of the Ni/Al ₂ O ₃ Catalyst	58
3.4.3	Results: X-Ray Diffraction Analysis of the Ni/Al ₂ O ₃ Catalyst	61
3.4.4	Results: Evaluation of Catalytic Activity and Reproducibility of Ni/γ-Al ₂ O ₃ ..	62
3.4.5	Results: Temperature Programmed Reduction of Ni/Al ₂ O ₃ Catalyst	63

3.4.6	Results: H ₂ Pulse Chemisorption of the Ni/Al ₂ O ₃ Catalyst	64
3.4.7	Discussion	65
3.5	Characterisation of the Co/ZrO ₂ catalyst.....	68
3.5.1	Results: Zirconia Support Characterisation	68
3.5.2	Results: Gas Adsorption Analysis of the Co/ZrO ₂ Catalyst.....	69
3.5.3	Results: Thermogravimetric Analysis of the Co/ZrO ₂ Catalyst.....	70
3.5.4	Results: X-Ray Diffraction Analysis of the Co/ZrO ₂ Catalyst.....	73
3.5.5	Results: Evaluation of Co/ZrO ₂ Catalyst Batch Reproducibility.....	75
3.5.6	Results: Temperature Programmed Reduction of the Co/ZrO ₂ Catalyst	76
3.5.7	Discussion	77
3.6	Conclusions	80
4	Kinetics of CO ₂ Methanation on a Ni/γ-Al ₂ O ₃ Catalyst in Batch and Continuous Reactor Systems	81
4.1	Introduction	81
4.2	Background	81
4.3	Experimental	83
4.3.1	Apparatus	83
4.3.2	Control Experiments	84
4.4	Results: Batch Methanation over Ni/γ-Al ₂ O ₃	86
4.4.1	Effect of P _{H₂}	86
4.4.2	Effect of P _{CO₂}	88
4.4.3	Effect of Temperature.....	89
4.4.4	Effect of P _{H₂O}	90
4.5	Parameters Affecting the Measurement of Kinetics in a Fixed-Bed Reactor.....	91
4.5.1	Catalyst Stability	91
4.6	Determination of Methanation Kinetics in a Fixed-Bed Reactor.....	93
4.6.1	Effect of P _{H₂} and P _{CO₂}	93
4.6.2	Effect of Space Velocity	96
4.6.3	Effect of Temperature.....	96
4.7	Kinetic Determination	97
4.7.1	Mechanism Overview	97
4.7.2	Kinetics Investigations	99
4.7.3	Modelling Reaction Kinetics in the Batch Reactor.....	101
4.7.4	Modelling Reaction Kinetics in the Continuous Reactor.....	101
4.7.5	Candidate Kinetic Equations.....	102
4.7.6	Results: Identification of Kinetic Models based on Batch Observations.....	104
4.7.7	Results: Comparison with Fixed-Bed Experiments	107
4.7.8	Results: Identification of Fixed-Bed Kinetic Models	110

4.8	Discussion	114
4.9	Conclusions.....	118
5	Kinetics of Carbon Dioxide Hydrogenation on a Co/ZrO ₂ Catalyst	119
5.1	Introduction.....	119
5.2	Background.....	119
5.3	Experimental	123
5.3.1	Materials	123
5.3.2	Apparatus.....	123
5.3.3	Control Experiments and Catalyst Deactivation	124
5.4	Results.....	126
5.4.1	Effect of P_{CO_2} and P_{H_2}	126
5.4.2	Effect of Pressure.....	127
5.4.3	Effect of Space Velocity	128
5.4.4	Effect of Temperature	129
5.5	Kinetic Modelling of CO ₂ Methanation on Co/ZrO ₂	131
5.5.1	Kinetic Rate Equations	131
5.5.2	Modelling Kinetics in the Fixed-Bed Reactor.....	132
5.5.3	Evaluation of Power-Law Methanation Kinetics	132
5.5.4	Evaluation of Langmuir-Hinshelwood Methanation Kinetics.....	134
5.6	Discussion	136
5.7	Conclusions.....	139
6.	Modelling Reaction and Diffusion in a Wax-Filled Hollow Cylindrical Pellet of Fischer-Tropsch Catalyst	140
6.1.	Introduction	140
6.2.	Background.....	141
6.2.1.	The Fischer-Tropsch Process.....	141
6.2.2.	The Fischer-Tropsch Product Distribution	142
6.2.3.	The Influence of Process Conditions on Selectivity.....	143
6.2.4.	Intra-Particle Reaction-Diffusion Modelling.....	144
6.2.5.	Pellets of Cylindrical Geometry	146
6.3.	Model Development	147
6.3.1.	Model Assumptions	147
6.3.2.	Mathematical Description.....	149
6.3.3.	Manipulation of the Energy Equation	151
6.3.4.	Boundary Conditions.....	151
6.3.5.	Diffusivity.....	154
6.3.6.	Solubility of CO and H ₂ in Fischer-Tropsch Wax	156
6.3.7.	Fischer-Tropsch Wax Density	157

6.3.8. Kinetics and Selectivity	157
6.3.9. Summary of Model Parameters.....	158
6.4. Solution Methodology.....	159
6.4.1. Algorithm	159
6.4.2. Sensitivities	160
6.4.3. Validation of 2-D Model	162
6.4.4. Thermal Gradients.....	162
6.5. Results: Evaluation of Effectiveness Factor for 1-D and 2-D Geometries	163
6.6. Results: Effectiveness Factors for 2-D Hollow Cylindrical Pellets	166
6.7. Comparison with Simplified Effectiveness Factor Models	170
6.8. Evaluation of α under Different Geometries.....	172
6.9. Discussion	175
6.10. Conclusions	179
7 Conclusions.....	180
8 Future Work	185
9 References	187
10 Nomenclature	207
10.1 Abbreviations.....	207
10.2 Symbols	209
10.3 Greek Symbols.....	211
A1. Appendix A. Derivation of Langmuir-Hinshelwood Expressions for CO ₂ Methanation.	212
A1.1. Introduction	212
A1.2. Carbide-Type Mechanism	213
A1.2.1. Carbide Mechanism: Carbon Monoxide Dissociation Rate-Limiting Step	213
A1.2.2. Carbide Mechanism: Other Rate-Limiting Steps.....	216
A1.3. Formyl Intermediate Mechanism	220
A1.3.1. Pathway 1: CO* → COH* → COH ₂ * → CH*	223
A1.3.2. Pathway 2: CO* → COH* → CH* + OH*	226
A1.3.3. Pathway 3: CO* → COH* → CH*+O*	229
A1.3.4. Pathway 4: CO* → COH* → C* → CH*	232
A1.3.5. Pathway 5: CO* → COH* → COH ₂ * → COH ₃ → CH ₂	235
A2. Appendix B: Consideration of Heat and Mass Transfer Effects	238
A2.1. Introduction	238
A2.2. Estimation of Transport and Thermodynamic Properties	238
A2.2.1. Viscosity	238
A2.2.2. Specific Heat	239
A2.2.3. Thermal Conductivity	239
A2.2.4. Density	241

A2.2.5. Diffusivity.....	241
A2.3. Heat and Mass Transfer Considerations in the Batch Reactor Experiments	242
A2.3.1. Intraparticle Mass Transfer.....	242
A2.3.2. Intraparticle Heat Transfer.....	242
A2.3.3. External Heat Transfer.....	243
A2.3.4. External Mass Transfer.....	244
A2.4. Heat and Mass Transfer Considerations for the BTRS.....	245
A2.4.1. Intraparticle Heat and Mass Transport.....	245
A2.4.2. Dilution in Fixed-Beds	245
A2.4.3. Axial Dispersion	245
A2.4.4. Radial Dispersion	246
A2.4.5. Pressure Drop	246
A2.4.6. Heat Transport in a Fixed-Bed Reactor	247
A2.4.7. Mass Transport in a Fixed-Bed Reactor	247
A2.5. Summary.....	248
A3. Appendix C: Literature Review of Carbon Dioxide Methanation Kinetics and Thermodynamics	249
A3.1. Mechanisms	249
A3.2. Thermodynamics of CO ₂ Methanation	254
A3.3. Published Kinetics Investigations.....	256
A4. Appendix D: Method of Numerical Solution.....	261
A4.1. Background.....	261
A4.2. Discretisation of the System	262
A4.2.1. Specification of Internal Node Residuals	264
A4.2.2. Treatment of Elemental Boundaries	266
A4.2.3. Specification of System Boundaries	267

1 Introduction

1.1 Background

The rise of CO₂ levels in the atmosphere during the last century has resulted in a measurable impact on global temperatures and climate. An increasing global demand for energy and its satisfaction through extraction and combustion of fossil fuel reserves have rapidly increased atmospheric concentrations of carbon dioxide, with levels rising from 315 ppm in 1960 to concentrations in excess of 400 ppm in recent years (NASA, 2017). The inexorable increase in atmospheric carbon is strongly suspected as the cause of increased desertification, melting of polar ice sheets and rising sea levels (McCarthy *et al.*, 2001). Without action the unabated use of fossil fuels is likely to result in the rise in mean global temperature exceeding the 2°C target (McGlade and Ekins, 2015) considered to be allowable.

The production of synthetic fuels could reduce the demand for fossil fuel extraction and thus the conversion of carbon stored within fossil fuels to atmospheric carbon. Currently, synthetic liquid fuels can be produced through gasification of coal or biomass to form synthesis gas (a CO and H₂ mixture) and catalytic reaction of the gas *via* the Fischer-Tropsch reaction to form higher hydrocarbons. Natural gas may be similarly synthesised by the catalytic methanation of mixtures of H₂ and either CO or CO₂, typically using a nickel catalyst. If biomass is used as a feedstock, the net carbon contribution of produced fuels to atmospheric CO₂ levels can be reduced.

This Dissertation examines two aspects of synthetic fuel production, synthetic natural gas production *via* CO₂ methanation, represented by reaction (1.1), and the Fischer-Tropsch synthesis, represented by reactions (1.2) and (1.3).



The experimental studies presented herein have examined the methanation of carbon dioxide over nickel and cobalt catalysts, with a modelling study investigating mass transfer phenomena within commercial Fischer-Tropsch catalyst pellets.

Originally discovered by Sabatier and Senderens (1902), the CO₂ methanation reaction (1.1) provides a means to upgrade CO₂ to valuable synthetic natural gas. The recent rise in social and political interest in the mitigation of atmospheric CO₂ has resulted in increased interest in the research and development of carbon capture and sequestration (CCS) technologies. These technologies, where implemented, could prevent the release of carbon

dioxide into the atmosphere, with their use most practicable for large emitters, such as power plants. In CCS, the CO₂ would be stored in geological formations or injected into depleted oil reservoirs. However, it might also be employed as a feedstock for the production of synthetic fuels and value-added chemicals, *e.g.* liquid fuels *via* the Fischer-Tropsch process, synthetic natural gas (SNG), dimethyl ether and methanol, thus reducing the need for further fossil fuel extraction.

The International Energy Agency (IEA, 2017) has estimated that fossil fuels constituted 82% of the global total primary energy supply in 2015, with natural gas making up 22% of the total. In the United Kingdom, natural gas fuelled 30% of electrical generation, with natural gas itself constituting 29% of all UK fossil fuel imports (Department for Business, Energy & Industrial Strategy, 2017). Hence, synthetic natural gas (SNG) production potentially provides a means to provide domestic energy security and satisfy energy demands without further extraction.

Recent investments, such as the GoGreenGas project (UK) (GoGreenGas, 2016) or the GoBiGas project (Sweden) (Larsson *et al.*, 2015), have resulted in the commissioning of commercial BioSNG plants for the generation of synthetic natural gases from wastes and biomass *via* CO methanation. At the industrial scale, the conversion of CO₂, rather than CO, to methane has also been identified and proposed as a means to balance electricity generation from renewable sources, with methane formation providing chemical energy storage during peak generation periods (Schaaf *et al.*, 2014). By producing SNG, existing infrastructure for the distribution and storage of natural gas could be exploited, reducing the need for new infrastructure. SNG production also allows for medium to long term storage of renewable energy at an efficiency of ~64% (Schaaf *et al.*, 2014), with the hydrogen produced by electrolysis.

Novel uses for synthetic natural gas have been developed. For example, Audi AG has installed a plant for the production of SNG for use within their natural gas/petrol dual fuel automobiles. The company operates a power-to-gas power plant, based in Lower Saxony, Germany, to provide carbon neutral gas to drivers of Audi cars. The hydrogen for the natural gas is produced by the hydrolysis of water using, primarily, renewable electricity whilst the carbon dioxide is produced by the combustion of straw and plant wastes (Audi, 2017).

CO₂ methanation is vital in space exploration applications, with it currently being applied to recover oxygen, in the form of water, from carbon dioxide in the International Space Station (NASA, 2011). The reaction is also central to plans for human occupation of Mars, with the conversion of the CO₂ from the Martian atmosphere and water reportedly from surface ice vital to the generation of propellant (Holladay *et al.*, 2007).

Liquid fuels are vital to many current means of transport, and the Fischer-Tropsch reaction provides a route to synthesise them. The process represented by equations (1.2) and (1.3) is a step-wise polymerisation reaction between carbon monoxide and hydrogen capable of producing a wide range of hydrocarbon chain lengths. Since its discovery in the early 1920s, industrial interest in the Fischer-Tropsch (FT) process has exhibited periods of growth and decline corresponding to changes in oil prices. Its initial development and eventual commercialisation took place in Germany between 1926 and 1945 (Schulz, 1999). Just after the end of World War II fears of shortages of liquid fuels prompted the development of processes based on fixed-bed, fluidised-bed, circulating-bed and slurry reactors (Schulz, 1999). However, discoveries of large reserves of oil, resulting in readily-available and cheap petroleum, caused a significant decline in global interest in the FT process. The exception was in South Africa, where the introduction of apartheid and the subsequent trade embargoes resulted in the commercialisation of the FT process by the South African Coal and Oil Company (SASOL) utilising the country's abundant coal reserves to operate CTL (coal-to-liquid) plants.

To the present day, SASOL has played a major role in the research and development of the Fischer-Tropsch process, and is responsible for the industrial development of FT slurry reactor technology (Schulz, 1999). Currently, given economic and environmental pressures, the Fischer-Tropsch process has garnered much attention. Numerous commercial GTL (gas-to-liquid) and CTL plants are operated primarily for the production of transport fuels. Biomass gasification provides a means to generate a lower carbon-footprint liquid fuel *via* the FT process, with commercial interest in the production of jet fuel from biomass, *e.g.* Velocys BTL (Velocys, 2017). Within the UK, a project supported by British Airways to convert biomass to jet fuel plant was proposed in 2012; however, the project was recently shelved owing to a decline in crude oil prices (Neslen, 2016).

The Fischer-Tropsch process itself produces a wide spectrum of hydrocarbons (C_1-C_{100+}), with the exact product composition highly dependent on the operating conditions. Within industrial reactors, the reaction often suffers from mass transfer limitations, with the large catalyst particles employed filling with the liquid hydrocarbon products. The reactors are frequently operated under conditions that favour the production of heavy and waxy hydrocarbons, since this reduces the quantity of methane and light gases formed. The heavier products may then be cracked and transformed into fuel-grade hydrocarbons.

In summary, this research considers the determination and uncertainty in the kinetic expressions and parameters for the CO_2 methanation reaction on Nickel and Cobalt based catalysts. The numerical modelling work examines the significance of shape on the Fischer-

Tropsch reaction in industrial scale pellets. Both of these elements are vital for improving the understanding of the relevant processes, and thus useful for synthetic fuel production in industrial scenarios.

1.2 Objectives and Structure

A primary objective of the research presented herein was the development of an improved understanding of the mechanisms and kinetics of reaction for the methanation of carbon dioxide using cobalt and nickel catalysts. Development of a more complete understanding of the underlying mechanisms for CO₂ methanation could provide important insights into efficient catalyst and reactor design, and thus improvements in the SNG production process. This dissertation further examines the Fischer-Tropsch process through modelling of the transport processes within a commercial catalyst pellet. Through numerical modelling of a Fischer-Tropsch pellet, the importance of pellet structure on an industrial-scale and its impact on key performance parameters, namely effectiveness factor and hydrocarbon selectivity, could be revealed. The core objectives of the dissertation are outlined below:

- (i) Development and characterisation of nickel and cobalt catalysts for the examination of the CO₂ methanation reaction.
- (ii) Investigation of the CO₂ methanation reaction within a pressurised fixed-bed reactor to study kinetics across a range of pressures and temperatures under differential conversion.
- (iii) Formulation of a set of kinetic equations for the description of the intrinsic kinetics of CO₂ methanation and comparison of developed models with experimental results.
- (iv) Comparison of the reaction kinetic models obtained from both continuous and batch reactor systems.
- (v) Development and application of a two-dimensional mass transfer model for the evaluation of commercial Fischer-Tropsch catalysts having the form of hollow cylinders.

Chapter 1 outlines the background and motivation for the investigation of methanation and Fischer-Tropsch reactions. Chapter 2 details the experimental methodologies and the specification of the experimental apparatus used. Chapter 3 presents the characterisation and development of the Ni/Al₂O₃ and Co/ZrO₂ catalysts employed within the experimental chapters in this Dissertation. The kinetics of the Ni/Al₂O₃ is examined in Chapter 4 for both batch and continuous reactors, with a wide range of potential kinetic schemes trialled for the description of the reaction. Chapter 5 examines the kinetics of CO₂ methanation on the zirconia supported cobalt catalyst. Chapter 6 presents a two-dimensional mass transfer model for the characterisation of hollow-cylindrical Fischer-Tropsch catalyst pellets. A literature review outlining the relevant prior investigations and background is provided in the introduction of individual chapters. The conclusions are presented in Chapter 7, with suggestions for future work presented in Chapter 8.

2 Experimental

2.1 Introduction

This Chapter outlines the experimental apparatus and techniques used to perform the research detailed in this Dissertation. The experimental work in this thesis can be divided into three main categories: (a) synthesis of cobalt- and nickel-based catalysts, (b) investigations of the kinetics of reaction for cobalt- and nickel-based hydrogenation catalysts in pressurised fixed-bed and spinning basket reactors, and (c) the physical and chemical characterisation of the catalyst particles.

Two types of reactor were used to investigate the kinetics of carbon dioxide hydrogenation under both transient and steady state conditions. Details of the two reactors, namely, (i) the Bench Top Reactor System, BTRS (Autoclave Engineers) (a fixed-bed reactor), and (ii) the Carberry Spinning Basket Reactor (Autoclave Engineers), including the methods of product analysis, are described below. The catalysts were characterised principally using gas adsorption analysis (BET), X-ray diffraction (XRD), thermo-gravimetric analysis (TGA), and temperature-programmed reduction (TPR). These techniques are also described.

2.2 Determination of Kinetics under Transient Conditions

A primary objective of this dissertation has been to characterise and compare the methanation of carbon dioxide under both steady and transient operating conditions. The kinetics of the hydrogenation of CO₂ have often been measured in the literature using bench-scale micro-reactors, but at steady conditions; however, studies of batch and transient kinetics are seldom encountered in the field.

To undertake studies under transient conditions, a spinning-basket reactor was used. A schematic diagram of the apparatus is shown in Figure 2.1. The spinning basket reactor (Carberry Reactor, I.D. 75 mm, 401A-8801 Autoclave Engineers, PA, USA), constructed of thick-walled 316 stainless steel, consisted of a removable basket mounted on a rotating shaft. This shaft was coupled to an external drive motor *via* a magnetic coupling, the ‘magnedrive’. The external magnetic coupling was driven by a belt drive connected to a D.C. motor (180 V, 370 W) with a maximum rotational speed of 2500 rpm. The speed of the basket was manipulated by controlling the voltage supplied to the D.C. motor.

Within the reactor, wall-mounted baffles and impellers above and below the basket helped ensure the gas was well mixed. The walls of the rotationally-symmetric, cross-shaped basket were formed from 316 stainless steel mesh with an aperture size of 1.4 mm (US Mesh

Size 14). The body of the reactor was heated electrically by two band heaters (ME51J1JP1, Watlow) clamped to the exterior wall of the reactor. The total power of these heaters was 2 kW. The temperature within the reactor was measured using a K-type thermocouple positioned adjacent to the basket, protruding into the gas phase from the base of the reactor. A second K-type thermocouple was located between the lower band heater and outer-wall of the reactor. Its purpose was to ensure that the reactor's rating was not compromised by too high a temperature caused by the substantial temperature gradient across the thick walls of the reactor. A cascade controller (PM8C1CJ-ACCJCAA, Watlow) consisting of two PID loops used the input from the internal thermocouple to alter the set-point for the external wall temperature. In the event of the outer wall temperature exceeding the rating, the power to the band heaters was switched off by a non-latching trip actuated by a solid-state relay (DIN-A-MITE, Watlow). When the wall temperature cooled below the limit, the power to the band heaters resumed. At steady state, the measured internal temperature was maintained at the set point to a precision of $\pm 0.1^\circ\text{C}$.

Prior to a series of experiments, the basket was loaded with a known mass of catalyst, typically 5.0 g of catalyst pellets mixed evenly with 5.0 g of inert glass beads of equal size to prevent hot spots from forming due to catalyst contact. Once the basket was fastened within the reactor, the reactor was pressure tested at room temperature with 10 bar of nitrogen over a period of 24 hours. The catalyst activation process was commenced upon a successful pressure test, that is, a loss of less than 0.2 bar over 12 hours, as measured by the analogue pressure gauge on the reactor's inlet line.

In the Carberry experiments a nickel on alumina catalyst was studied for its methanation kinetics. Prior to use, the catalyst was activated through reduction in hydrogen. Metallic catalysts are often prepared through impregnation of a support material with a metal salt (e.g. nickel nitrate) and then heated to decompose these salts. This yields a dispersion of metal oxide particles across the support's surface. The unreduced catalyst in this case was inactive for the methanation of CO₂, and thus required reduction of the nickel oxide particles to nickel. The catalyst was first completely reduced using hydrogen *ex-situ* with the preparation detailed further in §3.3.2. The operating temperature limit of the Carberry precluded direct reduction within the reactor; however *ex-situ* reduction followed by passivation and re-reduction within the Carberry yielded an active phase. The passivation technique exposes reduced metals to diluted oxygen at low temperatures, yielding a thin oxide barrier layer on the surface of the reduced metal particles, which prevents further oxidation of the particles in air. This layer may then be more easily reduced than the bulk oxide formed during calcination. Further information on the catalyst preparation methods and relevant

background information is given in Chapter 3.

The reduction process for the passivated catalyst started with evacuating the reactor using a vacuum pump (BOC Edwards RV3) at room temperature. The reactor was then filled with 1.0 barg of nitrogen and heated to the reduction temperature of 250°C. Prior to reduction, the stirrer speed was set to 10 Hz (600 rpm) to prevent any concentration gradients in the gas phase. When the reactor temperature stabilised at the desired reduction set point, a flow of hydrogen (Air Liquide, 99.993% purity) was passed through the reactor, metered using rotameter to provide 300 cm³/min (at STP) of H₂ at atmospheric pressure for a period of 6 hours.

After 6 hours at 250°C, the flow of H₂ was discontinued and the reactor evacuated using the vacuum pump. The reactor was then filled with nitrogen at 1 bar and the set-point of the temperature controller was altered to cool the reactor to the desired reaction temperature. At the end of a batch, the reactor was evacuated of reaction products and subsequently charged with nitrogen to a pressure of 1 barg at the reaction temperature. This provided an inert atmosphere for the catalyst, allowing its activity to be maintained between individual runs.

Prior to an experiment, the stirrer speed was set to 600 rpm, and the reactor temperature was then allowed to stabilise at the desired temperature set-point. The reactor was then evacuated using the vacuum pump before being isolated and then charged with the reactant gases. A cylinder containing pre-mixed reactant gases was used, as this allowed for the rapid pressurisation of the evacuated reactor, minimising the charging time. The pre-mixed gases consisted of 72 vol% hydrogen, 4 vol% argon, as the inert internal standard, and 24 vol% carbon dioxide. The initial pressure in the reactor was normally set between 10 to 16 bara.

The charging procedure for the reactor began with setting the outlet pressure of the regulators on cylinders containing the reactant gases to 2-5 bar above the desired initial pressure. The needle valve on the inlet line, shown in Figure 2.1, was then firmly closed. The plug valve isolating the desired reactant gases was then opened and the needle valve was opened and used to throttle the flow. Once the reactor pressure approached the desired initial charging pressure, the needle valve was gradually closed until the set-point was reached. At this point, the pre-mixed gas cylinder was isolated at the plug valve. This procedure took approximately 15 seconds, with the initial charging pressure being reached to a precision of ±0.1 bar, as measured by the pressure gauge PG1 on the inlet line. A secondary, analogue pressure gauge connected directly to the reactor's top closure confirmed the accuracy of the reading of PG1.

Once the desired initial pressure in the reactor had been reached, the timer was started. In order to quantify the reaction kinetics, gas samples were taken from the reactor at intervals for analysis. Due to the stoichiometry of the hydrogenation reactions, the overall reactor pressure decreased as the reaction progressed. The changing pressure was used as an indication of the extent of reaction, allowing the samples to be spaced to capture the most detail when the reaction was fast, with less frequent sampling when the rate decreased and the batch approached full conversion.

Gas samples were withdrawn from the reactor using a gas tight syringe *via* the sample manifold, shown in Figure 2.1. In order to obtain a sample of gas representative of the bulk composition in the reactor, the sample manifold and the gas-tight syringe were evacuated using the vacuum pump. Once complete, the sample manifold was isolated from the vacuum pump using a plug valve. The sampling needle valve was then opened until the gas tight syringe was filled with 4 ± 0.5 ml of sample gas at atmospheric temperature and pressure. The syringe and sample manifold was then once again evacuated, isolated from the vacuum source and the sample needle valve again used to fill the gas syringe with $4\text{ ml}\pm0.5$ ml of sample gas at atmospheric temperature and pressure. This repeat procedure ensured that the gas in the dead volume of the 1/16" line and fittings between the sample manifold and the reactor contained gas representative of the bulk. The sample of gas was analysed by gas chromatography. Typically, 6-8 samples were taken for each experiment to minimise the errors arising from excessive removal of reactant gases.

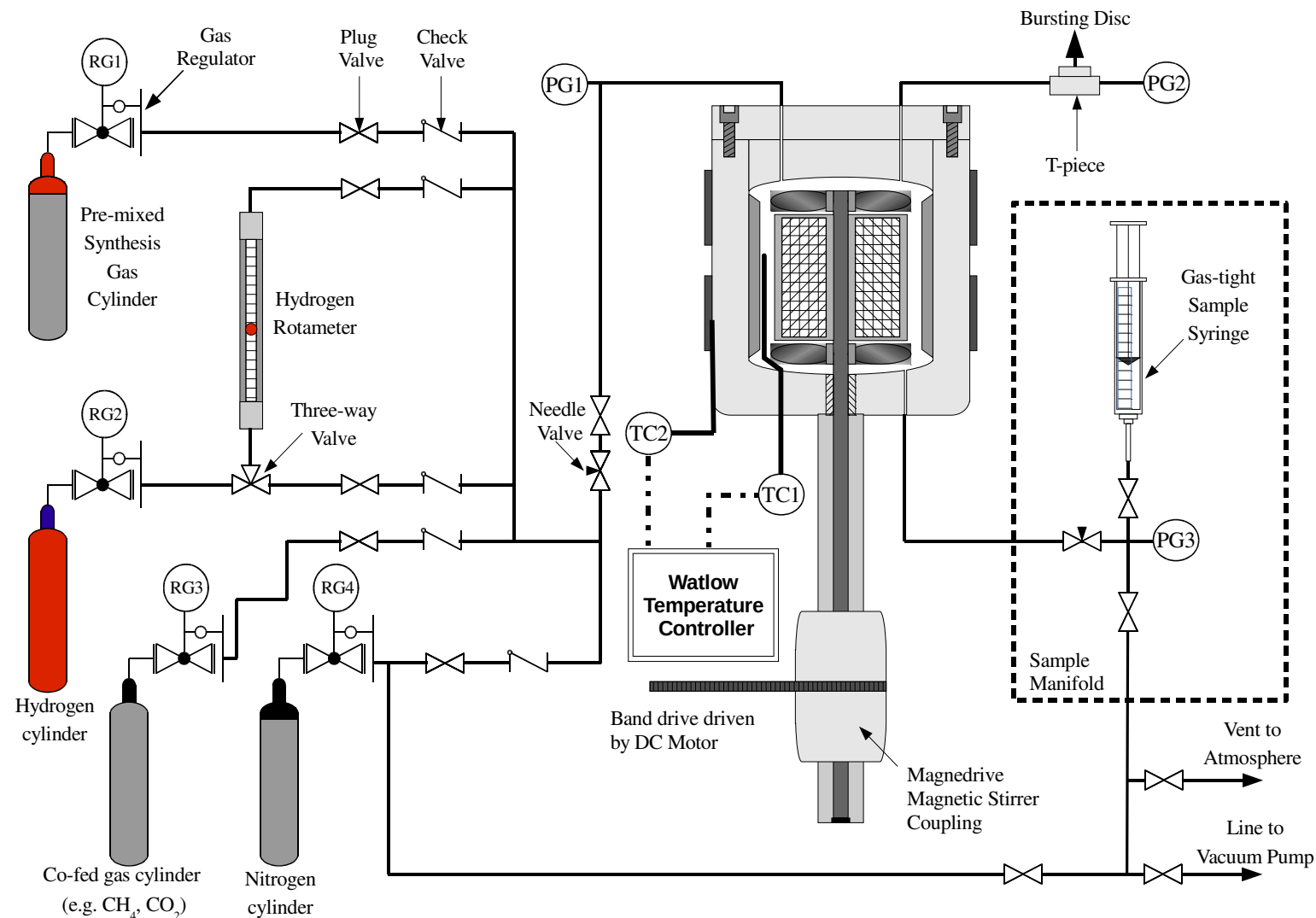


Figure 2.1. Schematic diagram of the arrangement of the Carberry spinning basket reactor.

2.3 Gas Chromatography: Sample Analysis

2.3.1 Introduction

Compounds injected into the gas chromatograph (GC) are mixed with carrier gas (mobile phase) and passed through columns coated or filled with a stationary phase, which adsorbs species. This results in a partitioning between the gas and sorbent phases. Species with greater adsorption strengths on the stationary phase are retained for longer; hence species of differing adsorption strengths may be separated. The retention time, *i.e.* the time a compound remains within the column, is affected by both size and functionality. For instance, a small molecule, *e.g.* H₂, is quickly eluted, whereas CO is retained for a much greater time. In order to separate similar species, such as ethane and ethylene, the stationary phase must be selected to prevent overlap of the effluent gas traces.

In this work, the GC (Agilent 7890A, Agilent Technologies) was fitted with both flame ionisation (FID) and thermal conductivity detectors (TCD) to analyse gas eluted from the columns. Flame ionisation has sensitivities for organic compounds at concentrations as low as 50 ppb, with a standard deviation of 5% (McNair and Miller, 2011). The FID technique involves passing hydrocarbons through a flame to form CHO⁺ ions, which are collected by a negatively biased collector, and subsequently transformed into a signal (Poole, 2012). The response factor, *i.e.* the signal strength relative to the concentration of species present, is directly related to the quantity of carbon combusted in the flame. Hence response factors for hydrocarbons scale linearly with carbon number.

A thermal conductivity detector compares the thermal conductivity of a sample gas to that of the carrier gas. Lighter gases tend to have a greater thermal conductivity than heavier gases; hence helium is often used as a carrier gas (McLennan and Kowalski, 1995). When a species elutes from the column, the thermal conductivity of the gas passing over the sensor is changed, which alters the voltage across the resistance wire, and thus provides a signal. The sensitivity of these detectors is often maximised using a reference detector, which is exposed only to pure carrier gas, hence the effect of detector temperature or carrier flow perturbations may be countered. Owing to the similarity of the thermal conductivities of hydrogen and helium, two separate channels were required to analyse gas mixtures containing H₂, CO, CO₂, N₂ and Ar. The first channel was used to analyse hydrogen. For this channel, nitrogen was used for both the carrier and reference gases. Hence, when hydrogen passed through the sensor, the thermal conductivity in the sensor significantly increased relative to the reference. For species other than hydrogen, a second channel used helium as the carrier and reference

gases. In the TCD chromatogram shown in Figure 2.2 b), the switch between channels is clearly visible at approximately 2 minutes. Methane and C₂ hydrocarbons were detected by the TCD sensor; however, these signals were not used for the analysis, as the FID detector provided superior resolution of different hydrocarbons. A summary of the conditions used for the GC is given in Table 2.1.

Table 2.1 Parameters used for the Agilent 7890A Gas Chromatograph**Oven Temperature Programme**

Immediately after sample injection, the oven temperature was held at 60°C for 3 minutes, followed by a temperature ramp of 5°C/min to 100°C. The temperature was then ramped at 10°C/min to 200°C, where it was held for 6 minutes. At the end of the run, the oven returned to 60°C. A 3 minute equilibration time at 60°C was used to ensure each analysis began with all columns stabilised.

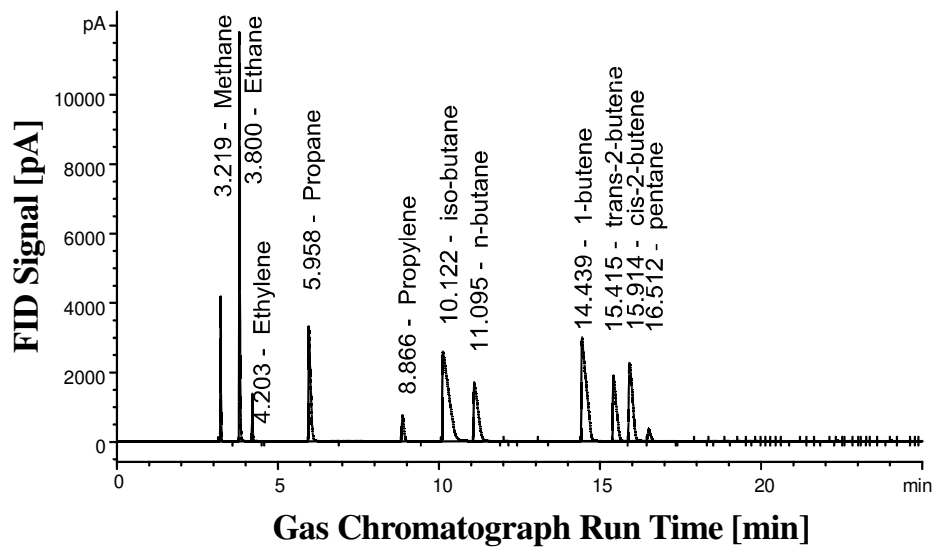
FID Configuration

Carrier Gas	Helium (1.44 bar constant column head pressure, 1.0-0.6 cm ³ /min at STP [25 °C 1 bar] flow)
Detector Temperature	250°C
Detector Gases	Hydrogen (35 cm ³ /min at STP), Air (350 cm ³ /min at STP) Nitrogen (15 cm ³ /min at STP)
Column	GS-GasPro PLOT Column 60 m × 0.32 mm
Products Analysed	C ₁ -C ₉ Hydrocarbons

TCD Configuration

Detector Type	Tungsten Rhenium Filament
Detector Temperature	200°C
Channel A Column	Hayesep Q
Channel A Carrier Gas	Nitrogen
Products Analysed on Channel A	Hydrogen
Channel B Column	Hayesep Q, MolSieve 13X, Hayesep Q
Channel B Carrier Gas	Helium
Products Analysed on Channel B	Carbon Monoxide, Carbon Dioxide, Nitrogen, Argon, & C ₁ -C ₂ Hydrocarbons.

a)



b)

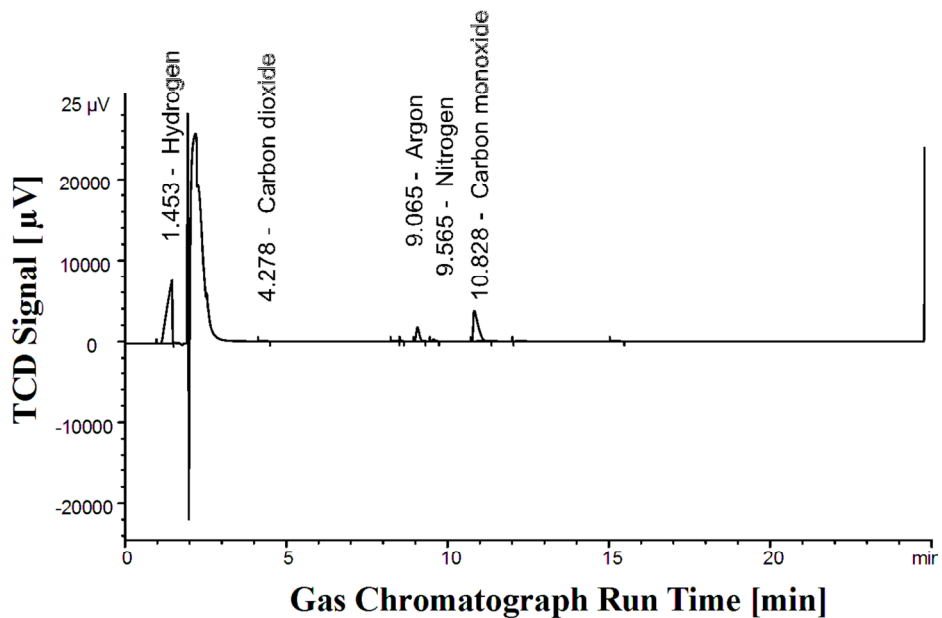


Figure 2.2 a) An FID chromatogram produced by the calibration standard **b)** A TCD chromatogram of a sample containing H₂, CO, CO₂, N₂ and Ar. Each identified peak is labelled with its retention time and compound.

2.3.2 Quantitative Analysis of Chromatograms

The compositions of the samples obtained from the Carberry reactor were analysed using off-line gas chromatography. Each gas-tight syringe was attached to the injection manifold on the GC. The manifold, shown schematically in Figure 2.3, was then evacuated using a vacuum pump (through opening V1 and V3 together, then closing V3), before the valve on the syringe was opened, allowing the reaction gases to enter the sampling loop. Because the volume of the gas in the syringe exceeded the volume of the sampling loop, the syringe plunger moved until the pressure in the sampling loops and the syringe equalled atmospheric pressure. The gas contained within the sampling loops was then analysed using the TCD and FID channels. The method used for the analysis of the sample gas was based on the manufacturer's recommendations. Excess sample gas was vented to atmosphere through opening V4.

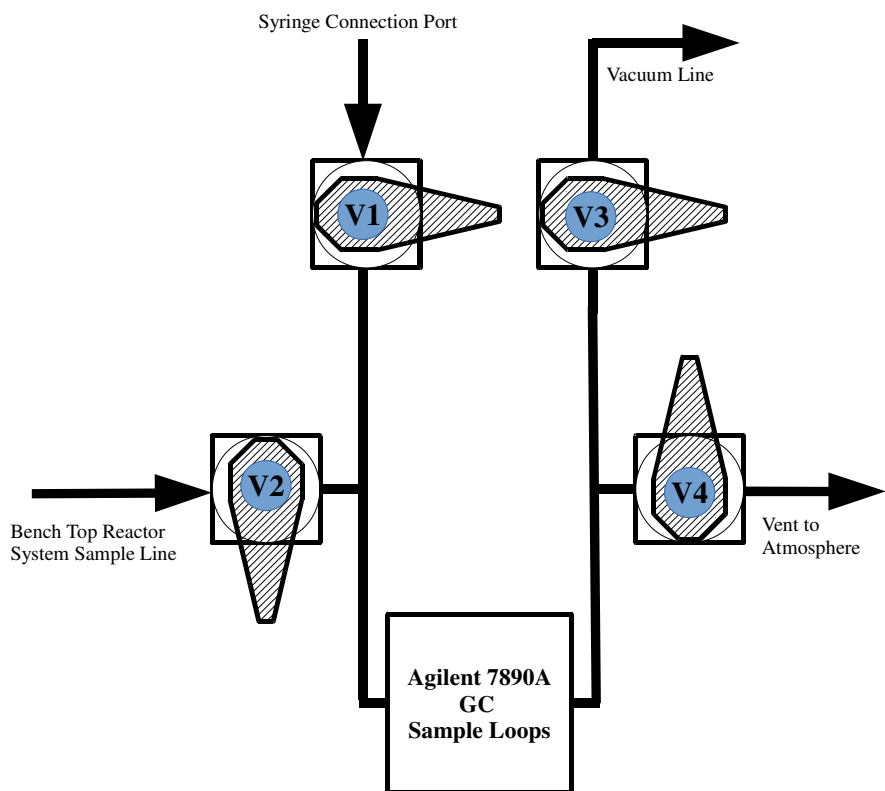


Figure 2.3. A schematic diagram of the injection manifold. The valve arrangement was used for both off-line, single-sample injection and online sampling of the products from the BTRS.

After the sample of gas had entered the GC, it passed into three separate sampling loops (SL1, SL2, SL3) shown in Figure 2.4. Prior to injection to the columns, the gas passed freely through the sample loops *via* the green pathway. Upon initiation of the analysis, the switching valves were engaged to isolate the sample loops. The rotation of SV2 passed helium

carrier gas through sample loop SL2 (Volume = 250 µL) and through the GS-Gaspro column to the flame ionisation detector for hydrocarbon analysis (red pathway).

Nitrogen carrier gas was passed through sample loop 3 (Volume = 1 ml) upon switching SV2. This carrier was used solely for the analysis of hydrogen and transported the species within sample loop 3 through column 4 to the TCD. Column 4 is a Hayesep Q column in series with a Molecular Sieve 13X column (light blue pathway). As the molecular sieve column may be poisoned by carbon dioxide, the column flow was reversed by switching SV4 after the elution of hydrogen.

For the analysis of heavier permanent gases, sample loop 1 was used. The species within sample loop 1 were transported to the columns with a helium carrier upon switching SV1. The gases passed through the Hayesep Q columns and were separated according to differential adsorption on the porous polymer. Heavier compounds such as CO₂ and C₂₊ had longer retention times within the columns. The lighter compounds (H₂, N₂, O₂) passed into the molecular sieve. The flow of helium continued in this configuration until the H₂ eluted from the molecular sieve and was vented. SV3 then switched, retaining the N₂, CO and CH₄ compounds within the molecular sieve column. CO₂ and compounds within column 2 were then passed to the TCD. After the elution of CO₂, species remaining within column 1, namely heavier hydrocarbon species, were flushed from the column by switching SV1 and reversing the flow. SV3 was once again switched and the compounds remaining in the molecular sieve column were passed to the detector. Once eluted, the valves switched once more to bypass the molecular sieve, passing any species remaining in column 2 into the detector.

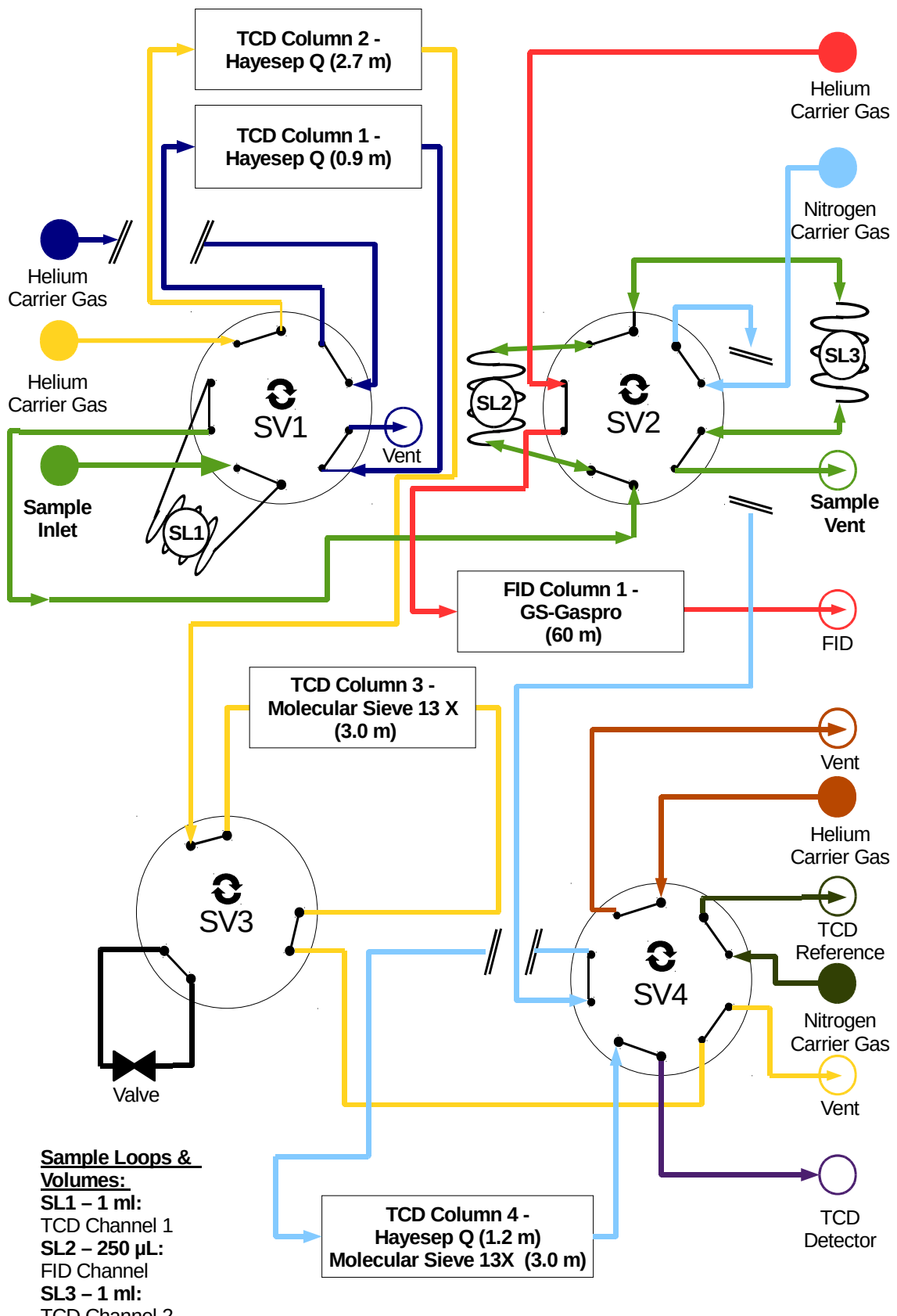


Figure 2.4 A diagram of the sample loops and column connections to the 10-way valves (SV1, SV2, SV4) and 6-way valve (SV3). Adapted from Agilent (2011)

A computer using Agilent ChemStation (Rev B.04.03, Agilent Technologies) was used to analyse and store the results. The assignment of TCD and FID signals was based on the reference chromatogram using the calibration gas. The calibration gas contained C₁-C₄ light hydrocarbon gases, CO, CO₂, Ar, N₂ and H₂.

The concentration of each compound was determined by multiplying the area under a peak by the response factor of the relevant compound. The response factors for each compound were determined by measuring areas under peaks for a gas mixture of known composition. The response factor was defined as:

$$RF_j = \frac{\text{Mole fraction of species } j}{\text{Peak area for species } j} \quad (2.1)$$

The compositions measured by the gas chromatograph were not representative of the composition within the batch reactor because hydrogenation reactions form water. Within the reactor, the partial pressure of the water was below its dew point partial pressure. However, upon sampling, it was possible for condensation to form on the walls of the sampling syringe. Accordingly, the partial pressure of a component *j* (p_j) within the reactor was determined by ratio from the known pressure of the argon standard supplied in the original feed gas. In the experiments in the Carberry apparatus, a pre-mixed synthesis gas was used containing 4 mol% argon. Hence, the partial pressure of argon (p_{Ar}) was known to be 4% of the initial pressure charged from the pre-mixed cylinder. Equation (2.2) was used to determine the partial pressures of each species within the reactor.

$$p_j = \frac{x_j p_{Ar}}{x_{Ar}} \quad (2.2)$$

where x_j and x_{Ar} are the measured mole fractions of species *j* and argon respectively. The pressures are given by p_j for species *j* and p_{Ar} for argon.

2.4 Determination of Kinetics under Steady-State Conditions

2.4.1 Introduction

The use of a continuous, fixed-bed reactor provided a means of validating and comparing the kinetic results determined using the Carberry spinning basket reactor. The reactor system, Bench Top Reactor System (BTRS-JR-PC, Autoclave Engineers, Erie, PA), consisted of a fixed-bed reactor capable of pressurised operation at temperatures and pressures up to 650°C and 50 barg respectively.

2.4.2 Description of the Apparatus

The line diagram for this apparatus is shown in Figure 2.5. The hydrogenation reactions were carried out in a down-flow arrangement. The fixed-bed contained a known mass of catalyst, which had been thoroughly mixed with inert alumina particles of the same size fraction. Both the catalyst particles and the alumina were sieved to a size fraction between 106-212 µm. The bed of catalyst (~50 mm) was supported centrally within the reactor tube (8 mm ID, 430 mm length) on a plug of quartz sand (~190 mm length), separated by quartz wool (~5 mm length). A layer of quartz sand (~70-100 mm in length) was poured on to the top of the bed to ensure that the gases entering the reactor were heated to the desired temperature. In a typical experiment, ~0.5 g of catalyst was diluted with 1.5-2.0 g of alumina. The dilution of the catalyst particles was necessary in order to maintain an isothermal catalyst bed, given the substantial exothermicity of the reaction.

When preparing the fixed-bed reactor, the mixture of catalyst and alumina particles was poured on to the supporting quartz plug within the tube. The resulting bed was then separated from the top quartz sand layer by a small plug of quartz wool, as shown in Figure 2.6. A K-type thermocouple (Autoclave Engineers) was inserted from the top of the reactor and the tube was sealed. Between experimental runs, the tube was thoroughly cleaned, with particular attention paid to the sealing faces and threads on the tube closure. The sealing of the reactor was verified with a pressure test at 30 bar and room temperature for a period of at least 24 hours.

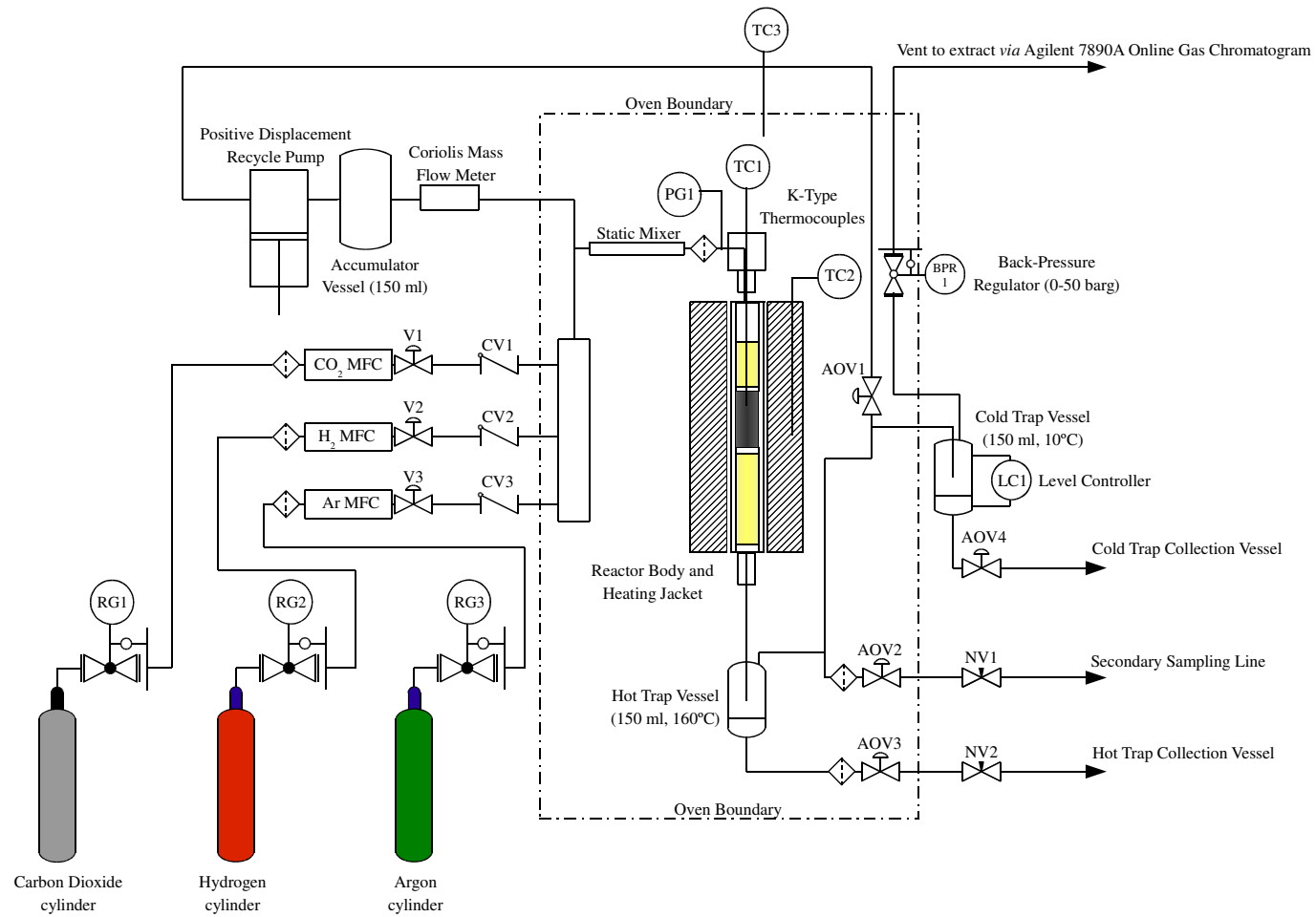


Figure 2.5 Schematic diagram showing the Bench Top Reactor System (BTRS). The recycle was unused and blanked off during the experiments in this Dissertation.

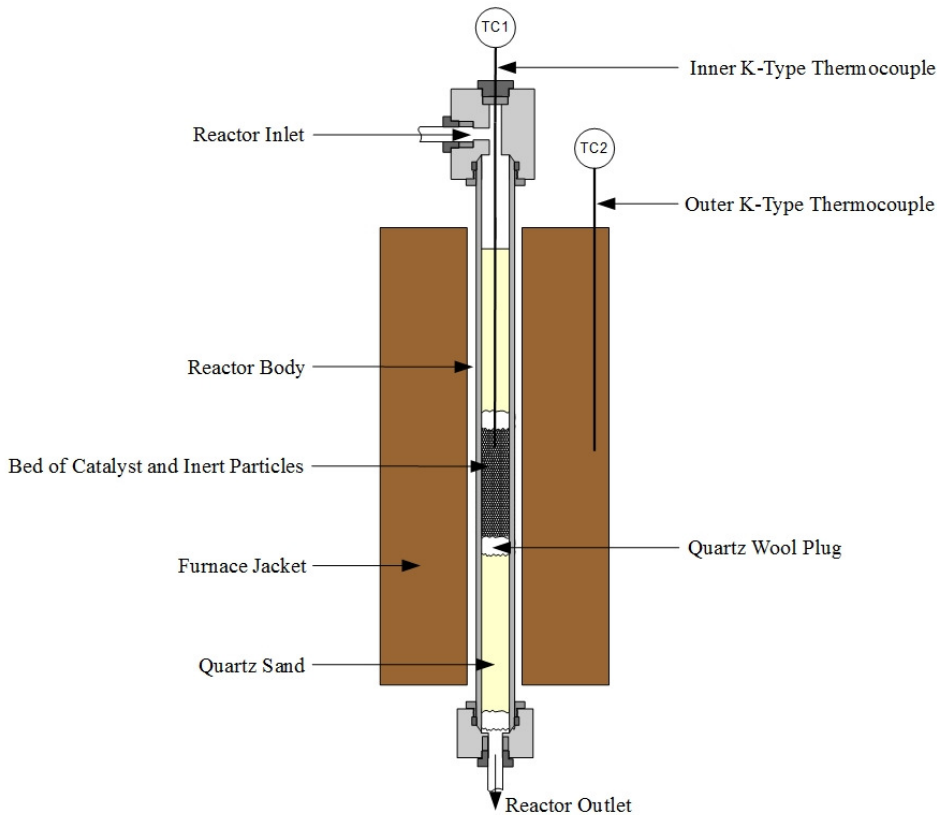


Figure 2.6 Schematic of reactor internals for 8 mm internal diameter reactor.

Once it had been ascertained that the apparatus was gas-tight, the system was depressurised and purged using argon. The temperature within the oven shown in Figure 2.5 was raised to 160°C and held for a sufficient time for temperature equilibration of the reactor and pipework. Following this, electrical power was supplied to the furnace jacket surrounding the reaction tube so that the temperature in the tube reached the reduction temperature of 250°C. Once the temperature within the centre of the reactor had reached a steady state (~1 hour), hydrogen gas at atmospheric pressure was passed over the catalyst at 300 cm³/min (at STP) for a period of 6 hours. After this period, the reactor was purged of hydrogen using argon. The apparatus was then prepared for kinetic experiments by raising the pressure to the desired set point, typically 10-20 barg, and changing the temperature of the reactor, by means of its external furnace, to the desired reaction temperature. This resulted in a reactor filled with argon at the desired temperature and pressure.

An experiment was commenced by admitting the reactant feed gas to the bed. The gases were supplied by three mass flow controllers (SLA5800, Brooks Instruments). The carbon dioxide (Air Liquide), and hydrogen (Air Liquide) reactants, together with argon (BOC plc.) as a standard, were supplied at 50 barg from cylinders *via* the mass flow controllers to the system. The mass flow controllers were re-calibrated before each experimental campaign using a digital bubble film flowmeter at a range of flows appropriate

to each controller. The recalibrations were required to account for slight changes in the heat capacity of the reactant gases with inlet pressure. In the case of CO₂ calibration, the soap film was exposed to CO₂ for approximately 30 minutes prior to measurement to remove the influence of CO₂ dissolution on the flow measurements. All set points were adjusted using a connected computer (Hewlett Packard) with Wonderware Industrial Automation software (Wonderware, Schneider Electric), which also acted as a data logger for flow, temperature and pressure measurements.

Prior to being passed over the catalyst bed, the gases were premixed by an inline mixer and heated to 160°C within the oven compartment. The oven was capable of operating at 200°C; however, the heating elements were found to degrade significantly and fail when operating at temperatures exceeding 160°C.

According to Delgado *et al.* (2005), there would be a significant effect on the measured behaviour due to radial variation in gas velocity in the bed if the ratio of bed diameter to particle diameter were < 15. In the present system, using an 8 mm ID bed and a maximum diameter of particles of 212 µm, this ratio is 38, hence any radial variation is unlikely to be significant enough to influence the reactors behaviour, and thus plug flow of the gases could be safely assumed.

The gases leaving the base of the reactor were first passed through a hot trap, consisting of a 150 ml stainless steel vessel maintained at reaction pressure and 160°C. The trap could be drained as necessary into a collection drum, with the flow of any condensate or gas being metered by a needle valve (NV2 in Figure 2.5). However no condensate was observed from the hot trap for CO₂ methanation. Gaseous reactants and products leaving the hot trap then passed through the cold trap, maintained at 15°C by a cooling jacket surrounding the trap. The remaining gaseous components were then passed through the back pressure regulator, reducing their pressure to atmospheric. This gas phase was then passed through an online Agilent 7890A GC for FID and TCD analysis.

Any condensate collected in the cold trap was drained by opening AOV4 into a collection vessel below the BTRS either manually *via* the control interface or automatically due to the action of the level controller.

Temperature control within the reactor was achieved using three K-type thermocouples. Two of these thermocouples (TC1 and TC2 in Figure 2.6) were used in the control of the temperature of the fixed-bed, whilst the third (TC3 in Figure 2.5) provided input to a PID controller to maintain the temperature of the oven, and thus the hot liquid trap, at 160°C. Within the fixed-bed, a K-type thermocouple (1/16" OD stainless steel sheathed thermocouple supplied by Autoclave engineers) was inserted into the catalyst particles. It was

positioned close to the top (~5-10 mm deep) of the diluted catalyst plug to detect exothermic runaway. This internal thermocouple was linked to a solid-state relay to disable the gas supplies and heaters in the event of the bed temperature approaching the alarm limit. A second identical K-type thermocouple measured the external jacket temperature. The signal from this thermocouple was in turn used as an input for a PID controller to maintain the jacket temperature at the desired set-point.

2.4.3 Product Analysis

The gaseous products from the reactor were analysed online using the gas chromatograph detailed in §2.3. All parameters used for the analysis were the same as those used for the analysis of Carberry samples. Gas samples from the BTRS were injected online, in that sampled gas flowed continuously through the sample loops of the gas chromatograph. The gas within the sample loops was then injected at intervals into the columns through a switching of the GC's automated valves, in the same manner as the stagnant gas from the Carberry gas syringes was injected into the TCD and FID channels.

As with the analysis of the Carberry samples, an inert standard in the form of argon was included. The majority of the experiments with the BTRS were differential ones (<10% conversion of CO₂), so that the volumetric flow into the reactor could be considered to be equivalent to the volumetric flow out of the reactor.

2.4.4 Considerations in the Operation of a Fixed-Bed Reactor

A control experiment was carried out to verify that the catalyst support and reactor body were inactive for CO₂ methanation. A detailed consideration of the heat and mass transfer within the fixed-bed is given in the Appendix (§A2). For the investigations of chemical kinetics within the BTRS, conversions were maintained at low levels and under these conditions the system was found to be free from both inter-particle and intra-particle heat and mass transfer limitations.

2.4.5 Spatial Temperature Differences

Axial temperature gradients within the bed were characterised by the insertion of K-type thermocouples at different axial positions along its axis. The temperature profiles were measured in an inert bed consisting of quartz sand at atmospheric pressure. The temperature profiles were measured for reactor jacket temperatures of 260°C with the oven maintained at 160°C. The observed temperature profile is shown in Figure 2.7. In order to obtain reliable kinetic measurements, near-isothermal conditions must be used. Hence, it was important to locate the catalyst within the bed where the temperature was most uniform, and to minimise the potential for hotspots by mixing the catalyst inventory with inert diluent. The central 50 mm of the bed were identified as being pseudo-isothermal, that is exhibiting a difference in temperature of less than 1°C axially.

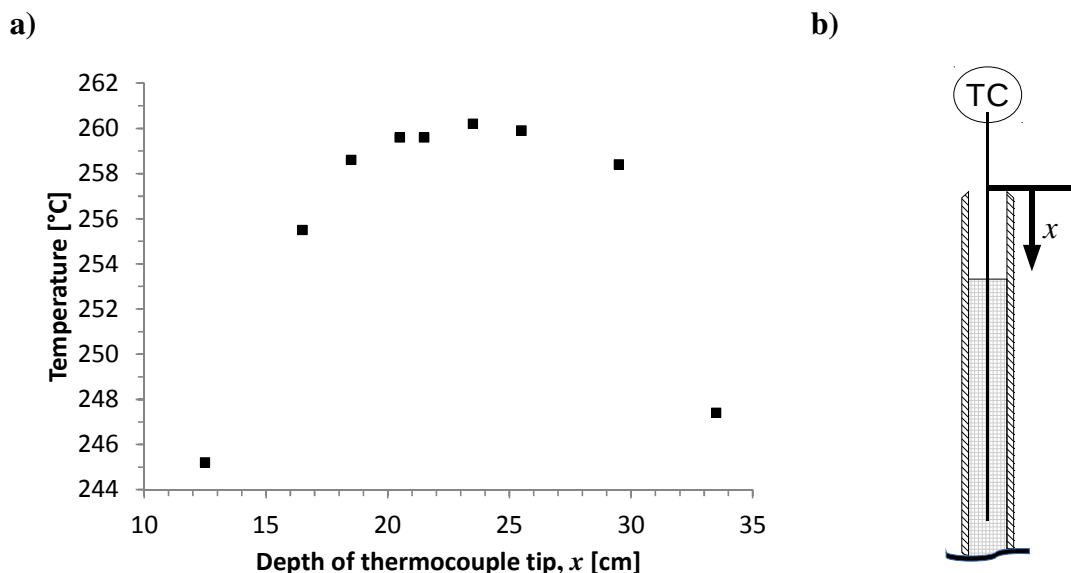


Figure 2.7 a) Axial temperature profiles within the fixed-bed at 260°C. **b)** Diagram of temperature measurement reference point used.

2.5 Catalyst Particle Characterisation

This section outlines the details of the equipment used in the characterisation of the nickel and cobalt catalysts. Catalysts were characterised by gas adsorption analysis, X-ray diffraction, thermogravimetric analysis (TGA) and chemisorption analysis (TPR/H₂ Pulse). Further details of the temperature programmes and settings used for the TGA and chemisorption experiments are given subsequently in Chapter 3.

2.5.1 Gas Adsorption Analysis

The pore size distribution and specific surface areas of various catalyst samples were determined using a gas adsorption analyser (ASAP 2000, Micromeritics). The samples were placed in a sampling tube prior to being degassed *in vacuo* at room temperature. Nitrogen at 77 K was then introduced to the degassed sample. The introduction of nitrogen results in a gradual increase in pressure within the sample tube, depending on the adsorption of nitrogen to the surface of the catalyst. The nitrogen was then desorbed from the surface by degassing the vacuum tube. The quantities of nitrogen adsorbed and desorbed permit the specific area to be calculated using the BET model (Brunnauer *et al.*, 1938). The pore size distribution was determined from these measurements using the BJH model (Barrett *et al.*, 1951).

2.5.2 Thermogravimetric Analysis

Thermogravimetric analysis (TGA) was used to characterise the behaviour of the cobalt and nickel catalysts under reductive conditions. The purpose of these studies was to investigate how the reduction and passivation processes affected the mass of active metal available under the reaction conditions. A cantilever type TGA (TGA/DSC1, Mettler-Toledo) was used, with its configuration shown in Figure 2.8 and Figure 2.9. In each experiment, a mass of catalyst sample, typically 20-60 mg, was placed into a 70 µL alumina crucible. The crucible was then placed onto a balance beam within an electrically-heated furnace chamber. The microbalance, accurate to 1 µg, was connected to the balance beam within a cooled balance enclosure, with the balance protected from reactive gases by a protective gas flow of argon (~50 cm³/min at STP), which flowed from the balance chamber, through the furnace chamber, to the exhaust. An additional purge flow of argon (~50 cm³/min at STP) was used to purge the furnace of reactants and products, with the reactant gases supplied *via* a fine capillary mounted on the cantilever arm terminating just above the crucible. The reduction of the material was achieved using a stream of 5% H₂/N₂. The temperature of the crucible could

be held isothermally or ramped, with the reduction experiments using a ramp rate of 10°C/min. Samples were typically dried at 120°C for 90 minutes *in situ* under the protective and purge gas flows.

The masses measured by the TGA were normalised based on the dried mass; that is, the measured mass of the sample after 90 minutes at 120°C under the protective argon gas flow. The use of relative mass allowed for the subtraction of changes in weight associated with the catalyst support; hence the measured mass changes could be attributed directly to changes in the oxidation state of the surface metal.

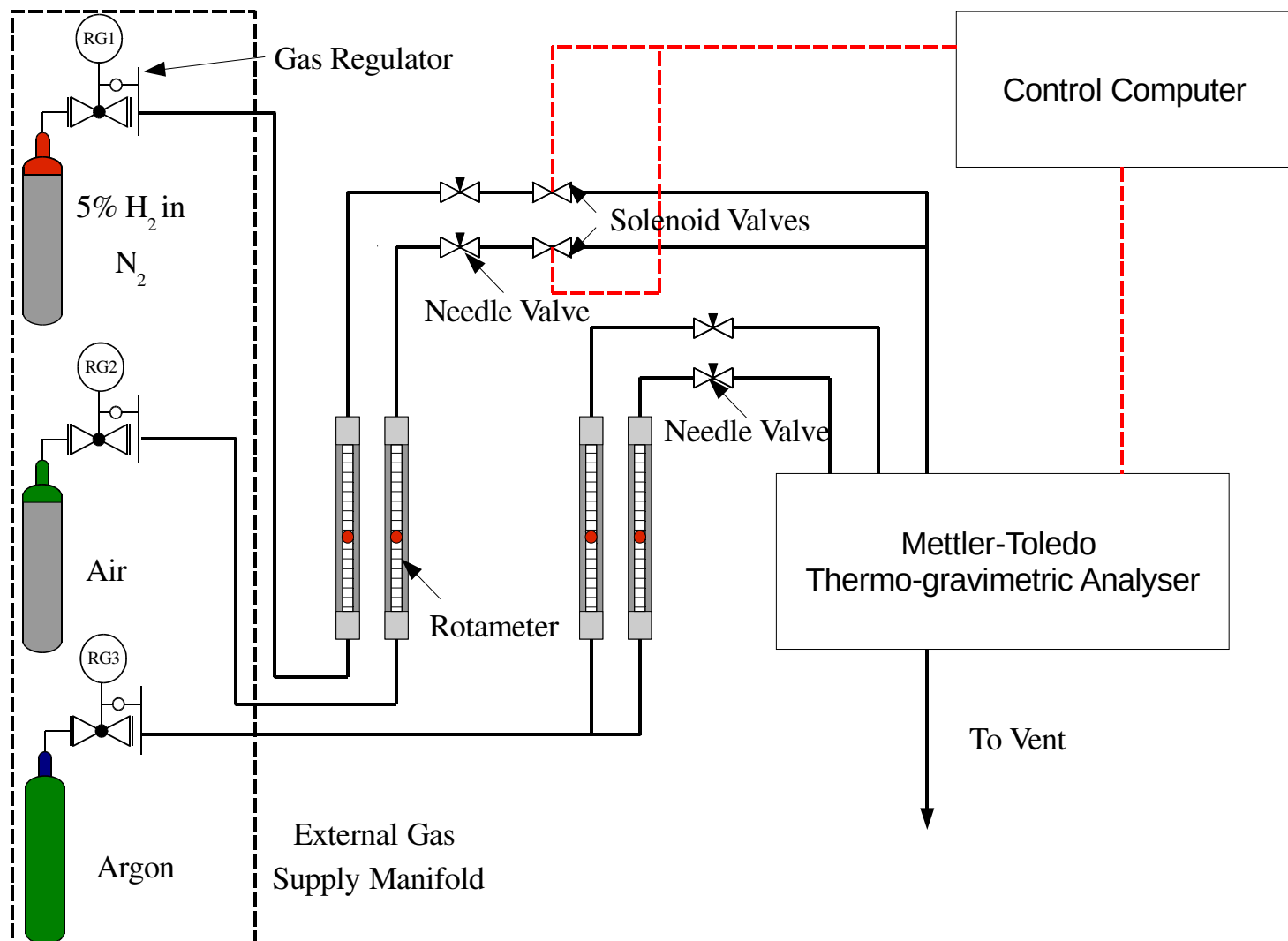


Figure 2.8. Schematic diagram of the Thermogravimetric Analyser.

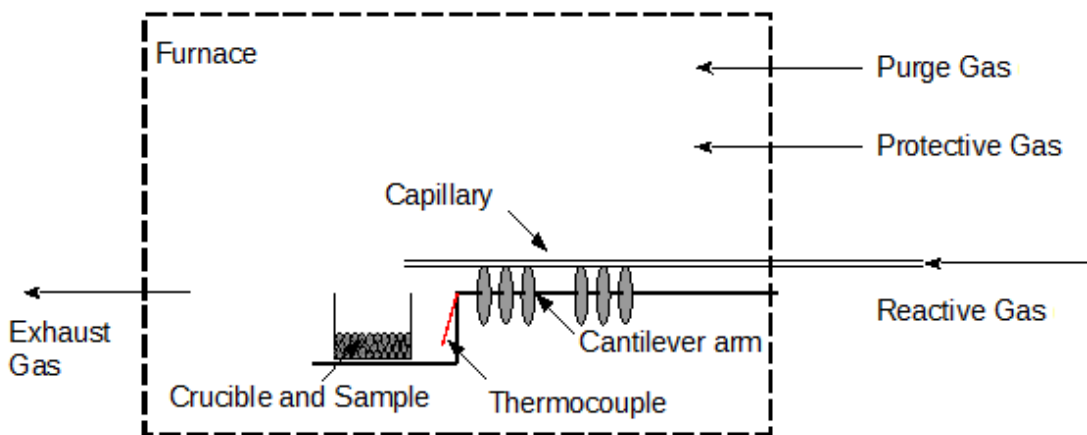


Figure 2.9. Schematic diagram of furnace chamber of the thermogravimetric analyser, showing cantilever arm and sample placement.

2.5.3 X-Ray Diffraction

X-ray diffraction was used to identify any differences in the crystalline phases present in the samples. The samples were ground and sieved to a size fraction of 106–212 µm. The ground samples were placed in the centre of a highly-crystalline sample holder formed of Si and Pt. The apparatus is shown in Figure 2.10, consisting of the sample holder, a beam gun and the X-ray detector. Measurements were taken by rotating the beam gun about the stationary sample.

The X-rays were generated by a Philips PW 1820HT generator, operating at 40 kV and 40 mA. The reflection angle was varied between 5° and 80° at a rate of 0.06 °/s. Peaks were assigned to different compounds through comparison with known inorganic compounds.

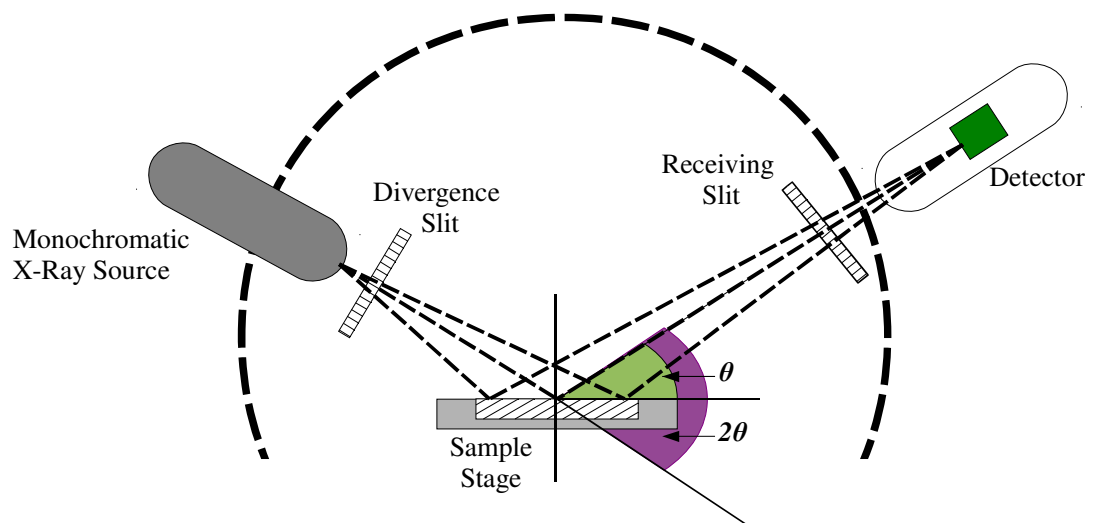


Figure 2.10. A schematic diagram of the X-Ray diffractometer.

2.5.4 Temperature Programmed Reduction and Pulse Chemisorption Measurements

Temperature programmed reduction (TPR) and pulse chemisorption studies were performed using a Micromeritics Autochem II 2920. In each experiment, batches of ~0.1 g of powdered catalyst were loaded atop a quartz wool plug within a U-shaped quartz reactor. The mass of each batch was measured using a balance accurate to 0.1 mg.

The U-shaped reactor was inserted within a furnace jacket assembly, with the sample temperature measured by a K-type thermocouple in contact with the powdered sample. Once sealed, TPR or pulse chemisorption experiments were carried out. The gas flowrates were controlled using mass flow controllers. The machine employed a TCD to monitor differences in thermal conductivity between the reactor outlet and a reference gas. This permitted the extent of reactant consumption to be determined.

The temperature programmed reduction and the H₂ pulse chemisorption experiments used 5 vol% H₂ in Ar (BOC Gases). The reference gas was argon (Air Liquide, 99.998% purity). The samples were dried *in situ* under a flow of helium or argon at 120°C for 30 minutes prior to analysis.

3 Synthesis and Characterisation of Supported Nickel and Cobalt catalysts

3.1 Introduction

Nickel catalysts are generally used in the methanation of either CO or CO₂, whilst Co-based catalysts are employed in the hydrogenation of carbon oxides to higher hydrocarbons. When CO₂ rather than CO is hydrogenated, the products over cobalt are shifted to lighter hydrocarbons and methane.

In this Dissertation, a supported nickel catalyst and a supported cobalt catalyst have primarily been used to catalyse the hydrogenation of carbon dioxide. The experimental studies conducted employed either a catalyst consisting of 4.5 wt% cobalt supported on zirconia or a 12 wt% nickel supported on alumina catalyst, with the preparation and characterisation of these materials described below in §3.3-§3.5. The purpose of this Chapter is to describe the methods of synthesis and characterisation of the catalysts used. The objective in synthesising catalysts was to obtain a stable and consistent material for use in studies of kinetics, rather than aiming at a catalyst formulation of high activity. The following section presents an overview of the literature concerning the preparation of cobalt and nickel catalysts and how the method of synthesis can influence the resulting activity.

3.2 Background

This section summarises previous investigations of the hydrogenation of carbon oxides, with a focus on those using cobalt or nickel catalysts. These catalysts are most commonly formulated using either impregnation or co-precipitation methods. The former disperses the active metal within a stable and inert support structure, whereas the latter forms a bulk catalyst, consisting of an intimate mixture of the active phase with a binder material. Catalysts employing cobalt or nickel as the active phase are often of the supported type, since the use of a catalyst support permits the efficient dispersion of the active metal across a high surface area within the porous material. Apart from effective dispersion of active metal, supported catalysts usually offer desirable mechanical and thermal properties requisite for operation within industrial reactors (Perego and Villa, 1997).

The main constraint of the impregnation method is the maximum amount of active metal that can be effectively incorporated. The solubility of the metal salt in the impregnation solvent and the pore volume of the support limit the maximum metal loading achieved in a

single impregnation step. Excess metal loadings may result in pore blockage and thus a reduced efficacy for the given loading of metal. On the other hand, co-precipitation methods form a bulk catalyst, with the active metal dispersed throughout the structure of the catalyst rather than being confined to the surfaces of the pores. The co-precipitation method may be used to produce catalysts of higher metal loadings than those prepared by impregnation. For example, Kruissink *et al.* (1981) developed co-precipitated nickel alumina catalysts for CO methanation with nickel contents ranging from 24.5 to 41.2 wt%. Cobalt-based catalysts for CO₂ hydrogenation catalysts have similarly been prepared by co-precipitation, *e.g.* Akin *et al.* (2002) (36 wt% Co) and Riedel *et al.* (1999) (32.5 wt% Co). High loadings may not make efficient use of the active metal, due to its incorporation into the bulk. Increased metal loadings have been found to favour sintering, with Bartholomew (2001) reporting the activation energy for sintering decreases with increasing metal fraction. This increase in sintering may result in the formation of larger particles, and thus a reduced active surface area.

Recent research on nickel catalysts for methanation has focused on the enhancement of catalytic activity, mainly through the use of either novel supporting materials and, or, the incorporation of dopants. Doping elements such as Fe, Co, Ce and La have been recently demonstrated by Lu *et al.* (2016) to enhance the dispersion and thermal stability of nickel on a zirconia support. Promotion may influence the structure of a catalyst, with the presence of the promoter altering the form of the active metal crystallites during the preparation process. For instance, vanadium oxide was reported to improve CO and CO₂ methanation rates through the enhancement of nickel dispersion (Liu *et al.*, 2014). Liu *et al.* (2014) attributed the enhancements to the formation of mixed vanadium nickel oxides during calcination, with subsequent reduction resulting in the formation of smaller nickel particles (~3 nm), yielding an increased nickel surface area. A promotor's action may be electronic in nature, with MacLaren *et al.* (1987) reporting potassium addition to nickel resulted in a decreased work function, a greater binding energy for CO and consequently an improved methanation activity.

The nature of the support and the interaction with the active metal phase strongly influences the overall reducibility, stability and methanation activity of the catalyst. The extent of bonding between the support and the metal may influence both the geometric form of the particles on the surface, as well as their electronic character. Recent studies have sought to improve the CO₂ methanation activity of nickel through investigation of novel supports, *e.g.* USY zeolite (Westermann *et al.*, 2015), iron bearing olivine (Wang *et al.*, 2016), and hydrotalcite-like structures (Abate *et al.*, 2016). Ceria, when used as a support, has been noted for its promotion of CO₂ methanation, with Rahmani *et al.* (2014) and Feng *et al.* (2014)

reporting increased reaction rate. Pan *et al.* (2013) found that their support containing a mixture of ceria and zirconia showed high CO₂ methanation activity, attributing this to an increase in ‘medium’ basic sites for CO₂ adsorption.

Developments in cobalt catalysts for the hydrogenation of carbon oxides have focused on modifications applied to staple catalyst supports *e.g.* Al₂O₃, TiO₂, SiO₂ (Owen *et al.*, 2016, Kangvansura *et al.*, 2014), as well as on the utilisation of novel supports *e.g.* graphene (He *et al.*, 2013), carbon nano-fibres (Diaz *et al.*, 2013,), and BaZrO₃ perovskite (Shin *et al.*, 2016). The behaviour of cobalt in the hydrogenation of CO compared with CO₂ differs significantly in its product selectivity, with CO₂ mainly producing methane and CO a spectrum of linear alkenes and alkanes. Some have attempted to shift the selectivity of the CO₂ methanation towards higher hydrocarbons by judicious doping of the cobalt, *e.g.* Owen *et al.* (2016), Dorner *et al.* (2009). These attempts have met with some success, with Owen *et al.* (2016) achieving a selectivity for C₂₊ hydrocarbons of 40-80% using a promoted (Na, Mo) mixed silica-titania support, albeit with a significant proportion of the CO₂ being converted to CO (20-67% CO selectivity) *via* the reverse water gas shift reaction.

Zirconia has been used as both a support and a promoter in the hydrogenation of carbon oxides, and has been applied in the Fischer-Tropsch process to increase the selectivity to C₅₊ hydrocarbons. The effect of zirconia promotion appears dependent on the type of support. For example, Hong *et al.* (2010) reported no influence of zirconia when used with Co on a wide-pored silica support; however, promotion of narrow pored silica (MCM-41) resulted in larger but easier to reduce cobalt particles. This observation differed from that of All *et al.* (1995), who found that the co-impregnation of zirconia and cobalt increased both the observed reaction rate and the dispersion of cobalt on their silica support. A similar increase in dispersion was reported by Mu *et al.* (2010); however, the authors noted that the increase in dispersion resulted in a lower reducibility. Using zirconia as a support, Chen and Sun (2004) formulated a Co/ZrO₂ catalyst for CO hydrogenation. The catalyst showed high dispersion at low loadings; however the selectivity towards methane was undesirably high. This observation runs counter to the work of Enache *et al.* (2004), who reported that their Co/ZrO₂ catalyst exhibited superior reducibility and superior activity at low pressure, but with similar selectivity, to an alumina-supported reference catalyst.

Methane remains the dominant product for the majority of cobalt catalysts during the hydrogenation of carbon dioxide, and a few investigators have focused on improving the selectivity and maximising the intrinsic activity and stability of cobalt for the production of synthetic natural gas (SNG) *e.g.* Beaumont *et al.* (2016), Razzaq *et al.* (2015). Beaumont *et al.* (2016) supported platinum and cobalt nanoparticles on a mesoporous silica (MCF-17),

achieving a 6-fold increase in methanation activity, which they attributed to an increased reducibility of the cobalt and a greater availability of surface hydrogen due to spill-over from the platinum nanoparticles. This behaviour differs from that observed by Porosoff and Chen (2013), who found platinum promotion increased the rate, but shifted the selectivity towards methane on their alumina-supported cobalt catalyst. They attributed the shift to changes in the d-band centre of the bimetallic catalyst particle. The differences in the observations may be due to the greater loading of Pt and the formation of mixed Co-Pt particles in the catalyst of Porosoff and Chen (2013), rather than the separate discrete nanoparticles of Beaumont *et al* (2016).

3.2.1 Method of Preparation

A myriad of conditions have been selected by workers for the preparation of carbon oxide hydrogenation catalysts. A selection of these are summarised below in Table 3.1 for both nickel- and cobalt-based hydrogenation catalysts. In most cases, a calcination step is applied at a temperature such that the metal salt precursor is decomposed into the respective metal oxide. Calcined material is then activated *via* reduction of the metal oxide, typically in a hydrogen atmosphere. The reduction temperature is then often selected based on temperature programmed reduction (TPR) analysis of the calcined material, e.g. Abello *et al.* (2013), Weatherbee and Bartholomew (1982), such that the metal oxide is reduced to the metallic phase.

Table 3.1 A summary of calcination and reduction temperatures for a selection of studies.

Support	Precursor salt	Method	Calcination Temperature [°C]	Reduction Temperature [°C]	Reference
Cobalt Catalysts for CO Hydrogenation					
Al ₂ O ₃ & SiO ₂	Co(NO ₃) ₂	Multi-step IWI	400	350	Zhang <i>et al.</i> (2002)
SiO ₂	Co(NO ₃) ₂ Co(CH ₃ CO ₂) ₂	IWI	Up to 400	400	Giradon <i>et al.</i> (2005)
SiO ₂	Co(NO ₃) ₂ (Solutions and melts)	Impregnation	350	420-450	Iglesia <i>et al.</i> (1995)
Al ₂ O ₃ , MgO, TiO ₂ , SiO ₂ , ZSM-5 and C	Co(NO ₃) ₂	Impregnation	500-550	350	Bessell (1993)
Cobalt Catalysts for CO₂ Hydrogenation					
SiO ₂ , Al ₂ O ₃ , MgO, TiO ₂ , Nb ₂ O ₅ , CeO ₂ , ZrO ₂	Co(NO ₃) ₂	Impregnation	500	550	Das and Deo (2012)
ZrO ₂	Co(NO ₃) ₂	Impregnation	500	350	Chitpong <i>et al.</i> (2009)
SiO ₂	Co(NO ₃) ₂	Impregnation	350	250 or 350	Gnanamani <i>et al.</i> (2016)
Al ₂ O ₃ , SiO ₂	Co(NO ₃) ₂	IWI	400	350	Zhang <i>et al.</i> (2002)

Nickel Catalysts for CO ₂ Hydrogenation					
Al ₂ O ₃	Ni(CH ₃ CO ₂) ₂	Sol-gel	700	700	Hwang <i>et al.</i> (2011)
Al ₂ O ₃	Ni(NO ₃) ₂	Coprecipitation	450	500	Abello <i>et al.</i> (2013)
Ceria-Zirconia	Ni(CH ₃ CO ₂) ₂	Sol-gel/ Wet Impregnation	500	400	Aldana <i>et al.</i> (2013)
Rice-husk ash alumina	Ni(NO ₃) ₂	IWI	500	800	Chang <i>et al.</i> (2003)
SiO ₂	Ni(NO ₃) ₂	IWI	Direct Reduction of precursor	477	Weatherbee and Bartholomew (1982)
Al ₂ O ₃	Ni(NO ₃) ₂	IWI	450	700	Lim (2014)

The majority of studies contained in Table 3.1 select reduction temperatures around 250-500°C. Under these conditions, the temperature may reduce the metal oxide into the metallic phase. However, complete reduction is not always obtained, nor sought, since the use of higher reduction temperatures may promote thermal sintering and thus a reduction in the observed reactivity.

In this dissertation, both γ -alumina and yttria-stabilised zirconia have been used as supports, with the catalysts prepared using incipient wetness impregnation. This consists of introducing a solution of a metal salt into the support material, such that the volume of solution is equal to the internal pore volume. The resulting catalyst precursor is then transformed into the catalyst through drying, calcination of the metal salts to metal oxides, and reduction of the metal oxides to the active metal phase.

The means of preparation can have a significant influence on the activity of an impregnated catalyst. It is important to use deionised water for the solution of the metal salt to avoid contamination of the catalyst by the ions present in water. Sodium, for example, has a negative effect on the hydrogenation rate for cobalt Fischer-Tropsch catalysts, even for a modest increase in sodium ion concentration from 20 ppm to 120 ppm in the impregnated solution (Borg *et al.* 2007). The metal salt selected also has a significant impact on the final activity. Cobalt nitrate hexahydrate is commonly used in the preparation of cobalt catalysts, owing to its solubility in water and cost. However, Kraum and Baerns (1999) reported that catalysts prepared using organic cobalt salts may display higher Fischer-Tropsch activity than those prepared *via* nitrate. The authors attributed the change to a diminished interaction between the support and metal particles. Van de Loosdrecht *et al.* (1997) reported a greater activity for catalysts prepared using the nitrate than those prepared using citrate or EDTA salts. However, the authors noted that this could have been owing to the nitrate precursor forming larger, and thus more easily reduced, cobalt particles. The conclusions of van de Loosdrecht *et al.* (1997) appear at odds with Kraum and Baerns (1999), however the differences in reducibility and particle size noted by van de Loosdrecht *et al.* (1997) support their reactivity trend. Differences in the support material, with van de Loosdrecht *et al.* (1997) employing mainly γ -alumina and Kraum and Baerns (1999) using titania for their comparison, may also explain the discrepancies.

Similarly, nickel nitrate hexahydrate is commonly used as a precursor in the preparation of nickel catalyst, *e.g.* Zhou *et al.* (2013) and Vance and Bartholomew (1983). Campelo *et al.* (1983) compared nickel surface areas for AlPO₄ supported nickel prepared from nitrate, acetate and chloride salts, noting the trend nitrate>acetate>>chloride. The trend in surface area corresponded reasonably with the author's observed 1-hexene hydrogenation

rates, with the nitrate preparation exhibiting the greatest reactivity. This differs from the trends observed for titania-supported nickel produced by Urasaki *et al.* (2013). These workers determined the influence of the precursor on CO hydrogenation in reformate gas, with the activity decreasing in the following order acetate > nitrate > formate > chloride > sulphate. It appears the effect of the precursor salt for nickel depends on both the support and the salt, with nitrate and acetate precursors yielding the highest activities for hydrogenation. Chloride salts may also form HCl on decomposition, hence it is prudent avoid their use when working with metal bodied reactor systems.

The drying step has been shown to influence the distribution of the active metal salt within the support as well as the metal particle size and its dispersion within the final catalyst. Munnik *et al.* (2014) examined the influence of drying on cobalt distribution using transmission electron microscopy (TEM) and scanning electron microscopy (SEM). These authors prepared a series of catalysts consisting of 16.2 wt% Co supported on silica using incipient wetness impregnation. The nitrate impregnated support was then dried at temperatures between 25°C and 175°C in nitrogen prior to calcination at 350°C. Munnik *et al.* (2014) reported that under all drying conditions the cobalt crystallite size determined by XRD post calcination remained consistently ~8-9 nm. However, the distribution of these crystallites within the support varied, with the most uniform obtained for material dried at 100°C. Whilst the observed cobalt crystallite size was not significantly influenced, the distribution of crystallites within the catalyst was altered. The aggregation of cobalt has been associated with deactivation in CO hydrogenation catalysts and may result from greater migration of cobalt within the pores.

After drying, the catalyst precursor is subjected to calcination to decompose the metal nitrate to a metal oxide. This step has a significant influence on the dispersion and subsequent reducibility of the metal. The temperature must be high enough to decompose the salt; however, excessive temperatures can result in a stronger interaction between the metal and support, and thus the potential formation of irreducible and inactive compounds (*i.e.* metal aluminates, titanates and silicates). The rate of nitrate decomposition has been shown to be important for the formation of active cobalt catalyst, with van de Loosdrecht *et al.* (2003) noting that high concentrations of water and NO_x in the gas phase during decomposition can enhance sintering of cobalt. High rates of heating, in excess of 1°C/min, gave decreased activity when the resulting catalyst was used to hydrogenate CO.

Finally, it is necessary to activate the nickel or cobalt for CO and CO₂ hydrogenation. The reduction step is commonly achieved by passing hydrogen across the calcined catalyst at elevated temperature. A dispersed catalyst is obtained when there is a strong interaction

between the support and the metal oxide crystallites; however, strong interaction may result in a material which is difficult to reduce (Soled *et al.*, 2003). The use of high reduction temperatures, as with calcination, may result in the agglomeration of metal particles, resulting in a loss of active metal surface area. Hence, the temperature at which the maximum activity is obtained is specific to the metal and support, with low temperatures resulting in partial reduction, and higher temperatures enhancing crystallite agglomeration and consequently loss of metal surface area. In agreement with the observations of van de Loosdrecht *et al.* (2003), Soled *et al.* (2003) reported an influence of the temperature ramp rate on the hydrogenation activity of supported cobalt catalyst prepared *via* direct reduction in hydrogen of the nitrate precursor. The authors noted a lower ramp rate yielded a greater metal surface area, and thus a greater activity.

The aim of the preparations used herein was to produce a catalyst with stable and moderate activity. Hence formulations and methods for the preparation of high activity catalyst are beyond the scope of this work. For information on high activity or industrially relevant catalyst formulations, the reader is directed to the patent literature.

3.3 Experimental

3.3.1 Catalyst Selection

This thesis examines a nickel supported on alumina catalyst and a cobalt supported on zirconia catalyst. The nickel on alumina catalyst was selected and prepared in a similar manner to that of Lim (2014). The key purpose in the use of the Ni/Al₂O₃ catalyst was to investigate the differences in behaviour of the CO₂ methanation reaction under batch and continuous reaction conditions. The adoption of the alumina support and preparation method used by Lim allowed for the formation of a nickel reducible and active within the temperature constrained Carberry reactor. An unpromoted catalyst on an inert support was used such that any differences in behaviour could be attributed to reaction differences on the nickel rather than interaction with the support or promoters.

A Co/ZrO₂ catalyst was utilised to examine the kinetics over cobalt. Cobalt was selected as the active metal since it has received far less investigation than nickel for the CO₂ methanation reaction. A zirconia support was chosen for further examination having provided reasonable activity and stability for carbon oxide hydrogenation during initial studies. Zirconia was also identified as a support which had not received significant investigation in the relevant literature for CO₂ hydrogenation.

3.3.2 Preparation of the Nickel on Alumina Catalyst

The details of this process are described in the following section and any differences between the preparation method of Lim (2014) and that used herein will be highlighted. This nickel on alumina catalyst was selected in order to expand upon the initial kinetic studies of Lim (2014). A similar preparation method was adopted in order to produce an active catalyst capable of being reduced within the Carberry reactor. The differences in the method necessitated by safety considerations and equipment differences are outlined in Table 3.2.

The 12 wt% Ni/Al₂O₃ catalyst was prepared using the single step incipient wetness impregnation of γ -alumina (3 mm diameter spheres SA 62125, Saint Gobain Norpro). A 3.6 M solution of Ni(NO₃)₂ was prepared by mixing 12.7 g Ni(NO₃)₂·6H₂O with deionised water to a total volume of 12 ml. This was then combined with 18.75 g of γ -alumina support in a crystallising dish of 115 mm diameter.

Prior to calcination, the impregnated catalyst was dried for 24 hours at 120°C (5°C/min ramp from room temperature) in a chamber furnace (EF Series, Lenton Furnaces). The calcination was also undertaken in the furnace in still air, with the temperature being ramped between 120°C and 450°C at a heating rate of 5°C/min. Lim's (2014) preparation used a horizontal quartz tube within a Carbolite furnace fed with a 150 cm³/min flowrate of air, with an unspecified ramp rate to the calcination temperature. As noted previously, this can have a significant impact on the dispersion of catalysts derived from nitrate salts.

The reduction of the Ni/Al₂O₃ catalyst pellets was achieved in the apparatus shown in Figure 3.1. The temperature of the catalyst was raised to 700°C under a flow of nitrogen. A flow of 100 cm³/min (at STP) of 5% H₂ in N₂ was then introduced for the reduction of the catalyst. The reduction was for 6 hours before the hydrogen flow was discontinued. Lim (2014) reportedly reduced the calcined nickel under a flow of 100 cm³/min (at STP) flow of pure H₂. This was not possible with the apparatus in Figure 3.1, due to safety concerns regarding the use of pure hydrogen above its auto-ignition temperature.

After reduction, the flow of nitrogen was restarted. The furnace was allowed to cool to room temperature. Once at room temperature, the passivation procedure was commenced whereby the nickel metal was gradually re-oxidised. Due to the exothermic nature of the oxidation, the oxidant, in this case 5% O₂ in N₂, was bled into the nitrogen flow. For the first 1.5 hours of the procedure, 0.1 L/min (at STP) of 5% O₂ in N₂ was passed into the reactor, diluted by 1.5 L/min (at STP) of N₂. The nitrogen flow was then reduced by one third of the original flow each hour until the nitrogen was switched off. The passivation process was used to increase the reducibility of the Ni/Al₂O₃ catalyst for use in the batch reactor. Owing to the

Carberry reactor's temperature limit, a reduction temperature above 250°C could not be used. Through the passivation procedure, the quantity of active nickel available was maximised, with the efficacy of the procedure having been demonstrated by Lim (2014).

Table 3.2 A comparison of the preparation conditions used in this study and those of Lim (2014)

Parameter	This study	Lim (2014)
Ni weight%	12	12
Calcination Temperature	450°C	450°C
Calcination Ramp Rate	5°C/min	Unspecified
Calcination Environment	Static Air	Air (100 cm ³ /min at STP)
Calcination Time	3.5 hours at 450°C	3.5 hours held at 450°C
Reduction Temperature	700°C	700°C
Reduction Ramp Rate	Isothermal reduction	Isothermal reduction
Reduction Environment	5% H ₂ in N ₂ (100 cm ³ /min at STP)	100% H ₂ (100 cm ³ /min at STP)
Reduction Time	6 hours	6 hours
Passivation Method	Passivated with nitrogen diluted 5% O ₂ in N ₂ . Flowrates and duration: 1500 cm ³ /min N ₂ / 100 cm ³ /min 5% O ₂ (1.5 hour) 1000 cm ³ /min N ₂ /100 cm ³ /min 5% O ₂ (1 hour) 500 cm ³ /min N ₂ /100 cm ³ /min 5% O ₂ (1 hour)	Passivated with nitrogen diluted 5% O ₂ in N ₂ . Flowrates and duration: 150 cm ³ /min N ₂ / 50 cm ³ /min 5% O ₂ (1.5 hour) 100 cm ³ /min N ₂ /100 cm ³ /min 5% O ₂ (1 hour) 50 cm ³ /min N ₂ /150 cm ³ /min 5% O ₂ (1 hour) 0 cm ³ /min N ₂ , 100 cm ³ /min 5% O ₂ (1 hour)

3.3.3 Preparation of the Cobalt on Zirconia Catalyst

The cobalt on zirconia catalyst was prepared using the incipient wetness impregnation of zirconia catalyst support pellets (Saint Gobain Norpro, SZ 61157, 3 mm diameter cylindrical pellets) with a cobalt nitrate solution (Sigma-Aldrich). The pore volume of the pellets was reported as 0.26 cm³/g by the manufacturer and a 4.5wt% loading of cobalt metal was selected to allow the catalyst precursor to be obtained through a single impregnation step.

Incipient wetness impregnation was achieved by introducing a volume of Co(NO₃)₂ solution equal to that of the pore volume of a given mass of catalyst support. The introduced solution was drawn into the particle until the entire pore volume within the particle was filled. The catalyst was prepared batchwise, with 19.2 g of dry support being combined with a ~5 ml volume of 3.08 M Co(NO₃)₂ solution in a crystallising dish. The solution was prepared beforehand by mixing 8.95 g of Co(NO₃)₂·6H₂O with deionised water until the total volume was 10 ml.

The nitrate solution was added until the originally white pellets had evenly taken up the pink colour of the nitrate solution and the surface of the pellets had a glistening appearance. Excessive addition was avoided by placing a white card below the evaporating dish, such that excess nitrate solution was plainly visible.

Following impregnation, the catalyst precursor particles were dried in a chamber furnace (EF Series, Lenton Furnaces) at 120°C (5°C/min ramp from room temperature) for 24 hours. In order to transform the nitrate catalyst precursor into cobalt, the catalyst was calcined within the chamber furnace at a temperature of 450°C. The temperature was ramped between the drying temperature and the calcination temperature at a ramp rate of 5°C/min. Once the calcination set-point was reached, the temperature was held for 3.5 hours, after which the furnace was cooled to ambient temperature. Whilst the onset of decomposition for cobalt nitrate may occur at far lower temperatures than 450°C, this temperature was selected as it ensured the complete elimination of nitrate species from the catalyst precursor. The thermogravimetric experiments of Keely and Maynor (1963) demonstrated that temperatures in excess of 350°C are required to ensure near complete conversion of cobalt nitrates to cobalt oxides (>70 %wt loss).

The calcined catalyst was reduced directly within the reactor at 250°C under a flow of 300 cm³/min of H₂ for 6 hours. It is noted that the method of preparation of the cobalt catalyst might not be optimal for producing the highest activity catalyst. The use of a lower reduction temperature means the cobalt particles within the support cannot be fully reduced. The 5°C/min ramp rates used in the calcination may also have resulted in a reduced activity, with

high ramp rates associated with reduced activities in the literature.

3.3.4 Physical and Chemical Characterisation of the Catalysts

The prepared catalysts were characterised using various techniques, as described in Chapter 2 (§2.5). The surface area and pore size distribution were measured by gas adsorption analysis and determined by applying the BET and BJH models. Temperature-programmed studies were carried out using a Mettler-Toledo thermogravimetric analyser (TGA) and a Micromeritics Autochem 2920. Powder X-ray diffraction (XRD) was used to determine the different crystalline phases in each of the solid samples. Catalysts were analysed in their calcined state, as well as after having been reduced and passivated. Calcined catalyst supports were also analysed to provide a basis for comparison.

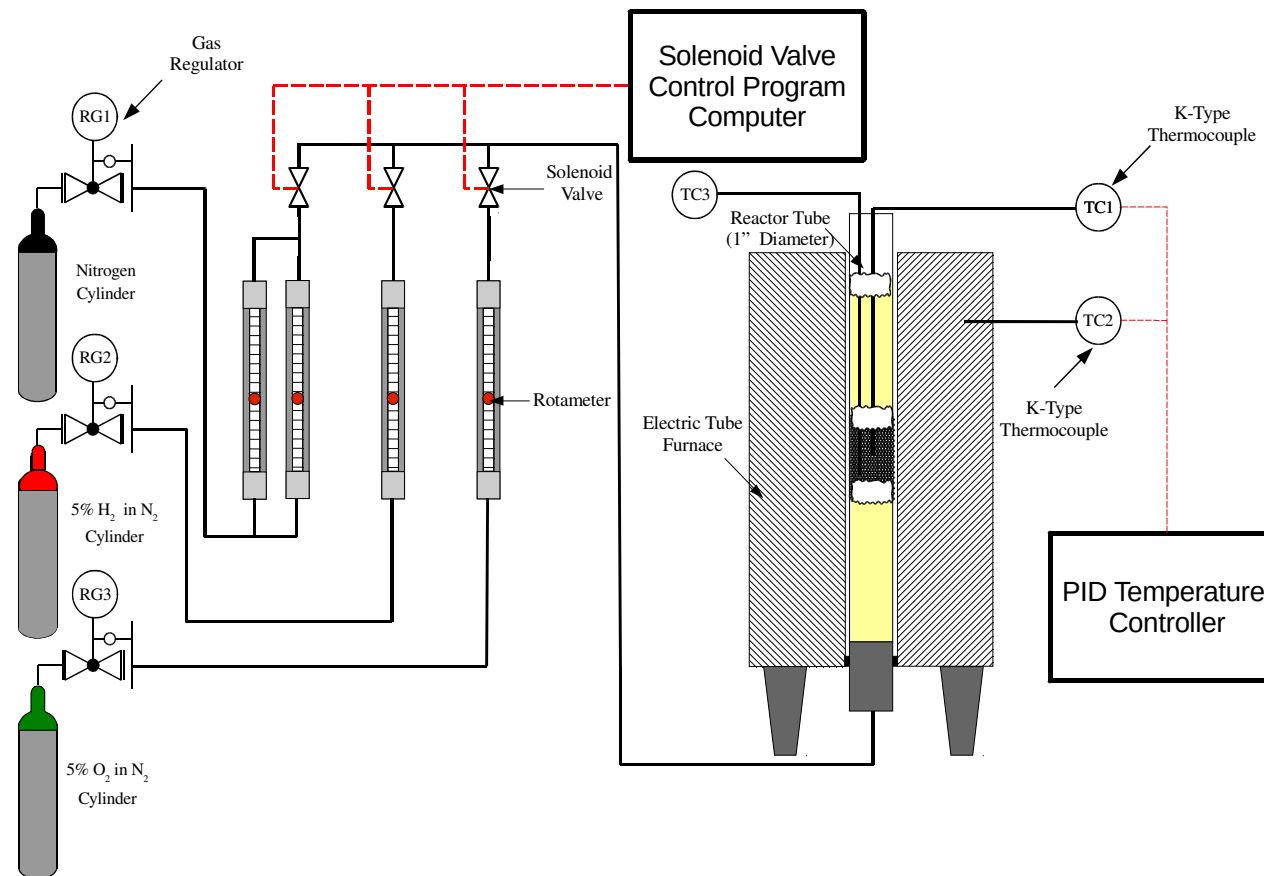


Figure 3.1. A schematic diagram of the catalyst preparation apparatus. Three cylinders were used to feed nitrogen, 5% hydrogen in nitrogen and 5% oxygen in nitrogen to a bank of rotameters at a pressure of 1 barg. The gas flows were manipulated using the rotameters with the gases entering the bed set by computer-controlled solenoid valves. The reduction temperatures were set using a PID temperature controller.

3.4 Characterisation of the Ni/Al₂O₃ Catalyst

3.4.1 Results: Gas Adsorption Analysis of the Ni/Al₂O₃ Catalyst

Table 3.3 shows the surface area, pore volume and pore widths, as determined by BET analysis, of catalyst and support samples at different stages of the preparation process. The analysis shows that the average pore diameter, determined assuming cylindrical pores, does not change significantly with the preparation. The impregnation and calcination of the support result in a slight decrease in the available surface area per gram as well as a slight decrease in pore volume. The addition of nickel to the support increases the catalyst mass, with the impregnation of the catalyst increasing the mass by 17.3%. In order to make a meaningful comparison of the catalyst material, the surface areas and pore volumes were compared on the basis of equivalent support mass.

The reduced and passivated catalyst material showed a decreased surface area and increased pore diameter. This may be attributed to minor structural rearrangement, blockage of micro-pores and sintering of the alumina support material at the elevated reduction temperature (700°C). The adsorption-desorption isotherms observed for the prepared catalyst were Type IV according to the IUPAC classification (Sing, 1982), a form corresponding to a mesoporous material, in agreement with the manufacturer's specifications.

Table 3.3. BET surface area and pore properties of the Al₂O₃ support and the Ni/Al₂O₃ catalyst.

Material	Alumina Support		Ni(NO ₃) ₂ Impregnated Support	
	Untreated	Calcined	Calcined	Calcined, Reduced and Passivated
BET Surface Area [m ² /g _{support}]	183.3	181.0	177.9	162.8
t-Plot External Surface Area [m ² /g _{support}]	182.6	183.9	177.4	160.2
BJH Ads Pore Volume [cm ³ /g _{support}]	0.547	0.525	0.505	0.516
Pore Width [nm]	10.98	11.34	10.85	12.27

3.4.2 Results: Thermogravimetric Analysis of the Ni/Al₂O₃ Catalyst

The composition of the Ni/Al₂O₃ catalyst was examined by thermogravimetric analysis. A sample of catalyst was subjected to a ramp in temperature to 120°C at 10°C/min from 50°C under the background flow of argon. The sample was then held at 120°C for 90 minutes to remove adsorbed water. At $t = 5880$ s, the capillary gas was set to a flow of 50 cm³/min (at STP) 5% H₂/N₂, and the temperature was ramped to 800°C at a rate of 10°C/min, where it was held for at least 2000 s before cooling under the argon background.

The changes in mass of the support, the calcined catalyst and the passivated catalyst are shown in Figure 3.2. The masses are shown as relative masses, determined by division of the measured mass by the sample mass after the drying period at 120°C. Relative masses were used for ease of comparison between the samples. After the drying period under argon, the gas switch to 5% H₂ in N₂ resulted in a transient disturbance in the balance reading. During the temperature ramp, all samples appeared to lose mass. For the support material, this continued mass loss on the support was attributed to removal of strongly adsorbed water.

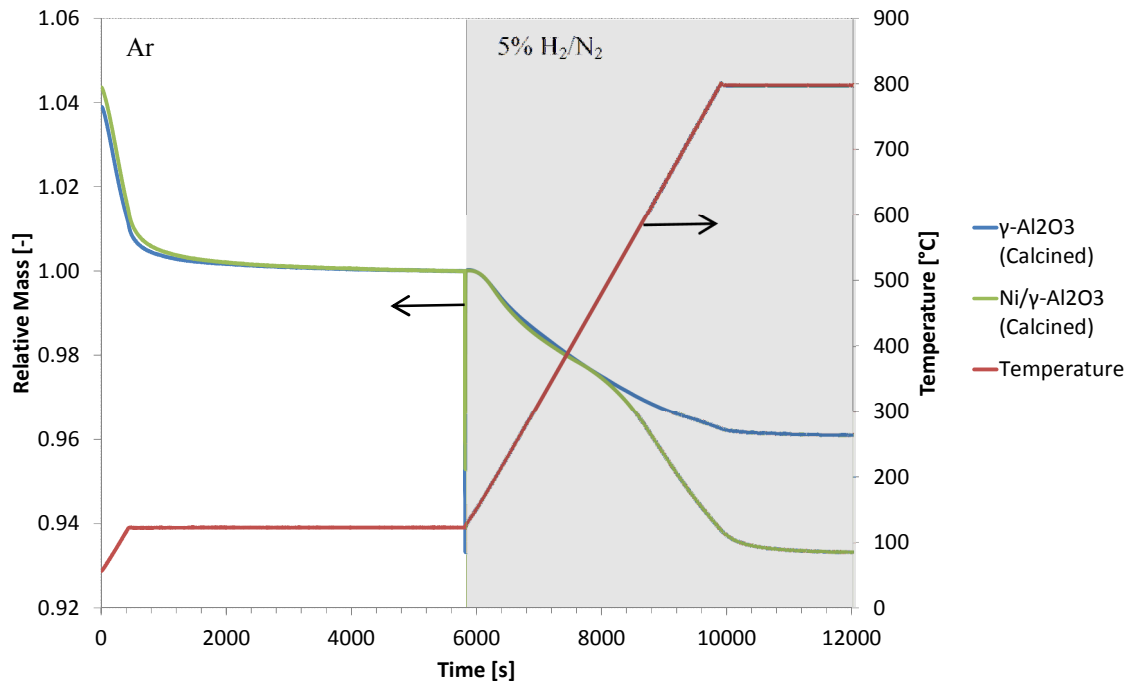


Figure 3.2. Thermogravimetric analysis of calcined Ni/Al₂O₃ and calcined support. The shaded rectangles indicate period the capillary gas (5% H₂/N₂) was switched on. Initial sample mass ~34 mg.

In order to determine the mass lost due to nickel oxide reduction, the mass of the support material was subtracted from that of the calcined catalyst mass. By assuming all the nickel oxide (NiO) was converted to metallic nickel, the weight percentage of nickel on the catalyst was determined to be 13.5 %. The loading was calculated from the difference in mass

between the calcined catalyst before and after reduction at 800°C, less the contribution of water desorption, determined from the mass loss of the support.

Figure 3.3 shows the rate of mass change with temperature of the calcined nickel alumina due to nickel reduction. The mass loss due to drying was accounted for by subtracting the mass profile of the calcined support. The rate of mass change showed a small peak at ~200°C and a larger peak at ~630°C showing significant breadth. The rate of mass loss was non-zero at 800°C; however this value reached near zero after being held at 800°C for approximately two minutes. The broad peak around 630°C indicated that the nickel required a high reduction temperature, and that the use of 700°C should ensure a near-complete reduction of the active material.

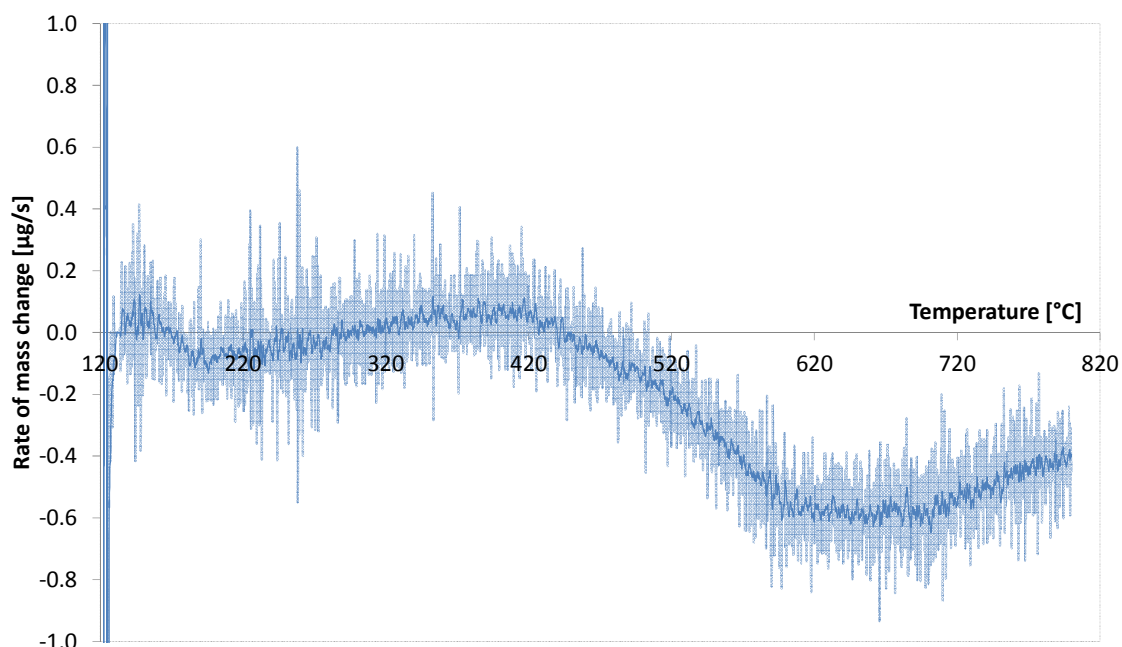


Figure 3.3. Rate of mass change due to nickel reduction with temperature for a 10°C/min ramp under a flow of 5% H₂/N₂. The light blue curve represents the gradient determined by 4th order central differencing. The dark blue line is a moving average of the gradient over six seconds. Initial sample mass 34 mg.

The quantity of nickel available on the passivated nickel catalyst was verified by reducing and oxidising the sample. The support and passivated catalyst were dried under the argon background at 120°C for 40 minutes before the capillary gas was set to a 50 cm³/min flow (at STP) of 5% H₂/N₂. The temperature was ramped at 10°C/min to 250°C, where it was held for 30 minutes before being heated at 10°C/min to 800°C. The sample was held at 800°C for 20 minutes under the 5% H₂/N₂ flow. The capillary gas was then switched to a 50 cm³/min (at STP) flow of air and held for 20 minutes at 800°C. The gas was then switched back to 5% H₂/N₂ and held at 800°C for a further 20 minutes before cooling to room temperature.

Figure 3.4 demonstrates that the switch between a reducing gas and oxidising gas had no significant influence on the support material, and thus the alumina support was irreducible. The passivated catalyst displayed a significant increase in mass upon exposure to air due to the re-oxidation of the metallic nickel present on the support.

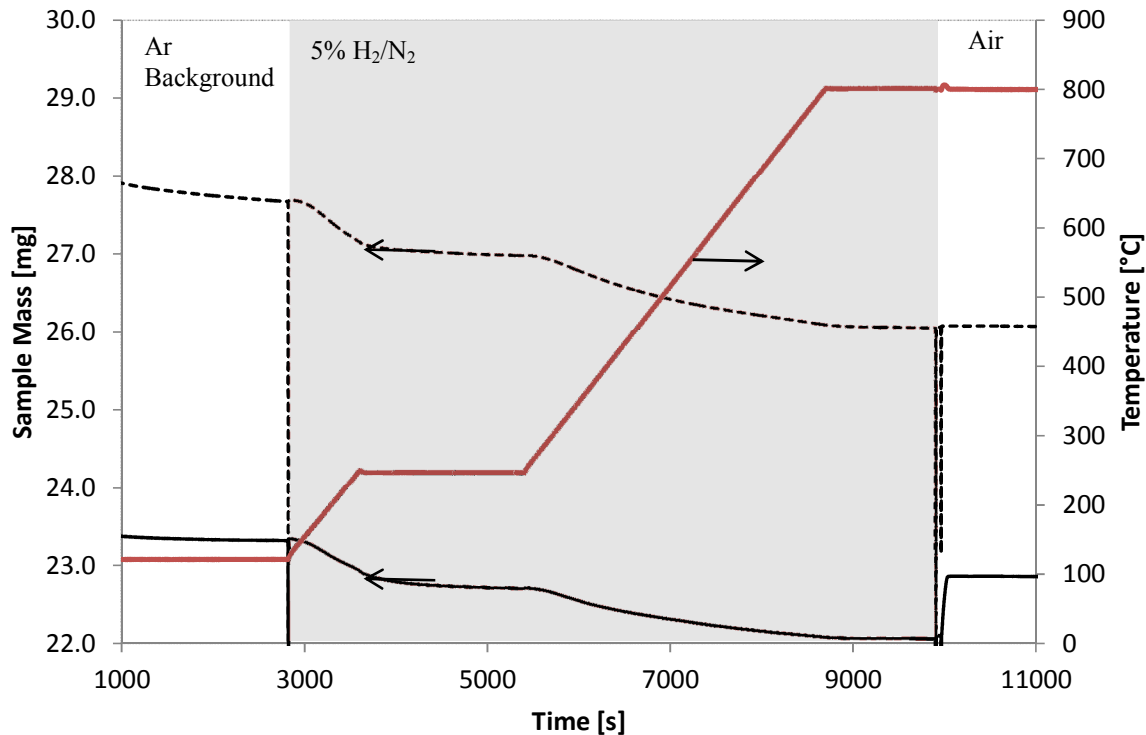


Figure 3.4. Thermogravimetric analysis of passivated nickel alumina (solid line) and support material (dashed line). The shaded areas indicate a change in capillary gas.

The mass change associated with the re-oxidation of an initial mass of 24.2 mg of passivated catalyst was determined to be 0.79 mg, corresponding to a nickel loading of 11.9 wt%, which agreed well with the expected metal loading of 12.0 wt%. The temperature at which the passivation layer was removed is demonstrated clearly in the TPR experiments in §3.4.5.

3.4.3 Results: X-Ray Diffraction Analysis of the Ni/Al₂O₃ Catalyst

The X-ray powder diffraction patterns obtained from the calcined support and the catalyst in calcined and passivated forms are shown in Figure 3.5. Reference diffractograms given in Figure 3.6 were generated using Mercury 3.9 software (CCDC, Cambridge), with structure (.cif) files obtained from the crystallography open database (COD) (Downs *et al.*, 2003, Gražulis *et al.* 2009, 2012, 2015, Merkys *et al.*, 2016). The cif files used were obtained from diffractograms for nickel, nickel oxide, nickel aluminate and γ -alumina deposited within the database.

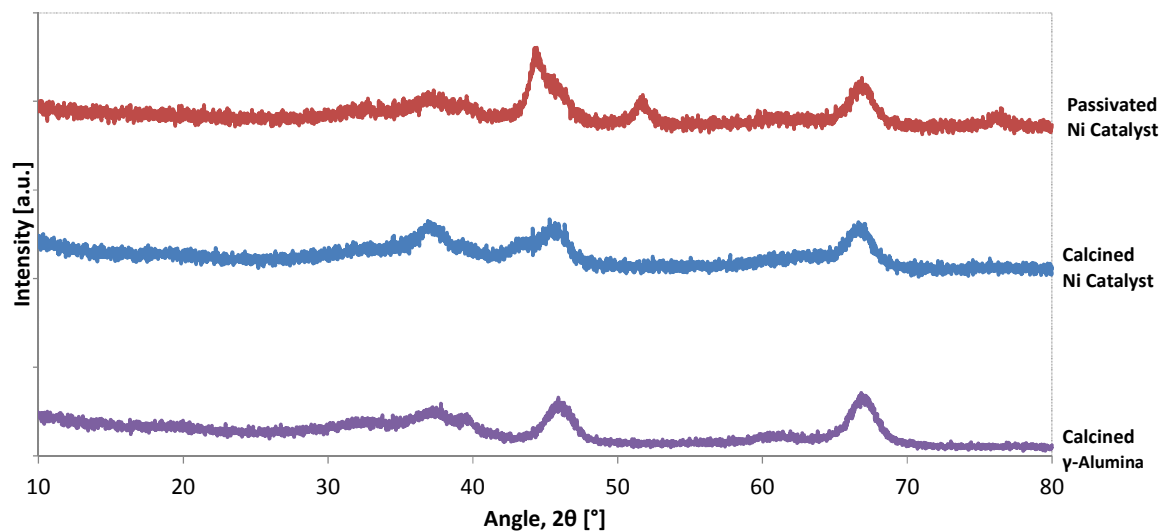


Figure 3.5. XRD diffractograms for passivated and reduced Ni/Al₂O₃, calcined Ni/Al₂O₃ and calcined Al₂O₃. Plots are vertically offset for ease of comparison.

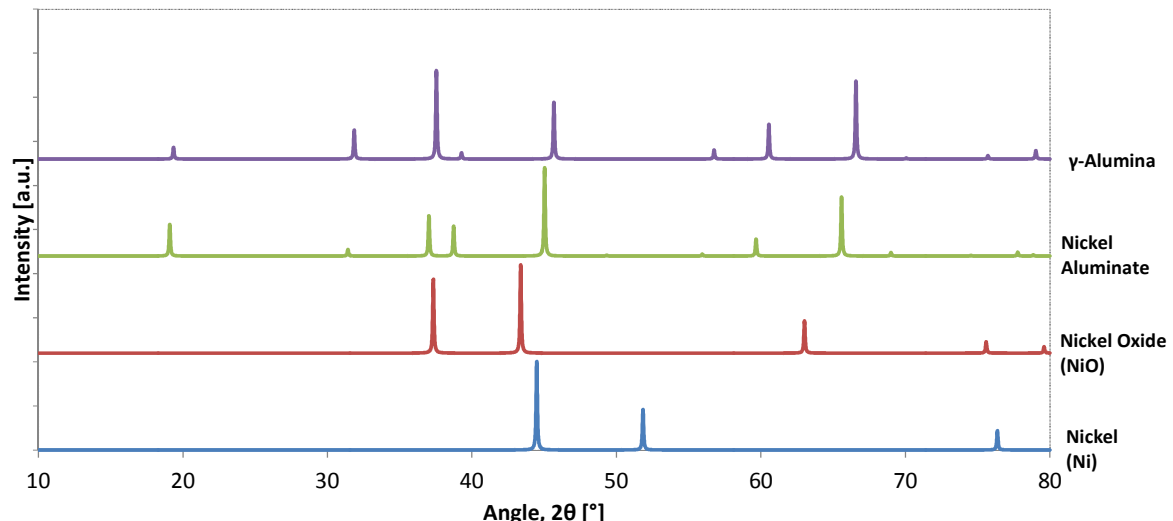


Figure 3.6. Reference XRD diffractograms for γ -Al₂O₃, NiAl₂O₄, NiO, and Ni. Plots are vertically offset for ease of comparison.

The passivated catalyst, calcined catalyst and support display common features. As might be expected, these peaks correspond reasonably with the peaks at $\sim 37.5^\circ$, $\sim 45.7^\circ$ and $\sim 66.6^\circ$ in the reference diffractogram for γ -alumina. In the diffractograms of the calcined catalyst, the peak between 42.5° and 48° appears broader than the alumina diffractogram, with a slight increase in intensity in the peak between 36° and 39° . This may be due to overlap of the alumina diffractogram and the contribution of nickel oxide crystallites, with nickel oxide showing peaks at $\sim 37.4^\circ$ and $\sim 43.4^\circ$.

The passivated catalyst shows an additional peak which might arise from the presence of metallic nickel on the surface. This peak at $\sim 51.9^\circ$ is clearly identifiable as the (2 0 0) plane in metallic nickel, with the slight peak at $\sim 76.5^\circ$ attributable to the (2 2 0) plane. The (1 1 1) plane of metallic nickel is at $\sim 44.5^\circ$, and is seen to overlap with the pattern of the support material.

The XRD pattern for nickel aluminate overlaps significantly with that of γ -alumina, making it difficult to determine whether it has been formed. The peak at $\sim 19.1^\circ$ in the nickel aluminate reference pattern is absent from all diffractograms, and the agreement of the thermogravimetric experiments on the passivated catalyst with the expected metal loading indicated nickel aluminate formation is negligible.

3.4.4 Results: Evaluation of Catalytic Activity and Reproducibility of Ni/ γ -Al₂O₃.

The reactivity of the nickel catalyst was lower than that used by Lim (2014). The reasons for the difference might be due to differences in the preparation of the catalyst. The lower specific rate of reaction in the present work is beneficial for comparing the kinetics of reaction between the Carberry and Bench Top Reactor system since the measured results are less likely to be subject to the influence of internal mass transport limitation. The differences between the reactivities, as measured in the Carberry reactor, are shown in Figure 3.7. The measurements were carried out as described in §2.2, with reasonable consistency found between the batches produced *via* the method described in §3.3.2.

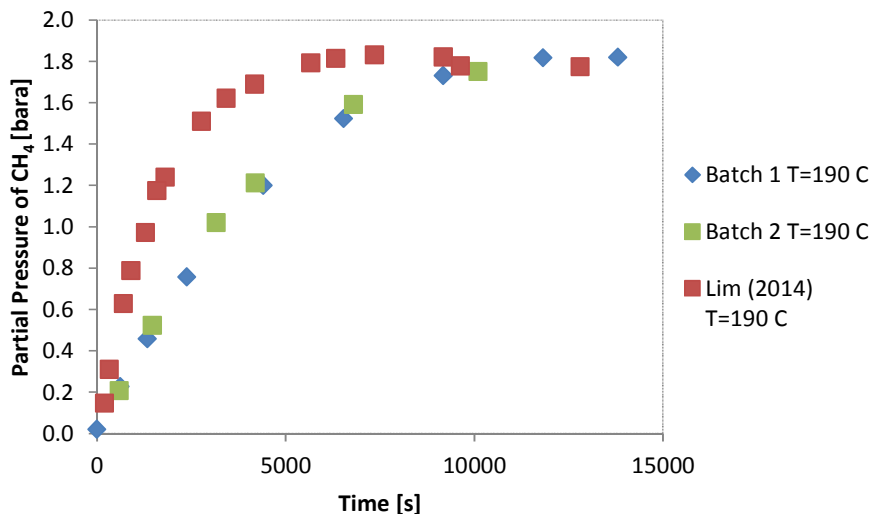


Figure 3.7. Partial pressures of methane *versus* reaction time for each preparation of Ni/ γ -Al₂O₃ catalyst. The methanation conditions were 190°C and 10 bara initial charging pressure for a 5.0 g batch of Ni/ γ -Al₂O₃ catalyst.

3.4.5 Results: Temperature Programmed Reduction of Ni/Al₂O₃ Catalyst

The Ni/Al₂O₃ catalyst was examined by temperature programmed reduction (TPR) in its calcined and passivated states. The catalyst was initially dried by passing 10 cm³/min (at STP) of argon over the catalyst at 120°C for a period of 30 minutes. A stream of 5% H₂ in Ar was then passed through the reactor at a rate of 50 cm³/min (at STP), with the temperature ramped between 120°C and 900°C at a rate of 10°C/min. The gas leaving the U-tube reactor passed through a cold trap maintained at approximately -77°C using an isopropanol/liquid nitrogen slurry. Hence it may be assumed any water produced *via* drying or reduction was removed from the gas phase prior to passing over the TCD.

The consumption of hydrogen in the reduction of the catalyst is represented by the peaks shown in Figure 3.8. The catalyst in the calcined state shows two peaks, a smaller peak at ~250°C and a larger and broader peak ranging from 300°C to 900°C reaching a maximum at approximately 550°C. The TPR profile indicates that the majority of the reduction corresponds with the second peak, which is in agreement with the mass loss profiles of the calcined nickel catalyst obtained by thermogravimetry. The passivated catalyst shows a single peak centred at approximately 230°C, which indicates that the catalyst is probably fully reduced within the batch reactor. The area of the passivated material peak is less than that of the calcined material, with similar masses having been examined. The area of the passivated material peak was estimated to be 23% of that of the calcined material scaled on a mass basis. This agrees reasonably with the value estimated using the TGA of 27%, and indicates 20-30% of the nickel is re-oxidised by passivation.

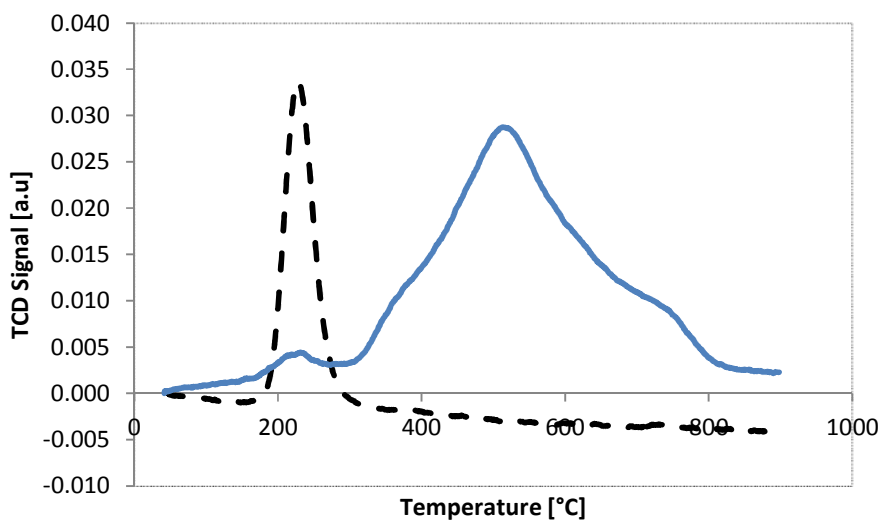


Figure 3.8. Temperature programmed reduction profiles for passivated (dashed line) and calcined nickel catalyst (solid line). The TPR experiments were ramped to 900°C at 10°C/min.

3.4.6 Results: H₂ Pulse Chemisorption of the Ni/Al₂O₃ Catalyst

Metal surface areas of catalysts are typically determined using hydrogen or carbon monoxide pulse chemisorption. Since nickel is known to form the highly toxic and volatile nickel carbonyl with CO, hydrogen chemisorption was used to determine the metallic surface area and metal particle size for the Ni/γ-Al₂O₃ catalyst. Approximately 120 mg of passivated material was heated to 250°C at a rate of 10 °C/min under a flow of 50 cm³/min (at STP) of 5% H₂ in Ar. The catalyst was held under the 5% hydrogen flow for 30 minutes at 250°C. The hydrogen was then purged from the surface of the catalyst under a helium flow, with the temperature ramped at 10°C/min to 400 °C to ensure the desorption of hydrogen adsorbed during the reduction procedure. Upon cooling to 40°C, a series of 25 pulses of 5% H₂/Ar were applied to the reduced material and the uptake of H₂ measured. The dispersion was calculated to be 11.5%. The metal surface area was measured to be 9.2 m²/g_{cat} and a mean particle diameter was determined to be 8.79 nm (hemispherical form), 7.32 nm (cubic crystallite) for a 1:1 stoichiometry of H:Ni atoms. The assumption of a 1:1 stoichiometry for nickel supported on alumina catalysts has been reported to be representative of the true behaviour by Bartholomew and Pannell (1980).

3.4.7 Discussion

The XRD analysis demonstrated that nickel oxide is present in the calcined catalyst, with the reduction and passivation of the catalyst resulting in the observation of peaks corresponding to metallic nickel. The reduction behaviour was determined with both TGA and TPR analysis, with reasonable agreement observed between the techniques. The calcined catalyst was observed with both techniques to reduce over a broad temperature range between ~300-800°C and both techniques displayed a minor peak ~250°C. A difference in the peak maxima location was noted, with the TPR peak maximum at ~500°C, with a broader maximum observed between 600-700°C for the sample characterised by TGA. The shift in the position of the maxima is thought to be due to differences in the way the catalysts were exposed to the reducing gas in the TPR and TGA. For the TPR analysis, the gas is passed through the catalyst bed, whereas under TGA analysis, the reducing gas is passed above the crucible. In passing the gas above the crucible, the concentration of hydrogen at the catalyst surface could have been diminished by dilution by the protective gas or through diffusional gradient within the crucible. Increased concentrations of water due to differences in transport can inhibit the reduction process, with Zielinski (1982) reporting an upwards shift in the temperature of a H₂-TPR peak maxima for their nickel catalyst upon saturating the hydrogen stream with water vapour at 0°C. The TGA background was also reported by Lim (2014) to be slightly oxidising due to unavoidable atmospheric penetration. The presence of traces of oxygen within the background might have countered the mass loss due to reduction through re-oxidation and thus the net rate of metal reduction will be slower, yielding a shift in maximum mass loss rate to higher temperatures.

In both TGA and TPR analysis, the calcined nickel catalyst showed a small peak at a temperature of approximately 250°C. In the processes of reduction and passivation, it was determined that the majority of the nickel was reduced, with the remaining passivation layer reducible at approximately 250°C. The reduction behaviour of supported nickel oxide has been noted to display varying numbers of peaks in the literature, dependent on the loading and preparation conditions, with two forms of NiO (α and β) having been reported to exist in supported nickel catalysts. Reduction peaks in the range 200-300°C have been ascribed in the literature to a variety of species. For instance, Mile *et al.* (1990) attributed a peak at 250°C to the reduction of Ni³⁺ in non-stoichiometric nickel oxide, whilst Rynowski *et al.* (1993) attributed a low temperature peak at 200°C to the decomposition of residual nickel nitrate. The reduction of bulk NiO has also been reported to occur in this range; with both Li and Chen (1995) and Zielenski (1982) noting unsupported nickel oxide reduced with H₂

consumption maxima at 220°C and 230°C respectively under H₂-TPR. The reduction temperature for bulk nickel oxide has been reported to occur over a range of temperatures, with Richardson *et al.* (2003) reporting near complete nickel oxide reduction at 175°C after 10 hours.

It is clear that the lower temperature peak is minor for the calcined nickel alumina catalyst. The nitrate decomposition peak of Rynowski *et al.* (1993) was observed at 200°C in H₂-TPR for a nickel alumina catalyst calcined at 300°C. However it was noted the nitrate precursor was fully decomposed at calcination temperatures above 350°C. Since the nickel catalyst in this study was calcined at 450°C for 3.5 hours, the reduction of residual nitrate seems unlikely. The presence of non-stoichiometric nickel or indeed the reduction of bulk NiO are both feasible explanations for the lower temperature peak, however the attribution of the peak to bulk NiO reduction appears more likely, with agreement between this and the sharper reduction peak of the passivated nickel catalyst.

The peak, or peaks, occurring at higher temperature (300-800°C) have been observed by others in supported nickel oxide, due to the oxide's interaction with the support material. The difficulty in reducing nickel supported on alumina has been attributed to the formation of amorphous surface nickel aluminate (Zielinski, 1982, Li and Chen, 1995) or to limitations in the kinetics of nucleation of metallic nickel (Coenen, 1979). The XRD analysis of the prepared nickel alumina catalyst did not indicate the presence of a nickel aluminate species; however, this does not preclude the presence of an interaction between nickel and its alumina support. Indeed, Li and Chen (1995) proposed that surface nickel spinel might not show the long range three-dimensional order requisite for the characteristic XRD pattern of NiAl₂O₄ to be observed.

The passivation of nickel at room temperature can maintain most of the metal in its reduced state, provided excessive exotherms are avoided (Bartholomew and Farrauto, 1976). In reducing and passivating the catalyst, the TPR profile is shifted from a broad high-temperature peak to a single peak with a maximum at ~250°C. The nickel oxide appears to be reduced to metallic nickel, which upon passivation is covered by a thin layer of nickel oxide. The reduction of the passivation layer appears to show a comparable reduction temperature to that of bulk nickel oxide reported in the literature, suggestive of a lack of interaction between the passivation layer on the surface of the nickel particles and the support. The presence of metallic nickel in the passivated sample was further confirmed by its XRD pattern, with the (2 0 0) plane for metallic nickel clearly present. The low-temperature reduction of the passivation layer is below the maximum reduction temperature of the Carberry, and thus indicates reduction of the passivated material in the Carberry results in near complete nickel

availability.

The measured nickel dispersion of 11% appears reasonable; with an average nickel particle size of 7.3-8.8 nm. The agreement between the nickel particle size and the pore size range, measured using gas adsorption analysis, suggests the nickel was successfully dispersed within the porous structure of the nickel, with its metal surface area ($9.2 \text{ m}^2/\text{g}_{\text{cat}}$) accounting for approximately 6.7% of total surface area ($138.6 \text{ m}^2/\text{g}_{\text{cat}}$).

Whilst the TPR and TGA experiments have demonstrated there is interaction between the metal and the support, the thermogravimetric analysis has demonstrated that the alumina alone is unreactive to reduction and oxidation. The stability of the support was further demonstrated by the gas adsorption analysis. The measured pore volumes and surface areas were noted to decrease slightly upon impregnation and calcination of the catalyst, with the pore volumes and surface area decreasing further between the calcined and passivated material. The small changes in the adsorption properties between the calcined support and the impregnated support appear to be due to pore blocking effects brought about by the presence of nickel. The surface area decreased upon reduction and passivation, with the average pore size noted to increase. This observation is in agreement with the investigation of Schaper *et al.* (1983). Their investigation noted a decrease in BET surface area of air calcined γ -alumina with calcination temperature between 600°C and 1100°C due to sintering *via* surface diffusion.

The reactivity of the catalyst was lower than that produced by Lim (2014). The difference might have arisen from variations in the method of preparation, with the calcination and drying steps noted earlier to have a significant influence on the final activity of the catalyst. The calcination in static air might have resulted in a difference in particle size; however, direct comparison cannot be made since Lim (2014) did not measure nickel crystallite size in his characterisation. The review of the literature has demonstrated the importance of the temperature and its rate of change, as well as the gas environment. Hence the differences in preparation conditions necessitated by safety and apparatus provide sufficient explanation of the differences in the measured reaction rates.

3.5 Characterisation of the Co/ZrO₂ catalyst

3.5.1 Results: Zirconia Support Characterisation

In order to select appropriate calcination and reduction temperatures, the support was calcined in still air for 6 hours at 4 different temperatures (450, 500, 600 and 800°C) to determine if the calcination temperature affected morphological properties. The results are given in Table 3.4.

Table 3.4. Gas adsorption properties of calcined ZrO₂ support.

Measured Value	Zirconia Support Calcination Temperature				
	Untreated	450°C	500°C	600°C	800°C
BET Surface Area [m ² /g _{support}]	97.7	90.9	79.2	54.2	34.5
t-Plot External Surface Area [m ² /g _{support}]	109.5	104.2	88.4	56.3	33.8
Pore Volume [cm ³ /g _{support}]	0.145	0.145	0.147	0.132	0.131
Average Micro-Pore Width [nm]	5.95	6.40	7.45	9.79	15.17

The calcination step does not appear to significantly alter the support properties at 450°C, with changes of < 10% in all properties relative to the untreated case. As the calcination temperature was increased the measured surface area decreased, whilst the pore volume decreased to a much lesser extent. The discontinuity in the measured BET surface area and the calcination temperature is highlighted in Figure 3.9.

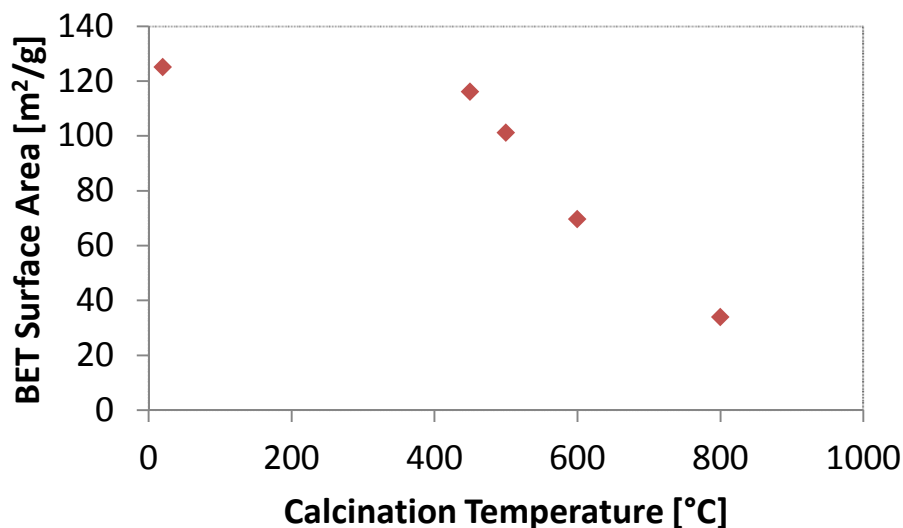


Figure 3.9. BET surface area versus calcination temperature of the ZrO₂.

3.5.2 Results: Gas Adsorption Analysis of the Co/ZrO₂ Catalyst

Table 3.5 shows the surface area, pore volume and pore widths, as determined by BET analysis, of catalyst and support samples at different stages of the preparation. The analysis shows that the average pore diameter increased slightly progressively through the preparation. The impregnation and calcination of the support decreased the available surface area as well as the pore volume. This suggested that some pores may have been filled or blocked by cobalt particles. The addition of cobalt to the support increased the catalyst mass, hence to make a meaningful comparison of the catalyst material, the surface areas and pore volumes were compared on the basis of equivalent support mass.

The reduced and passivated catalyst material showed a similar surface area and increased pore diameter to the calcined material. The adsorption-desorption isotherms observed for the prepared catalyst were Type IV according to the IUPAC classification (Sing, 1982). A hysteresis form of this type corresponds to mesoporous material, in agreement with the structure of the catalyst support particles. The BET calculated pore volume lies below the manufacturer's stated pore volume (0.26 cm³/g). This discrepancy may be due to the presence of macro-pores in the zirconia support.

Table 3.5. BET properties of the untreated and calcined zirconia (450°C), and calcined (450°C) and reduced catalyst material.

Measured Value	Untreated Zirconia Support	Calcined Zirconia Support	Calcined IWI Cobalt Zirconia Catalyst	Calcined, Reduced and Passivated Catalyst
BET Surface Area [m ² /g _{support}]	97.7	90.9	85.8	84.7
t-Plot External Surface Area [m ² /g _{support}]	109.5	104.2	98.6	97.0
BJH Adsorption Pore Volume [cm ³ /g _{support}]	0.182	0.156	0.147	0.156
Pore Width [nm]	5.95	6.40	6.38	6.96

3.5.3 Results: Thermogravimetric Analysis of the Co/ZrO₂ Catalyst

Thermogravimetric analysis permitted the determination of the mass of cobalt confined within the catalyst support. For the experiments shown in Figure 3.10 the ground catalyst material was dried at 120°C for 1.5 hours under argon. The capillary gas was then switched at $t = 5820$ s to 50 cm³/min (at STP) 5% H₂/N₂. The temperature was then ramped to 800°C at 10°C/min.

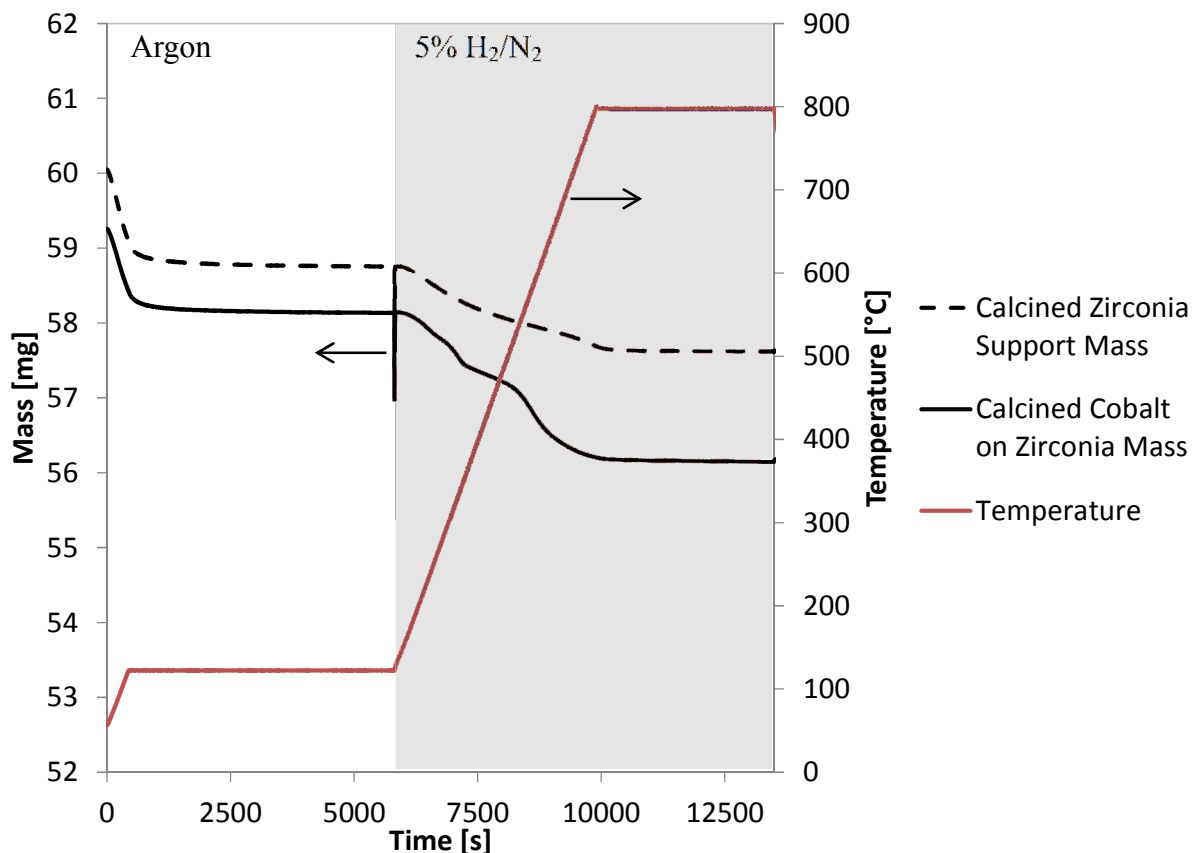


Figure 3.10. TGA reduction for calcined support (dashed line) and calcined Co/ZrO₂ (solid line). Capillary gas set to 5% H₂/N₂ (grey shading) as indicated.

The loss of mass when reducing the calcined Co/ZrO₂ material, less the contribution from the support, was determined to be ~0.9 mg. Assuming that all the cobalt is initially in the form of Co₃O₄, and is reduced fully to metallic cobalt at 800°C, the corresponding mass of cobalt on the support was ~2.5 mg, and consequently yielded a metal content of 4.2 wt% (initial dry mass ~ 59.1mg). The weight fraction is in reasonable agreement with the design metal loading of 4.5 wt%.

A separate experiment, shown in Figure 3.11, investigated the oxidation and reduction behaviour of the catalyst at 800°C. The catalyst was reduced in the same manner as that of Figure 3.10 and the temperature was held for 20 minutes at 800°C under a flow of 50 cm³/min (at STP) of 5% H₂/N₂ to ensure reduction of the catalyst. The H₂/N₂ gas was discontinued and

after 1 minute the capillary gas was switched to 50 cm³/min (at STP) air and held at 800°C for 20 minutes to re-oxidise the sample. After oxidation, the air was switched off, with the capillary gas switched after 1 minute to a flowrate of 50 cm³/min (at STP) 5% H₂ in N₂. The reducing conditions were held for 20 minutes before cooling under argon.

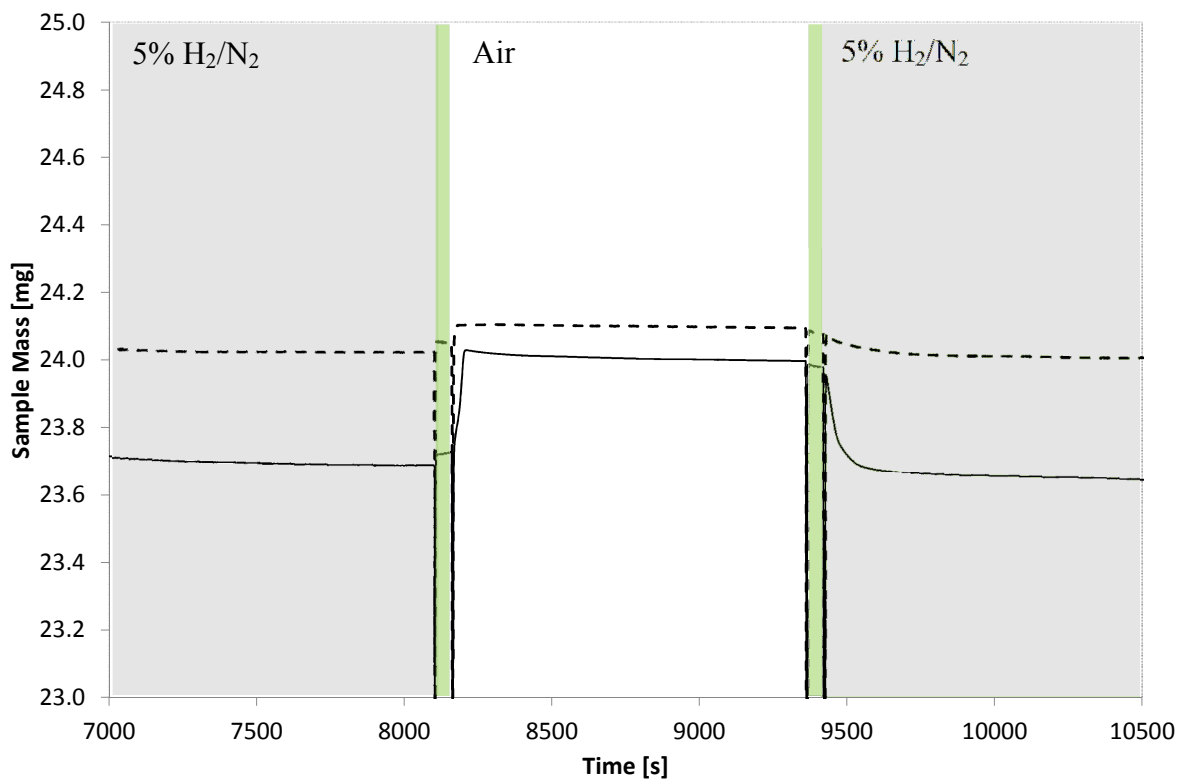


Figure 3.11. TGA plots for calcined support (dashed line) and Co/ZrO₂ (solid line). Capillary gases switched between 5% H₂/N₂ (grey shading) and Air as indicated. Green shading indicates Ar background environment only.

In Figure 3.11, the high-temperature re-oxidation step of both materials indicated that the support displayed a degree of reducibility. The loading of the catalyst was determined by comparing the mass loss under 5% H₂/N₂ between 120°C and 800°C. The mass lost by the support and the catalyst under a reducing atmosphere was approximately 0.59 mg and 0.98 mg respectively. The mass loss due to cobalt reduction was thus determined to be ~0.39 mg, in agreement with a loading of 4.3 wt% on a cobalt basis (Initial mass 25.1 mg). The re-oxidation of the catalyst however yielded a lower change in mass, with gains of 0.32 mg and 0.08 mg for the catalyst and support, respectively. The change in mass represents ~1 wt% of the catalyst, 62.4 % of the mass change determined by reducing the oxidised catalyst between 120°C and 800°C. The difference indicates the possibility of encapsulation or the formation of mixed oxide compounds occurring at elevated temperature.

Figure 3.12 shows the rate of change of mass with temperature of the calcined Co/ZrO₂ as the cobalt oxide is reduced. The loss of mass due to drying and reduction of the

ZrO_2 support was accounted for by subtracting the profile, obtained under similar conditions, for the zirconia support alone. The rate of mass change showed a small peak at $\sim 200\text{-}260^\circ\text{C}$, a larger peak at $\sim 260\text{-}360^\circ\text{C}$ and a significant, broad peak from $\sim 450\text{-}750^\circ\text{C}$ with a maximum at $\sim 580^\circ\text{C}$. The broad peak around 580°C indicated that a high reduction temperature is required to transform all the cobalt to metal.

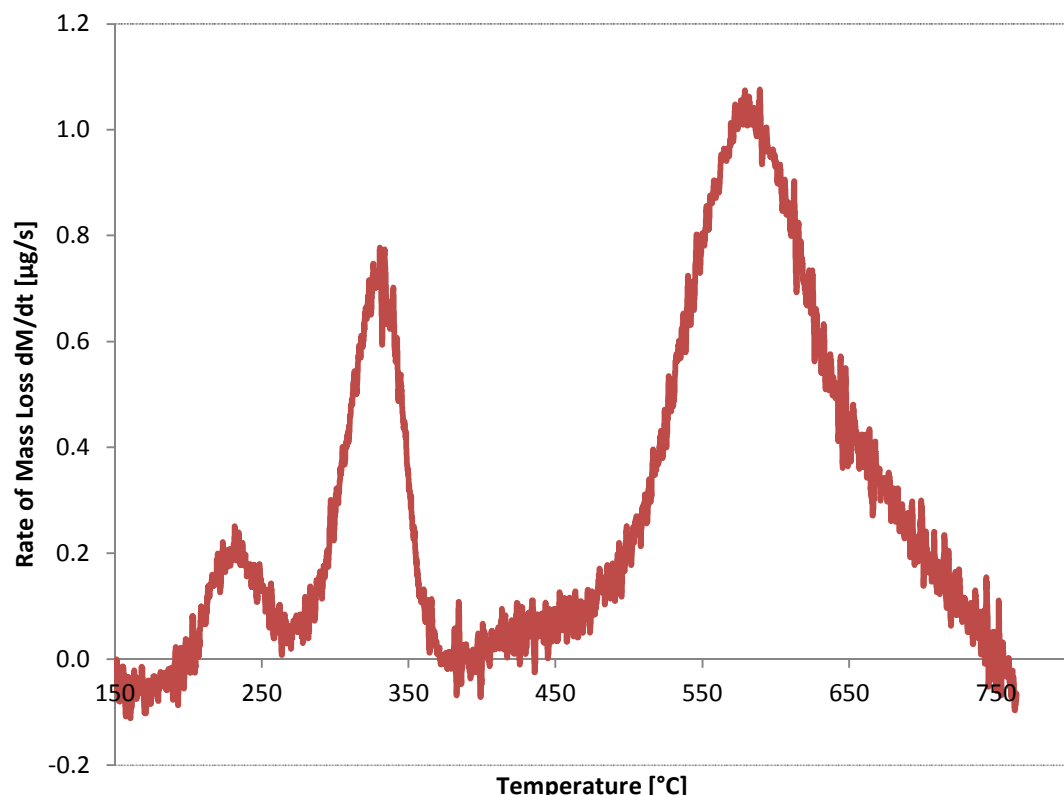


Figure 3.12 Rate of differential mass change due to cobalt reduction with temperature for a $10^\circ\text{C}/\text{min}$ ramp under a flow of 5% H_2/N_2 . The influence of water loss is removed through subtraction of the support. The red curve represents the gradient determined by 4th order central differencing. Sample mass: 60 mg.

The activation process was undertaken at 250°C for a period of 6 hours. This process was investigated using TGA to determine the extent of catalyst reduction under reactive conditions. The materials of interest were first dried at 120°C for 40 minutes under argon. The gas feed was then switched to $50 \text{ cm}^3/\text{min}$ (at STP) H_2/N_2 , and the temperature was ramped to 250°C at $10^\circ\text{C}/\text{min}$, and held for a period of 6 hours. After the isothermal hold, the temperature was ramped to 800°C where it was held for 20 minutes. The catalyst was then re-oxidised under a flow of $50 \text{ cm}^3/\text{min}$ (at STP) air for 20 minutes, followed by re-reduction for a further 20 minutes and run termination. The mass change after 6 hours under a flow of $50 \text{ cm}^3/\text{min}$ 5% H_2/N_2 indicated that approximately 21 % of the oxygen is removed during reduction at 250°C .

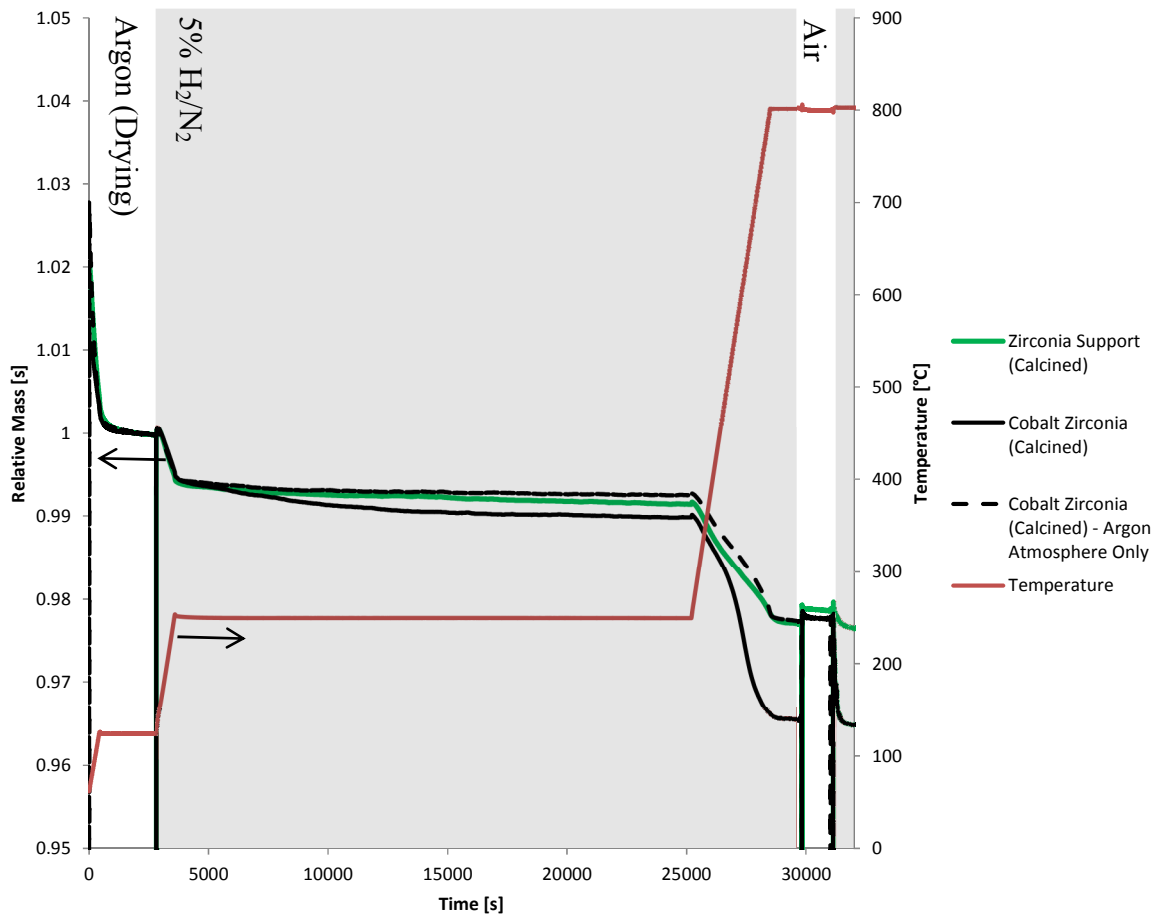


Figure 3.13. Isothermal reduction of calcined Co/ZrO_2 and ZrO_2 support material at 250°C for 6 hours followed by reoxidation and reduction at 800°C . Capillary gas is indicated by shaded sections. Co/ZrO_2 heated in argon only is shown by the dashed line.

3.5.4 Results: X-Ray Diffraction Analysis of the Co/ZrO_2 Catalyst

Figure 3.14 shows the XRD diffractograms of the calcined cobalt catalyst, the cobalt catalyst after reduction and passivation, and the calcined support material. The reduction and passivation of the catalyst was achieved by treating 5.0 g of calcined catalyst with 150 cm^3/min (at STP) hydrogen at 250°C for 6 hours, followed by the passivation process outlined in §3.3.2. Figure 3.15 displays the reference patterns generated using the method employed in §3.4.3, with the crystallographic information files (cif) of cobalt, Co_3O_4 and CoO and yttria-stabilised zirconia from the crystallography open database.

The diffractograms for the calcined catalyst, calcined support and passivated catalyst appear to be identical in form. The peaks may be attributed to the yttria-stabilised zirconia (YSZ) support, with good agreement between the peaks of the reference pattern at $\sim 30.1^\circ$, $\sim 34.8^\circ$, $\sim 37.4^\circ$, $\sim 50.2^\circ$ and $\sim 59.6^\circ$. Two smaller peaks at $\sim 62.6^\circ$ and $\sim 73.6^\circ$ are also consistent with YSZ in a tetragonal form.

The absence of peaks due to the presence of cobalt or cobalt oxides might be due to the relatively low loading on the support. XRD is typically sensitive to species in mixed compounds comprising greater than a few percent by mass (Newman *et al.*, 2016). The absence of XRD peaks has also been reported where the metal particles are particularly small or highly dispersed *e.g.* Razzaq *et al.* (2013).

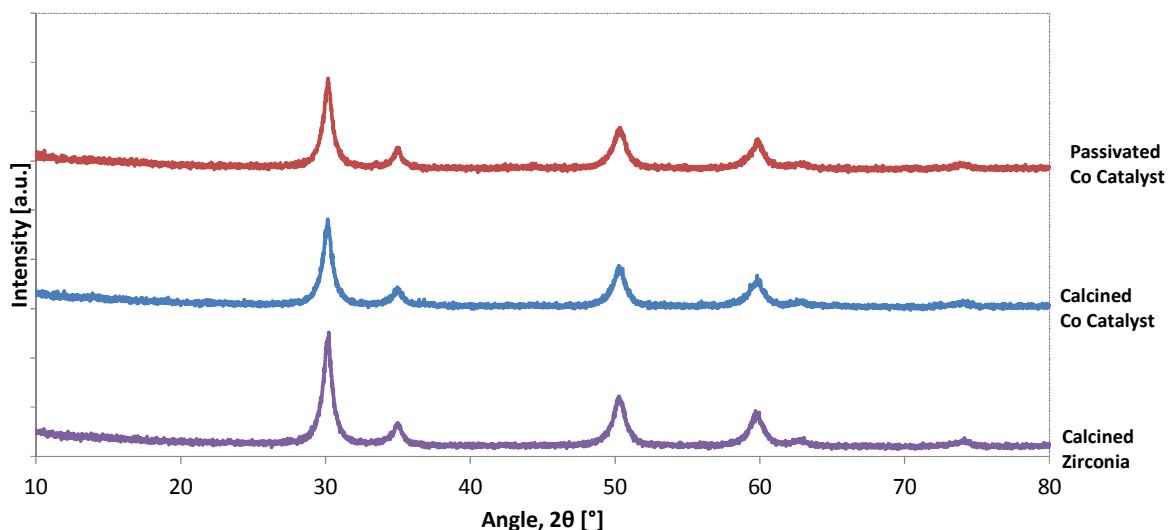


Figure 3.14. XRD diffractograms of reduced and passivated Co/ZrO₂ catalyst, calcined Co/ZrO₂ catalyst and calcined ZrO₂.

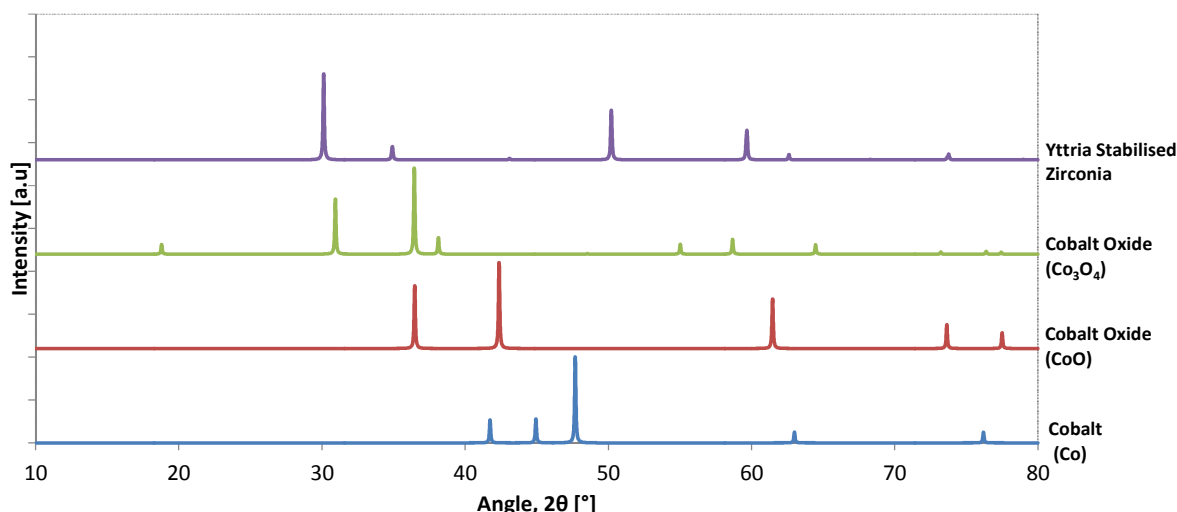


Figure 3.15. XRD reference diffractograms for YSZ, Co₃O₄, CoO and Co.

3.5.5 Results: Evaluation of Co/ZrO₂ Catalyst Batch Reproducibility

The reproducibility of the Co/ZrO₂ catalyst was examined in the Carberry batch reactor by undertaking successive batch methanation of carbon dioxide. Two 10.0 g catalyst loads were taken from two separately-prepared batches of catalyst. These calcined catalyst samples were then loaded into the reactor and reduced for 6 hours at 250°C under a 150 cm³/min (at STP) flow of hydrogen. The reactivity of the two batches of catalyst was determined at 200°C and an initial charging pressure for the H₂/CO₂ mix (72% H₂, 24% CO₂, 4% Ar) of 10 bara. The results are shown in Figure 3.16. The reproducibility of the catalyst is reasonable, with the concentration profiles showing good consistency.

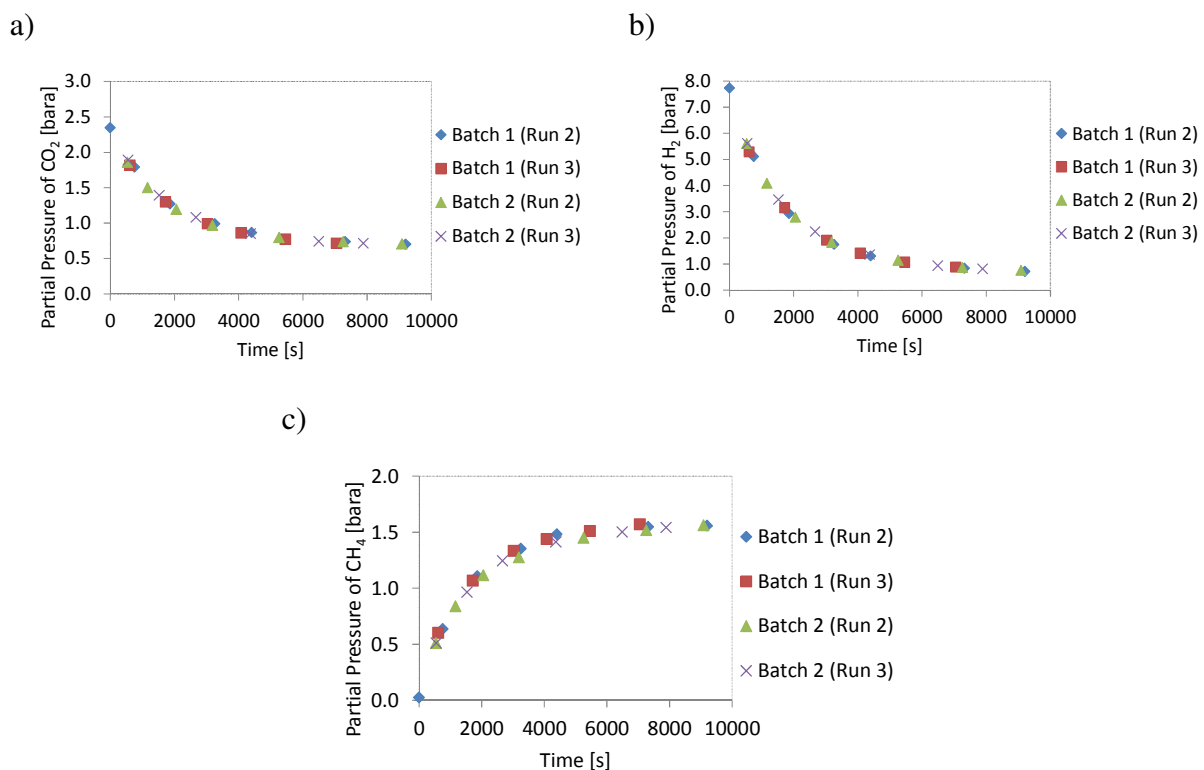


Figure 3.16. Partial pressures of a) carbon dioxide, b) hydrogen and c) methane versus time for 2 different catalyst batches. The methanation conditions were 190°C and 10 bara initial charging pressure for a 10.0 g batch of Co/ZrO₂ catalyst.

3.5.6 Results: Temperature Programmed Reduction of the Co/ZrO₂ Catalyst

Temperature-programmed reduction (TPR) experiments were used to investigate the reduction behaviour of the calcined support and the Co/ZrO₂ catalyst in both the used and calcined states, with the profiles shown in Figure 3.17. The temperature-programmed reduction was achieved by increasing the temperature of the sample at 10°C/min under a flow of 50 cm³/min (at STP) 5% H₂/Ar between 50°C and 800°C. Further details of the equipment are given in §2.5.4

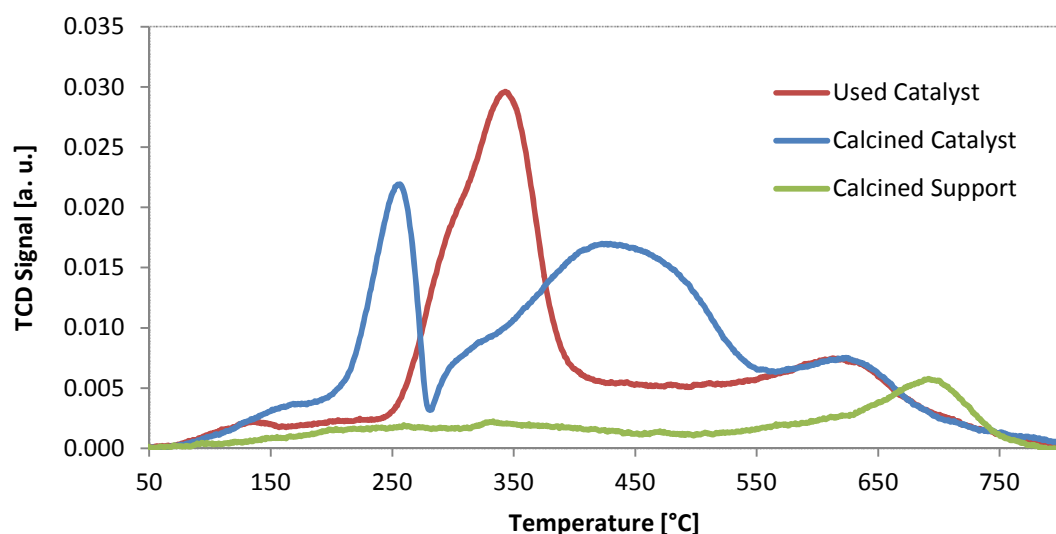


Figure 3.17. Temperature programmed reduction of calcined Co/ZrO₂ catalyst, used Co/ZrO₂ catalyst and calcined ZrO₂. Temperature ramp set at 10°C/min under a flow of 50 cm³/min (at STP) 5% H₂/Ar.

From the TPR profiles, the calcined catalyst showed two peaks centred at ~250°C and ~450°C, commonly attributed to reduction from Co₃O₄ to CoO and from CoO to Co, respectively. A high-temperature peak at ~600°C is also present in both the profiles of the calcined and used catalyst. This high-temperature peak shows similar form to the reduction peak present in the support material, which exhibits a small peak at ~700°C. The absence of a peak at 700°C for both states of catalyst suggests that the presence of cobalt might shift the reduction of the support to lower temperature through dissociation of the H₂. On examination of the peak areas, less the area contributed by the support, the broad ~450°C peak area is ~3 times that of the ~250°C peak, in agreement with the conversion of Co₃O₄ to CoO.

The TPR profile of the used catalyst shows two peaks, the first is a broad peak between ~250 °C and ~400 °C, with the previously discussed smaller secondary peak at ~600 °C. The reduction of the catalyst appears to have shifted to a lower temperature after the CO₂ methanation reaction.

3.5.7 Discussion

From the gas adsorption analysis, it is clear that the zirconia based catalyst support can undergo significant structural transformation under certain process conditions. The loss of surface area appears consistent with the literature. Méthivier and Pijolat (1993) annealed tetragonal zirconia for 2 hours at 700°C and 850°C, observing BET surface area losses of 30% and 48% respectively. The loss was attributed to tetragonal crystallite growth, with increasing water partial pressure noted to enhance crystallite growth. Similarly, Mercera *et al.* (1990) reported BET surface area losses of 97% upon calcination at 850 °C, maintained for 15 hours. Crystallite growth, phase transformation from tetragonal to monoclinic and inter-crystalline sintering, were all reported to be responsible for the surface area loss. In agreement with the behaviour of the zirconia support used in this Chapter, Mercera *et al.* (1990) also observed a decrease in both surface area and pore volume in their samples, accompanied by a shift in the pore size distribution to a higher mean as the calcination temperature increased. The yttria stabilisation of the Saint-Gobain zirconia inhibits the transformation of the tetragonal phase to the monoclinic phase, and thus the loss of surface area could be attributed to inter-crystalline sintering and crystal growth. It is clear from the XRD analysis that the zirconia phase is not altered by the calcination and reduction processes, with the small decreases in pore volume and surface area partly attributable to growth or crystallite sintering and partly attributable to pore blockage and filling upon impregnation with cobalt.

The reduction behaviour of the catalyst was examined under TPR and TGA. As observed with the Ni/γ-Al₂O₃ catalyst, the TPR analysis showed a shift in the positions of the reduction peaks to lower temperatures relative to those obtained by the TGA. In this case, two distinct peaks were observed in the TPR analysis, with three peaks determined from the gradient of the TGA analysis. Since water is condensed prior to the TCD detector in the TPR analyser employed, the small low temperature peak indicated by the TGA analysis might be due to a small difference in the water adsorption properties of the calcined support and the calcined catalyst material.

The TPR profile of Figure 3.17 is consistent with the reduction of Co₃O₄ to CoO represented by the first peak and subsequent reduction of CoO to metallic cobalt, represented

by the broader, high-temperature peak. These assignments have previously been made for supported cobalt catalysts, *e.g.* Ji *et al.* (2009) Giradon *et al.* (2005). Since the relative areas of the peaks with maxima at ~250°C and ~450°C were found to have a ratio of 2.9, there is clear agreement with the stoichiometry of the reduction, and thus indicate the ~250°C peak and ~450°C peak may be attributed to Co₃O₄ and CoO reduction respectively. Residual nitrate decomposition has been associated with low-temperature peaks in H₂-TPR. However in the case of the Co/ZrO₂ catalyst in this study, this appears unlikely. The calcination temperature of 450°C is significantly greater than that required for bulk nitrate decomposition, with Ji *et al.* (2009) reporting little evidence of residual nitrate in their alumina support cobalt above a calcination temperature of 300°C.

The thermogravimetric analysis of the Co/ZrO₂ catalyst yielded a relatively small degree of reduction, with a value below the threshold required (25% O loss) for complete transformation of Co₃O₄ to CoO, and thus for a stepwise reduction of Co₃O₄ → CoO → Co, suggests the absence of metallic phase cobalt. However, the disagreement between the positions of the reduction peaks in the TPR and the TGA indicate that the reductive environment within the TGA differs from that in the TPR analyser. The sharpness of the peak at 250°C in the TPR (Figure 3.17) demonstrates a rapid reduction of Co₃O₄, whilst the TGA mass loss during reduction at 250°C is slower. A potential explanation for this behaviour is oxygen contamination, with traces of oxygen reducing the net rate of reduction through re-oxidation of the catalyst within the TGA. Oxygen intrusion was also reported to be a potential issue by Lim (2014) in their TGA experiments, observing some oxidation under ‘inert’ at high temperatures.

It is clear from the TPR/TGA studies that the Co/ZrO₂ catalyst cannot be reduced completely into metallic cobalt without significant loss of support surface area. The identity of the active phase in the hydrogenation of CO and CO₂ has often been ascribed to metallic cobalt; however, recent work has proposed that the CoO phase may have catalytic activity. Thus, Meleat *et al.* (2014) examined the hydrogenation of CO and CO₂ on TiO₂ and SiO₂ supported cobalt catalysts. The catalysts consisted of 10 nm Co nanoparticles deposited on the support and were subjected to alternating periods of reduction and oxidation. Catalysts in the ‘reduced’ state were formed by oxidation in 20% O₂/Ar at 350°C for 3 hours, followed by reduction in 20% H₂/He for 1 hour at 450°C, whilst catalysts in the ‘oxidised’ state were formed by oxidation in 20% O₂/Ar at 350°C followed by reduction in 20% H₂/He at 250°C. For the silica supported material, the ‘reduced’ state yielded the expected behaviour, with an increased activity at the higher reduction temperature. However, for the TiO₂-supported catalyst, the ‘oxidised’ state was found to yield a turnover frequency up to 5 times higher than

the ‘reduced’ state catalyst. Meleat *et al.* (2014) further examined the ‘oxidised’ TiO₂-supported catalyst *in situ* using X-ray adsorption near edge structure (XANES), reporting that during the reaction the near-surface of the catalyst consisted of Co²⁺, with *in situ* X-ray diffraction confirming the presence of crystalline cubic CoO. Lee *et al.* (2015) also proposed CoO acted as an active phase for the Fischer-Tropsch reaction, having demonstrated Fischer-Tropsch activity for sub-nanometre CoO_x clusters supported on Al₂O₃, MgO and ultra-nanocrystalline diamond.

The Co/ZrO₂ catalyst reduced at 250°C appeared active for the hydrogenation of carbon dioxide, which suggests either an active CoO phase exists on the zirconia support, or sufficient metallic phase cobalt is developed during the reduction.

3.6 Conclusions

A 12 wt% Ni/ γ -Al₂O₃ catalyst and a 4.5 wt% Co/ZrO₂ were made by incipient wetness impregnation of an Al₂O₃ and a ZrO₂ support respectively. The catalyst materials and their supports were examined using gas adsorption analysis, XRD and temperature programmed studies. The reduction and passivation process was noted to produce a metallic nickel catalyst upon reduction at 250°C, the maximum temperature for the Carberry batch reactor. The catalyst was compared to the material developed by Lim (2014) and was found to have a much lower activity upon testing within the Carberry batch reactor.

Comparison between the rate of mass loss and the TPR profiles revealed significant differences in the peak temperatures despite an identical ramp rate, with the differences attributed traces of oxygen lowering the net rate of reduction for both the nickel and cobalt catalysts. Reduction of the Co₃O₄ phase under TPR conditions was observed to rapidly occur about the Carberry reduction temperature of 250°C, however under TGA conditions, some Co₃O₄ was observed to remain. Additionally, the changes in the gas adsorption properties with calcination temperature were determined, permitting selection of a calcination temperature high enough to sufficiently decompose the precursor without significant impact on the support morphology.

4 Kinetics of CO₂ Methanation on a Ni/γ-Al₂O₃ Catalyst in Batch and Continuous Reactor Systems

4.1 Introduction

The methanation of CO₂ was investigated over a wide range of partial pressures of products and reactants using (i) the gradientless, spinning-basket reactor operated in batch mode and (ii) the laboratory-scale fixed-bed reactor operating continuously. The rate and selectivity of CO₂ methanation, using a 12 wt% Ni/γ-Al₂O₃ catalyst, were examined at temperatures between 443 – 493 K and pressures up to 20 barg. The kinetic measurements were compared with mathematical models of the reactors, in which different kinetic expressions were explored. The ability of the kinetic expressions derived from the batch results to predict the behaviour in the fixed-bed reactor was then evaluated, with the discrepancies between the systems discussed.

Parts of the work presented in this chapter were presented at the RSC Faraday Discussions Carbon Capture and Storage conference. The associated article is published as R. A. Hubble, J. Y. Lim, J. S. Dennis, Kinetic Studies of CO₂ methanation over a Ni/γ-Alumina catalyst, Faraday Discussions, 2016, DOI: 10.1039/c6fd00043f.

4.2 Background

The methanation of carbon dioxide might be used as a means to produce synthetic natural gas (SNG), an efficient energy carrier which could be distributed through the existing infrastructure for natural gas (Abelló *et al.*, 2013, Kopyscinski *et al.*, 2010, Lim *et al.*, 2016). Studies of methanation might also provide insights into related hydrogenation reactions, such as the Fischer-Tropsch synthesis and CO methanation. Nickel-based catalysts are frequently applied in these methanation reactions, owing to the abundance of Ni and its low cost relative to other highly active transition metals, such as ruthenium or rhodium (Lim *et al.* 2016). Nickel catalysts are often supported in CO₂ methanation, with a large number of studies investigating the activity of nickel across various supports *e.g.* Al₂O₃, SiO₂, TiO₂, ZrO₂ (Chang *et al.*, 2003, Kim *et al.*, 2010, Schild *et al.*, 1991, Vance and Bartholomew, 1983).

The activity and selectivity of methanation reaction on nickel catalysts have principally been studied in continuous, fixed-bed micro-reactors, and few investigations have performed large kinetic studies examining the rate and selectivity of CO₂ methanation. The type of support employed often significantly influences both the activity and selectivity. Hence, it is not unreasonable to expect that rate expressions will differ between catalysts, with the potential for mechanistic pathways to differ owing to differences in the metal-support interactions (Lim *et al.*, 2016).

Broadly, two main mechanisms have been proposed. The first assumes that the reaction occurs *via* the dissociative adsorption of CO₂ to form CO and O surface species, *e.g.* Zagli and Falconer (1981), Weatherbee and Bartholomew (1982), Fujita *et al.* (1993), whilst the second assumes that the conversion of CO₂ occurs *via* a carbonate or formate intermediate, *e.g.* Aldana *et al* (2013). Only a few studies have proposed rate expressions for the methanation of carbon dioxide, *e.g.* Weatherbee and Bartholomew (1982), van Herwijnen *et al.*(1973), Koschany *et al.* (2016), with their conclusions based on experiments performed in fixed-bed reactors. Further discussion of the mechanisms is presented in §4.7.1 and in the appendices (§A1,§A3).

The primary objective of this work was to investigate the kinetic behaviour of a nickel γ -alumina catalyst. Using a batch and a continuous reactor, the catalyst activity was investigated over a wide range of conversions and partial pressures of reactants. Batch reactors provide a means with which to characterise the kinetics in an environment free of temperature and concentration gradients. This permits kinetics to be examined at high conversions.

Very few studies have used a batch reactor to examine the behaviour of CO₂ methanation, with most of these studies conducted at conditions far from those which would be used in industry. For example, the batch investigation of Porosoff and Chen (2013) examined CO₂ methanation on cobalt and nickel supported catalysts with *in situ* Fourier Transform Infra-red (FTIR) spectroscopy used to evaluate the CH₄ and CO selectivity at 30 torr (0.04 bar) and 573 K. Lim *et al.* (2016) also explored the methanation of CO₂ over a Ni/ γ -Al₂O₃ catalyst in the Carberry batch reactor. The authors developed a kinetic model, finding the rate of reaction in batch to be determined by the rate of dissociation of CO.

Here, the aim was to develop the previous work of Lim *et al.* (2016) to determine the influence of a range of partial pressures of hydrogen, water and carbon dioxide on the reaction kinetics at pressures under both batch and continuous modes of operation. In doing so, the

applicability of various kinetic equations, and thus their underlying mechanistic assumptions, was evaluated. The activity of the catalyst employed by Lim *et al.* (2016) was found to be significantly higher and could not be reproduced within a reasonable margin of error, as noted in §3.4.4. This disparity was attributed to necessary differences in the method of preparation, with the lower specific activity in the present research being beneficial in avoiding diffusional limitations. Since the activity of the catalyst employed in this thesis was notably different to that used by Lim *et al.* (2016), the batch experiments were repeated and expanded upon and quantitatively compared to the kinetic results obtained from the same catalyst measured at steady-state.

4.3 Experimental

4.3.1 Apparatus

CO_2 methanation was examined under batch conditions within the spinning basket reactor (Parker Autoclave 280 ml Carberry Reactor, ID= 75 mm). The cruciform mesh basket was loaded with 5.0 g of the 3 mm diameter Ni/ γ -Alumina catalyst pellets, diluted with 5.0 g of 3 mm inert glass beads. The reactor system was heated to 523 K with the catalyst under nitrogen. Reduction of the passivated catalyst occurred under a flow of 300 cm^3/min (at STP) H_2 at 523 K and atmospheric pressure for a period of 6 hours. The stirrer speed was set to 600 rpm.

In a typical batch experiment, the reactor was set to the desired reaction temperature and then evacuated prior to the introduction of the reactant gases. The reactants were introduced from cylinders of hydrogen, carbon dioxide, and a premixed cylinder (24% CO_2 , 72% H_2 , and 4% Ar). The base experiment consisted of charging the reactor with 10 bara of the $\text{CO}_2/\text{H}_2/\text{Ar}$ mixture. The initial H_2 and CO_2 partial pressures were varied by introducing 1-4 bar charges of CO_2 and 1-6 bar charges of H_2 into the reactor, prior to the introduction of 10 bara of the $\text{CO}_2/\text{H}_2/\text{Ar}$ mixture. The influence of water on the reaction kinetics was determined by reacting H_2 and CO_2 in stoichiometric proportion to complete conversion. This yielded a mixture of H_2O and CH_4 to which a 10 bar charge of the $\text{CO}_2/\text{H}_2/\text{Ar}$ mixture was added. Under the reaction conditions used in this study, a significant proportion of the total pressure at the end of an experiment was due to water. The greatest partial pressure was 7.6 bara H_2O at complete conversion, and was obtained by the co-feeding of 4 bara of H_2O with 10 bara of the $\text{CO}_2/\text{H}_2/\text{Ar}$ mixture. The water co-feeding experiments were carried out between 463 and 483 K, for which the saturation vapour pressures for water are approximately 13-19 bara respectively. Within the pores of the catalyst, the influence of

capillary curvature suppresses this pressure by ~5%, hence the partial pressure of water never exceeded the saturation vapour pressure and it thus may be assumed that a condensed phase is not present.

The CO₂ methanation reaction was also undertaken in the pressurised, stainless-steel, fixed-bed reactor (Parker Autoclave Benchtop Reactor System, ID=8 mm), described in Chapter 2, over a temperature range of 443-493 K, with an interval of 10 K at reaction pressures between 5-20 barg. A ~500 mg batch of ground catalyst (150-212 µm) was mixed with ~1500 mg of alumina ground to the same size range to give a homogeneous mixture and loaded into the reactor. In order to maintain the passivation layer of the catalyst, the reactor system was first purged of air using argon before heating to 523 K. At 523 K, a flow of 300 cm³/min (at STP) H₂ (Gas Hourly Space Velocity, GHSV = 7200 h⁻¹) was passed over the catalyst at atmospheric pressure for 6 hours. Post reduction, the reactor was purged with argon and cooled to the desired reaction temperature.

Prior to introducing the reactant gases, the system was raised to the desired reaction pressure using argon. The H₂ and CO₂ reactants, as well as Ar (as a balance gas) were then mixed and introduced to the reactor at H₂/CO₂ molar ratios between 0.25 and 15.

4.3.2 Control Experiments

The measurements of chemical kinetics could have been complicated by deactivation of the catalyst. Hence, it was important to verify that the rate of deactivation was insignificant relative to the rate of reaction. In Figure 4.1, the reproducibility of the catalyst under batch conditions is demonstrated. Despite the high ratios of H₂O to H₂ generated as the reaction tended towards complete conversion of H₂, the catalyst appeared stable. The reaction conditions used to generate Figure 4.1, *viz.* T = 473 K and an initial charge of 10 bara CO₂/H₂/Ar mixture, were used as a reference condition throughout the course of the investigation, permitting any catalyst deactivation to be monitored.

Owing to the non-stoichiometric ratio of the CO₂/H₂ mixture, hydrogen was fully consumed during the course of a run. The selectivity for the reaction to methane was high, >98.5%, with C₂-C₄ alkanes forming the remainder of the product. No carbon monoxide or alcohols were detected in the analysis, and the overall carbon balance for each batch closed to within 96% of the original charge.

For brevity in the following sections, figures will only show the formation of methane to demonstrate the influence of hydrogen, carbon dioxide and water on the rate of reaction, and any influence this has on the methane selectivity is noted within the text.

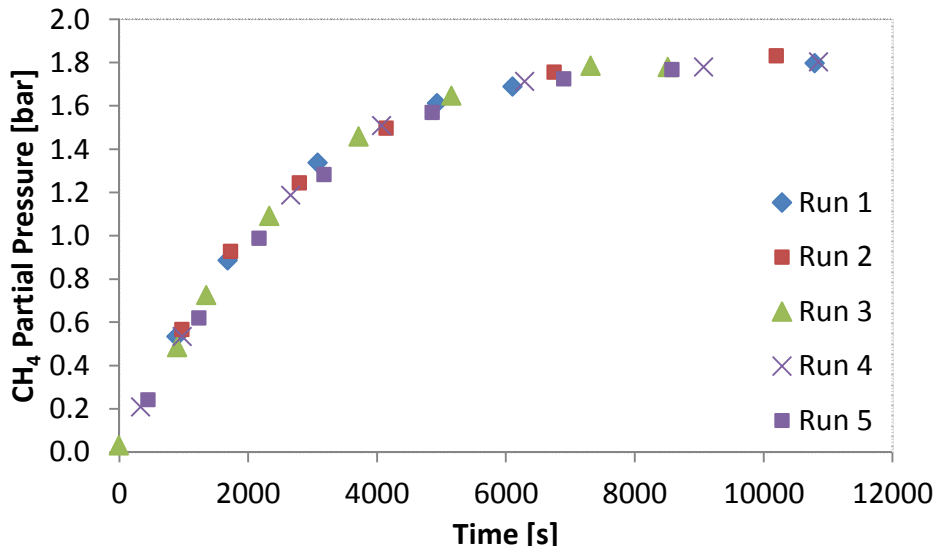


Figure 4.1. Reproducibility of five sequential runs of the carbon dioxide methanation reaction for an initial charge of 10 bara and 473 K with 5.0 g of 12 wt% Ni/ γ -Al₂O₃.

The reproducibility of the catalyst demonstrated in Figure 4.1 is very good and shows that deactivation was negligible over the course of an experiment. These reference experiments were repeated at intervals to verify the catalyst had not become deactivated upon changing conditions.

In order to accurately characterise the kinetics of the catalyst, the system must be free from heat and mass transfer limitations. The deviation from the intrinsic kinetic rate due to the influences of external heat and mass transport was predicted to be < 5% of the intrinsic rate by the Mears and Weisz criteria, under the conditions used in the study. This assumption was verified experimentally using replicate runs at different stirrer speeds, with the methane profile overlapping at each of the tested stirrer speeds between 7.1 and 14.0 Hz (426 and 840 rpm), as demonstrated in Figure 4.2.

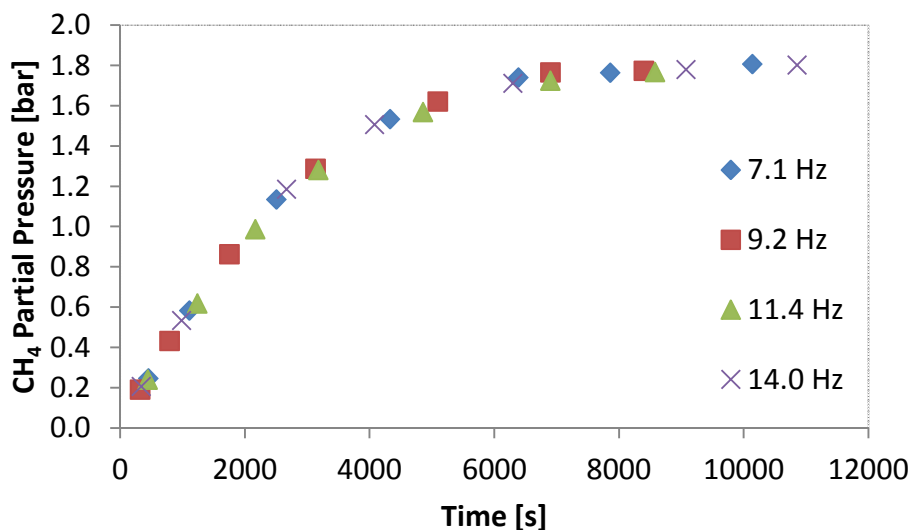


Figure 4.2. Influence of stirrer speed on the carbon dioxide methanation reaction for an initial charge of 10 bara at 473 K with 5.0 g of 12 wt% Ni/ γ -Al₂O₃.

Similarly, the total pressure was found to have no influence on the reaction through introduction of 2, 4 or 6 bar of N₂ alongside 10 bar charges of the CO₂/H₂/Ar mixture. The resulting methane profiles overlapped, indicating no influence of bulk diffusion on the reaction rate. The influence of internal heat and mass transfer limitations were not indicated by the Anderson and Weisz-Prater criteria. The independence of the observed reaction rate from stirrer speed, and total pressure were in agreement with the results determined by Lim (2014).

4.4 Results: Batch Methanation over Ni/ γ -Al₂O₃

4.4.1 Effect of P_{H_2}

The addition of hydrogen to the batch increased the ratio of hydrogen to carbon dioxide, resulting in further conversion of carbon dioxide. The concentration of methane as a function of time is given in Figure 4.3 for 0, 2, 4 and 6 bara H₂ co-feeding pressures. The figure is a composite of repeated batch runs owing to the limited number of samples which could be taken per batch experiment.

Due to the reaction stoichiometry, addition of hydrogen co-feeds in excess of 2.4 bara resulted in the complete conversion of carbon dioxide and thus an excess of hydrogen. The selectivity to methane, on a carbon basis, was evaluated using equation (4.1) at the end of each run, with it seen to increase slightly from 98.5 mol% at 0 bara H₂ co-feeding to 99.1 mol% for a 6 bara co-feed pressure.

$$\text{CH}_4 \text{ Selectivity (mol\%)} = \frac{P_{\text{CH}_4} \times 100}{P_{\text{CH}_4} + \sum_{n=2}^{} n(P_{\text{C}_n\text{H}_{2n}} + P_{\text{C}_n\text{H}_{2n+2}})} \quad (4.1)$$

The initial rate of methane formation appeared to be unaffected by the partial pressure of hydrogen. However, at higher CO₂ conversions, at around $t = 2000$ s, the profiles began to deviate, with the higher initial partial pressures of hydrogen maintaining a higher reaction rate until nearing complete conversion of the carbon dioxide. The profiles indicate that the rate is unaffected by hydrogen pressure at high hydrogen partial pressures; however, as conversion increases and the partial pressure of hydrogen falls, an influence on the rate becomes apparent. Additional hydrogen co-feeding experiments were carried out at 453, 463 and 483 K, with similar behaviour observed.

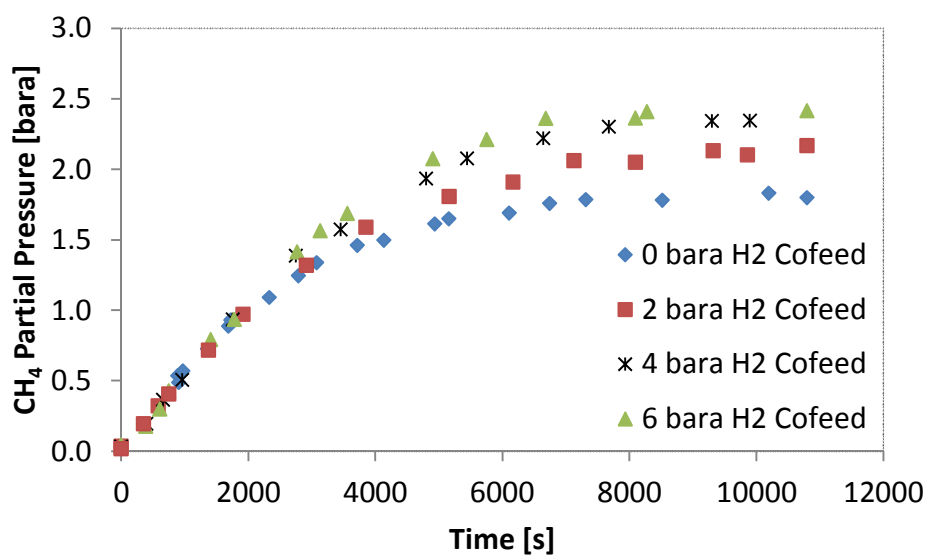


Figure 4.3. Methane pressure profile for different hydrogen co-feeding pressures. Reaction carried out with an initial charge of 10 bara H₂/CO₂/Ar mixture at 473 K, with 5.0 g of Ni/γ-Al₂O₃ catalyst.

4.4.2 Effect of P_{CO_2}

Additional carbon dioxide was introduced at pressures of 2 and 4 bara in addition to the 10 bara feed of $CO_2/H_2/Ar$ mixture. Under the conditions explored, the additional carbon dioxide appeared to have little influence on the concentration-time profile of methane within the reactor.

The profiles, shown in Figure 4.4, appear to overlap. As the reaction is limited by hydrogen, the batch at the highest conversion contained residual carbon dioxide. At the lowest hydrogen partial pressure, 0.6 bar of CO_2 remained in the batch, hence the figures indicate that the rate of methanation is independent of carbon dioxide partial pressures above 0.6 bar.

The selectivity for methane was slightly suppressed by the addition of carbon dioxide, with a methane selectivity of 98.1 mol% and 97.5 mol% for, respectively, 2 and 4 bara CO_2 co-feeding. This difference is not significant enough to be apparent in the methane concentration profile; hence the rates of methane production appear to be the same, irrespective of changes in selectivity. Additional CO_2 co-feeding experiments were carried out at 453, 463 and 483 K, with similar behaviour observed.

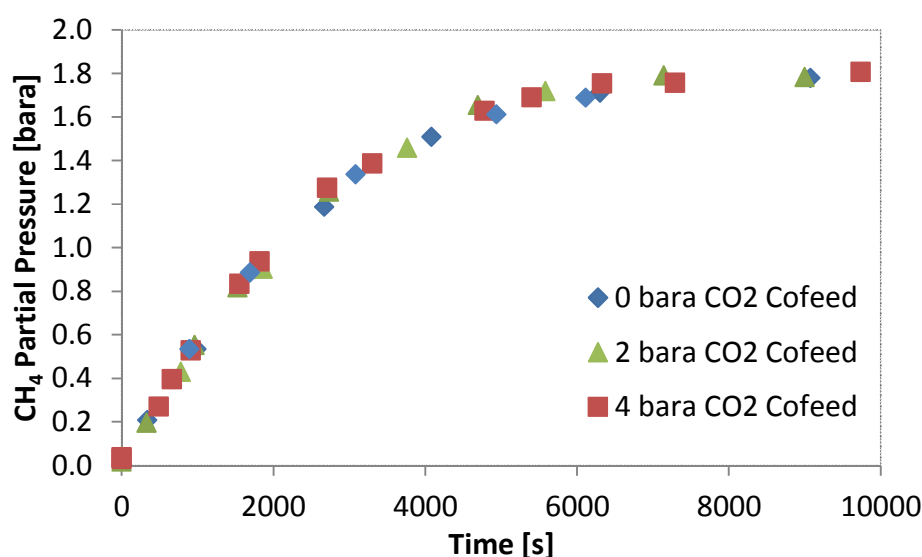


Figure 4.4. Methane pressure profile for different carbon dioxide co-feeding pressures. Reaction carried out with an initial charge of 10 bara $H_2/CO_2/Ar$ mixture at 473 K, with 5.0 g of $Ni/\gamma-Al_2O_3$ catalyst.

The apparent independence of the reaction rate on carbon dioxide provides further evidence that the reaction is not internally mass transfer limited by carbon dioxide. Were the reaction limited by the diffusion of carbon dioxide into the pores of the catalyst, an increase in

the boundary partial pressure of carbon dioxide would result in an increase in the observed reaction rate.

4.4.3 Effect of Temperature

The rate of methane formation was investigated between 443 K and 483 K, with the initial rates of reaction observed to increase with temperature. The selectivity to methane was observed to increase marginally with temperature from 98.3 to 99.2 %mol over the temperature range investigated. The carbon balance across the range of temperature remained >97% at all temperatures. The dependence of methane selectivity on temperature mirrors the literature, with Ashok *et al.* (2016) observing a similar trend for their nickel on CeO₂/ZrO₂ catalyst up to 250 °C.

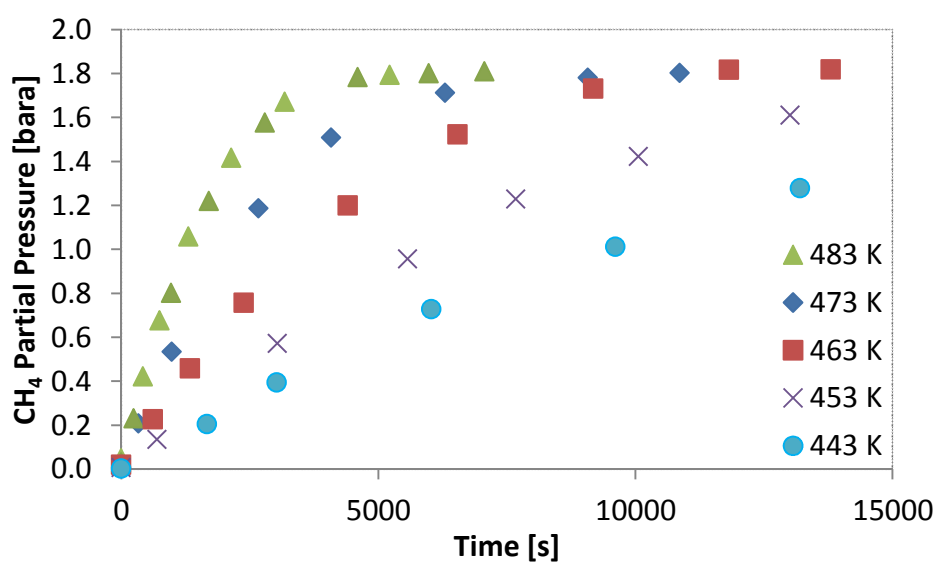


Figure 4.5. Methane pressure profiles at different reaction temperatures. Reaction carried out at an initial charge of 10 bara H₂/CO₂/Ar mixture with 5.0 g of Ni/γ-Al₂O₃ catalyst.

4.4.4 Effect of $P_{\text{H}_2\text{O}}$

Water was generated within the batch reactor using the reaction of stoichiometric quantities of carbon dioxide and hydrogen to form a 2:1 mixture of water and methane. Once at complete conversion, a 10 bara charge of the $\text{CO}_2/\text{H}_2/\text{Ar}$ mixture was added to the batch reactor and the measurements commenced. The increase in water partial pressure within the reactor was observed to have an inhibitory influence on the reaction rate, as demonstrated by the decreased initial rate of methane production in Figure 4.6. The influence of water co-feeding is significant with the initial rate decreasing by 36% with a 2 bar H_2O feed, and 44% with 4 bar H_2O at 473 K.

The inhibitory action on the rate of CO_2 methanation by water apparent in Figure 4.6 provides further explanation for the shape of the methane concentration profiles. At large CO_2 conversions, where the partial pressure of water is high and the partial pressures of carbon dioxide and hydrogen are lowered, the rate of methanation is noticeably reduced.

The increase in water partial pressure resulted in a slight decrease in the selectivity for methane, with the selectivity at 2 bara H_2O co-feeding decreasing from 98.5 mol% to 95.5 mol%. Similarly, with 4 bara H_2O co-feeding, the observed methane selectivity decreased to 94.4 mol%.

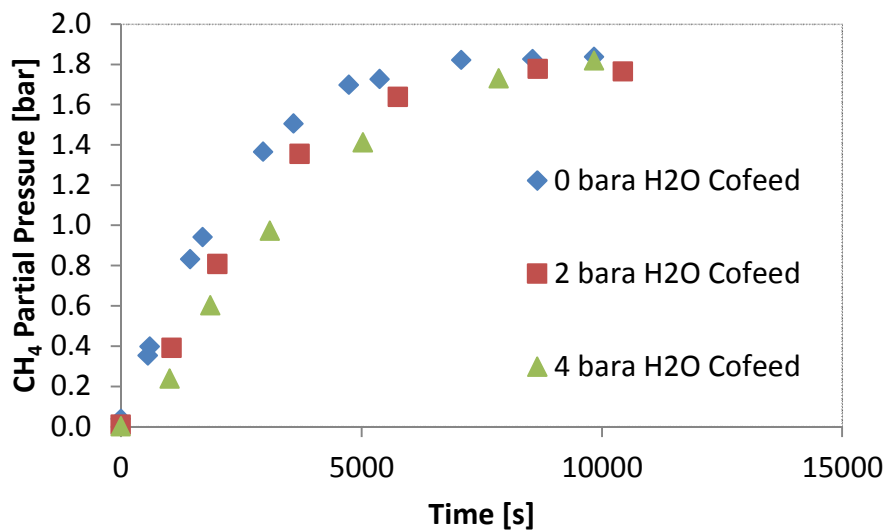


Figure 4.6. Methane pressure profile for different water co-feeding pressures. Reaction carried out with an initial charge of 10 bara $\text{H}_2/\text{CO}_2/\text{Ar}$ mixture at 473 K, with 5.0 g of $\text{Ni}/\gamma\text{-Al}_2\text{O}_3$ catalyst.

4.5 Parameters Affecting the Measurement of Kinetics in a Fixed-Bed Reactor

In order to characterise the reaction kinetics of the Ni/ γ -Al₂O₃ catalyst in the fixed-bed reactor, the influences of heat and mass transfer were eliminated. Blank tests were carried out to eliminate any possibility of methanation activity from the support, diluent and the reactor body, with the tests indicating all were inactive for CO₂ methanation.

The influence of heat and mass transfer within the reactor were quantified using the Weisz-Prater, Mears and Anderson criteria. These criteria were satisfied under all the conditions tested within the BTRS, indicating that intra-particle heat and mass transport would not limit the reaction, and thus the changes in rate could be attributed to chemical kinetics. Further details of the calculations using these criteria are in Appendix (§A2).

The pressure drop across the bed was small (~0.1 bar), hence the use of the inlet pressure measurement to determine the reactant pressures at the catalyst from the measured concentrations was valid. Dilution of the catalyst particles with inert particles in fixed-beds can, in some cases, alter the observed conversion due to bypassing or formation of concentration gradients across the bed due to differences in catalyst distribution. The influence of dilution is particularly noticeable at high conversions, or at high catalyst to diluent ratios. Catalyst dilution, however, is often required to reduce temperature gradients in strongly exothermic catalytic reactions. Here, the catalyst to diluent ratio was approximately, 1:3, and the criterion reported by Berger et al. (2002) was used to exclude the possibility of dilution influencing the reaction rate.

4.5.1 Catalyst Stability

The fixed-bed reactor provided a means to examine the catalyst at differential conversions; a task impracticable with the batch reactor. Prior to the variation of the partial pressures of reactants, the stability of the catalyst was ascertained. The Ni/ γ -Al₂O₃ catalyst appeared stable within the fixed-bed reactor, as demonstrated in Figure 4.7. The CH₄ concentration was initially seen to increase due to the reactor initially being filled with argon. This is followed by a gradual decay over time. The rate of deactivation at 473 K was most severe within the first 30 hours on stream, in which 4% of the peak catalytic activity was lost. Between 30 and 70 hours on stream, the catalytic activity decreased a further 2.5%. Industrially this rate of deactivation would be significant, since industrial reactors are expected to run for significantly longer than the experiments herein, however the observed

rate of deactivation is low enough to not significantly affect the kinetic analysis. A recent investigation of CO₂ methanation on nickel alumina catalysts by Koschany *et al.* (2016) noted that deactivation after an initial ageing period for their co-precipitated nickel catalyst had a similarly negligible impact on their experiments below 523 K, in agreement with the behaviour of the alumina-supported catalyst used here.

After the catalyst activity stabilised, the reaction parameters were varied. A reference measurement was made periodically in order to determine the extent of deactivation and thus allow for accounting of deactivation and catalyst consistency. Koschany *et al.* (2016) noted that deactivation phenomena were less severe when their fixed-bed was operated differentially than when operated at larger conversions. However, the stability of the catalyst's activity under batch conditions suggests deactivation was minor, even at high conversions.

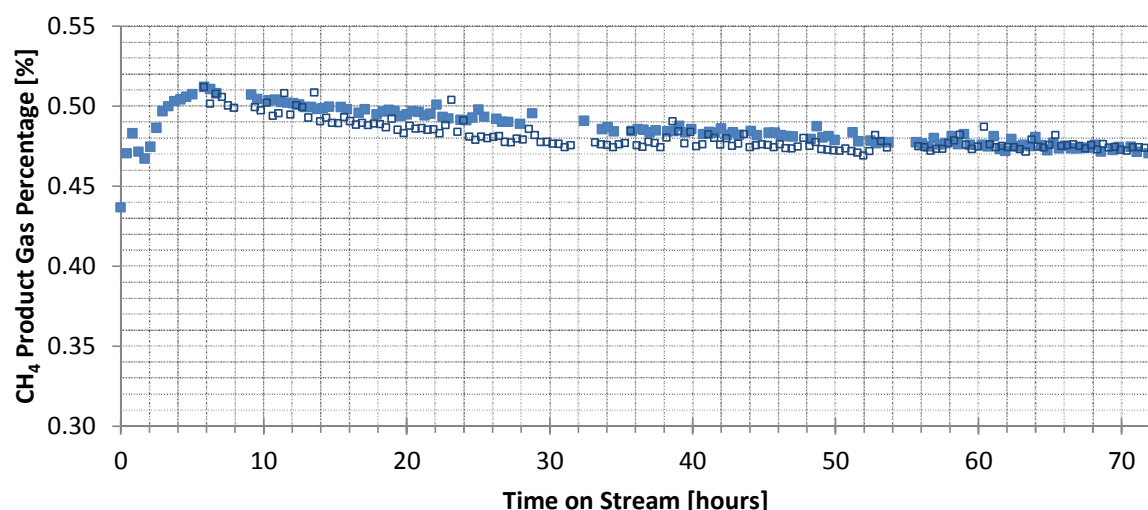


Figure 4.7. The variation of methane percentage in the BTRS product gas with time on stream. Conditions: 473 K, 20 barg, 150/50/6 cm³/min (at STP) H₂/CO₂/Ar (GHSV = 4994 h⁻¹), 0.5 g Ni/Al₂O₃ catalyst. The open and closed squares represent results from two separate runs under the same conditions.

The reproducibility of the experimental results was good, with the agreement between two separate runs over the initial deactivation period represented by the filled and open squares in Figure 4.7. For the investigation of reaction kinetics, the partial pressures of carbon dioxide and hydrogen were varied, whilst maintaining a set inlet space velocity. Each condition was held for a sufficient period of time, typically ~4-6 hours, such that the influence of mixing in the pipework after the reactor could be neglected. This was verified by comparing gas composition over the last 2 hours of a condition to check for consistency in the

measured composition. Owing to the low conversions, the methane product typically constituted <1% of the overall gas composition. A typical transition of methane concentration for a change in reaction conditions is shown in Figure 4.8. Here the pressure was increased from 10 barg to 20 barg with temperature maintained at 473 K. The methane concentration appears to be stable after 2 hours, equivalent to ~5 residence times of the reactor at a pressure of 20 barg.

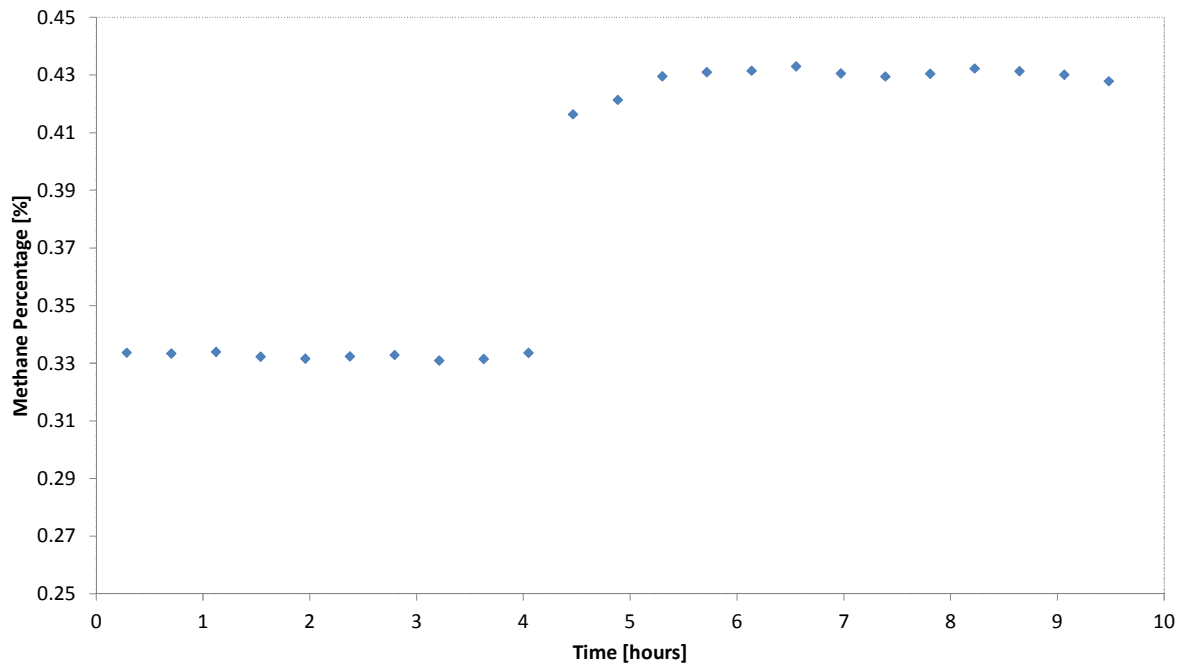


Figure 4.8. Demonstration of methane concentration stability and transition time between conditions. The pressure was switched from 10 barg to 20 barg at hour 4.

4.6 Determination of Methanation Kinetics in a Fixed-Bed Reactor

The results from the continuous reactor were obtained at 10 K intervals between 443 K and 493 K. The rate of methanation was investigated across total reaction pressures of 5–20 barg and H₂/CO₂ ratios between 0.25 and 15.

4.6.1 Effect of P_{H₂} and P_{CO₂}

The partial pressure of hydrogen was found to have a weak influence on the rate of methane production in the fixed-bed reactor. Figure 4.9 shows the variation of methane mole fraction at a constant molar inlet flowrate of feed. The rate of methane production appears to decrease slightly as the partial pressure of hydrogen is decreased, with the outlet concentration decreasing by approximately 5% upon changing the hydrogen partial pressure

from 8 to 5.3 bar at a constant flowrate of $206 \text{ cm}^3/\text{min}$ at STP ($\text{GHSV} = 4944 \text{ h}^{-1}$) and a CO_2 partial pressure of 2.7 bar. Changes in H_2 pressure were balanced with argon to maintain a constant total pressure. This weak influence agrees roughly with the observations from the batch reactor showing no notable change in rate at low conversions. Deactivation over the experimental period was small, with only a noticeable difference at a pressure of 20 barg. The extent of deactivation may be noted by the agreement of the two data points taken at the highest hydrogen pressure for each total pressure (8.0, 10.9 and 15.3 bar H_2 partial pressure.) These correspond to an inlet flow of $150/50/6 \text{ cm}^3/\text{min}$ (at STP) of $\text{H}_2/\text{CO}_2/\text{Ar}$ mixture for each reactor pressure. The variation of partial pressures were commenced and ended for each total pressure at this flow ratio, demonstrating the low level of catalyst deactivation over the experiments.

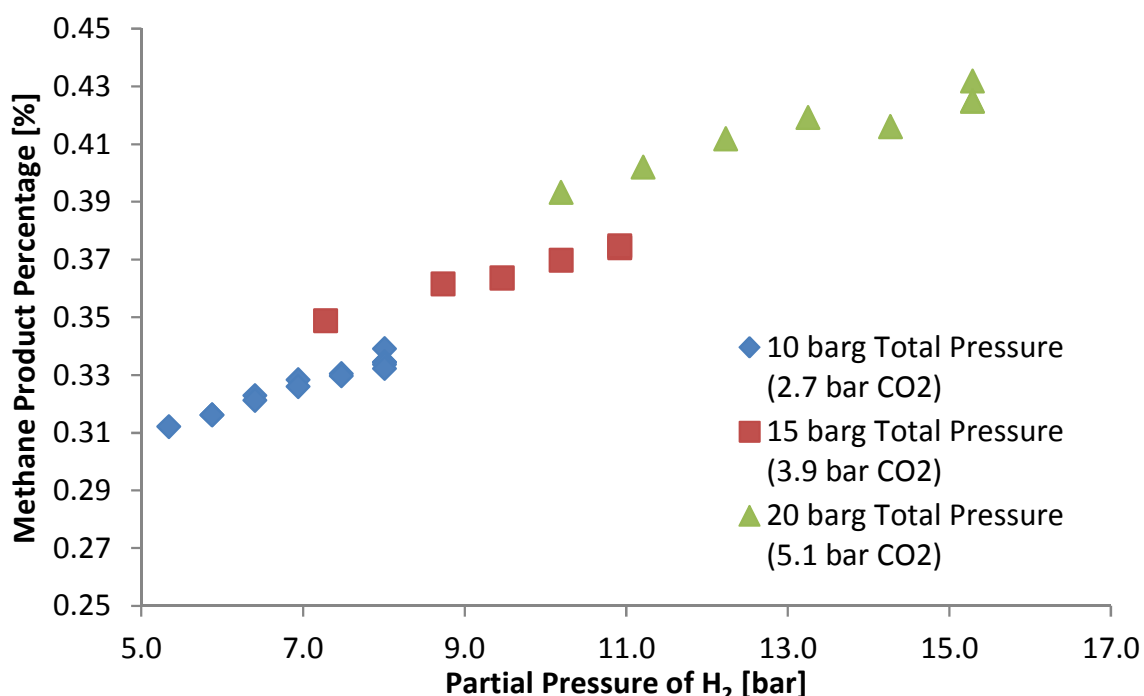


Figure 4.9. Influence of H_2 on CH_4 concentration in the product gases. The total flow was maintained at $206 \text{ cm}^3/\text{min}$ (at STP) ($\text{GHSV} = 4944 \text{ h}^{-1}$) with argon balancing and changes in H_2 pressure. The flow of CO_2 in was maintained at $50 \text{ cm}^3/\text{min}$ (at STP). The stated pressures are the total reaction pressure and that of CO_2 . The reaction temperature was 473 K.

It is clear from Figure 4.9 that CO_2 influences the rate of methanation, with the methane percentage increasing as the total reactor pressure does. The overlapping regions indicate an increased partial pressure of CO_2 at constant H_2 partial pressure yields a greater methanation rate. The partial pressure of carbon dioxide was confirmed to have an effect on the outlet concentration of methane through variation of the CO_2 partial pressure at set H_2

partial pressure, as seen in Figure 4.10. A weak positive correlation between methane percentage and carbon dioxide partial pressure was observed at total pressures of 10 and 15 barg. These observations differ from those of the batch reactor, where carbon dioxide appeared to have no influence on the methane production rate. Indeed, raising the carbon dioxide initial partial pressure from 2.4 (0 bar co-feed) to 6.4 bar (4 bar co-feed) in the batch reactor had little apparent influence on the rate of methane production.

The dependence of the rate of methane production on the partial pressure of carbon dioxide could not be accounted for by internal or external mass transfer effects. The calculated Mears and Weisz-Prater criteria were significantly below the value at which mass transfer limitation might be probable. The H₂ and CO₂ partial pressures were also varied at temperatures of 453, 463 and 483 K.

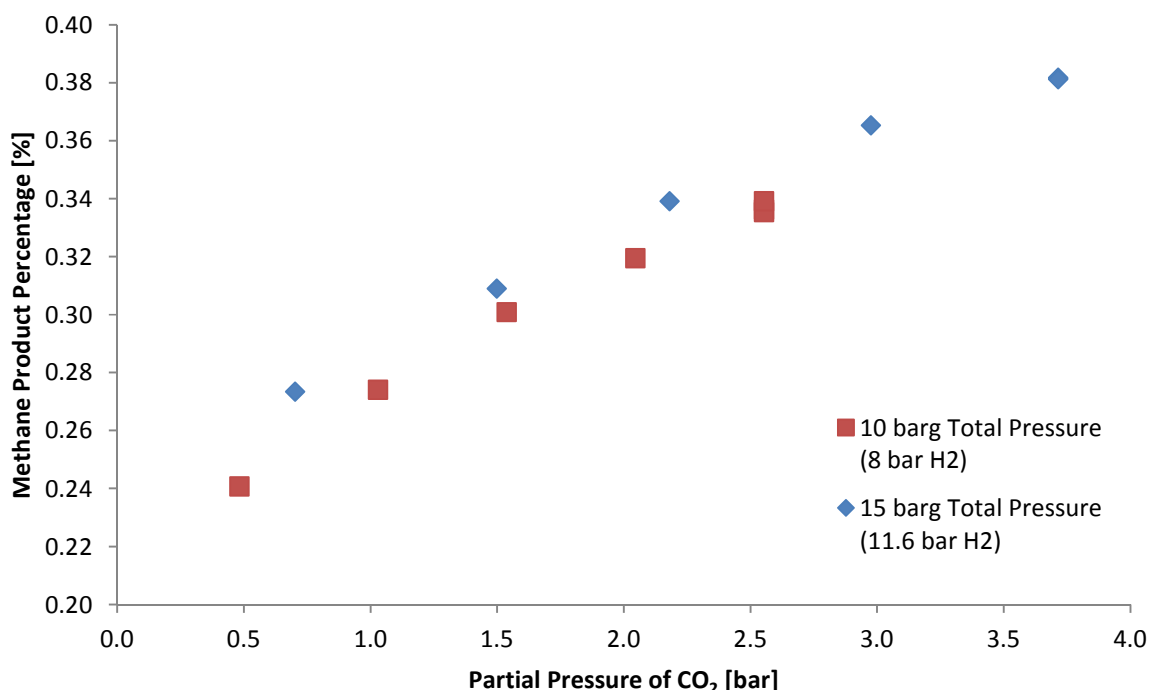


Figure 4.10. Influence of CO₂ on CH₄ concentration in the product gases. The total flow was maintained at 206 cm³/min (at STP) (GHSV = 4944 h⁻¹) with argon balancing any changes in CO₂ partial pressure. The stated pressures are the total reaction pressure and the H₂ partial pressure at the corresponding total pressure. The reaction temperature was 473 K.

4.6.2 Effect of Space Velocity

The methane concentration in the outlet stream was found to be inversely proportional to the inlet flow, as shown in Figure 4.11. The calculated rate per gram of catalyst was found to be invariant across the range of total flows tested. This confirms that the rate was not influenced by external mass transport, which otherwise would have resulted in an increased rate of production per gram with increasing flowrate.

Since the fraction of methane in the product gas was maintained below 1.2%, the partial pressure of water at the outlet of the bed remained significantly lower than those experienced by the catalyst in the batch reactor. Hence, the changes in conversion over the range of space velocities used were not expected to result in an increased inhibition of the reaction rate by adsorbed water.

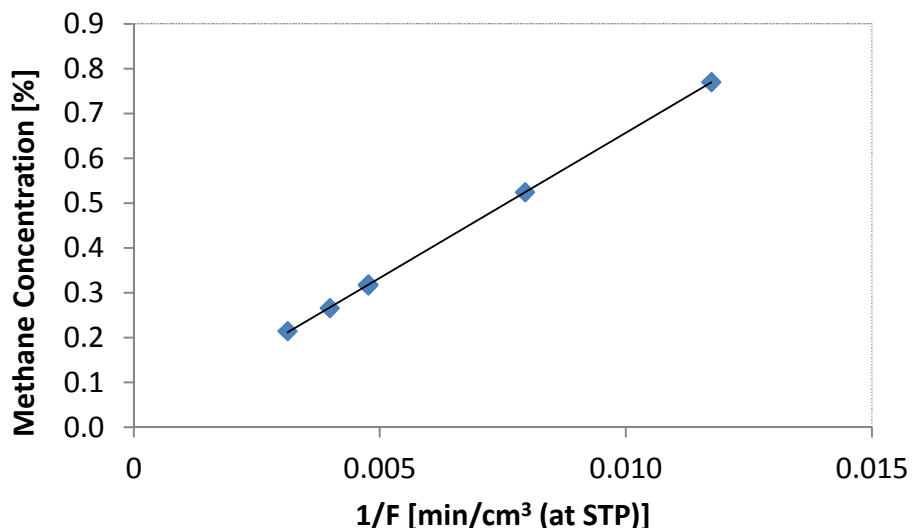


Figure 4.11. Variation of methane concentration with inverse space velocity at 10 barg, 473 K, 150/50/6 H₂/CO₂/Ar flow ratio.

4.6.3 Effect of Temperature

The influence of temperature on the rate of methanation rate determined between 443 K and 493 K, and is shown in Figure 4.12. The apparent activation energies at 5, 7, 10 and 20 barg were calculated to be 92.7±2.4, 93.1±3.6, 92.0±4.9 and 92.3±5.6 kJ/mol respectively. Their consistency indicates the rate-limiting step is independent of the total reaction pressure and that there is no bulk diffusion limitation. The presence of bulk diffusion

limitation would lower the activation energy significantly at higher reactor pressures, and a curvature would be observed in the Arrhenius plot.

The apparent activation energy is in good agreement with published values. For instance, values of 82-89 kJ/mol have been reported for a Ni/Al₂O₃-SiO₂ catalyst (Campbell and Falconer, 1989), 89 kJ/mol for a Ni/SiO₂ catalyst (Weatherbee and Bartholomew, 1982), 71-99 kJ/mol for SiO₂, Al₂O₃ and TiO₂ supported nickel catalysts (Vance and Bartholomew, 1983), and 107 kJ/mol reported for nickel supported on bentonite clay (Lu *et al.*, 2015).

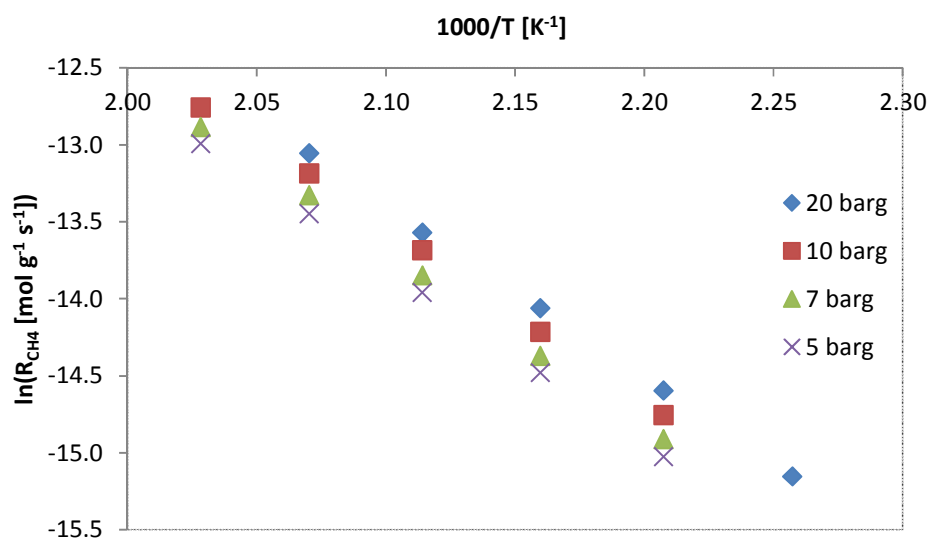


Figure 4.12. Arrhenius plots for 5, 7, 10 and 20 barg total pressures, 150/50/6 cm³/min at STP H₂/CO₂/Ar.

4.7 Kinetic Determination

This section will briefly review the current state of CO₂ methanation kinetics and the evidence for the associated mechanisms. It will also introduce candidate schemes for comparison and quantification of the kinetics under batch and continuous conditions. An in-depth review of the literature concerning the kinetics and mechanism is presented in the Appendix (§A3).

4.7.1 Mechanism Overview

Despite the apparent simplicity of the methanation reaction, the mechanism remains subject to debate, with the main point of contention found in the identity of the surface intermediate. The reaction mechanisms proposed within the literature may be divided into two categories. The first proposes that the reaction proceeds *via* direct hydrogenation of carbon dioxide to methane, whilst the latter proposes the reaction proceeds *via* a carbon monoxide

surface intermediate. Once formed, this carbon monoxide surface intermediate then reacts following an analogous mechanism to carbon monoxide hydrogenation. The route of formation of the intermediate has been suggested to occur either directly *via* dissociation of CO₂ to CO(ads) and O(ads) on the surface *e.g.* Eckle *et al.* (2011), or indirectly *via* the partial reduction of carbonate or formate surface species *e.g.* Westerman *et al.* (2015). An example reaction scheme for CO₂ methanation *via* the CO intermediate pathway is given in Table 4.1.

Table 4.1. Methanation reaction *via* CO and surface carbon intermediates, adapted from Weatherbee and Bartholomew (1982). The * represent surface sites.

Reaction Step	
H ₂ (g)+2*=2H*	(4.2)
CO ₂ (g)+2*=CO*+O*	(4.3)
CO*+*=C*+O*	(4.4)
C*+H*=CH*+*	(4.5)
CH*+H*=CH ₂ *+*	(4.6)
CH ₂ *+H*=CH ₃ *+*	(4.7)
CH ₃ *+H*=CH ₄ *+*	(4.8)
CH ₄ *=CH ₄ (g)+*	(4.9)
O*+H*=OH*+*	(4.10)
OH*+H*=H ₂ O*+*	(4.11)
H ₂ O*=H ₂ O(g)+*	(4.12)
CO*=CO(g)+*	(4.13)

A second pathway has also been proposed to proceed *via* a formate intermediate. The determination of the rate-limiting step and the true intermediate is complicated, since some IR studies show the coexistence of carbonyl and formate species on the surface of the catalyst. The true role of formate in the reaction is unknown, with conflicting studies proposing it either acts as a side product, or that it is in fact a key intermediate, *e.g.* Aldana *et al.* (2013), which may either decompose to CO or be hydrogenated directly. The investigations in support of a formate intermediate have employed reducible supports or those with basic sites, which have been noted to enhance CO₂ adsorption. Thus, it appears support differences might provide a reason for the observed differences in behaviour.

4.7.2 Kinetics Investigations

A summary of the published kinetic equations for nickel based CO₂ methanation catalysts are given below in Table 4.2. The kinetics of carbon dioxide hydrogenation has been investigated over a number of decades, with the majority of studies characterising the rate of methanation by a Langmuir-Hinshelwood type expression. The literature is discordant on the best form for kinetic representation, reflecting the uncertainty in the underlying kinetic mechanisms. The majority of studies favour a CO dissociation based mechanism, with a rate-limiting step of either CO dissociation or hydrogenation of the resultant carbon species. The role of hydrogen in the rate-limiting step is uncertain, with the apparent order of reaction positive but variable between zeroth and first order depending on the study in question. Similarly the apparent order of reaction with respect to P_{CO₂} varies between studies; with some authors reporting zeroth order behaviour and others predicting orders between 0 and 1.

Table 4.2. Kinetic equations for the methanation of carbon dioxide on Nickel.

Kinetic Equation		Catalyst [Metal/Support]	Apparent E_A [kJ/mol]
Binder and White (1950)	$R_{CH_4} = \frac{a \left(P_{CO_2} P_{H_2}^4 - \frac{P_{CH_4} P_{H_2O}^2}{K_{Eq} P_{H_2}^2} \right)}{(1 + b P_{H_2}^{0.5} + c P_{CO_2})^5}$	Ni/Kieselguhr	-
Dew <i>et al.</i> (1955)	$R_{CH_4} = \frac{a P_{CO_2}^{0.5} P_{H_2}^2}{(1 + b P_{H_2})^3}$	Ni/Kieselguhr	54.8-58.1
Šolc (1962)	$-R_{CO_2} = a P_{CO_2}^{0.66}$	Ni/Cr ₂ O ₃	85.6
Van Herwijnen <i>et al.</i> (1973)	$-R_{CO_2} = \frac{a P_{CO_2}}{(1 + b P_{CO_2})}$	Ni/ γ -Al ₂ O ₃ (33.6 wt% NiO)	105.8
Weatherbee and Bartholomew (1982)	$R_{CH_4} = \frac{a P_{CO_2}^{0.5} P_{H_2}^{0.5}}{\left(1 + b \sqrt{\frac{P_{CO_2}}{P_{H_2}}} + c \sqrt{P_{H_2} P_{CO_2}} + d P_{CO_2} \right)^2}$	Ni/SiO ₂	94
Chiang and Hopper (1983)	$-R_{CO_2} = \frac{a P_{H_2} P_{CO_2}}{(1 + b P_{CO_2} + c P_{H_2})}$	Ni/Kieselguhr (58 wt% Ni)	61.1
Ido <i>et al.</i> (1984)	$-R_{CO_2} = \frac{a P_{H_2}^{0.5} P_{CO_2}}{(1 + b P_{CO_2})}$	Ni/Al ₂ O ₃	-
Inoue <i>et al.</i> (1984)	$-R_{CO_2} = \frac{a P_{H_2} P_{CO_2}}{(1 + b P_{CO_2} + c P_{H_2} + d P_{H_2O})}$	Ni deposited on reactor tube wall.	-
Kai <i>et al.</i> (1988)	$-R_{CO_2} = \frac{a P_{H_2}^{0.5} P_{CO_2}^{0.33}}{(1 + b P_{H_2}^{0.5} + c P_{CO_2}^{0.5} + d P_{H_2O})^2}$	Ni/La ₂ O ₃	72.5
Ibraeva <i>et al.</i> (1991)	$-R_{CO_2} = \frac{a P_{H_2}^{0.5} P_{CO_2}}{(b P_{CO_2} + P_{H_2}^{0.5})}$	Ni/NKM-4A catalyst	78.6
Koschany <i>et al.</i> (2016)	$R_{CH_4} = \frac{a P_{H_2}^{0.5} P_{CO_2}^{0.5}}{\left(1 + b \left(\frac{P_{H_2O}}{P_{H_2}^{0.5}} \right) + c P_{H_2}^{0.5} + d P_{CO_2}^{0.5} \right)^2}$	Ni/Al ₂ O ₃ (Co-precipitated)	77.5
Lim <i>et al.</i> (2016)	$R_{CH_4} = \frac{a P_{CO_2}^{0.5} P_{H_2}^{0.5}}{\left(1 + b \sqrt{\frac{P_{CO_2}}{P_{H_2}}} + c \sqrt{P_{H_2} P_{CO_2}} + d P_{H_2O} \right)^2}$	Ni/ γ -Al ₂ O ₃ (Impregnation)	92.0

4.7.3 Modelling Reaction Kinetics in the Batch Reactor

The primary objectives of this study were the identification of rate expressions for the methanation of CO₂ consistent with the experimental measurements and comparison of the two reactor systems. For the batch reactor, the changes in partial pressures were modelled as a set of differential equations, given by,

$$\frac{dP_i}{dt} = \frac{\nu_i RT m_{\text{cat}}}{V_{\text{Reactor}}} R_{\text{CH}_4} \quad (4.14)$$

where P_i is the partial pressure of species i , ν_i is its stoichiometric coefficient, R is the gas constant, T is the reaction temperature, m_{cat} is the catalyst mass, V_{Reactor} is the gas volume of the reactor, and R_{CH_4} is the specific rate of methanation. Equation (4.14) was solved for each species concurrently as an initial value problem, using the initial conditions for the experiments, that is, the species pressures at $t = 0$ s. This provided an estimate of the temporal variation of the partial pressure of CO₂, H₂, CH₄ and H₂O within the batch for a given kinetic model and parameter set.

Carbon monoxide was not detected and the reaction was highly selective for methane, with only small quantities of ethane and higher alkanes formed. Hence, it was assumed that the reaction could be represented solely by equation (4.15). The closure of the carbon balance indicated that equation (4.15) is, indeed, the primary reaction.



4.7.4 Modelling Reaction Kinetics in the Continuous Reactor

The Bench-Top Reactor system (BTRS) was modelled under the assumption of constant volumetric flow through the reaction zone. The overall fraction of hydrocarbons in the product stream was maintained below ~1.2%, hence the molar, and thus volumetric flow decreased by less than 2.4%. The product concentration was determined through integration of the rate equation across the bed. However under all but the most extreme conditions the hydrocarbon mole fraction could be related to the rate under the assumption of differential reaction without significant error, as shown by equation (4.16).

$$R_{\text{CH}_4} = \frac{x_{\text{CH}_4} \rho_m \dot{V}}{m_{\text{cat}}} \quad (4.16)$$

Here R_{CH_4} is the specific rate of methanation, x_{CH_4} is the methane mole fraction in the analysed gas, ρ_m is the molar density of an ideal gas at STP, m_{cat} is the catalyst mass and \dot{V} the total volumetric flowrate into the reactor.

4.7.5 Candidate Kinetic Equations

The form of the kinetic equation is dependent on the selected reaction pathway and the assumed rate-limiting step. Lim *et al.* (2016) suggested that a nickel alumina catalyst might be modelled using a Langmuir-Hinshelwood (LH) type expression based on a rate-limiting step of CO dissociation. Of the four equations examined by Lim *et al.* (2016), two of the kinetic expressions provided the best agreement with their experimental results and are given as equations (4.17) and (4.18).

$$R_{CH_4} = \frac{a_I P_{H_2}^{0.5} P_{CO_2}^{0.5}}{(1 + b_I P_{H_2}^{0.5} + c_I P_{H_2}^{0.5} P_{CO_2}^{0.5} + d_I P_{H_2} O)^2} \quad (4.17)$$

$$R_{CH_4} = \frac{a_{II} P_{H_2}^{0.5} P_{CO_2}^{0.5}}{\left(1 + b_{II} \left(\frac{P_{CO_2}}{P_{H_2}}\right)^{0.5} + c_{II} P_{H_2}^{0.5} P_{CO_2}^{0.5} + d_{II} P_{H_2} O\right)^2} \quad (4.18)$$

In order to examine the kinetics of the carbon dioxide methanation reaction more broadly, a number of candidate schemes were tested against the experimental results obtained for both the batch and continuous reactor. These expressions were derived from first principles, on the assumption of different rate-limiting steps. Thus, 63 kinetic assumptions were examined of differing rate-limiting steps across both carbide and formate intermediate reactions schemes, expanding upon the four equations evaluated by Lim. The detailed derivations of the expressions are presented in Appendix (§A1).

The forms of the derived Langmuir-Hinshelwood kinetics were dependent on the assumed rate-limiting step and the means of water removal from the surface. The equations were derived through assumption of a rate-limiting step with pseudo-equilibrium assumed for the remaining reaction steps. The position of the pseudo-equilibrium constants for either (i) hydrogenation of surface O to OH or (ii) hydrogenation of OH to H₂O were assumed to be significantly large such that the forward reaction was considered irreversible. The assumptions of irreversibility for either oxygen hydrogenation or hydroxyl hydrogenation have previously been applied by Lim *et al.* (2016) and Koschany *et al.* (2016) in their derivations of LHHW CO₂ hydrogenation mechanisms.

A third form of Langmuir-Hinshelwood equation was derived for each limiting step on the assumption of quasi-equilibrium for all steps of oxygen hydrogenation. Under this assumption of quasi-equilibrium of the steps from oxygen hydrogenation to water desorption,

the derived rate was proportional to the inverse of the water partial pressure (P_{H_2O}), raised to a positive power of n , as shown in equation (4.19).

$$R_{CH_4} \propto \frac{1}{P_{H_2O}^n} \quad (4.19)$$

Equations of this form were found to be unsuitable for the description of observed kinetics, since at low conversions the rate was not observed to tend towards infinity.

The rate-determining steps assumed were C hydrogenation, CO dissociation, CH hydrogenation, and CO₂ adsorption for a carbide type mechanism. Similarly, equations for the formate pathway were derived for rate-determining steps of CO hydrogenation to CHO, CHO dissociation, and CHO hydrogenation.

The parameters for each model were estimated based on a least-squares minimisation. The agreement of the model and the batch experimental results was studied by comparing the solution of the ODEs with the partial pressures of the species. The difference between the model and experimental values was evaluated at each experimental time point for CH₄, with the objective function to be minimised given by equation (4.20). The a , b , c , d parameters were restricted to positive quantities, such that they represented physically realistic quantities.

$$obj_j = P_{j,Exp} - P_{j,Mod} \quad (4.20)$$

The fixed-bed measurements were compared with the prediction of candidate rate expressions by fitting results with a least-squares minimisation for the objective function given by equation (4.21) for data-point i .

$$obj_i = (x_{CH_4,i}^{exp} - x_{CH_4,i}^{mod}) \quad (4.21)$$

Here the *exp* and *mod* superscripts indicate experimentally obtained or modelled methane mole fractions. The objective function (*obj*) was minimised across the dataset using the MATLAB optimisation function *lsqnonlin* and the Levenberg-Marquardt algorithm, with the Langmuir-Hinshelwood parameters constrained to physically realistic positive values

Methane mole fraction in the outlet is reasonable to determine the rate of methanation, since the reaction has demonstrated a very high selectivity towards methane.

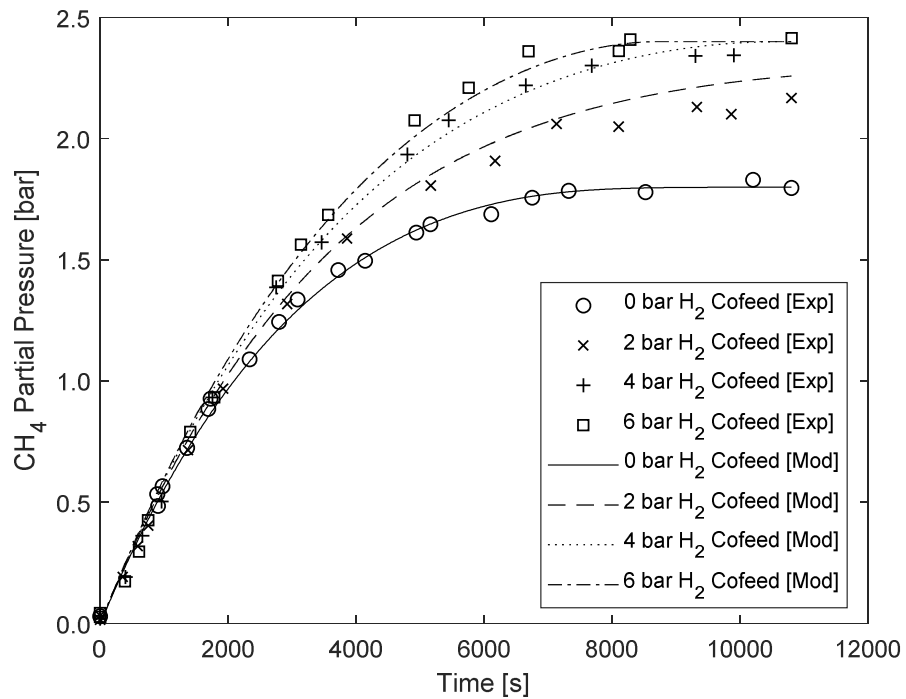
4.7.6 Results: Identification of Kinetic Models based on Batch Observations

Weatherbee and Bartholomew (1982) derived an equation, which was later modified by Lim (2014), equation (4.22), and gave the lowest sum of squares error when fitted to results from the Carberry reactor both in Lim's (2014) research and in the present work. The degree of fit obtained is demonstrated in Figure 4.13 and Figure 4.14. The rate expression below assumes an irreversibility of the CO₂ methanation reaction. This is reasonable under the conditions studied with the equilibrium position favouring near complete conversion up to reaction temperatures of ~600 K.

$$R_{CH_4} = \frac{a_{II} P_{H_2}^{0.5} P_{CO_2}^{0.5}}{\left(1 + b_{II} \left(\frac{P_{CO_2}}{P_{H_2}}\right)^{0.5} + c_{II} P_{H_2}^{0.5} P_{CO_2}^{0.5} + d_{II} P_{H_2} o\right)^2} \quad (4.22)$$

Figure 4.13 a) and b) show the quality of fit for the hydrogen co-feeding and the reaction run with the 10 bara of the CO₂/H₂/Ar mixture over a range of temperatures. The influence of hydrogen partial pressure on the methane partial pressure at 473 K appears well described. The quality of the fit is fair across the temperature range, as demonstrated in Figure 4.13 b); however, the mean percentage deviation in CH₄ partial pressure from the measured and predicted partial pressures was 4.5 % across the fitted dataset.

a)



b)

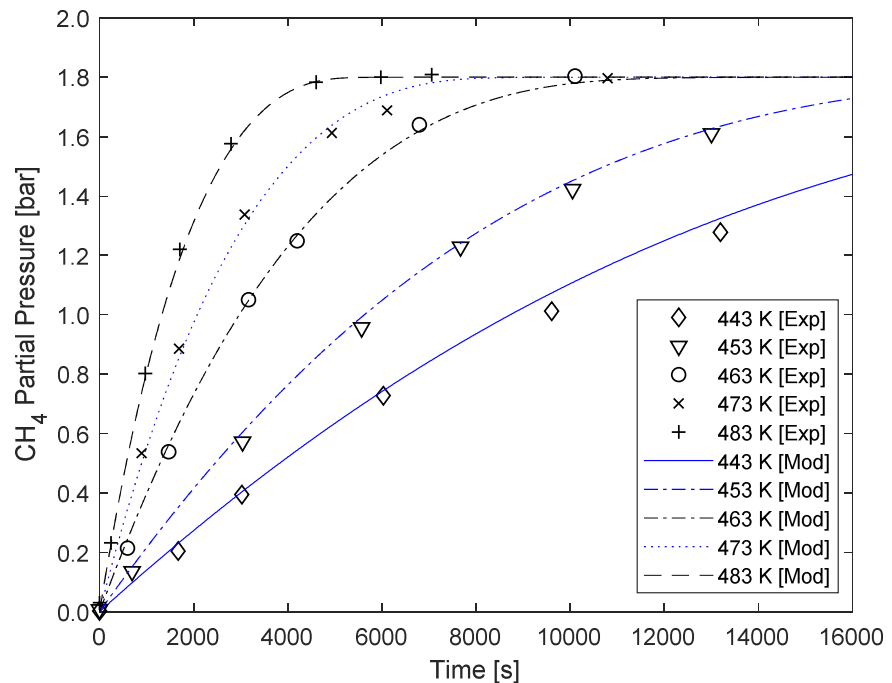


Figure 4.13. Comparison between model and experiment for the modified Weatherbee and Bartholomew (1982) expression. A charging pressure of 10 bara H₂/CO₂/Ar mix was used in a) at 473 K with the stated co-feed pressures of hydrogen. In b), the temperature was varied as shown with no cofeed. The mass of catalyst was 5.0 g.

A parity plot comparing the measured and modelled CH₄ partial pressures is given in Figure 4.14. The dashed lines are plotted to indicate deviations of +/- 10 % from parity. It is clear the majority of data points are bounded by this region with the exception of outliers at the lowest CH₄ partial pressures. A greater error at the lowest partial pressures may be expected since the rates are both highest at the lowest conversions and the percentage error in the reaction duration due to non-instantaneous nature of reactor charging is greatest.

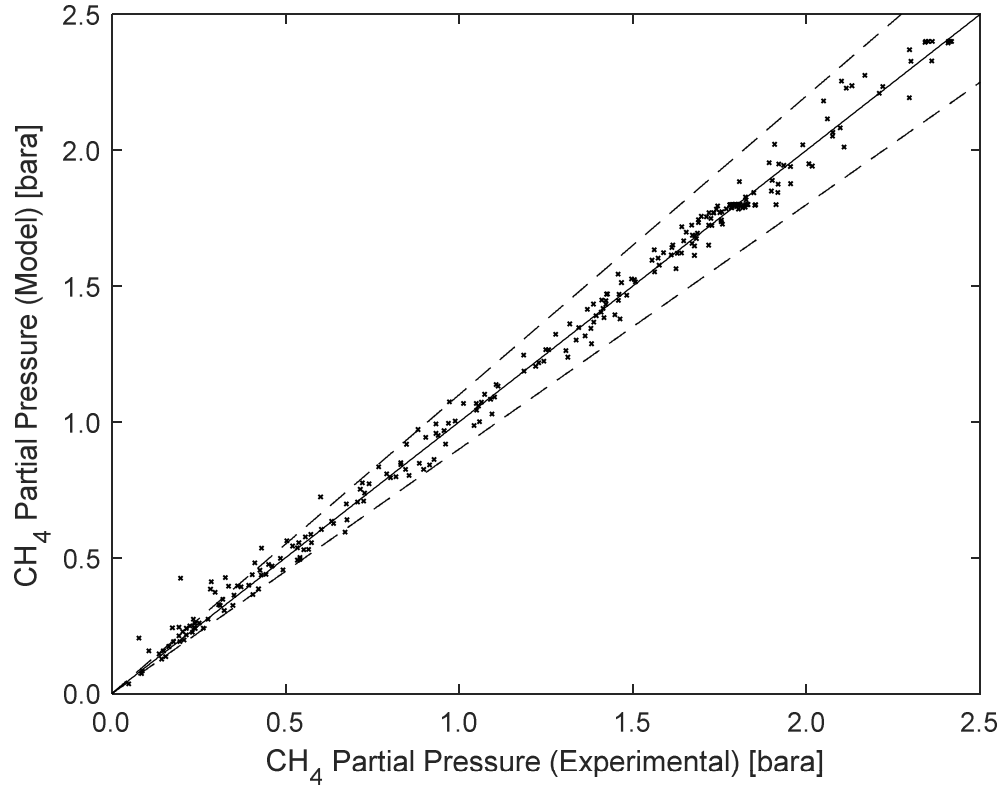


Figure 4.14. Parity plot comparing experimentally determined CH₄ partial pressures and CH₄ partial pressures as determined by the modified Weatherbee and Bartholomew (1982) equation. Parity is represented by the solid line and a ±10% deviation from this is shown by the dashed lines.

The parameters for the modified Weatherbee and Bartholomew (1982) equation are summarised in their pre-exponential constant and activation energy, using the Arrhenius form given by equation (4.23). All parameters were reported relative to the reference temperature of 473 K. For example, for a_I , shown by equation (4.23) comprises the pre-exponential constant, $A_{473\text{ K}}$, and the activation energy E_A . For adsorption parameters, such as parameter b , E_B was replaced by ΔH_B .

$$a_I = A_{473\text{ K}} \exp\left(-\frac{E_A}{R}\left(\frac{1}{T} - \frac{1}{473}\right)\right) \quad (4.23)$$

Table 4.3 Values of pre-exponential and energy parameters for equation (4.22).

Parameter	Value	
$A_{473\text{ K}}$	$(0.81 \pm 0.06) \times 10^{-6}$	[mol g ⁻¹ bar ⁻¹ s ⁻¹]
$B_{473\text{ K}}$	0.23±0.04	[-]
$C_{473\text{ K}}$	0.20±0.03	[bar ⁻¹]
$D_{473\text{ K}}$	0.13±0.02	[bar ⁻¹]
E_A	72.6	[kJ/mol]
ΔH_B	-35.7	[kJ/mol]
ΔH_C	-13.4	[kJ/mol]
ΔH_D	-5.8	[kJ/mol]

4.7.7 Results: Comparison with Fixed-Bed Experiments

The kinetic parameters determined in §4.7.6 were compared against the results obtained under continuous, differential conditions. The parity between the experimentally determined rates in the BTRS and the predicted rates determined from equation (4.22) is shown in Figure 4.15.

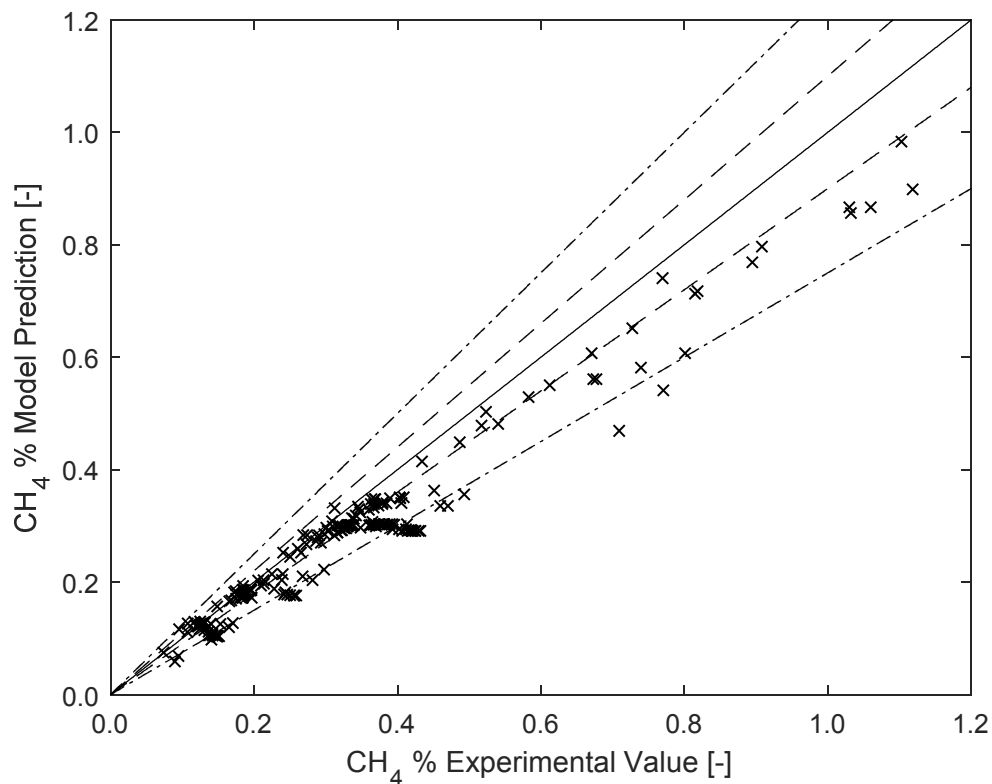


Figure 4.15. Parity plot comparing experimentally determined reaction rates and model determined rates from equation (4.22). The solid line represents parity between experimental data and model predictions, with the dashed lines (- -) representing +/- 10% deviation and the dotted dash line (-.-) representing +/- 25% deviation.

The fit of the parameters determined from batch experiments to the fixed-bed results indicated a significant variation, with the predicted rates in some cases exceeding +/- 25% of the measured value. In order to analyse the cause of the deviations between the behaviour in the batch reactor and the continuous system, the percentage residuals were plotted against hydrogen and carbon dioxide partial pressures. The percentage residuals were computed as defined in (4.24).

$$\% \text{ Residual} = 100 \times \frac{(x_{CH_4,Mod} - x_{CH_4,Exp})}{x_{CH_4,Exp}} \quad (4.24)$$

Here $x_{CH_4,Mod}$ and $x_{CH_4,Exp}$ represent the model determined and experimentally measured methane percentages. The dependence of the residuals on hydrogen partial pressure is demonstrated in Figure 4.16. There does not appear to be a clear correlation between the residual value and the hydrogen partial pressure, with the error spread either side of zero. The magnitude of the error appears to increase with the partial pressure of hydrogen. However, due to the operation of the reactor within practicable H₂/CO₂ ratios, the increased hydrogen

partial pressure is accompanied by an increased carbon dioxide partial pressure, which might account for the error.

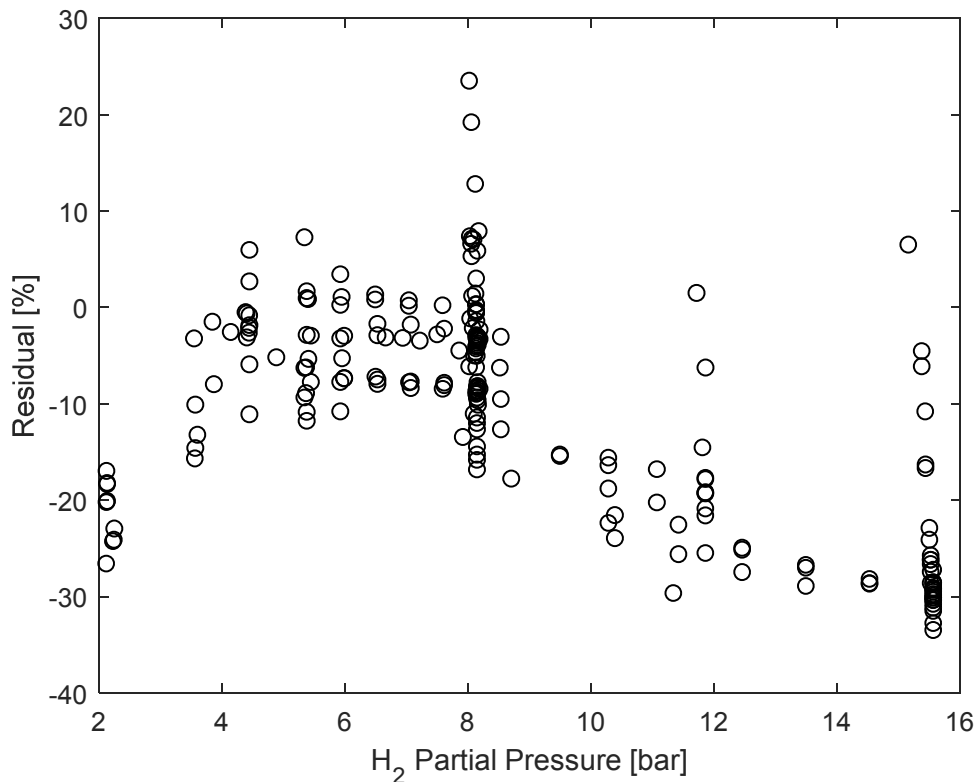


Figure 4.16. Residual plot comparing experimentally determined reaction rates and model determined rates from equation (4.22) at different H_2 partial pressures.

The influence of CO_2 partial pressure on the residual is plotted in Figure 4.17. The residuals appear to show a clearer dependence on the partial pressure of carbon dioxide. The model underestimates the rate as the partial pressure of CO_2 increases above 2-3 bar, as is evident from the negative residuals. Below a partial pressure of 2 bar, the model appears to predict in some cases greater rates of methanation than observed.

The dependence of the residuals is in accord with the experimental observations, with carbon dioxide showing little influence on the reaction rate in the batch reactor whilst displaying a weak positive dependence on the CO_2 partial pressure in the continuous reactor.

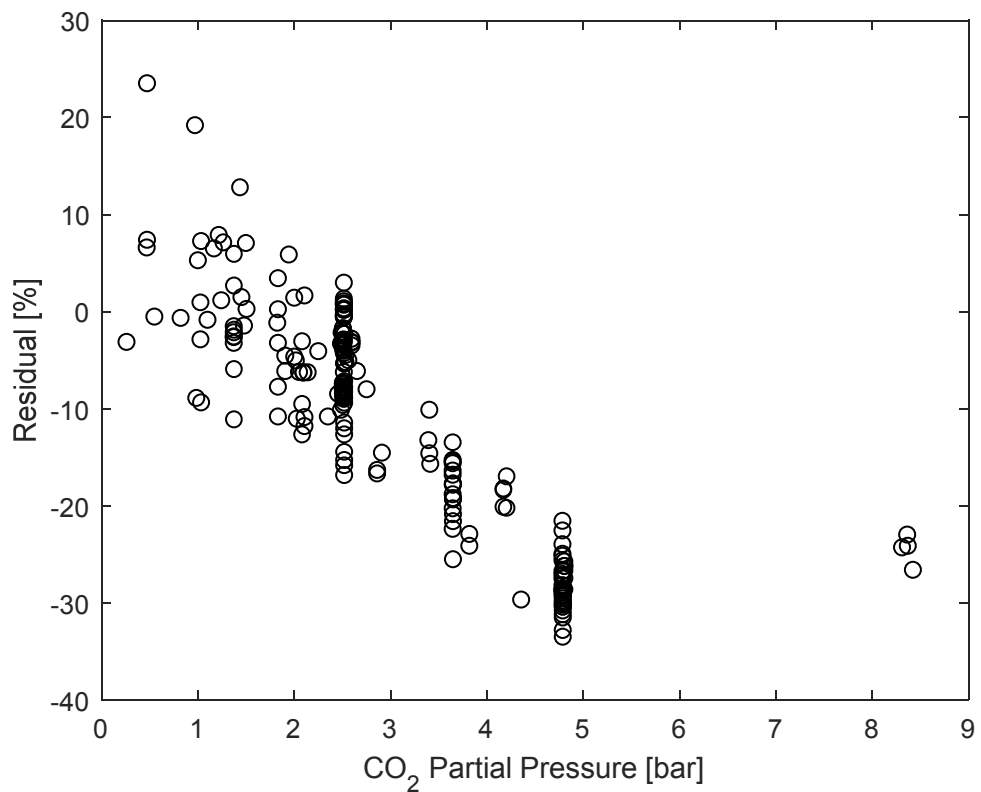


Figure 4.17. Residual plot comparing experimentally determined reaction rates and model determined rates from equation (4.22) at different CO₂ partial pressures.

In order to examine further the differences in the kinetics, the kinetics of the fixed-bed reactor alone were investigated.

4.7.8 Results: Identification of Fixed-Bed Kinetic Models

Under the differential conversions of the fixed-bed experiments, the influence of water inhibition is negligible due to the low partial pressures of water in the product gases. Hence the kinetics were fitted without consideration of water inhibition. The lowest sum of squares fit was provided by equation (4.25), with a parity plot of the resulting estimated and measured rates shown in Figure 4.18.

$$R_{CH_4} = \frac{a P_{CO_2}^{0.33} P_{H_2}^{0.5}}{(1 + b P_{H_2}^{0.5} + c P_{CO_2}^{0.33})^2} \quad (4.25)$$

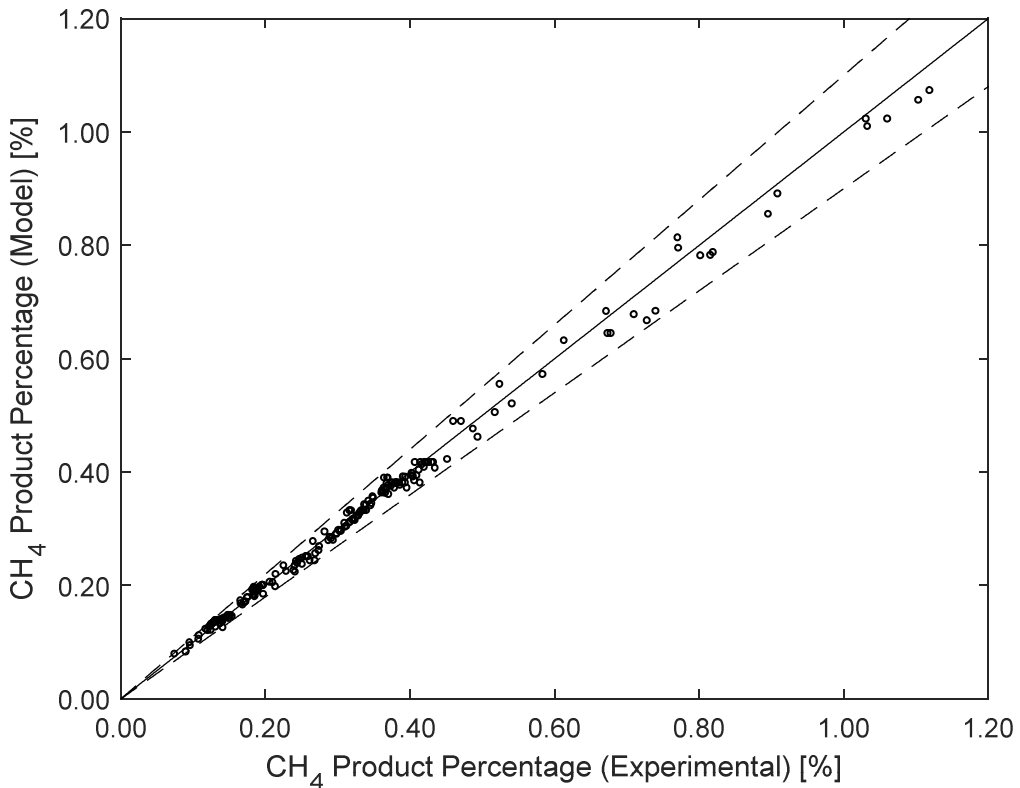
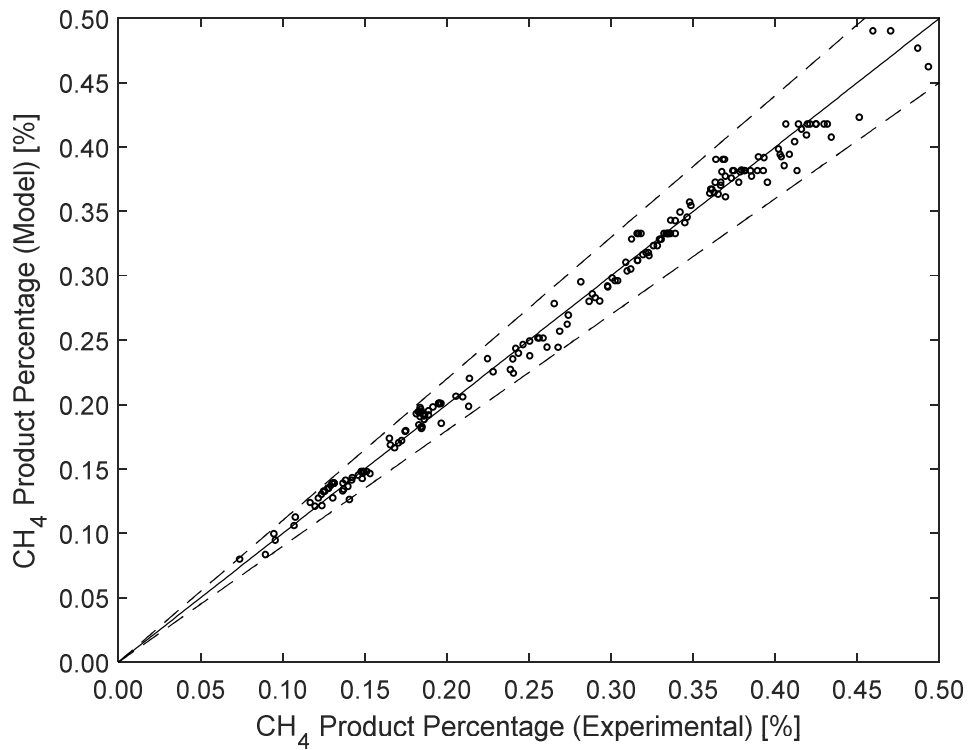


Figure 4.18. Parity plot for experimentally determined fixed-bed methanation rate versus predicted values by equation (4.25).

The mean percentage error determined by equation (4.25) was 2.8%, with a clear majority of the results lying within a $\pm 10\%$ bound from parity. The form of equation (4.25) suggests that the results are best fitted by the assumption of a C hydrogenation rate-limiting step, rather than the CO dissociation limiting step assumed for the dataset obtained from the Carberry reactor.

For comparison, both equation (4.25) and equation (4.22), for the CO-dissociation mechanism, were fitted to the fixed-bed results, with the parity plots given in Figure 4.19 a) and b). The mean percentage errors for these equations were 2.8% and 3.8% respectively. Whilst both fits appear reasonable, there appears to be more significant deviations from parity for the CO dissociation based rate equation, with a greater number of results scattered beyond the $\pm 10\%$ bound from parity.

a)



b)

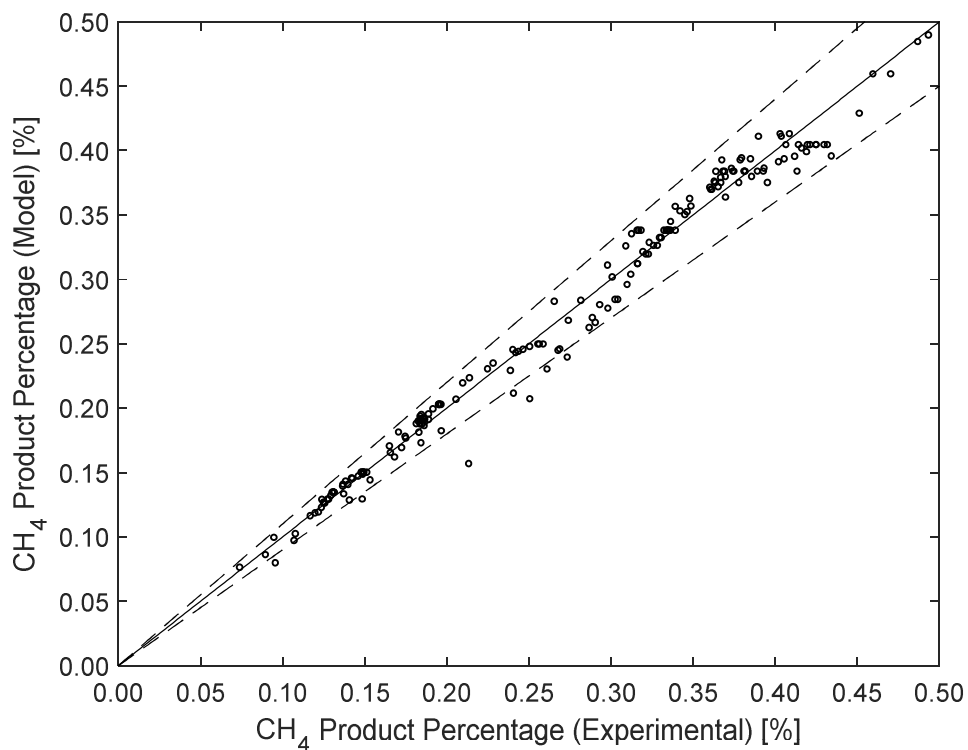


Figure 4.19. Parity plots between 0-0.5 % methane concentrations for (a) equation (4.25) and (b) equation (4.22).

Equation (4.25), based on C hydrogenation, yielded a greater mean percentage error of 5.0% when fitted to the Carberry results, compared with the 4.5% obtained by fitting Equation (4.22).

The developed parameters are summarised in their pre-exponential constant and activation energy form. All parameters were reported relative to the reference temperature of 473 K.

Table 4.4 Values of kinetic parameters for equation (4.25)

Parameter	Value	
$A_{473\text{ K}}$	$(1.05 \pm 0.06) \times 10^{-6}$	$[\text{mol g}^{-1} \text{ bar}^{-0.83} \text{ s}^{-1}]$
$B_{473\text{ K}}$	0.22 ± 0.02	$[\text{bar}^{-0.5}]$
$C_{473\text{ K}}$	0.31 ± 0.02	$[\text{bar}^{-0.33}]$
E_A	85.9	[kJ/mol]
ΔH_B	-3.4	[kJ/mol]
ΔH_C	-11.7	[kJ/mol]

The kinetic expressions were not fitted using both datasets simultaneously due to differences in magnitude between the fitted variable for the Carberry (partial pressure) and that of the fixed-bed (methane percent). Due to the differences in the extents of the errors in each system, fitting across both might have led to inappropriate weighting favouring errors from one dataset.

4.8 Discussion

This study set out to assess the agreement between the results obtained under batch and continuous operation. The agreement in the absolute rates between the powdered catalyst within the fixed-bed system and those within the Carberry reactor matched reasonably near the reference conditions and at lower pressures. This agreement and the similarity in the activation energies with those reported in the literature indicated the absence of mass transfer limitation within the larger particles, as predicted by the Weisz-Prater criterion. The insensitivity of the reaction to carbon dioxide and hydrogen within the Carberry batch reactor further indicated a lack of reactant mass transfer limitation, since an increase in the surface reactant partial pressures in a particle limited by mass transfer would have resulted in an increase in reaction rate.

The zeroth order kinetics observed for CO₂, in the batch reactor agreed with the behaviour observed by van Herwijnen *et al.* (1973), who reported the order in CO₂ varied between 0 and 1, approaching zero at CO₂ partial pressures above 0.015 atm. Weatherbee and Bartholomew (1982) similarly observed the rate tending towards zeroth order with respect to CO₂ as its partial pressure was changed from ~0.3 kPa to 3 kPa, with a 5.6 kPa H₂ partial pressure. The influence of hydrogen in this study was similarly noted to have a zeroth order influence except under conditions where carbon dioxide was near full conversion. This agreed with the conclusions of Weatherbee and Bartholomew (1982), who observed diminishing order with increasing hydrogen partial pressure. The trends observed for the catalyst also agreed with those observed by Lim *et al.* (2016), with the exception being that the catalyst activity was approximately a factor of ~2 lower in this study.

Under steady-state and differential reaction conditions, it was possible to show that the catalyst displayed positive reaction orders in both carbon dioxide and hydrogen. This type of behaviour is in line with the observations of Chiang and Hopper (1983) who reported reaction orders of 0.21 and 0.66 for H₂ and CO₂ respectively on a Ni/Kieselguhr catalyst. The more recent study by Schlereth (2015) similarly determined a power law fit with reaction orders of 0.31 and 0.16 for H₂ and CO₂ respectively on a co-precipitated Ni/Al₂O₃ catalyst. In agreement with the fixed-bed reactor investigations of Schlereth (2015) and Kai *et al.* (1988), the reaction rate was observed to increase with both reaction pressure and reaction temperature. The measured apparent activation energies for the reaction across both reactors compared favourably with the literature, with apparent activation energies reported for nickel-based methanation typically in the range of 70-100 kJ/mol. The observed behaviour under

continuous reaction conditions differs from that of the batch reactor, with the main difference between the systems being conversion and thus water partial pressure.

For the batch reactor, the results agree with the work of Lim *et al.* (2016), finding a carbide mechanism based on a CO dissociation rate-limiting step provided the lowest least square fit. Under differential conversion, the lowest least square fit was provided by equation (4.25), representing a C hydrogenation limiting step. Comparing the CO-dissociation based rate expression (4.22) with the fixed-bed results showed a correlation between the partial pressure of CO₂ and the residual error between the model and the data. As the partial pressure of CO₂ increased above those near and below the reference condition, the model underestimated the reaction rate. With regard to the influence of hydrogen, there was no clear correlation between the error and the H₂ partial pressure; however the magnitude of error was noted to slightly increase. From the residual plots, it appeared clear the CO dissociation model fitted to the batch reactor data was not an optimum predictor for the rate of methanation under differential conditions.

It appears from the collected results that a clear single mechanism cannot be distinguished for the entire range of conversions, with inferences from the experimental results providing a reduced set of equations. However without identification of the surface species and in-depth micro-kinetic or DFT modelling, the analysis here only gives a broad identification of potential mechanisms. Koschany *et al.* (2016) similarly noted that the assumptions required in the derivation of the Langmuir-Hinshelwood equations might result in ambiguity concerning the mechanism. Indeed, in some cases, identical equations might be derived for reactions proceeding *via* different pathways.

The rate-limiting steps of both equations (4.22) and (4.25) both suggest a carbide-type mechanism in accord with the literature. The hydrogenation of carbon and the dissociation of CO were both suggested as potential and competing rate-limiting steps in the work of Sughrue and Bartholomew (1982), and thus might be sensitive to the conditions of operation. As noted earlier in §4.7.1, the methanation of CO₂ *via* a CO dissociation rate-limiting step or a C hydrogenation rate-limiting step have both found support in the literature, *i.e.* Weatherbee and Bartholomew (1982) and Fujita *et al.* (1991) for CO dissociation, with C hydrogenation indicated by the work of Peebles *et al.* (1983). Hence operation of different rate-limiting steps on the catalyst's surface under differing reaction conditions remains a possibility, with Peebles *et al.* (1983) reporting a delicate balance between C formation and C hydrogenation in their study.

Weatherbee and Bartholomew's (1982) original study indicated C hydrogenation, CH hydrogenation or CO dissociation could be possible routes for formation of methane on their catalyst, with CO dissociation providing the best fit with their experimental results. Lim *et al.* (2016) later reported the equation agreed with their measurements, employing the *b* parameter determined by Weatherbee and Bartholomew (1982) in the fitting of their results. Weatherbee and Bartholomew (1982) found that their *b* parameter appeared unphysical, counter to what is conventionally expected for adsorption equilibria, with the CO₂ component modelled by an endothermic adsorption energy. The authors rationalised this by stating that reported enthalpies in Langmuir-Hinshelwood equilibrium constants can significantly differ from those obtained directly through chemisorption experiments due to the assumptions made in the derivation of the Langmuir isotherm. Weatherbee and Bartholomew (1982) further reported that the presence of other adsorbed species, *i.e.* C, O, and H, might significantly influence the adsorption of a particular species. In this Dissertation, the *b* parameter was determined by data fitting rather than use a parameter developed for a different material, and an exothermic adsorption energy was found to sufficiently represent the parameters temperature sensitivity. The remaining adsorption enthalpies were found to be similarly exothermic.

The adsorption terms for water on the surface of the catalyst have been examined for both hydroxyl and molecular water form. The adoption of a water-based adsorption term provided the lowest least-squares residuals for the Carberry batch results. The assumption of a molecular water most abundant surface intermediate agreed with the conclusions of Lim *et al.* (2016) to account for the observed inhibitory behaviour. Similar inhibition terms were noted to adequately describe the kinetics measured by Inoue *et al.* (1984) and Kai *et al.* (1988). The investigation into the kinetics of co-precipitated Ni/γ-Al₂O₃ by Koschany *et al.* (2016) concluded OH as the most abundant surface species (MASI), however a difference in adsorption properties might reasonably be expected between different catalyst formulations.

The enthalpies for the adsorption parameters determined from the fixed-bed data were calculated to be exothermic, but to exhibit relatively low values. Sehested *et al.* (2005) measured H₂ adsorption enthalpies on nickel of -43 kJ/mol using temperature programmed adsorption experiments. The adsorption enthalpy for the H₂ surface intermediate term was predicted to be -3.2 kJ/mol, however does show consistency with other kinetic studies. The H₂ enthalpy is not dissimilar in magnitude to those determined by Koschany *et al.* (2016) (-6.2). Discrepancies in the observed enthalpies may be attributed to differences in catalyst formulation, the interaction with competing species and changes in adsorption enthalpy with coverage.

Although the Langmuir-Hinshelwood fit has provided a reasonable approximation of the kinetics at both differential and high conversions, the method remains simplified. Rostrup-Nielsen (1993) noted that the rate-determining step and the MASI may in some reactions vary across conversions and temperatures, with the nature of the site or the ensemble requirements for some steps changing depending on reaction conditions. Overall, results here have identified two rate expressions which provide good approximations of the kinetic data with assumptions consistent with the existing literature. The differences in the rate expressions suggest either a sensitivity of the rate-determining step to conversion, with water partial pressure the main difference between the systems, or the assumptions of the Langmuir-Hinshelwood equations provide a mathematically sufficient but oversimplified approximation for the kinetics of CO₂ methanation.

4.9 Conclusions

The methanation of CO₂ was investigated over a wide range of partial pressures of products and reactants within a gradientless, spinning-basket reactor operated in batch mode and a laboratory-scale fixed-bed reactor operating continuously. The rate and selectivity of CO₂ methanation, using a 12 wt% Ni/γ-Al₂O₃ catalyst, were explored at temperatures 443 – 493 K and pressures up to 20 barg. The behaviour of the batch reactor indicated that the rate increased with increasing partial pressures of H₂ at low partial pressures (<1 bar). However, the rate of reaction was found to be insensitive to changes in the partial pressures of H₂ and CO₂ at higher partial pressures. The fixed-bed reactor was observed to show positive order behaviour in both H₂ and CO₂ with the core difference between the fixed-bed and batch reactor systems noted to be the differences in water partial pressure and conversion.

Through quantification of the rates of reaction in the batch reactor, measurements were compared with different kinetic expressions. The rate expressions appeared to be consistent with the kinetic equation proposed by Lim (2014) based on a mechanism in which adsorbed CO₂ dissociated to CO and O surface species, where the rate-limiting step is the subsequent dissociation of adsorbed CO. The ability of this expression to predict the results from the continuous, fixed-bed reactor was then explored. Despite good agreement between the CO dissociation model and the results from the batch reactor, it was found that the kinetic expressions did not optimally represent the results from the packed bed experiments, with a C hydrogenation rate-limiting step providing the lowest error descriptor at differential conversion.

This study has indicated a fundamental difference in the kinetics of methanation on Ni/γ-Al₂O₃ between the fixed-bed and Carberry reactors, and partly agrees with the kinetic conclusions made in methanation studies, such as that of Lim (2014), however indicates a Langmuir approach using a single rate-determining step may not be representative over a full range of conversions. The semi-empirical nature of the Langmuir-Hinshelwood description was ascribed as a possible reason for the discrepancy and it was noted the quality of the fit of the Langmuir expression may be mathematical in basis rather than mechanistic, with the Langmuir approach suggested to be an oversimplification of the complex reaction set. The possibility of a sensitivity of the rate-limiting step to operating conditions was also proposed, and noted to be in agreement with some prior mechanistic studies.

5 Kinetics of Carbon Dioxide Hydrogenation on a Co/ZrO₂ Catalyst

5.1 Introduction

Cobalt provides an alternative catalyst for the production of methane from CO₂. This reaction was investigated over a wide range of partial pressures of hydrogen and carbon dioxide in a laboratory-scale fixed-bed reactor operating continuously. The rate of CO₂ methanation, using a 4.5 wt% Co/ZrO₂ catalyst, was explored at temperatures between 433 and 503 K, H₂/CO₂ ratios between 0.25 and 5, and pressures of up to 15 barg. The kinetic measurements were then compared with a mathematical model of the reactor, in which different kinetic expressions were evaluated.

5.2 Background

Studies of the direct hydrogenation of carbon dioxide to methane have primarily concentrated on nickel catalysts (Wang *et al.*, 2011), with fewer investigations concerning cobalt. As is the case for nickel-based CO₂ methanation, the reaction mainly produces CH₄ and CO, with CO selectivity often reported at elevated operating temperatures (~573 K). At lower temperatures, thermodynamics limits the extent of CO formation such that near complete conversion of CO₂ to methane is possible. Minor products observed over cobalt include light hydrocarbons (C₂-C₅) (Dorner *et al.*, 2009) and, under certain activation conditions and on promoted catalyst formulations, light alcohols (Gnanamani *et al.*, 2015).

Process conditions have been demonstrated to have a minor impact on the product selectivity. Dorner *et al.* (2009) examined the influence of feed composition and pressure on a platinum promoted Co/Al₂O₃ catalyst at CO₂ conversions between 3.5 and 41.2%. Methane selectivities at 493 K were found to increase both with H₂/CO₂ ratio between 1 and 3 and with pressure between 150 and 450 psig. The increased selectivity with H₂/CO₂ ratio may be attributable to increased H/C atomic ratios on the catalyst surface; however, the changes seen were slight, with maximum and minimum methane selectivities of 97.2 and 95.7 mol% reported.

A significant body of work exists concerning the role of carbon dioxide in the Fischer-Tropsch reaction. Its presence as a by-product in synthesis gas generated from gasification has necessitated research into its impact on the Fischer-Tropsch product distribution, with research primarily focussed on CO/CO₂ co-feeding studies. Both CO and CO₂ compete for the

active sites on the catalyst, and observations on the extent of this competition appear to be contingent upon catalyst formulation. Gnanamini *et al.* (2011) reported that CO₂ acted as an inert under their conditions (493 K, 19.9 bar) up to a H₂/CO outlet ratio of 124, which corresponded to a CO partial pressure of 0.06 bar. Below this pressure, CO₂ was observed to be reactive, forming mainly methane. However, CO₂ has also been reported to be reactive in the presence of CO at lower ratios. Yao *et al.* (2010) observed CO₂ hydrogenation above a CO₂/(CO₂+CO) ratio of 0.5 for their 10 wt% Co/TiO₂ catalyst (473 K and 20 bar). The selectivity to methane increased with CO₂/(CO₂+CO), reaching a maximum for a CO-free feed. The reason for the selectivity difference was ascribed to the lower adsorption strength of CO₂ and the negligible water gas shift activity of cobalt. At high CO partial pressures, very little CO₂ can adsorb on to the surface, and hence may be observed to act as a diluent. Whilst at low, or zero, CO partial pressure, CO₂ adsorption can occur; however, its weaker adsorption leads to higher surface hydrogen to carbon ratios, which favour methane production.

Carbon monoxide is considered to be a possible intermediate for the hydrogenation of carbon dioxide and the comparison of the respective behaviours of CO and CO₂ hydrogenation has been used in the literature to draw conclusions on the nature of the mechanism for CO₂ hydrogenation. It follows that were the hydrogenation of CO₂ to proceed *via* a CO surface intermediate, and thus follow a mechanism akin to the Fischer-Tropsch process, the reaction could be limited by the same elemental step. Yao (2011) reported that H₂/CO₂ displayed a higher reactivity than H₂/CO synthesis over their Co/TiO₂ catalyst with a conversion of respectively 25.1% and 14.6% on a carbon basis, at the same space velocity. The comparison made by Yao (2011) however employed different feed ratios for the H₂/CO (2:1) and H₂/CO₂ (3:1) synthesis gases, and thus the comparison was made at different hydrogen and carbon oxide partial pressures. Contrary to the conclusions of Yao (2011), Zhang *et al.* (2002) observed CO to be more rapidly hydrogenated than CO₂ on their Co/SiO₂ catalyst. The high selectivity to methane under CO₂ methanation and the lower reactivity led Zhang to conclude that a common reaction intermediate does not exist for CO₂ and CO methanation on cobalt, or the reaction proceeds *via* two pathways, one for methane production and one for higher hydrocarbons. The authors proposed a methanol type intermediate for the methanation reaction, and found through co-feeding of methanol for it to be >8 times more reactive than either of the carbon oxides. Spectroscopic investigations undertaken by Visconti *et al.* (2009), however, indicated the reactions proceeded *via* a common intermediate. These workers examined the surface of a Co/Al₂O₃ catalyst using FTIR at 20 bar and 493 K, reporting there was no evidence of different surface species under CO and CO₂ hydrogenation

conditions. Hence, the reaction was assumed to proceed *via* the same pathway with the differences in reactivity ascribed to weaker adsorption of CO₂ and differences in H/C surface ratio.

The kinetics of the methanation reaction have not been investigated to a significant extent on cobalt, and as with the nickel catalysed reaction, disagreement exists in the form of the mechanism and its kinetics. The apparent activation energy reported for the reaction differs significantly between studies, and in some cases at different reaction conditions. Weatherbee and Bartholomew (1984) examined the reaction rate of a 3wt% and 15wt% Co/SiO₂ catalyst for the methanation of carbon dioxide. The authors operated between 3.0-11.2 % CO₂ conversions and determined the activation energies separately for CO₂ consumption and CH₄ formation. The 15wt% catalyst examined at a total reaction pressure of 1 atm and temperatures between 456-476 K yielded apparent activation energies of 93 and 99 kJ/mol based on CO₂ and CH₄ respectively. However, these activation energies were reported to increase to 171 and 173 kJ/mol based on CO₂ and CH₄ respectively at 11 atm reactor pressure between 453-495 K. In order to reduce the impact of conversion on the obtained data, Weatherbee and Bartholomew investigated a 3wt% Co/SiO₂ catalyst, with diluted gas (1% CO₂ 4% H₂ in N₂) under differential conversion at 1 bar. The resultant apparent activation energies from data between 500-550 K were 79 kJ/mol and 66 kJ/mol for CO₂ and CH₄ respectively. These values were in agreement with those measured for 3wt% Ni/SiO₂ (81/80 kJ/mol) and 3 wt% Ru/SiO₂ (73/68 kJ/mol) catalysts also examined within the study. The significant differences in the apparent activation energies on cobalt were attributed to a shift in the rate-determining step.

Activation energies above those typically reported for nickel-based methanation (80-100 kJ/mol) have been reported by Lahtinen *et al.* (1994), who investigated C, CO and CO₂ hydrogenation on polycrystalline cobalt foils under UHV and at atmospheric pressure between 475 and 575 K. For C and CO₂ hydrogenation, methane was the major product, with hydrocarbons up to C₄ detected under CO hydrogenation. Apparent activation energies of 57, 86 and 158 kJ/mol were reported for C, CO and CO₂ hydrogenation respectively. The authors attributed the elevated activation energy for CO₂ hydrogenation to oxidation of the cobalt. Little influence of CO₂ pressure on turnover rate was noted on their catalysts (-0.05 order in CO₂); however, there were significant changes in the rate when the partial pressure of hydrogen was increased (0.90 reaction order for H₂). Using Auger electron spectroscopy, the surface ratio of cobalt to oxygen was probed during CO₂ hydrogenation, with the result suggesting that CO₂ was involved in the formation of CoO. Lahtinen *et al.* (1994) speculated that the reduction of the CoO formed was the limiting step in the hydrogenation reaction and

thus the reason for the significantly higher activation energy for CO₂ methanation.

Iablokov *et al.* (2012) deposited size-controlled cobalt nanoparticles within a MCF-17 support and measured CO₂ hydrogenation activity at 6 bar between 473 and 573 K. They found that the turnover frequency was size dependent; however, the activation energy was consistent at 75 ± 7 kJ/mol, irrespective of the size of the nanoparticles. The variation in turnover frequency with particle size was attributed to surface oxidation reducing the area for reaction on smaller nanoparticles. Iablokov *et al.* (2012) speculated that the higher activation energies of previous studies might occur as a result of a strong kinetic dependence on pressure, but they did not extend their study beyond 6 bar.

Akin *et al.* (2002) undertook a short kinetic evaluation of CO₂ hydrogenation over a co-precipitated 36 wt% Co/Al₂O₃ catalyst. The investigators fitted a Langmuir expression to experimental results obtained at 14 conditions (5 different CO₂ concentrations, 2 different H₂/CO₂ ratios and 3 space velocities) at a temperature of 503 K. A Langmuir-Hinshelwood equation, given by equation (5.1), was found to provide the best fit.

$$-R_{CO_2} = \frac{K_1 P_{H_2}}{\left(1 + K_2 P_{H_2}^{\frac{1}{3}}\right)^2} \quad (5.1)$$

Their expression was developed on the assumption of a carbide type mechanism (CO intermediate dissociating to surface carbon) with irreversible hydrogen adsorption as the rate-limiting step. The temperature of reaction was separately varied by the authors between 473 and 543 K; however an activation energy was not stated.

It is clear that the kinetics of carbon dioxide hydrogenation on cobalt warrant further investigation, with questions regarding the kinetics largely unanswered and significant uncertainty in the activation energy of the reaction. This is addressed in the following sections.

5.3 Experimental

5.3.1 Materials

All the experiments in this Chapter were performed using ~0.5 g of the 4.5 wt% Co/ZrO₂ catalyst described in Chapter 3. The catalyst used in this investigation was activated directly from the calcined catalyst by *in situ* reduction in the BTRS.

5.3.2 Apparatus

The kinetic measurements were obtained using the Bench-Top Reactor System (BTRS). Experiments were carried out in the 8 mm diameter fixed-bed reactor, with catalyst loaded axially within the central 50 mm of the tube, as described in §2.4 . The CO₂ methanation reaction was undertaken over the temperature range 443-503 K, at intervals of 10 K at reaction pressures between 5 and 15 barg.

Typically a mass of ~0.5 g (106-150 µm) of Co/ZrO₂ catalyst was diluted within unimpregnated support material of the same size, such that the volume of catalyst and diluent was ~2.5 cm³. The catalyst mixture was supported atop a plug of quartz wool, with a second plug of quartz wool placed on top of the material. The thermocouple was placed within the catalyst bed, with 70 mm of quartz sand loaded on top of the quartz wool plug to ensure adequate pre-heating of the reactant gases. In order to exclude oxygen from the system, the reactor was first purged of air using argon for an hour before heating to 523 K. At 523 K, a flow of 300 cm³/min (at STP) H₂ was passed over the catalyst at atmospheric pressure for 6 hours. Post reduction, the reactor system was purged with argon and cooled to the desired reaction temperature.

Prior to introduction of the reactant gases, the system was pressurised using argon to the desired reaction pressure. The reactant gases, H₂ (Air Liquide) and CO₂ (Air Liquide) and a diluent, Ar (Air Liquide), were supplied from gas cylinders fitted with 0-50 barg regulators. The durations of the experiments were limited by the inventory of the hydrogen cylinder, with runs stopped where the cylinder pressure approached 50 barg. The H₂ and CO₂ reactants, as well as Ar (as a balance gas) were mixed and introduced to the reactor at H₂/CO₂ molar ratios between 0.25 and 5 and space velocities ranging from 84 cm³/min (at STP) to 630 cm³/min (at STP).

5.3.3 Control Experiments and Catalyst Deactivation

The reactor body and support/diluent materials were evaluated for activity in order to verify the measured kinetics were representative of the cobalt catalyst alone. The reactor was prepared and loaded as outlined in the experimental section without any active catalyst material. The blank-bed was reduced for 6 hours at 523 K under a flow of 300 cm³/min H₂. The reactor and support material were found to be inactive under the experimental conditions tested.

The temperature profile within the reaction tube was characterised as in §2.4.5. A central 50 mm long zone was identified as approximately isothermal, with a deviation of <1 K within the region at 533 K. The Mears, Anderson and Weisz-Prater criterion were fulfilled for all experiments. Hence intra-particle and external heat and mass transfer limitations are not expected to affect kinetic measurements. Details of these calculations are given in the Appendix (§A2).

It would be difficult to obtain accurate kinetic measurements if deactivation were significant over the period of measurement, or if the catalyst activity varied between batches. The catalyst reproducibility, as noted in Chapter 3 (§3.5.5), was good, with only minor deviations in the measured activity between batches. The initial deactivation behaviour of the catalyst was characterised over the initial 24 hours of operation, as shown in Figure 5.1, and was found to be minor. A decrease of ~7% in the rate of methanation was observed over the first 12 hours, with the activity stabilising thereafter. Repeated reference runs at 473 K and 10 barg were employed periodically to evaluate the extent of any further deactivation.

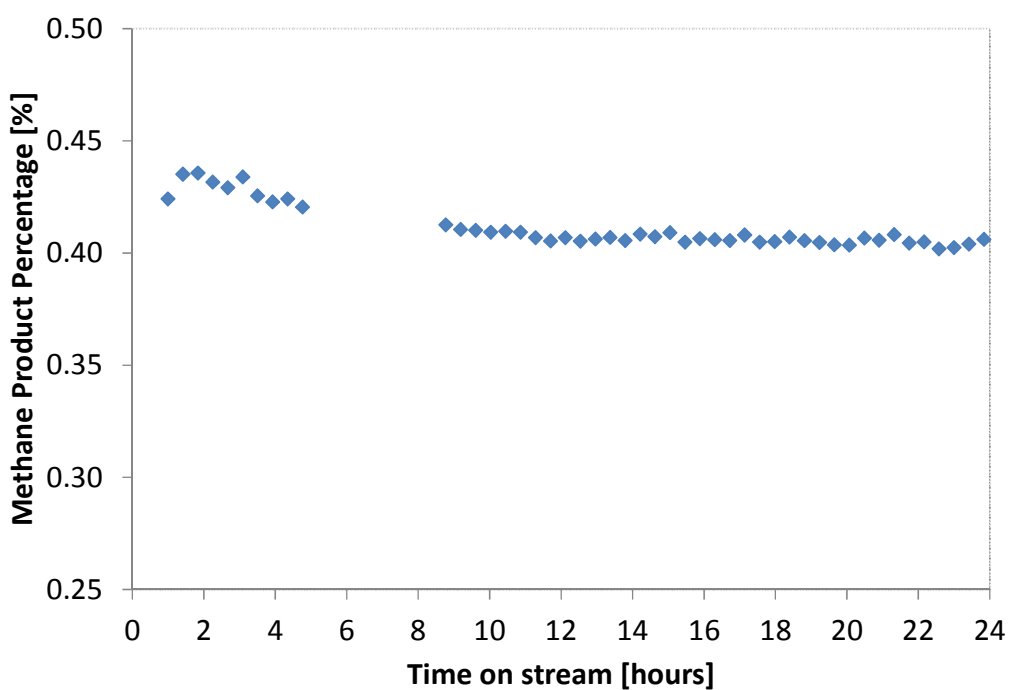


Figure 5.1. Methane percentage versus time on stream. Reaction conditions: 473 K, 10 barg, 150 H₂/50 CO₂/6 Ar [cm³/min (at STP)], 0.425 g 4.5 wt% Co/ZrO₂.

5.4 Results

5.4.1 Effect of P_{CO_2} and P_{H_2}

The influence of H_2 and CO_2 partial pressure on the methanation reaction rate was studied under differential conditions. The H_2/CO_2 ratio was varied at a constant space velocity of $155\text{ cm}^3/\text{min}$ (at STP).

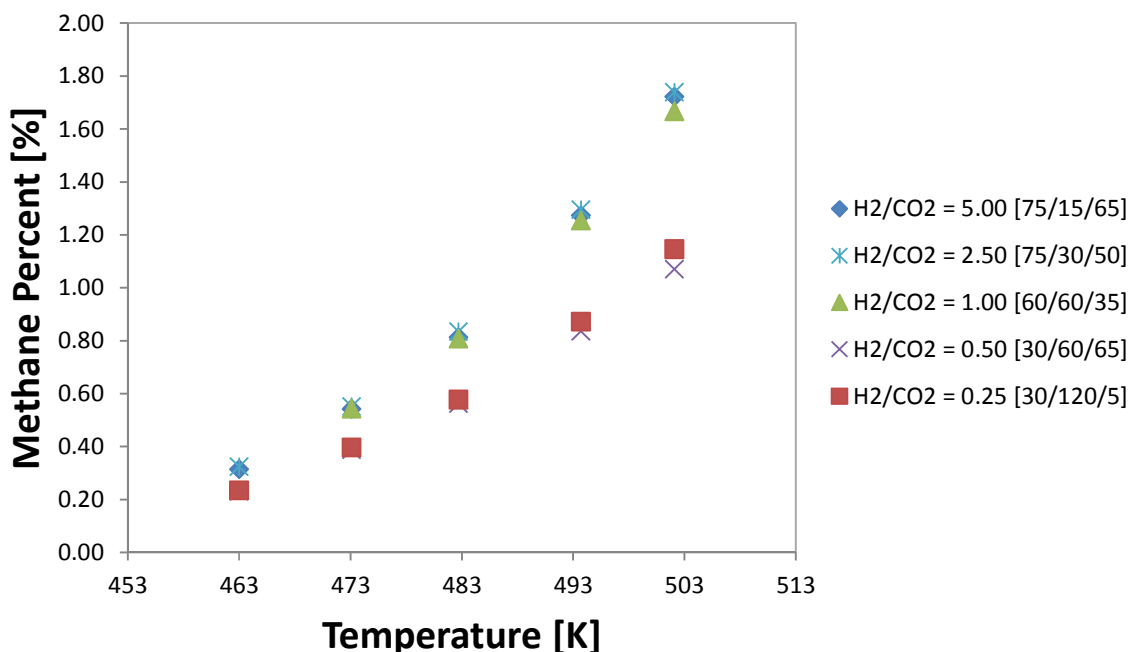


Figure 5.2. Influence of H_2/CO_2 on CH_4 concentration in the product gases between 463-503 K. The total flow was maintained at $155\text{ cm}^3/\text{min}$ (at STP) ($GHSV = 3720\text{ h}^{-1}$) with argon balancing the changes in H_2/CO_2 ratio. The total reactor pressure was maintained at 10 barg. The catalyst mass was 0.5 g Co/ZrO_2 .

The reaction rate displayed a weak dependence on the partial pressure of carbon dioxide. It is clear that the methanation rate is more strongly dependent on the H_2 partial pressure. At H_2/CO_2 ratios of 0.25 and 0.50, the partial pressure of hydrogen was constant with the CO_2 partial pressure increasing by a factor of 2. The methanation rate appears to increase slightly with CO_2 partial pressure between these conditions, but the influence is minor.

The effect of hydrogen partial pressure on the rate was further evaluated at constant carbon dioxide partial pressure and space velocity. Changes in the flowrate of hydrogen were balanced by argon, such that the total flow was maintained at $206\text{ cm}^3/\text{min}$ (at STP). The results shown in Figure 5.5 for 473 K indicate that there is a dependence of the methanation rate on the partial pressure of hydrogen, with the rate increasing by 13.8% on increasing the H_2 partial pressure from 5.3 bara to 8.0 bara, which corresponds to an increase in hydrogen

flow from $100\text{ cm}^3/\text{min}$ (at STP) to $150\text{ cm}^3/\text{min}$ (at STP). Similar trends were observed at 453 K and 463 K .

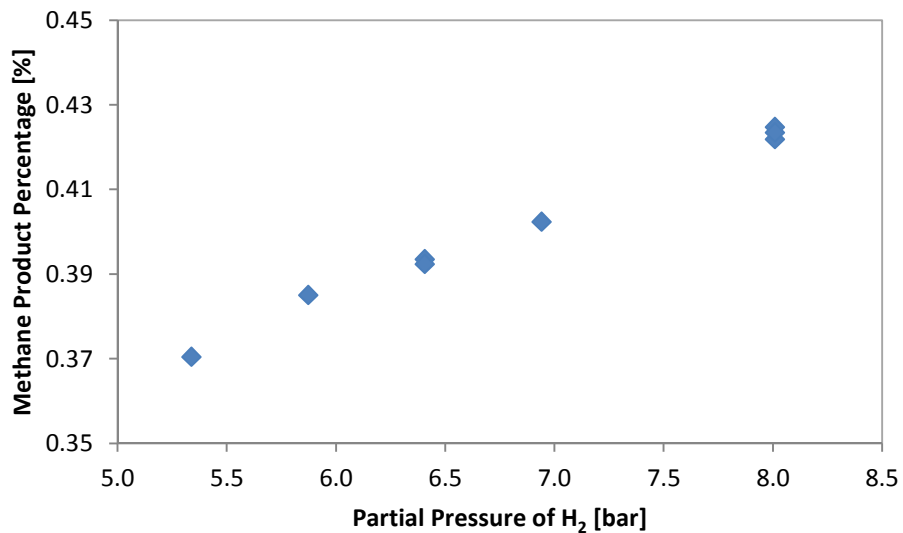
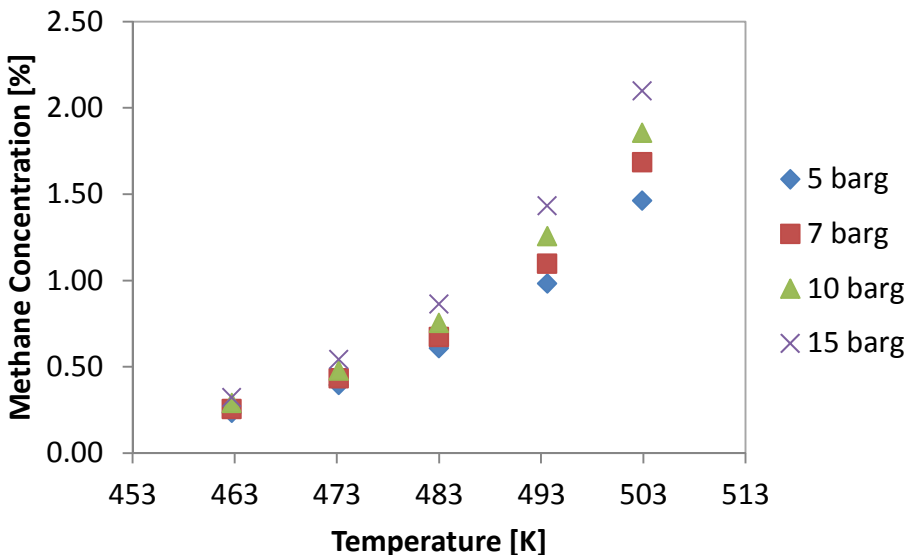


Figure 5.3. Influence of H_2 partial pressure on CH_4 concentration in the product gases. The total flow was maintained at $206\text{ cm}^3/\text{min}$ (at STP) ($\text{GHSV} = 4994\text{ h}^{-1}$) with argon balancing and changes in H_2 pressure. The flow of CO_2 in was maintained at $50\text{ cm}^3/\text{min}$ (at STP). The total pressure, CO_2 partial pressure and temperature were 10 barg , 2.7 bara and 473 K respectively.

5.4.2 Effect of Pressure

The reaction was carried out at total pressures of 5 , 7 , 10 and 15 barg . The influence of total pressure at a fixed H_2/CO_2 ratio of $3:1$ is shown in Figure 5.4 a) at temperatures between 463 K and 503 K . As the reaction pressure increased, the percentage of methane in the product gas increased. The dependence of the reaction rate is shown relative to a 5 barg reference at each temperature in Figure 5.4 b). The relative activity was defined as the ratio of the methanation rate at the reactor pressure and the rate at a reactor pressure of 5 barg , $R_{\text{CH}_4,P}/R_{\text{CH}_4,5\text{ barg}}$. There appears to be little influence of temperature on the relative activities over the range tested.

a)



b)

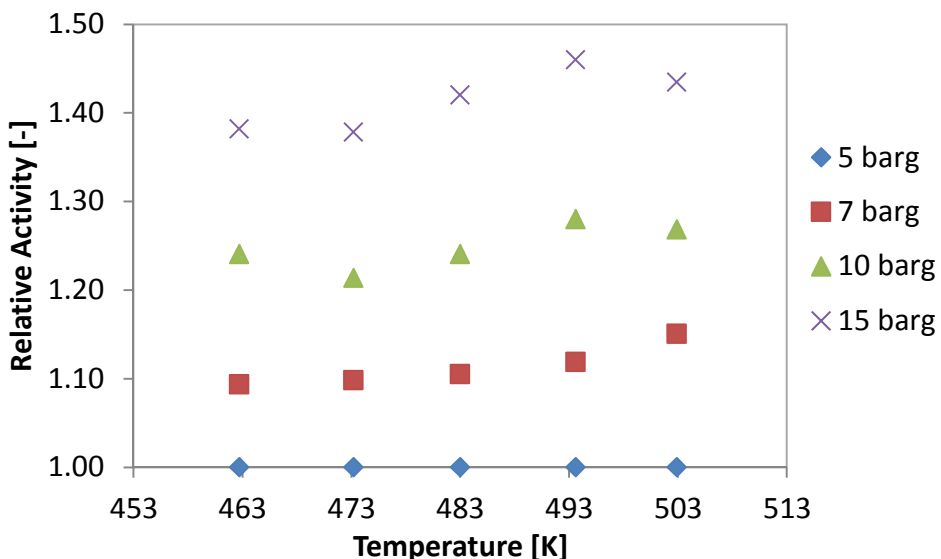


Figure 5.4. Variation of methane concentration with temperature and total pressure for a flowrate of 150/50/6 cm³/min (at STP) of H₂/CO₂/Ar.

5.4.3 Effect of Space Velocity

The total volumetric flow (F) was varied. The linearity of the methane percentage *versus* $1/F$ shown in Figure 5.5 demonstrates the expected trend for differential conversion, and indicates there is no significant influence of external heat and mass transport. This observation is in agreement with the calculated Mears and Weisz-Prater criteria, given in detail in Appendix (§A2).

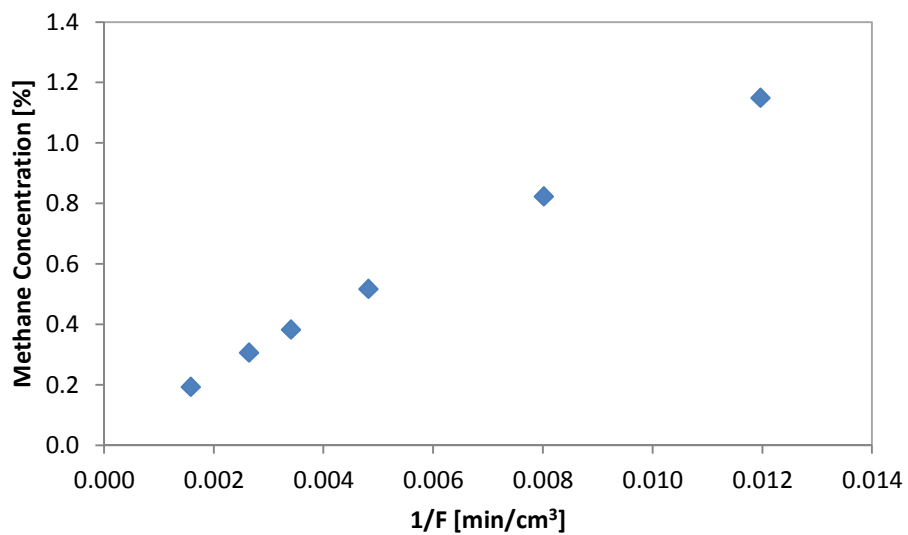
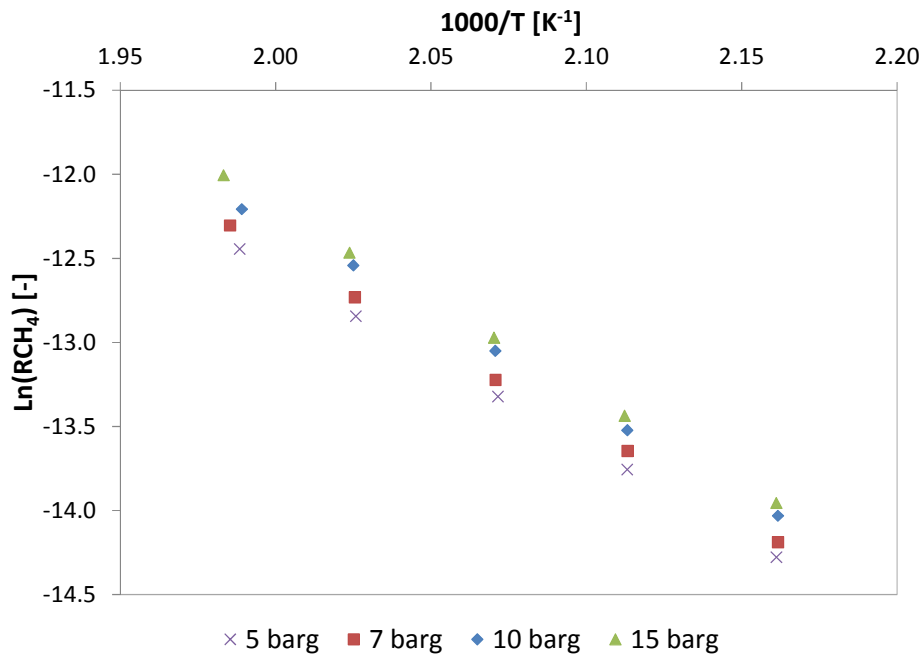


Figure 5.5. Variation of methane concentration with inverse space velocity at 10 barg, 473 K, 150/50/6 cm³/min (at STP) H₂/CO₂/Ar flow ratio.

5.4.4 Effect of Temperature

A temperature range of 70 K was investigated from 433 K to 503 K at 10 barg reactor pressure. Additional measurements were taken between 463 K and 503 K at pressures of 5, 7, 10 and 15 barg. The Arrhenius plots are shown in Figure 5.6. The apparent activation energies derived from the gradients are summarised in Table 5.1. All measured activation energies are consistent with the literature values for supported cobalt, *i.e.* Iablokov *et al.* (2012). The activation energy appears consistent across the range of reaction pressures and its agreement with the expected values for CO₂ methanation indicate the reaction kinetics were not influenced by mass transfer.

a)



b)

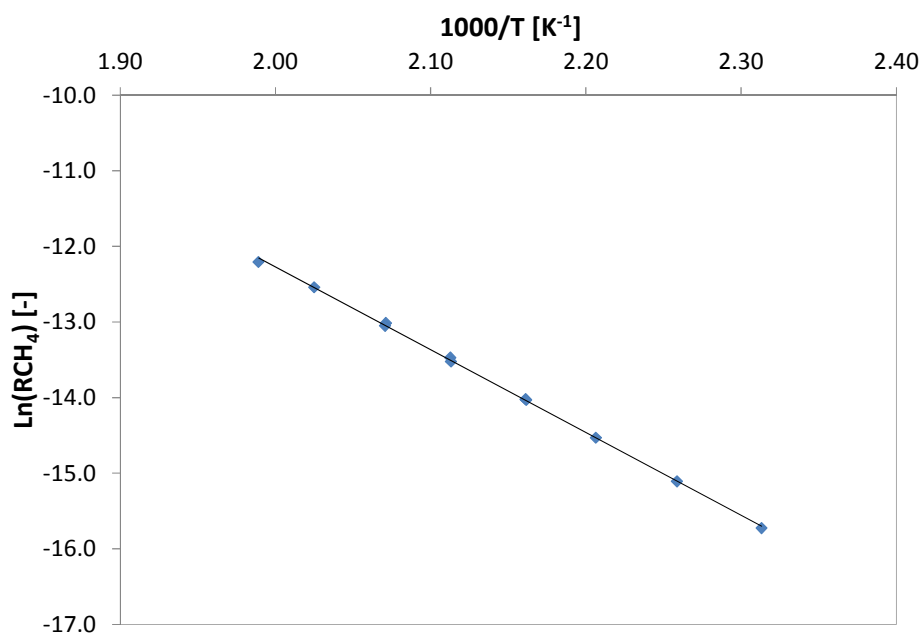


Figure 5.6. a) Arrhenius plot for the methanation rate [$\text{mol}_{\text{CH}_4}/\text{g}_{\text{cat}}\text{s}$] at pressures of 5, 7, 10 and 15 barg between 463-503 K. **b)** Arrhenius plot for the methanation rate [$\text{mol}_{\text{CH}_4}/\text{g}_{\text{cat}}\text{s}$] at 10 barg between 433-503 K.

Table 5.1. Activation energies for CO₂ methanation on Co/ZrO₂.

Condition	Activation Energy [kJ/mol]
10 barg (80 K range)	91.0±2.4
5 barg (50 K range)	88.0±2.7
7 barg (50 K range)	88.4±4.7
10 barg (50 K range)	89.0±7.7
15 barg (50 K range)	91.1±3.3

5.5 Kinetic Modelling of CO₂ Methanation on Co/ZrO₂

5.5.1 Kinetic Rate Equations

A selection of kinetic models were developed, and given in the Appendix (§A1), and evaluated for the quality of fit obtained for the Co/ZrO₂ methanation data. Both power law and Langmuir-Hinshelwood relations were evaluated for the quality of fit to the data. In all cases, the reaction parameters were treated as following an Arrhenius type relationship, with the Langmuir adsorption constants assumed to be of van't Hoff form. The influence of water on the kinetics of reaction was assumed to be negligible at the differential conversions used. Hence, in the case of a Langmuir-Hinshelwood fit, the kinetic equations were fitted with 6 adjustable parameters (3 pre-exponential constants and 3 activation energies). For the power-law fit, 4 adjustable parameters were optimised (2 reaction orders, 1 pre-exponential constant and 1 activation energy).

Whilst the power-law equations have no theoretical basis, the Langmuir-Hinshelwood type rate equations were derived under the assumption of a range of rate-determining steps and surface intermediates. The carbide-type mechanism assumed the formation of surface carbon *via* dissociative adsorption of CO₂ to CO and O, followed by the subsequent dissociation of CO to surface C and O. Methane is then formed through hydrogenation of C to CH₄, with the oxygen removed *via* hydrogenation to water. Kinetic equations for the carbide pathway were studied under the assumption of a rate-limiting step of CO₂ adsorption, CO dissociation, C hydrogenation, or CH hydrogenation. The assumed most abundant surface intermediates (MASI) were based on the selected rate-limiting step, *i.e.* H, CO and O for CO dissociation or H and C for C hydrogenation.

5.5.2 Modelling Kinetics in the Fixed-Bed Reactor

The Bench-Top Reactor system (BTRS) was modelled under the assumption of constant volumetric flow through the reaction zone. The overall fraction of hydrocarbons in the product stream was maintained below 2.5%, hence the molar, and thus volumetric flow decreased by less than 5%. The product concentration was determined through integration of the rate equation across the bed. The slight changes in reactant partial pressures were related to the overall pressure though multiplication of the species mole fraction with reactor position. The mole fractions were computed through a mole balance over an element of differential catalyst mass. The experimental measurements were compared with the prediction of candidate rate expressions by fitting results with a least-squares minimisation for the objective function given by equation (5.2) for data-point i .

$$obj_i = (x_{CH_4,i}^{exp} - x_{CH_4,i}^{mod}) \quad (5.2)$$

Here the exp and mod superscripts indicate experimentally obtained or modelled methane mole fractions. The objective function (obj) was minimised across the dataset using the MATLAB optimisation function *lsqnonlin* and the Levenberg-Marquardt algorithm, with the Langmuir-Hinshelwood parameters constrained to physically realistic positive values.

Under the majority of conditions the hydrocarbon mole fraction was well represented by the assumption of differential reaction, as shown by equation (5.3), with <1% error.

$$R_{CH_4} = \frac{x_{CH_4}\rho_m \dot{V}}{m_{cat}} \quad (5.3)$$

Here R_{CH_4} is the specific rate of methanation, x_{CH_4} is the methane mole fraction in the analysed gas, ρ_m is the molar density of an ideal gas at STP, m_{cat} is the catalyst mass and \dot{V} the total volumetric flowrate into the reactor.

5.5.3 Evaluation of Power-Law Methanation Kinetics

Based on the rate results obtained from the BTRS, parameters for a power law expression were estimated. The expression, shown by equation (5.4), represented the rate of methanation (R_{CH_4}) empirically by estimating the apparent reaction orders in CO_2 and H_2 , n_{CO_2} and n_{H_2} .

$$R_{CH_4} = a_{PL} P_{CO_2}^{n_{CO_2}} P_{H_2}^{n_{H_2}} \quad (5.4)$$

The temperature dependence of the reaction was incorporated into the expression

using an Arrhenius form for a_{PL} , shown by equation (5.5). The pre-exponential constant, $A_{473\text{ K}}$, was determined at a reference temperature of 473 K.

$$a_{PL} = A_{473\text{ K}} \exp\left(-\frac{E_A}{R}\left(\frac{1}{T} - \frac{1}{473}\right)\right) \quad (5.5)$$

The optimised parameters for the power-law expression are given in Table 5.2.

Table 5.2. Parameters for power-law methanation kinetics, equation (5.4), for the Co/ZrO₂ catalyst.

Parameter	Value	
$A_{473\text{ K}}$	$(5.39 \pm 0.04) \times 10^{-7}$ [mol g ⁻¹ bar ^{-0.50} s ⁻¹]	
E_A	84.9	[kJ/mol]
n_{CO_2}	0.034±0.024	[-]
n_{H_2}	0.463±0.030	[-]

The power-law expression fitted the experimental results with a mean percentage deviation of 6.8%. The parity plot of the power-law expression, shown in Figure 5.7, gives fair agreement with the experimental results, with some points exceeding > 10% deviation.

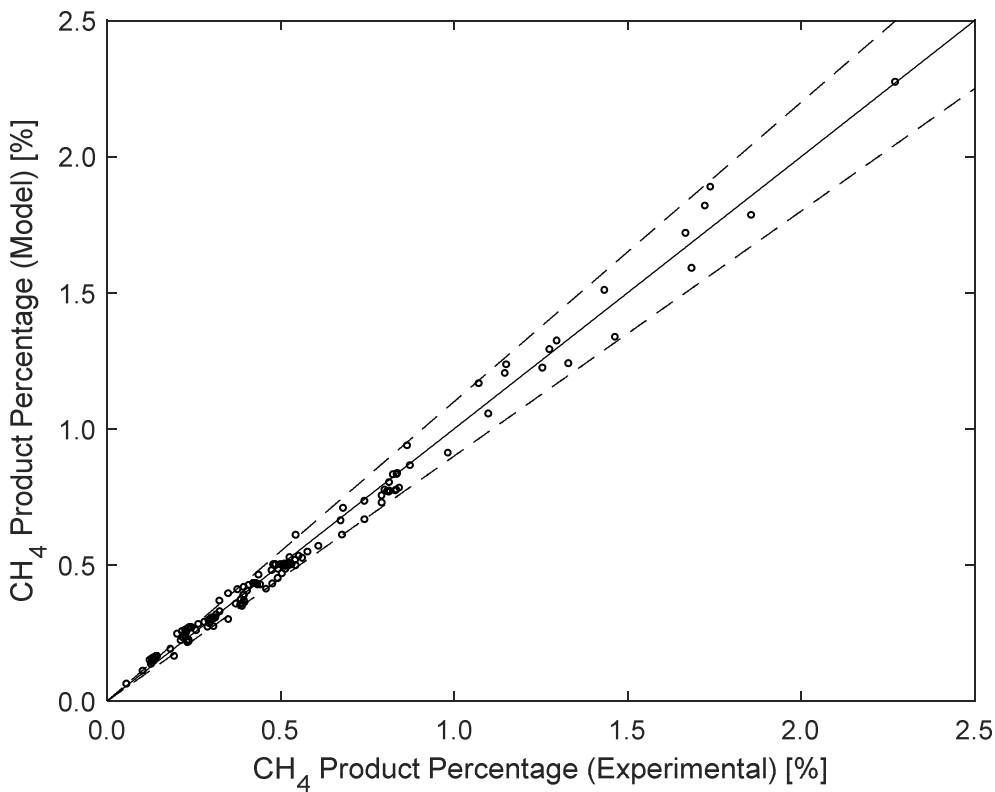


Figure 5.7 Parity plot for experimentally determined methane percentage [%] versus the values predicted by using equation (5.4).

5.5.4 Evaluation of Langmuir-Hinshelwood Methanation Kinetics

The results were fitted with Langmuir-Hinshelwood expressions with the best agreement provided by the CH hydrogenation expression given by equation (5.6). The quality of the fit between theory and experiment is shown by the parity plot in Figure 5.8. The fit appears to be reasonable with nearly all of the points contained within a ±10% range, and a mean percentage error of 4.2 %.

$$R_{CH_4} = \frac{a P_{CO_2}^{0.33} P_{H_2}}{(1 + b P_{H_2}^{0.5} + c P_{H_2}^{0.5} P_{CO_2}^{0.33})^2} \quad (5.6)$$

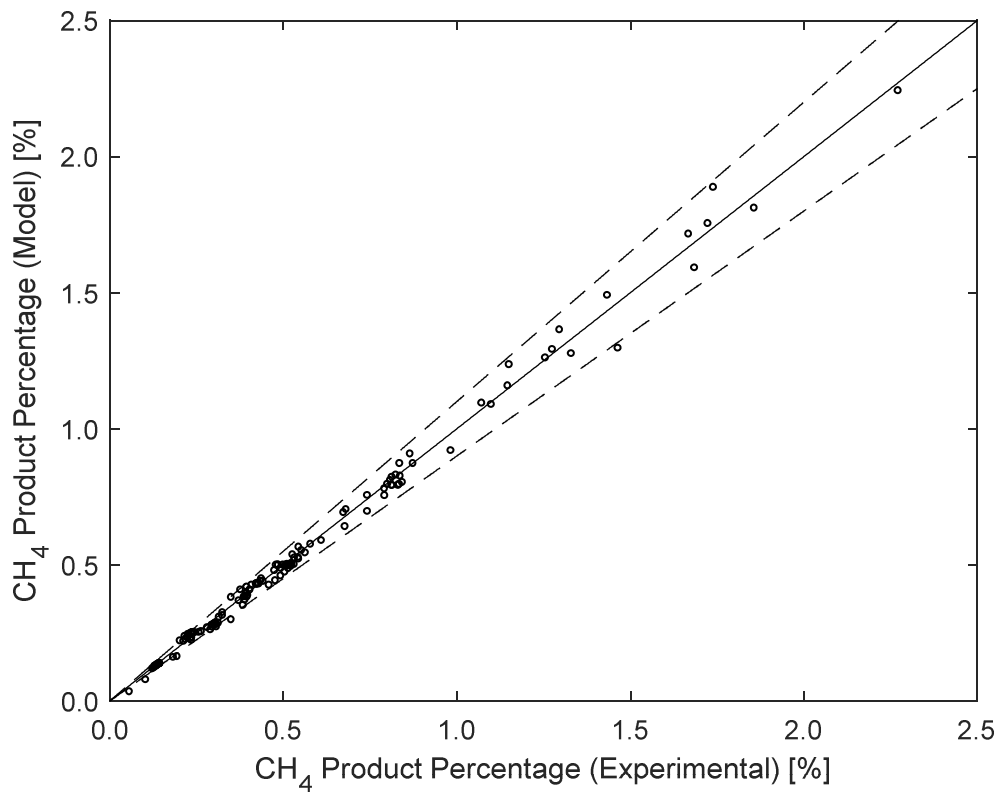


Figure 5.8. Parity plot for experimentally determined methane percentage [%] versus the values predicted using equation (5.6).

The Langmuir expression appears to give a lower error than the power-law expression; however the difference between the models is relatively small. The derived parameters for the expression are given in Table 5.3.

Table 5.3. LHHW parameters for CO₂ methanation on Co/ZrO₂.

Parameter	Value	
$A_{473\text{ K}}$	$(1.10 \pm 0.15) \times 10^{-6}$	[mol g ⁻¹ bar ^{-1.33} s ⁻¹]
$B_{473\text{ K}}$	0.17±0.03	[bar ^{-0.50}]
$C_{493\text{ K}}$	0.37±0.02	[bar ^{-0.83}]
E_A	52.6	[kJ/mol]
ΔH_B	-68.7	[kJ/mol]
ΔH_C	-20.1	[kJ/mol]

5.6 Discussion

The Co/ZrO₂ catalyst shows similar behaviour to the nickel catalyst, with a relatively weaker dependence on the partial pressure of CO₂ and a slightly stronger influence of H₂ partial pressure on the methanation rate. The hydrogenation of CO₂ on the catalyst was observed to produce almost exclusively methane with minor traces of ethane detected, in agreement with the observations of Dorner *et al.* (2009). The high methane selectivity is in accord with that of the nickel catalyst, with the methanation rate displaying a similar dependence on temperature, with the observed apparent activation energies on cobalt (88-91 kJ/mol) in good agreement with the values determined for the reaction over the nickel catalyst (92-93 kJ/mol).

With regard to activation energy, this study has found that they are pressure insensitive, consistent with the behaviour determined for the Ni/Al₂O₃ catalyst. The insensitivity of the reaction's activation energy to pressure indicates the rate-determining step is consistent across the tested pressure range (5-15 barg), however this finding lies contrary to some of the earlier studies on cobalt. The work of Weatherbee and Bartholomew (1984) reported two activation energies for their 15 wt% Co/SiO₂ catalyst, with the value dependant on the reaction pressure, 66 kJ/mol (1 bar) and 173 kJ/mol (11 bar). They further reported apparent activation energy of 99 kJ/mol at a 3 wt% loading examined at atmospheric pressure. Their study indicated an activation energy increase with pressure, and this behaviour was attributed to a change in the rate-determining step. The values obtained here are partly in disagreement with their work, with no pressure sensitivity observed at the 4 pressures examined, however their reported apparent activation energy for their 3 wt% Co/SiO₂ catalyst agrees reasonably with this study. The differences at pressure might be due to changes in the

rate-determining step. However, Weatherbee and Bartholomew (1984) conceded that their reactor was non-isothermal in operation, with an estimated maximum temperature rise of 25–30 K. This non-isothermal operation may partly be responsible for the differences observed; with the catalysts of 15 wt% loading operated at lower space velocities, and thus might have been subject to greater temperature gradients than the 3 wt% Co/SiO₂. Contrary to this Dissertation, Lahiten *et al.* (1994) found significantly higher activation energies (~155 kJ/mol) for CO₂ methanation on a cobalt foil. The authors also noted a different activation energy for CO and CO₂ methanation which they attributed to the additional oxygen removal from CO₂, assuming that the rate-limiting step was reduction of CoO by hydrogen. Their measured energies may indicate a different pathway in operation on the foil catalyst. The supported cobalt nano-particles of Iablokov *et al.* (2012) exhibited activation energies of 75±7 kJ/mol, in better agreement with those determined in this chapter. Lowered activation energies are often associated with results influenced by mass transfer; however, as noted earlier, the linearity of the Arrhenius plot and the satisfaction of the relevant criteria indicated mass transfer is not expected to be limiting in the experiments conducted herein.

It appears from the literature on the activation energy that two potential rate-limiting steps may be in operation. The first is limited by the chemical transformation of carbon dioxide to CH₄, possibly *via* a CO intermediate, whilst the latter is proposed to be limited by the renewal of the cobalt active site by reduction of CoO with hydrogen. The activation energy for the reduction of cobalt oxides in hydrogen obtained in cobalt TPR kinetic studies indicate values of 80 and 53 kJ/mol for H₂ reduction of bulk Co₃O₄ and CoO respectively (Ji *et al.*, 2009). Similarly, activation energies for hydrogen reduction of supported Co₃O₄ and CoO have been reported to be 94.4 and 83.0 kJ/mol respectively on SiO₂ (Lin and Chen, 2004) and 90 and 95 kJ/mol respectively on Al₂O₃ (Ji *et al.*, 2009). Hence, it is unclear whether CoO reduction can be the reason for the large activation energies measured by Lahiten *et al.* (1994) in CO₂ hydrogenation.

For CO₂ methanation on nickel or iron, the activation energies have generally been reported to be consistent with those of CO methanation, with many authors assuming the reaction proceeds *via* a CO surface intermediate. The apparent activation energy obtained in the present study appears consistent with those reported for the Fischer-Tropsch reaction (CO hydrogenation) on cobalt, with activation energies for supported catalysts reported in the 80–100 kJ/mol range, *e.g.* Yan *et al.* (2009), Withers *et al.* (1990). Hence it is not unreasonable to assume that the CO₂ methanation reaction might proceed *via* a similar pathway.

The power-law model was found to provide a reasonable approximation to the results of changing total pressure. The reaction rate was described well by a reaction order of 0.46 in

hydrogen, with only minor influence of the carbon dioxide partial pressure noted. The positive order is a clear indicator of the involvement of hydrogen in the rate-determining step for the reaction. The order with respect to hydrogen lies within those reported for nickel-based methanation, between 0 and 1, as noted in §4.8. For CO₂ methanation on cobalt, Lahiten *et al.* (1994) observed a reaction order of 0.9 in H₂ and ~0 (-0.05) in CO₂ on their cobalt foil at atmospheric pressure and temperatures between 475 K and 575 K. Their order with respect to hydrogen is higher than that of the present study (0.46), but both remain consistent with the literature for CO₂ hydrogenation on other metals, and the differences in the observed order could be owing to the use of supported catalyst rather than foil. The power-law exponents show a near zeroth order dependence on carbon dioxide and indicate that CO₂ is not inhibitory under the conditions examined. The dependence of methanation rate on hydrogen is similarly echoed in the conclusions of Akin *et al.* (2002), whose study determined the kinetics on their coprecipitated Co/Al₂O₃ catalyst depended solely on the partial pressure of hydrogen.

The comparison between the rates at 5 barg and those at higher total pressures shown in Figure 5.4 indicated little temperature sensitivity of the apparent reaction order. Hence the power-law model provides a fair representation for the Co/ZrO₂ results obtained at differential conversions over the temperature range studied. In the CO₂ methanation study of Schlereth (2015), the author reported reaction orders over their Ni/Al₂O₃ catalyst of ~0.3 in H₂ and ~0.1 in CO₂, with only a mild sensitivity to temperature. Their hydrogen order was observed to trend upwards with temperature, and their carbon dioxide order to trend downwards. However, the changes were small, with their H₂ order appearing relatively constant below 523 K. Since the carbon dioxide order observed in this study was very low, it is expected that the temperature behaviour shown Figure 5.4 reflects the relative constancy of the reaction orders, in agreement with the observations of Schlereth (2015).

The Langmuir-Hinshelwood equation developed in §5.5.4 provided a slightly better representation of the results than the power-law expression. The lowest residual equation was derived assuming a CH hydrogenation rate-limiting step. With regard to the literature, the proposal of this rate-limiting step was noted as a possibility by Weatherbee and Bartholomew (1982). Van Meerten *et al.* (1983) has also previously proposed this step as limiting for Ni-based CO methanation. However, the representation of CO₂ methanation kinetics *via* a single Langmuir-Hinshelwood expression might be an oversimplification of a complex reaction set. Mechanistic conclusions based on Langmuir-Hinshelwood fitting may well provide a guide for possible mechanisms in operation, but, given the number of assumptions required in the derivation, further surface science techniques or modelling studies (*e.g.* DFT) are required to provide a firmer identification of the mechanism.

5.7 Conclusions

The kinetics of methane formation over a zirconia supported cobalt catalyst were studied at H₂/CO₂ ratios between 0.25 and 5, pressures between 5 and 15 barg, and temperatures between 433 K and 503 K. A large set of rate equations were derived on the basis of reaction mechanisms proposed in the literature for the CO₂ methanation reaction and compared to the experimental results. Kinetics based on Langmuir-Hinshelwood mechanisms were then evaluated for goodness of fit and compared to a simpler empirical power law model and an existing literature model. The behaviour was then compared to the behaviours observed over the Ni/γ-Al₂O₃ catalyst investigated earlier within this Dissertation. The conclusions were:

- The rate of methanation on the Co/ZrO₂ catalyst displayed sensitivity to hydrogen partial pressure and temperature, with the reaction rate increasing with both. The reaction was observed to show a weak, near zeroth order, dependence on the carbon dioxide partial pressure at the tested conditions.
- In comparison with the Ni/γ-Al₂O₃ catalyst examined in this Dissertation, the Co/ZrO₂ catalyst displayed similar kinetic behaviour, with fair agreement between the partial pressure dependencies and apparent activation energies.
- A Langmuir-Hinshelwood approach was found to most aptly describe the intrinsic kinetics. The results were fitted with the lowest residual sum of squares with a reaction scheme based on the carbide pathway, with a rate-determining step of CH hydrogenation indicated and the reliability of mechanistic conclusions discussed.
- The activation energy of the reaction was observed at multiple pressures between 5 and 15 barg. The activation energy appeared to be insensitive to pressure, and was contrasted with the earlier studies by Lahiten *et al.* (1994) and Weatherbee and Bartholomew (1984). The values of the activation energy were found to be consistent with those reported over the more commonly studied nickel catalysts, and those reported for CO hydrogenation on cobalt.

6. Modelling Reaction and Diffusion in a Wax-Filled Hollow Cylindrical Pellet of Fischer-Tropsch Catalyst

6.1. Introduction

The modelling of transport mechanisms and reaction kinetics in pellets of Fischer-Tropsch catalyst enable an estimation of the effectiveness factor and the variation of the ratio of CO to H₂ across the radius of a catalyst particle. The former indicates whether the catalytic metal is being used optimally, whilst variations in the ratio of CO to H₂ affect the chain growth parameter, with high intra-pellet ratios of H₂ to CO causing excessive and undesired methane production.

This Chapter presents the derivation and evaluation of a pseudo-isothermal, steady-state, two-dimensional model for a catalyst pellet of cylindrical form, where intra-particle diffusion is modelled using Fick's law. The numerical model considers the case of a cobalt-based catalyst, normally used in low-temperature Fischer-Tropsch reactions, where the rate of condensable hydrocarbon generation is large enough to result in accumulation of liquid hydrocarbons within a catalyst's pores.

The pellet's morphology was considered in the analysis of effectiveness factor and product selectivity under typical Fischer-Tropsch conditions. The Fischer-Tropsch process is known to suffer from intra-particle transport limitations in industrially sized pellets of millimetre scale, with smaller particles deemed unsuitable due to excessive fixed-bed pressure drops. Current fixed-bed reactor simulations have highlighted the benefit of cylindrical and shaped pellets to provide improved hydrodynamic, heat and mass transport attributes under industrial conditions relative to spherical pellets. However, mass transport models have focussed on the investigation of transport within pellets with spherical symmetry, whilst extensive and detailed investigations of more complex shapes have not been carried out. Thus this study seeks to address the investigation of pellets of cylindrical symmetry.

6.2. Background

6.2.1. The Fischer-Tropsch Process

Synthesis gas, or *syngas*, is the primary feedstock for the Fischer-Tropsch process, and consists predominantly of a mixture of carbon monoxide (CO) and hydrogen (H₂). It is commonly produced by reforming natural gas, gasifying coal or gasifying biomass, with its exact composition depending on the feedstock from which it is derived and the conditions of the reaction. Where biomass and coal are the initial fuels, the derived synthesis gas may contain significant quantities of impurities and carbon dioxide (Okabe *et al.*, 2009). Syngas can be transformed directly to linear alkanes and alkenes using the Fischer-Tropsch (FT) process. The main reaction pathways are summarised by equations (6.1) to (6.5), below. Equations (6.4) and (6.5) describe secondary reactions which may occur in parallel with the Fischer-Tropsch reactions, namely the water gas shift and Boudouard reactions.



The * of equation (6.5) indicates a species bound to the surface of the catalyst.

From a thermodynamic standpoint, both methanation, reaction (6.1), and carbon deposition by the Boudouard reaction, reaction (6.5), are favourable compared to the formation of hydrocarbons, particularly at low temperatures (Snel, 1987). However, in practice, kinetic and mass transport factors dictate the observed activity and selectivity of the process (Snel, 1987), usually favouring hydrocarbon formation.

The Fischer-Tropsch process typically operates between 200°C and 340°C (Leckel, 2009) and at pressures ≥ 20 barg (Dry, 2002). Generally, an FT reactor will be operated in either a low-temperature (<260°C) or a high-temperature (310-340°C) regime (Leckel, 2009), with these operating conditions having a significant impact on the mean molecular weight of the products. Low-temperature operation produces predominantly heavy hydrocarbons and waxes, whilst lighter hydrocarbons are formed in high-temperature Fischer-Tropsch reactors. The product distribution is also influenced by the type of catalyst, with iron and cobalt employed on an industrial scale.

The exact nature of the Fischer-Tropsch mechanism remains uncertain. However, it is generally considered to be a polymerisation reaction initiated by the adsorption of reactants on

to the catalyst surface, followed by chain initiation, chain growth, chain termination and eventual desorption of the terminated chains (Adesina, 1996). Key to the formation of the desired hydrocarbon fraction is the rate of chain termination, with two pathways for termination having been proposed. Adsorbed surface chains may be removed either by desorption through β -hydrogen abstraction, to produce an alkene or *via* hydrogen addition to form an alkane. Of these mechanisms, the literature suggests that desorption to an alkene is significantly favoured. Schulz (2003) noted that the relative rate of β -hydrogen abstraction is approximately four times greater than the formation of an alkane. This figure was in agreement with the study of Sai-Prasad *et al.* (2008), who reported 70-80% of desorption resulted in alkenes, the balance consisting of linear alkanes.

6.2.2. The Fischer-Tropsch Product Distribution

The range of products from the Fischer-Tropsch reaction is often modelled with an Anderson-Schulz-Flory (ASF) distribution, which assumes that chain growth on the surface of the catalyst occurs only through the addition of a single monomer unit containing one carbon atom, with termination taking place *via* chain desorption (Novak *et al.*, 1981). A core assumption is that the ratio of chain propagation rate to chain termination rate is independent of chain length. Hence:

$$W_N = N(1 - \alpha)^2 \alpha^{N-1} \quad (6.6)$$

where

$$\alpha = \frac{k_p}{k_p + k_t} \quad (6.7)$$

Here, W_N is the weight fraction of product of carbon number N and α is the chain growth parameter. The rate constants k_p and k_t are, respectively, for chain propagation and chain termination. The chain growth parameter, α , describes the likelihood of chain growth and can be determined from the gradient of an ASF plot, *viz.* Figure 6.1 a). This single-parameter model can provide a reasonable fit to experimental results; however, it assumes that the chain growth parameter is independent of carbon number (Novak *et al.*, 1981). In simulation, the α parameter is significant, since it is necessary to determine the ratio of the rates of CO and H₂ consumption as well as the product composition. The parameter is notably sensitive to pressure, temperature and the local ratio of H₂ to CO. The influence of these on the products formed is reviewed in §6.2.3.

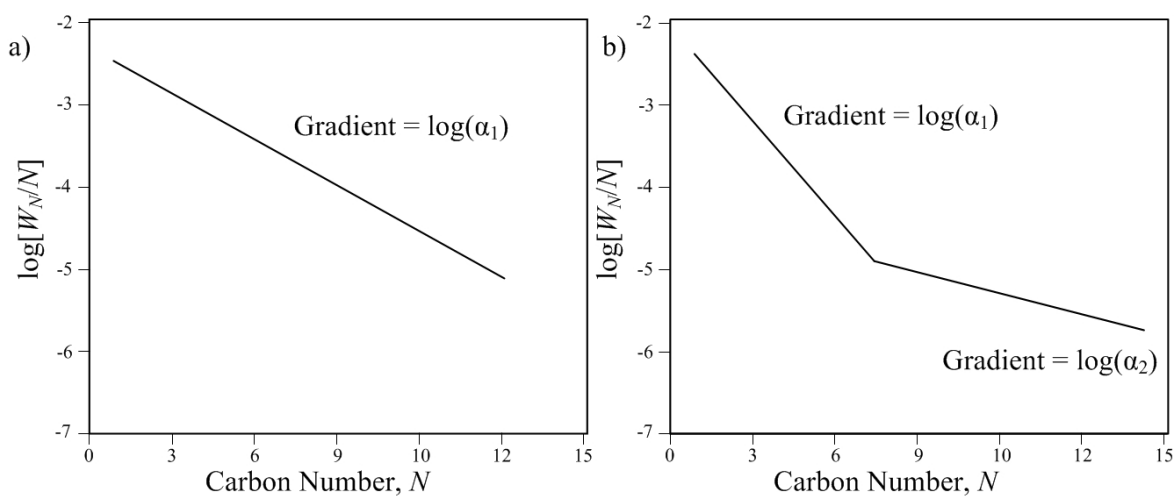


Figure 6.1 a) A single alpha ASF plot of $\log(W_N/N)$ against carbon number, N . b) An ASF plot showing dual alpha behaviour.

Experimentally, a product distribution may deviate from a single α distribution at higher carbon numbers, as shown in Figure 6.1 b). Various reasons for such deviations have been proposed, including the existence of two different reaction sites (Huff and Satterfield, 1984), alkene readsorption and reincorporation (Iglesia *et al.*, 1991), secondary reactions due to increased physisorption of larger chains (Kuipers *et al.*, 1996), coincident reaction *via* the carbide and CO insertion mechanisms (Gaube and Klein, 2008) and the influence of vapour-liquid equilibrium (Masuku *et al.*, 2011). However, single α distributions have been observed, with Raje *et al.* (1997) reporting a single alpha distribution, equation (6.6), provided a suitable fit to their reaction products obtained over an iron catalyst at two ratios of H₂/CO.

6.2.3. The Influence of Process Conditions on Selectivity

Chain growth is strongly influenced by the ratio of H₂ to CO. An increase in the H₂/CO ratio results in the product distribution shifting towards lower carbon numbers with a lower percentage of alkenes (van der Laan and Beenackers, 1999). The shift is attributed to both increased rates of termination and alkene hydrogenation caused by higher concentrations of surface hydrogen. The influence of H₂/CO ratio on product selectivity is particularly important in large catalyst particles. Owing to the broad range of hydrocarbons produced, condensable hydrocarbons may form within catalyst pellets operated under low-temperature Fischer-Tropsch conditions. The resultant liquid promotes development of intra-particle diffusion limitations, and consequently gradients in H₂/CO. This has a significant impact on the product distribution due to the greater diffusivity of H₂ relative to CO.

Pressure influences both product selectivity and catalyst activity, with increases in

pressure resulting in increased average chain length, decreased branching and decreased selectivity for methane (van der Laan and Beenackers, 1999). Generally, the fraction of C₅₊ hydrocarbons (hydrocarbons of carbon number 5 or greater) is used as a metric for FT catalyst liquid selectivity, and similarly is noted to increase with pressure. However, the relationship is not straightforward. For example, Bae *et al.* (2011) observed decreased C₅₊ selectivity upon increasing pressure between 10 and 20 bar, attributed to increased hydrogenation.

The temperature has a significant impact on the distribution, and it is generally acknowledged α decreases with increasing temperature. Experimental studies, *e.g.* van der Laan and Beenackers (1999), King (1978) and Bae *et al.* (2011), report accelerated reaction rates, improved light alkene selectivity and decreased mean carbon number upon increasing temperature (Soled *et al.*, 1995). Whilst improved rates and light alkene selectivity may be desirable, a balance must be struck between these and the increased methane selectivity. Significant methanation may be observed at high reaction temperatures, with Van Dijk *et al.* (1982) observing a high methane selectivity of 80-90% over an iron catalyst at 350°C. This trend in increased methane selectivity with temperature holds across all FT active metals. For instance, Varma *et al.* (1990) and King (1978) reported increased methanation selectivity for nickel and ruthenium, respectively.

6.2.4. Intra-Particle Reaction-Diffusion Modelling

Determining the effectiveness factor for a catalyst pellet is vital for the industrial design of Fischer-Tropsch fixed-bed reactors, and a number of studies have sought to examine the influence of pellet size on effectiveness, both experimentally and numerically. Evidence of internal diffusion limitation within Fischer-Tropsch pellets has been repeatedly presented since the work of Anderson *et al.* (1952); however, a quantitative analysis was absent until the work of Post *et al.* (1989), who quantified the effect of pellet and pore diameter on reaction rate using a Thiele modulus approach. In their analysis, the kinetics were reduced to a first order reaction dependent on the partial pressure of hydrogen. In fitting this model to experiments, the calculated hydrogen diffusivity was significantly lower than would be expected for gas phase diffusion, leading them to conclude that the mass transfer within low-temperature Fischer-Tropsch catalyst pellets is controlled by the diffusivity of reacting species through a hydrocarbon liquid medium.

Following Post *et al.* (1989), the concept of diffusion limitation affecting alkene selectivity was introduced by Iglesia *et al.* (1991). These authors postulated the diffusion limitations originated from the presence of a heavy paraffin phase, which increased pore

residence times and thus secondary reactions of 1-alkenes. Iglesia *et al.* (1991) attributed differing product distributions to increased diffusion limitation, suggesting 1-alkene products were reincorporated into chain growth, and thus produced a heavier and more paraffinic product. Higher chain lengths have been further associated with increased physisorption of alkenes on pore walls, and increased retention within the pores (Kuipers *et al.*, 1995).

Numerical models of greater complexity than that of Post *et al.* (1989) were later developed. The key benefits of these models were the use of representative kinetic descriptions, simulation of both hydrogen and carbon monoxide concentrations and the ability to encompass selectivity within the kinetics. Wang *et al.* (2001), for example, simulated a spherical catalyst particle filled with a ‘liquid wax’, employing kinetic equations including their own alkene readsorption kinetic model. The authors used this model to analyse the performance of iron FT catalyst spheres of industrially-relevant size, ~1-3 mm diameter, obtaining conclusions broadly aligned with those of Post *et al.* (1989). That is, the overall effectiveness factor decreased as the pellet diameter increased above a few hundred microns.

Vervloet *et al.* (2012) developed a reaction-diffusion model for a cobalt catalyst particle. Similar to Wang *et al.* (2001), a chain growth parameter model, dependent on the local H₂/CO ratio, was used to calculate the overall product distribution, and thus simulate shifts in the Fischer-Tropsch product distribution due to internal mass transfer limitations. Gardezi and Joseph (2015) later examined the performance of eggshell cobalt silica FT catalysts in a modelling study. The performance characteristics of cobalt supported on silica were evaluated seeking to determine an optimal shell thickness. Gardezi and Joseph (2015) concluded that there was an advantage to using egg-shell catalysts in the FT process, since the use of egg-shell distributions afforded more efficient metal usage and might allow for the use of larger particles, thus reducing the pressure drop across a fixed-bed reactor.

The underlying bases of these numerical studies are limited to simple spherical catalyst particles. The rotational symmetry of a spherical catalyst pellet allows the transport equations to be reduced to a one-dimensional, two-point boundary value problem, thus significantly reducing the computational requirements to solve the system. Industrially, catalyst pellets are formed into various shapes and configurations; hence the simulation of higher dimensional pellets is required to give an insight into how the behaviour of these pellets compares to the simplified models. Current numerical models do not allow for the characterisation of hollow cylindrical pellets, for instance, as single dimensional models cannot accurately predict how the ratio between cylinder radii and length impacts on the overall selectivity and effectiveness factor of a Fischer-Tropsch catalyst pellet.

An alternative approach to reaction-diffusion modelling and catalyst design was adopted by Becker *et al.* (2014) by introducing hypothetical “transport pores”. The authors examined the introduction of wider “transport pores” aimed at improving mass transport, promoting C₅₊ selectivity and increasing effectiveness factor. The resulting numerical model was based on a micro-structured reactor of slab geometry with a catalyst coated channel wall. A one dimensional mass transport equation was adopted with the kinetics derived from the work of Yates and Satterfield (1991). The transport pores were considered to be unreactive, uniformly distributed within the wall, and with a lower tortuosity than the reactive pores. The catalyst was then optimised for transport pore fraction to maximise the activity and selectivity for C₅₊ hydrocarbons. By introducing transport pores, a theoretical 47% performance increase could be obtained under their reference conditions.

6.2.5. Pellets of Cylindrical Geometry

Despite cylindrical pellets being used industrially, very few investigations directly concerning the use of cylindrical pellets in the Fischer-Tropsch process exist. Kaiser *et al.* (2014) compared powdered and cylindrical (1.5 mm diameter, 5 mm length) Co/TiO₂ catalyst pellets. In taking kinetic measurements, there were significant differences in the selectivity and apparent effectiveness factor between the catalyst in pellet and ground form. In order to explain their findings, the authors used a simplified analytical model for effectiveness factor for reaction-diffusion within a slab, obtaining a reasonable agreement between their experiments and theory. However, they noted that a more detailed numerical simulation would be required to achieve a more accurate solution.

Brunner *et al.* (2015) examined the effect of particle size and shape in a modelling study of a trickle bed recycle reactor. The authors employed a one-dimensional reactor model to examine the effect of pellet size and geometry on the performance of a wall cooled multi-tubular Fischer-Tropsch reactor. The size and shape of pellets were considered using an effective diameter model, namely the modelled diameter was calculated for a sphere of equivalent volume, with the effectiveness factor calculated assuming a first order reaction. The dimensions of the catalyst were noted to be limited by factors such as mechanical strength and pressure drop, with smaller particles resulting in lowered bed voidage and increased pressure drop. Of the particles examined, the calculated pressure drop was found to increase from hollow cylinder < trilobe < cylinder < sphere. However, the trilobes were reported to maximise catalyst effectiveness, with the lowest equivalent spherical diameter of 1.3 mm.

Nanduri and Mills (2015) and Nanduri (2014) considered intrapellet mass transport within a pellet of a cylindrical form and also examined the effectiveness factors of multi-holed cylindrical pellets. The authors developed a one-dimensional fixed-bed model with a ‘2D’ model of the catalyst particles in spherical and cylindrical geometry for an iron-based Fischer-Tropsch catalyst. The authors’ model examined the pellet in 2D through consideration of a radial plane which could not be reduced to a single dimension. This was due to the lack of rotational symmetry owing to the presence of multiple holes. In their 2D catalyst scale modelling approach, the influence of axial contributions on pellet-scale diffusion was not simulated.

This Chapter describes the formulation of a numerical model for a cylindrical geometry and discusses its results and their impact on the design and analysis of hollow cylindrical Fischer-Tropsch catalyst pellets. The research examines the influence of pellet dimensions in both axial and radial dimensions for hollow cylinders.

6.3. Model Development

For a cylindrical pellet, the problem must be considered as a two-dimensional problem, with the additional dimension increasing the complexity of the model to allow for diffusion in both the radial and axial directions.

6.3.1. Model Assumptions

In modelling a liquid-filled Fischer-Tropsch pellet, schematically represented in Figure 6.2, the liquid-filled pores and the support skeleton were considered uniform across the pellet. The model’s diffusivities and thermal conductivities were calculated to account for both the particle’s structural parameters, *viz.* voidage, tortuosity, skeletal density and thermal conductivity, and the transport properties of the liquid in the pores.

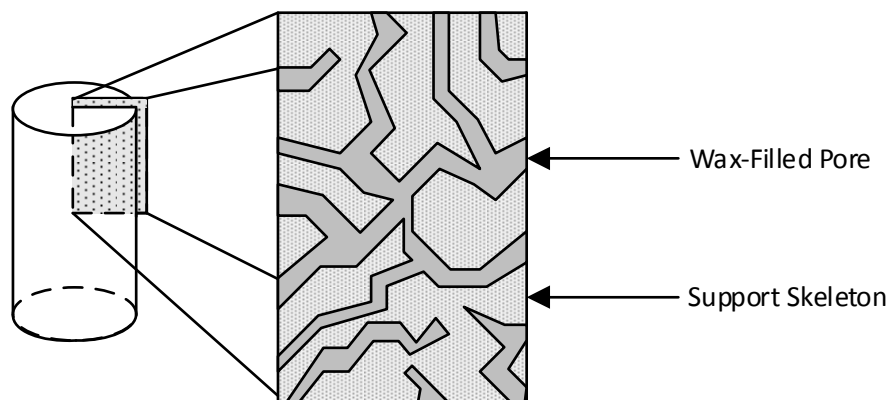


Figure 6.2. A schematic diagram of a liquid-filled Fischer-Tropsch catalyst pellet.

The model assumed that the reaction is at steady state, with the pores fully filled with liquid wax. The assumption of wax-filled pores has been noted to reflect the process behaviour by Wang *et al.* (2001), Madon and Iglesia (1994), and Huff and Satterfield (1985). In their study of pore-filling during reactor start-up, Huff and Satterfield (1985) reported that the time-scale for pore filling depended significantly on the chain growth parameter and the activity of the catalyst, varying between 129 to 5250 minutes for their fixed-bed model. Huff and Satterfield (1985) assumed that reactant and product mass transport within the pores could be ignored, with the vapour-liquid equilibrium (VLE) represented by Raoult's law. Despite the simplicity of their model, the pore filling times are of similar order to those determined by Madon and Iglesia (1994), who compared 110-180 μm and 850-1700 μm diameter Ru/TiO₂ catalyst experimentally for Fischer-Tropsch synthesis (489 K, 505 kPa, H₂/CO = 2). The larger particles were noted to display lower activity, and reached steady state within 20 hours. The smaller particles, however, reached steady state more rapidly, with less activity lost due to deactivation. The behaviour of the larger particles was attributed to the mass transport influence introduced by pore filling, with the attainment of steady state attributed to the complete filling of the pores.

In this Dissertation, the mass transport of species through the liquid-filled pores was described with Fick's law. The use of Fick diffusion has been confirmed as suitable through molecular dynamic simulations, with the Fick and Maxwell-Stefan diffusivities differing little for dissolved gas mole fractions below 0.1 (Makrodimitri *et al.*, 2011, Sanchez-Lopez *et al.*, 2016). The solubility of the CO and H₂ species within the waxy products is low enough such that these species may be considered dilute in concentration. The application of Fick's law is frequently used to describe the flux of CO and H₂ within the Fischer-Tropsch wax in published works, *e.g.* Wang *et al.* (2001), Gardezi and Joseph, (2015), Vervleot *et al.* (2012). The diffusivities of the species within the wax were assumed to depend only on the mean molecular mass of the wax within the pores and the process temperature. The selection of the diffusivity correlation is further discussed in §6.3.5.

The flux of reactants was assumed to be controlled by diffusion and the contribution of advection due to outflow of liquid products was assumed to be negligible. The concentrations of the species at the pellet boundary dissolved within the wax phase were assumed to be in equilibrium with those in the gas phase, as described by Henry's law.

The thermal conductivity was assumed to be uniform across the solid pellet, with the influence of convection and radiation neglected. The influence of external heat transport was neglected and the pellet temperature boundary was assumed to be equal to the bulk

temperature of the process fluid. The temperature gradients within the particle were found to be negligible for the conditions considered (<0.50 K), and thus the pellet was assumed to be isothermal to improve simulation speed.

6.3.2. Mathematical Description

The generalised species transport equation at steady state may be expressed as

$$-\nabla \cdot (D_i \nabla \cdot C_i) - R_i = 0 \quad (6.8)$$

where R_i is the reaction rate on a volumetric basis [mol/m³ s], C_i is the concentration [mol/m³], and D_i [m²/s] is the effective diffusivity of species i . Likewise, the steady state temperature (T) gradients may be expressed by equation (6.9). The molar heat of formation of species j , ΔH_j , and the rate of formation of species j , R_j , are summed over all species to calculate the overall heat of reaction, thus acting as the source term in the energy equation. The thermal conductivity, represented by \mathbf{k} , is a spatially-averaged combination of the thermal conductivities of the skeletal network of the support and the wax filling the pores.

$$-\nabla \cdot (\mathbf{k} \nabla \cdot T) - \sum \Delta H_j R_j = 0 \quad (6.9)$$

In cylindrical co-ordinates, equations (6.8) and (6.9) may be expressed as:

$$-D_i \left(\frac{1}{r} \frac{\partial}{\partial r} \left(r \frac{\partial C_i}{\partial r} \right) + \frac{\partial^2 C_i}{\partial z^2} \right) - R_i = 0 \quad (6.10)$$

$$-k \left(\frac{1}{r} \frac{\partial}{\partial r} \left(r \frac{\partial T}{\partial r} \right) + \frac{\partial^2 T}{\partial z^2} \right) - \sum \Delta H_j R_j = 0 \quad (6.11)$$

Here, r represents the radial position and z the axial position within the pellet. The flow of any liquid products out of a filled particle was neglected in line with literature pellet models. Hence, only the diffusion of the reactant species through the near quiescent hydrocarbon wax need be considered.

The following dimensionless variables were introduced.

$$\bar{C}_i = C_i / C_{i,0} \quad (6.12)$$

$$\bar{r} = r / r_p \quad (6.13)$$

$$\bar{z} = z / L \quad (6.14)$$

$$\bar{R}_i = R_i / R_{i,0} \quad (6.15)$$

$$\bar{T} = T / T_0 \quad (6.16)$$

Here the barred quantities \bar{C}_i , \bar{z} , \bar{T} , \bar{r} , \bar{R} represent the dimensionless concentration, axial position, temperature, radial position and reaction rate respectively. L is half the axial length and r_p is the radius of the pellet. The 0 subscripted terms represent the respective quantities at the pellet's outer surface, and the i subscript identifies the component.

The cylindrical system expressed in equation (6.8) may then be stated as:

$$-\frac{DC_{i,0}}{R_{i,0}r_0^2} \left(\frac{1}{\bar{r}} \frac{\partial}{\partial \bar{r}} \left(\bar{r} \frac{\partial \bar{C}_i}{\partial \bar{r}} \right) + \frac{r_0^2}{L^2} \left(\frac{\partial^2 \bar{C}_i}{\partial \bar{z}^2} \right) \right) = \bar{R}_i \quad (6.17)$$

Introducing two dimensionless groups, $\kappa_i = \left(\frac{D_i C_{i,0}}{R_{i,0} r_0^2} \right)$ and $\beta = \frac{r_0^2}{L^2}$ gives:

$$-\kappa_i \left(\frac{1}{\bar{r}} \frac{\partial}{\partial \bar{r}} \left(\bar{r} \frac{\partial \bar{C}_i}{\partial \bar{r}} \right) + \beta \left(\frac{\partial^2 \bar{C}_i}{\partial \bar{z}^2} \right) \right) = \bar{R}_i \quad (6.18)$$

For the evaluation and comparison of 1-D systems, the equations were reduced to (6.19)-(6.21).

Infinite Cylinder:
$$-\frac{DC_{i,0}}{R_{i,0}r_0^2} \left(\frac{1}{\bar{r}} \frac{\partial}{\partial \bar{r}} \left(\bar{r} \frac{\partial \bar{C}_i}{\partial \bar{r}} \right) \right) = \bar{R}_i \quad (6.19)$$

Sphere:
$$-\frac{DC_{i,0}}{R_{i,0}r_0^2} \left(\frac{1}{\bar{r}^2} \frac{\partial}{\partial \bar{r}} \left(\bar{r}^2 \frac{\partial \bar{C}_i}{\partial \bar{r}} \right) \right) = \bar{R}_i \quad (6.20)$$

Slab:
$$-\frac{DC_{i,0}}{R_{i,0}L^2} \left(\frac{\partial^2 \bar{C}_i}{\partial \bar{z}^2} \right) = \bar{R}_i \quad (6.21)$$

6.3.3. Manipulation of the Energy Equation

The conduction equation may be expressed in non-dimensional form as

$$-kT_0 \left(\frac{1}{r_0^2} \frac{1}{\bar{r}} \frac{\partial}{\partial \bar{r}} \left(\bar{r} \frac{\partial \bar{T}}{\partial \bar{r}} \right) + \frac{1}{L^2} \left(\frac{\partial^2 \bar{T}}{\partial \bar{z}^2} \right) \right) = \Delta H(r, z) R_{CO,0} \bar{R}_{CO} \quad (6.22)$$

This may then be simplified by introducing the dimensionless group $\gamma = \frac{kT_0}{\Delta H_0 R_{CO,0} r_0^2}$.

$$-\gamma \left(\frac{1}{\bar{r}} \frac{\partial}{\partial \bar{r}} \left(\bar{r} \frac{\partial \bar{T}}{\partial \bar{r}} \right) + \beta \left(\frac{\partial^2 \bar{T}}{\partial \bar{z}^2} \right) \right) = \frac{\Delta H(r, z)}{\Delta H_0} \bar{R}_{CO} \quad (6.23)$$

Here the terms \bar{r} , \bar{z} , \bar{T} and \bar{R}_{CO} represent the radial position, axial position, temperature and reaction rate of CO in non-dimensional coordinates. The $\Delta H(r, z)$ term represents the heat of reaction per mole of CO at a given radius and axial co-ordinate, the 0 subscript represents surface conditions. The dimensionless group γ is comprised of the effective thermal conductivity, k , the surface temperature, T_0 , the reaction enthalpy at the surface, ΔH_0 , the reaction rate of CO at the surface, $R_{CO,0}$, and the pellet radius, r_0 . For the evaluation and comparison with 1-D systems, the equations may be reduced to (6.24)-(6.26).

Infinite Cylinder:
$$-\frac{kT_0}{\Delta H_0 R_{CO,0} r_0^2} \left(\frac{1}{\bar{r}} \frac{\partial}{\partial \bar{r}} \left(\bar{r} \frac{\partial \bar{T}}{\partial \bar{r}} \right) \right) = \frac{\Delta H(r)}{\Delta H_0} \bar{R}_{CO} \quad (6.24)$$

Sphere:
$$-\frac{kT_0}{\Delta H_0 R_{CO,0} r_0^2} \left(\frac{1}{\bar{r}^2} \frac{\partial}{\partial \bar{r}} \left(\bar{r}^2 \frac{\partial \bar{T}}{\partial \bar{r}} \right) \right) = \frac{\Delta H(r)}{\Delta H_0} \bar{R}_{CO} \quad (6.25)$$

Slab:
$$-\frac{kT_0}{\Delta H R_{CO,0} L^2} \left(\frac{\partial^2 \bar{T}}{\partial \bar{z}^2} \right) = \frac{\Delta H(z)}{\Delta H_0} \bar{R}_{CO} \quad (6.26)$$

6.3.4. Boundary Conditions

The equations describing the heat and mass transfer within the cylindrical pellet are both second order with respect to each dimension, r and z . Hence, for each dimension, two boundary conditions must be applied. For the dimensionless species concentration and dimensionless temperature, the boundaries are given in Table 6.1 for the solid and hollow cylindrical cases.

Table 6.1. Boundary conditions for solid and hollow cylinder systems. Outer wall boundary conditions are common to both cases.

Outer wall Boundary	Inner Boundary (Solid Cylinder)	Inner Boundaries (Hollow Cylinder)	
$\bar{C}_i = 1$ at $\bar{r} = 1$	$\frac{\partial \bar{C}_i}{\partial \bar{r}} = 0$ at $\bar{r} = 0$	$\bar{C}_i = 1$ at $\bar{r} = r_{in}$	(6.27)
$\bar{T} = 1$ at $\bar{r} = 1$	$\frac{\partial \bar{T}}{\partial \bar{r}} = 0$ at $\bar{r} = 0$	$\bar{T}_i = 1$ at $\bar{r} = r_{in}$	(6.28)
$\bar{C}_i = 1$ at $\bar{z} = 1$	$\frac{\partial \bar{C}_i}{\partial \bar{z}} = 0$ at $\bar{z} = 0$	$\frac{\partial \bar{C}_i}{\partial \bar{z}} = 0$ at $\bar{z} = 0$	(6.29)
$\bar{T} = 1$ at $\bar{z} = 1$	$\frac{\partial \bar{T}}{\partial \bar{z}} = 0$ at $\bar{z} = 0$	$\frac{\partial \bar{T}}{\partial \bar{z}} = 0$ at $\bar{z} = 0$	(6.30)

Here $\bar{r} = 0$ along the centre line of the pellet, and $\bar{z} = 0$ at a distance of L normal from the top of the pellet. The boundary conditions are shown schematically in Figure 6.3. For hollow pellets, the boundary conditions were modified, such that at $\bar{r} = \frac{r_{in}}{r_0}$, \bar{C}_i and \bar{T}_i are equal to one, where r_{in} is the hole radius. For 1-D systems, the selected boundary conditions were equivalent to those of equations (6.27) and (6.28).

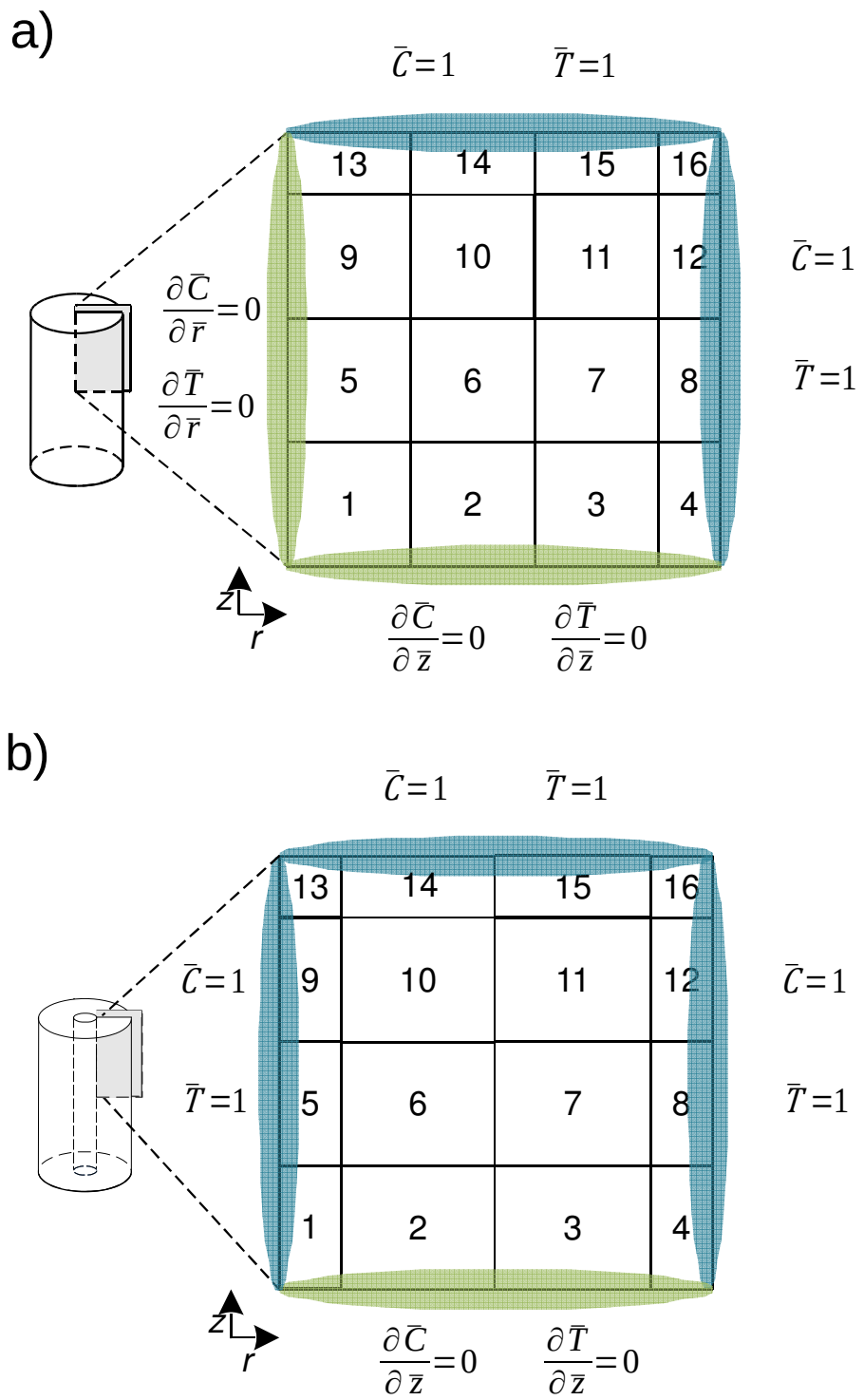


Figure 6.3. The boundary conditions for a solid (a) and hollow (b) cylindrical pellet and their locations. The blue shaded edges represent the surface boundary conditions, that is a concentration and temperature equal to that of the bulk, whereas the green shaded edges represent symmetry conditions, that is gradients perpendicular to the edge's face equalling zero.

6.3.5. Diffusivity

The diffusivity of CO and H₂ within a Fischer-Tropsch wax product was estimated using an appropriate correlation. The published literature concerned with mass transport phenomena in Fischer-Tropsch wax has taken a variety of approaches, utilising empirical models to quantify the diffusivity, *e.g.* Wilke-Chang correlation or Rough Hard Sphere model. A selection of the more commonly applied diffusivity models is presented in Table 6.2. The wax composition was assumed to be represented by C₂₈H₅₈, in line with the current literature models. However the model was capable of simulating diffusivities across a range of carbon numbers.

Table 6.2. A summary of correlations used in the modelling of diffusion in Fischer-Tropsch waxes.

Equation	Application of model
Akgerman (1984) (6.31)	Trickle bed FT reactor model: Brunner <i>et al.</i> (2012) Iron based Fischer-Tropsch reaction simulation: Hallac <i>et al.</i> (2015) Fischer-Tropsch Slurry Bubble Column Model: Sehabiague (2012)
Erkey <i>et al.</i> (1990)	
$D_{12} [\text{m}^2/\text{s}] = \frac{94.5 \times 10^{-9} \sqrt{T}}{(M_1)^{0.239} (M_2)^{0.781} (\sigma_1 \sigma_2)^{1.134}} \left[\bar{V}_2 - \left(1.206 + 0.0632 \frac{\sigma_1}{\sigma_2} \right) \frac{N_A \sigma_2^3}{\sqrt{2}} \right]$	
Wilke and Chang (1955) (6.32)	Wax diffusivity in a fixed-bed model: Jess and Kern (2009) Damköhler number calculation: Madon and Iglesia (1994) Monolith loop reactor: DeDeugd <i>et al.</i> (2003)
Akgerman (1987) (<i>n</i> -C ₂₈ H ₅₈ solvent only)	1-D Spherical Pellet models: Wang <i>et al</i> (2001), Vervloet <i>et al.</i> (2012), Gardezi and Joseph (2015)
$D_{CO} = 5.584 \times 10^{-7} \exp\left(-\frac{1786.29}{T}\right)$ (6.33)	Tubular Reactor Simulation: Kaskes <i>et al.</i> (2016)
$D_{H_2} = 1.085 \times 10^{-6} \exp\left(-\frac{1613.65}{T}\right)$ (6.34)	

The equations in Table 6.2 represent the correlations used to determine the binary diffusivities D_{12} of H₂ and CO in Fischer-Tropsch wax. The equation of Akgerman (1984) is based on the rough hard sphere model, with the terms T , \bar{V} , \bar{V}_0 , M_1 , M_2 , σ_1 and σ_2 representing the temperature [K], the molar volumes of the solute, the molar volume of the solvent, the molecular mass of solute [g/mol], the molecular mass of solvent [g/mol] and the hard sphere diameters [\AA] of the solute and solvent respectively. The Wilke-Chang equation is based on hydrodynamic theory, with the symbols φ , M_2 , μ and v_m representing the association parameter [dimensionless, 1.0 for alkanes], solvent molecular mass [g/mol], the viscosity of the solvent [cP] and the molar volume of the solute at its normal boiling point [cm³/gmol]. The frequently cited correlation by Erkey *et al.* (1990) is a republished version of the Akgerman (1984) equation.

The core difficulty in the selection of a diffusion model is identifying a model which yields accurate diffusion values within the range of interest. Akgerman (1984) noted that older models are often extrapolated far beyond their validated range, particularly for diffusion coefficients at high temperature. Indeed, the data employed in the development of the Wilke-Chang correlation were determined mainly below 50°C (Wilke and Chang, 1955). In their comparison of models, Sehabiague (2014) examined the Wilke-Chang and Erkey models across a temperature range of 350-550 K, reporting that the Wilke-Chang model consistently underestimated the diffusivity of both H₂ and CO for SASOL wax. Akgerman (1984) similarly reported Wilke-Chang diffusivities to underestimate the diffusivity of H₂ within heavy *n*-paraffin solvents.

In this Dissertation, the binary diffusivity used was calculated using the correlation of Akgerman (1984). Rodden *et al.* (1988) further compared the rough hard sphere theory to experimental diffusion results obtained in eicosane at elevated pressure (1.38 MPa) and temperatures (100-260 °C), concluding the hard sphere model of Akgerman (1984) could correctly represent the measurements.

In considering the diffusivity of a species through a porous medium, the observed diffusivity differs from the bulk diffusivity due to the structure of the medium. Often this is accounted for using an effective diffusivity, estimated using the geometrical and structural properties of the pellet, such that:

$$D_{\text{eff}} = D_{\text{bulk}} \frac{\varepsilon}{\tau} \quad (6.35)$$

where τ is the tortuosity factor, and ε the voidage. As the tortuosity factor is difficult to determine, some authors, *e.g.* Fan *et al.* (1995), have simplified the expression using

$$\tau = \frac{1}{\varepsilon} \quad (6.36)$$

so that:

$$D_{eff} = \varepsilon^2 D_{bulk} \quad (6.37)$$

The concentrations of the reactants within the Fischer-Tropsch wax have been assumed to be dilute, and thus the effective diffusivity was assumed to be dependent only on the properties of the wax and the voidage and tortuosity of the catalyst support. The assumption that the diffusivity of the reactants is influenced only by the properties of the wax is necessary to simplify the system, since a concentration dependent diffusivity parameter would require the simulation of hundreds of components and the vapour liquid equilibrium of poorly characterised heavy hydrocarbons. To date, all pellets models have employed this simplifying assumption to quantify the mass transport of CO and H₂.

6.3.6. Solubility of CO and H₂ in Fischer-Tropsch Wax

The surface boundary condition, that is the liquid phase concentration of a reactant species at the surface of the pellet, requires knowledge of the solubility of the reactant in the liquid wax. Owing to the industrial application of Fischer-Tropsch slurry phase reactors, a significant body of solubility data exists for CO and H₂ in Fischer-Tropsch products, with the differing solubility of H₂ and CO acknowledged as having a significant influence on the observed activity and product selectivity (Shi and Davis, 2005). For a sparingly-soluble gas, a Henry's law approximation is appropriate, such that

$$P_i = H_i y_i \quad (6.38)$$

where P_i is the partial pressure and y_i is the mole fraction of species i in the solvent. The required Henry constants, H_i , were determined using the correlations developed by Marano and Holder (1997a). The Marano and Holder (1997a) model was developed from fitting experimental solubilities and has been extensively applied in the modelling of one-dimensional Fischer-Tropsch pellets, with both Vervloet *et al.* (2012) and Becker *et al.* (2016) adopting the method to determine their boundary conditions. Since the Marano and Holder (1997a) correlation was developed specifically for the solubility of CO, H₂ and other light gases from solubility results over a range of carbon numbers (16-36) and temperatures (300-553 K), it is expected the correlation should be as accurate as more complicated equation of state models at the required modelling conditions.

6.3.7. Fischer-Tropsch Wax Density

The Fischer-Tropsch wax density as a function of carbon number was accounted for using the empirical correlation developed by Marano and Holder (1997b). Their correlation, based on experimental results for FT waxes, was used to predict the liquid molar volume as a function of carbon number, with the value transformed into mass density using the mean molecular mass of the paraffin.

6.3.8. Kinetics and Selectivity

The intrinsic kinetics of the Fischer-Tropsch reaction were modelled using the Langmuir-Hinshelwood-Hougen-Watson type kinetic equation originally proposed by Yates and Satterfield (1991), *viz.*

$$r_{CO+H_2} = \frac{A e^{-\frac{E_A}{R_{Gas}T}} P_{CO} P_{H_2}}{\left(1 + B e^{-\frac{E_B}{R_{Gas}T}} P_{CO}\right)^2} \quad (6.39)$$

The parameters A , B and activation energies were calculated by Maretto and Krishna (1999) and listed in Table 6.3. Parameters are given in Arrhenius form as shown by (6.40).

$$A = A_{493\text{ K}} e^{-\frac{E_A}{R_{Gas}}(\frac{1}{T} - \frac{1}{493})} \quad (6.40)$$

Table 6.3 Parameter for equation obtain by Maretto and Krishna (1999)

$A_{493\text{ K}}$ [$\mu\text{mol s}^{-1} \text{g}^{-1} \text{bar}^{-2}$]	$B_{493\text{ K}}$ [bar^{-1}]	$E_A [\text{kJ mol}^{-1}]$	$E_B [\text{kJ mol}^{-1}]$
8.853	2.226	37	-69

The rate of CO consumption was determined by dividing the rate of $\text{CO}+\text{H}_2$ consumption by the H_2 to CO usage ratio + 1 (~3.1). The pressure terms were transformed to liquid-phase reactant concentrations by applying Henry's law in the same manner as Vervloet *et al.* (2012) and Gardezi and Joseph (2015).

As noted earlier, the selectivity of the reaction is determined by the temperature and the ratio of hydrogen to carbon monoxide. The selectivity model of Vervleot *et al.* (2012), equation (6.41), was adopted to determine how the selectivity was influenced by hollow cylinder size. Vervleot *et al.* (2012) developed the model by fitting their equation to the published selectivity results of de Deugd *et al.* (2003). The authors later applied the model in the reaction-diffusion model of a spherical pellet, with Gardezi and Joseph (2015) adopting the model in their consideration of egg-shell distributions in spherical pellets.

$$\alpha = \frac{1}{1 + k_s \left(\frac{C_{H_2}}{C_{CO}} \right)^\sigma \exp \left(\frac{E_S}{R_{Gas}} \left(\frac{1}{493.15} - \frac{1}{T} \right) \right)} \quad (6.41)$$

Equation (6.41) determines the chain growth parameter (α) at a point within the pellet where C_{H_2} and C_{CO} represent the wax phase concentrations in mol/m³ of hydrogen and carbon monoxide respectively. The dimensionless parameter k_s represents the ratio of the propagation and the termination reaction rate constants and E_S represents the effective activation energy of k_s . The values of these parameters were obtained from the work of Vervleot *et al.* (2012) with k_s equal to 5.67×10^{-2} , E_S equal to 120 kJ/mol and $\sigma = 1.76$.

6.3.9. Summary of Model Parameters

Additional model parameters are outlined in Table 6.4. The average thermal conductivity was determined using the Landauer equation, which has been reported to describe the influence of porosity on the thermal conductivity more accurately than simpler models (Smith *et al.*, 2014). The base thermal conductivities were assumed to be 1.3 W/m K for the support skeleton and 0.14 W/m K for the Fischer-Tropsch wax within the pores. The conductivity selected for the support is typical of silica, a commonly used support in the Fischer-Tropsch reaction, with the Fischer-Tropsch wax thermal conductivity calculated from the results of Marano and Holder (1997b). The influence of the impregnated metal on the thermal conductivity of the support was neglected.

The porosity and tortuosity of the pellet were assumed to be 0.5 and 2 respectively. The selected voidage and tortuosity is consistent with the supports used in this Dissertation and of supported Fischer-Tropsch catalysts examined in the literature.

Table 6.4 Catalyst physical properties used in the model.

Catalyst Physical Properties	Heat Transfer Physical Properties
Density of particle (inclusive of voids) [kg/m ³]	1000
Mean thermal conductivity of pellet [W/m K]	0.53
Porosity of pellet [-]	0.5
Tortuosity of Pellet [-]	2

6.4. Solution Methodology

6.4.1. Algorithm

The algorithm used is outlined in Figure 6.4. Details in the formulation of the boundary conditions, and details of the orthogonal collocation method are given in Appendix (§A4).

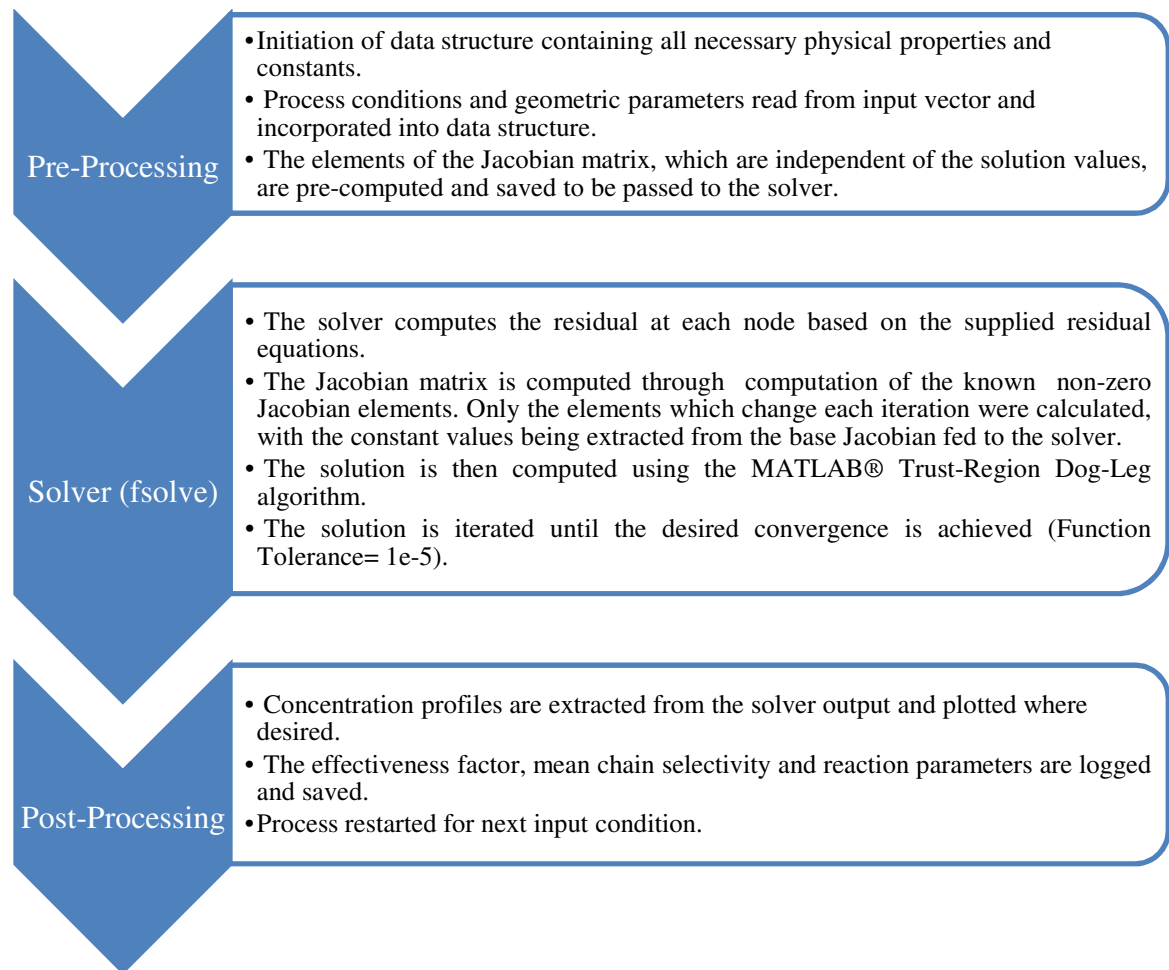


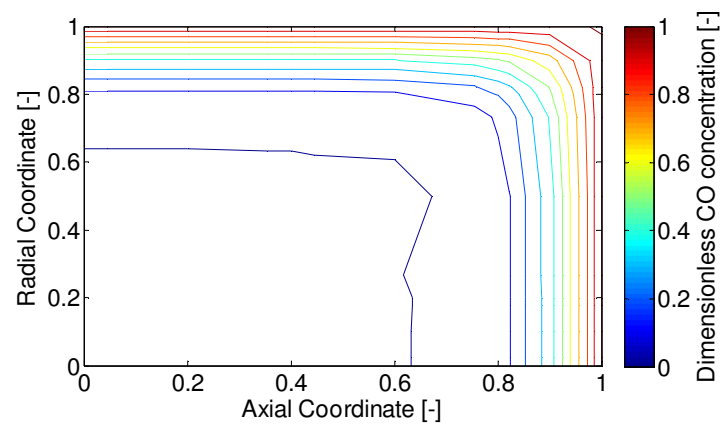
Figure 6.4. A flowsheet of the simulation steps applied in the determination of the concentration and selectivity profiles within the catalyst pellet.

6.4.2. Sensitivities

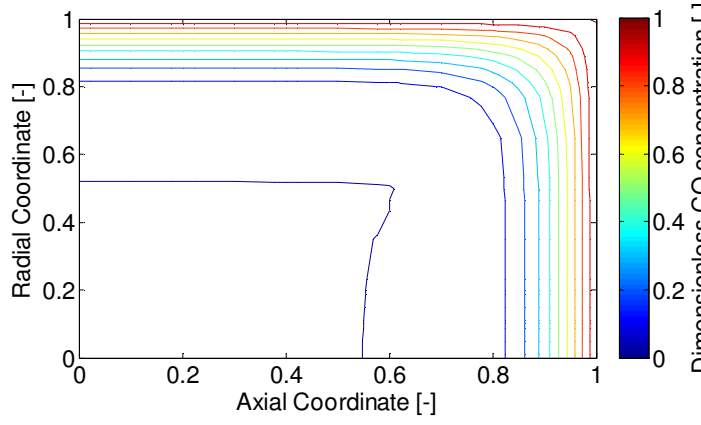
The accurate determination of the concentration profiles and the associated metrics of effectiveness factor and selectivity require a fine mesh of collocation points, such that the solution developed is independent of the mesh spacing, and thus representative of the modelled behaviour, rather than artefacts of the numerical methods. A balance between the number of elements, and thus total number of collocation points, must be found to minimise the computation time and memory usage, whilst maintaining an accurate solution. The number of collocation points per element was maintained at 5, with the number of elements varied to analyse the solution's sensitivity to the mesh spacing.

Figure 6.5 demonstrates the sensitivity of effectiveness factor and the concentration profiles for a number of grids. The concentration gradients and effectiveness factors were found to be invariant to increasing element number above a 12×12 grid. The element sizes were refined to increase the number of elements in the regions of sharpest concentration gradients. For the 2-D simulations displayed in the following sections, a larger grid (30×30) was used to ensure accuracy across the full range of operating conditions and boundary conditions. A typical simulation with 900 elements lasted between 2-5 minutes (Intel *i3* 2.2 GHz processor, 8 GB RAM), depending on the boundary condition.

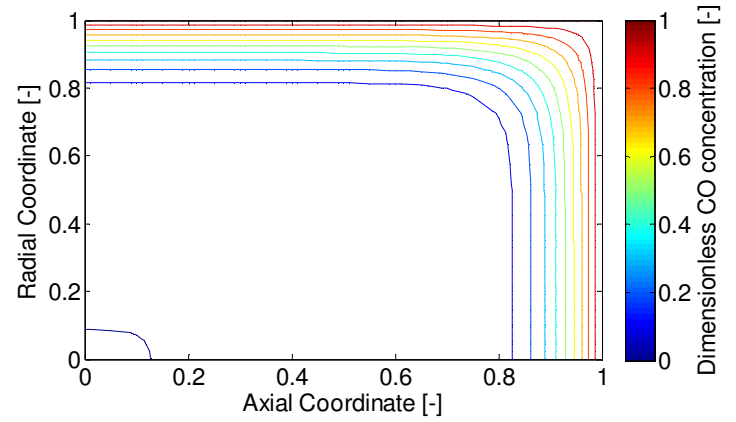
a) NE = 9 (3×3), $\eta=0.650$, $\chi=2.8$ seconds



b) NE = 36 (6×6), $\eta = 0.630$, $\chi = 4.52$ seconds



c) NE = 144 (12×12), $\eta = 0.620$, $\chi = 19.7$ seconds



d) NE = 225 (15×15), $\eta = 0.620$, $\chi = 38.11$ seconds

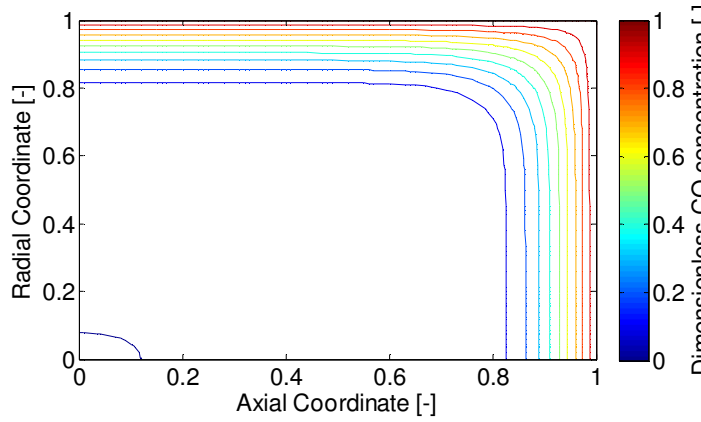


Figure 6.5 Carbon monoxide concentration profiles across the pellet using different numbers of elements (NE). The conditions used are $r_p=1.5$ mm, $L=1.5$ mm $T=220$ °C and $P=10$ bara, $H_2/CO=2$. The calculated effectiveness factor (η) and simulation times (χ) are stated for each simulation. Above 144 elements, the effectiveness factor becomes insensitive to element number.

6.4.3. Validation of 2-D Model

The two-dimensional model was validated by comparing its predictions to analytical solutions for 1-D systems using simple first-order kinetics. The concentration profiles in the axial and radial dimensions were examined for pellets of large radii, such that the axial concentration profile was unaffected by radial contributions, and similarly at large pellet length, such that the radial profiles were unaffected by pellet length. Each profile was found to be in agreement with the analytical solution for a first order reaction in the respective 1-D cases (slab and infinite cylinder). With respect to the effectiveness factors determined for a finite hollow cylinder, the model was run using first-order single reactant kinetics and compared to the analytical solution presented by Wijngaarden *et al.* (1998). The numerical model solution for the simple first-order kinetics agreed well with that predicted by the Wijngaarden *et al.* (1998) analytical model.

6.4.4. Thermal Gradients

As noted in §6.3.1, the pellet was assumed to be isothermal. The observed temperature gradients for a solid cylindrical pellet at typical reaction conditions are shown in Figure 6.6. The observed gradients do not exceed 0.2 K, and the performance parameters (η and α) differed by <0.5% between the isothermal and temperature-dependent simulations. Hence, the simulations used within this chapter were assumed to be isothermal to improve simulation speed. The assumption of isothermality reduces the number of variables to solve for from 3 to 2, reducing memory requirements. The removal of the exponential sensitivity due to the Arrhenius expression reduces the extent of non-linearity in the system, improving simulation stability.

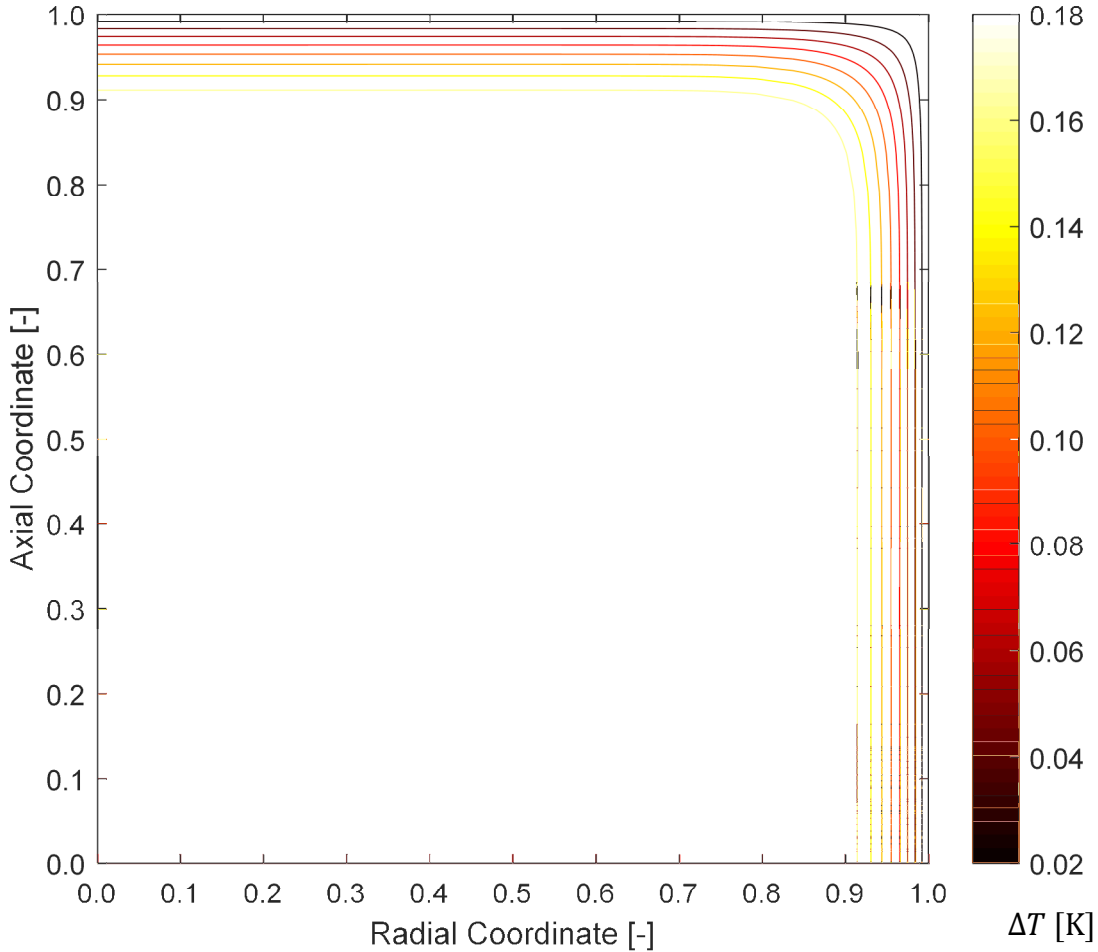


Figure 6.6. Temperature increase between pellet surface and radial location. Gradient shown for a cylindrical pellet ($r = 2$ mm, $L = 4$ mm) at $T = 513$ K, $P = 40$ bar, $H_2/CO = 2$.

6.5. Results: Evaluation of Effectiveness Factor for 1-D and 2-D Geometries.

In order to compare catalyst pellets of different dimensions and forms, the generalised Thiele modulus (Φ) was defined according to the definition of Aris (1957), equation (6.42). The concentration of carbon monoxide was taken to be the limiting reagent.

$$\Phi = \left(\frac{V_p}{S_p} \right) \sqrt{\frac{(-R_{CO})^s}{D_{CO,eff} C_{CO}^s}} \quad (6.42)$$

Here, $\left(\frac{V_p}{S_p} \right)$ represents the characteristic diffusion length, defined as the catalyst particle's volume divided by its external surface area, $-R_{CO}^s$ and C_{CO}^s represent the surface reaction rate of CO and surface concentration of CO respectively, and $D_{CO,eff}$ represents the effective

diffusivity of CO within the catalyst's pores. The effectiveness factor was defined as equation (6.43).

$$\eta = \frac{\int_0^1 \int_{\bar{r}_{in}}^1 \bar{r}(\bar{r}, \bar{z}) \overline{R_{CO}}(\bar{r}, \bar{z}) d\bar{r} d\bar{z}}{\int_0^1 \int_{\bar{r}_{in}}^1 \bar{r} d\bar{r} d\bar{z}} \quad (6.43)$$

The evaluation of effectiveness factor across the different pellet models provided a means to determine the expected error when assuming a 1-D, instead of a 2-D, shape for conditions typically employed in the Fischer-Tropsch process (473-513 K, 10-40 bara). Figure 6.7 compares slab and sphere models at constant temperature and pressure and 3 separate H₂/CO ratios. Both geometries exhibited effectiveness factors greater than one at boundary H₂/CO ratios greater than ~1.25. Under these conditions, the lower diffusivity of CO within the wax relative to hydrogen results in increased intra-particle H₂/CO ratios above that of the boundary value. This increase in H₂/CO ratio causes an increased reaction rate within the particle because the inhibitory action of CO is reduced.

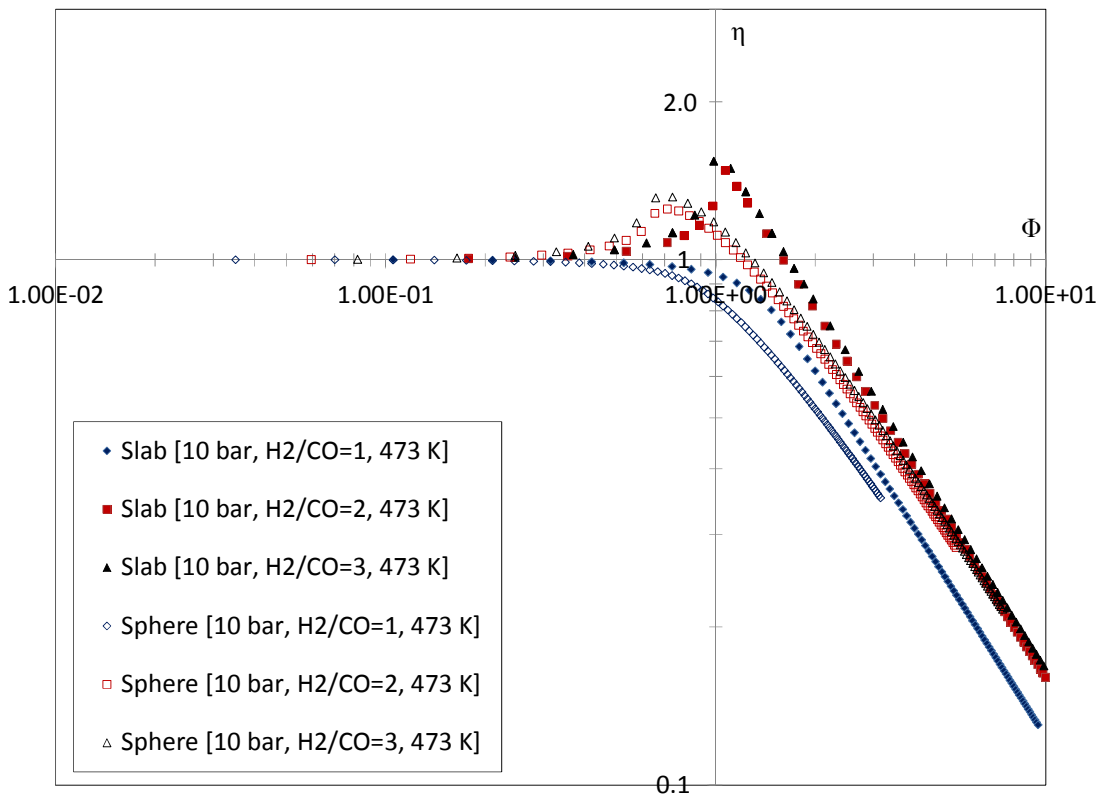


Figure 6.7. Effectiveness factor (η) versus generalised Thiele modulus (Φ) for sphere and slab geometry at $T=473$ K, $P=10$ bar and H₂/CO ratios of 1, 2 and 3.

At a H₂/CO ratio of ~1.1, hydrogen and carbon monoxide are both limiting, with H₂ becoming the limiting reagent below this ratio. The position of the high Thiele asymptote to which the shapes converge is a function of H₂/CO ratio. This variation is due to the expression

of the generalised modulus assuming a pseudo- first order reaction in CO. However, for the Yates and Satterfield (1991) form of kinetics the average reaction order with respect to CO is a function of H₂/CO ratio, and thus depends on the surface boundary condition and the extent of conversion within the pellet.

The influence of the reaction pressure and temperature were characterised for spherical geometry in Figure 6.8. By increasing the reaction pressure, the concentration of CO and H₂ in the Fischer-Tropsch wax increased according to Henry's law. The surface reaction rate however increases to a lesser extent due to the inhibitory influence of CO. Hence, an increase in pressure increases the thickness of the reaction zone, and thus reduces the fraction of 'inert' core within the pellet. The changes in the peak effectiveness factor are due to the form of the kinetics. At high CO concentrations, the rate is almost proportional to H₂/CO ratio. However at low CO concentrations, the magnitude of the rate is proportional to the H₂ concentration, and thus higher H₂ concentrations at the boundary result in greater rates within the pellet as the CO concentration decreases.

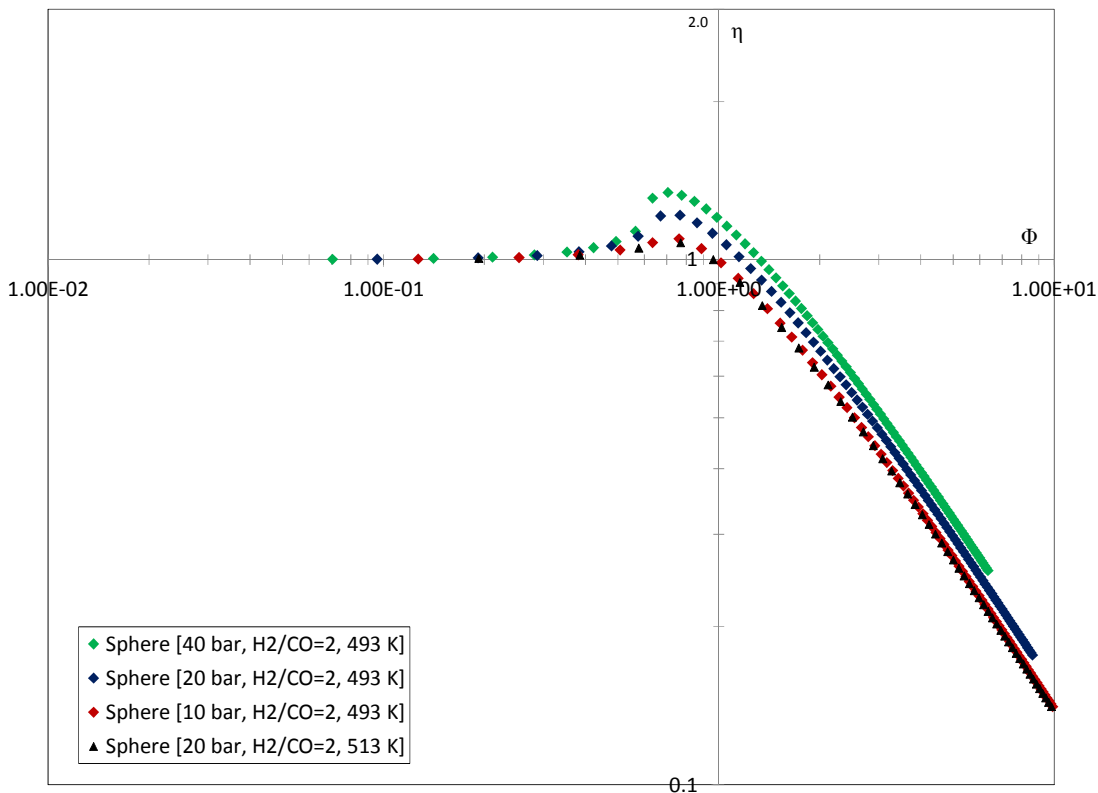


Figure 6.8. Effectiveness factor (η) versus generalised Thiele modulus (Φ) for a sphere under different reaction pressures and temperatures.

The temperature of reaction has been reported in the literature to increase the methane selectivity. The Henry constant for both CO and H₂ has been shown experimentally to decrease with temperature, with the correlation of Marano and Holder (1997a) accounting for this behaviour. Similarly, the influence of decreases in the density of the wax has also been

accounted for using the empirical correlation developed by Marano and Holder (1997b). Overall, the molar concentration of hydrogen and carbon monoxide within the Fischer-Tropsch wax increases with temperature by 1.14% for H₂ and 4.58% for CO between 220°C and 240°C. The form of the effectiveness factor curve appears to change with temperature, with the 513 K curve peaking lower than that of the 493 K curve. The increased solubility of the reactants within the wax phase is accompanied by an increase in methane selectivity, which in turn results in a higher rate of hydrogen consumption. This increased H₂ consumption and increased relative CO solubility appear to result in the reduced magnitude of the peak effectiveness factor in the η -Φ plot.

The peaking of the effectiveness factor due to the increased intra-particle H₂/CO ratio is also accompanied by a decline in the chain growth parameter, α , and thus an increased methane selectivity. The influence of mass transport on the selectivity is further discussed in §6.8.

6.6. Results: Effectiveness Factors for 2-D Hollow Cylindrical Pellets

The two-dimensional mass transport model developed within this chapter was applied to the domain shown in Figure 6.9 to investigate the effect of hollow cylinder dimensions on the effectiveness factor and α parameter. At the inner radius (r_{in}) and the outer radius (r_{out}), the concentration and temperature were assumed to be equal to that of the bulk. The axial boundary conditions were those as employed in the conventional cylinder model.

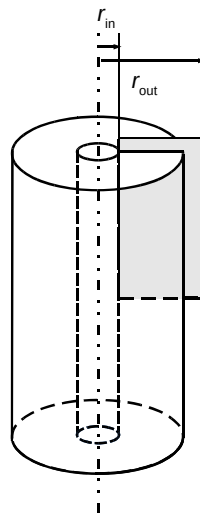


Figure 6.9. Zone of solution for a hollow cylindrical pellet. The concentration and temperature at the inner radius was assumed equal to that of the outer radius.

The patent literature concerning hollow cylindrical pellets suggests dimensional bounds for industrial hollow pellets, with outer radii stated to be between 0.5 and 20 mm and ratios of inner to outer radii between 0.1 and 0.7. A selection of patents related to hollow cylinders and their dimensional ranges are given in Table 6.5.

It is clear that the dimensions of hollow cylinders may vary significantly in both diameter, and aspect ratio. From the patent literature, it appears the length of the pellet varies from 0.5 up to 3.75 times the external diameter. To examine the changes in selectivity and activity with the changes in the dimensions of the pellet, the performance of the catalyst was analysed over the range of conditions summarised in Table 6.6.

Table 6.5. Dimensions of hollow cylindrical pellets in patent literature. A † indicates a value was not explicitly stated.

Diameter [mm]		Length [mm]	Notes	Reference
Internal	External			
3-8	5-12	3-12		US Patent 4382021
1-3	3-6	3-6	1.0-1.5 mm wall thickness	US Patent 4366093
1.8	5	5		US Patent 4740644
1-2	4-6	†	Length of 1.75 to 3.75 external diameter.	US Patent 5166120
2-2.8	4.0-7.0	6.1-6.9	D_{in}/D_{out} ratio of 0.4-0.5	European Patent 1053789 A1
†	0.5-5	†	D_{in}/D_{out} of 0.1-0.4.	European Patent 0428223
†	3-20	†	D_{in}/D_{out} of 0.1-0.7 Length of 0.2 to 2 times external diameter.	US Patent 4656157A

Table 6.6. Simulation conditions for 2-D hollow cylinder model using Yates and Satterfield (1991) kinetics.

Temperature [K]	473, 493, 513
Pressure [bara]	10, 20, 40
H ₂ /CO ratio [-]	1, 2, 3
Outer Radii (r_{out}) [mm]	Variable
Length [mm]	Variable
r_{in}/r_{out} radii ratio, μ [-]	0.2, 0.4, 0.5, 0.6, 0.8

The effectiveness factors for the 2-D hollow cylinder model are shown in Figure 6.10 relative to those of the 1-D slab, 1-D hollow cylinder and sphere models. The points for the 2-D hollow cylinder encompass radius ratios (μ) between 0.2 and 0.8, with length/diameter

ratios (λ) between 0.25 and 4 and outer radii of 1.5, 2.0 and 3.0 mm. The values of the hollow cylinder effectiveness factor are bounded between those of the slab and the sphere at generalised Thiele moduli below ~ 0.75 and above ~ 1.15 . Between these values, the predicted effectiveness factor is greater than both, with the peak values transitioning between that of a sphere and that of a slab.

It is clear that the difference between the 2-D hollow cylinder and a 1-D slab or sphere analogue can be significant, the effectiveness factor being over- or underestimated by the 1-D analogue depending on the value of the generalised Thiele modulus. The evaluation of the effectiveness factor for the 1-D hollow cylinder demonstrates that it is reasonably approximated by a slab of analogous V_p/S_p .

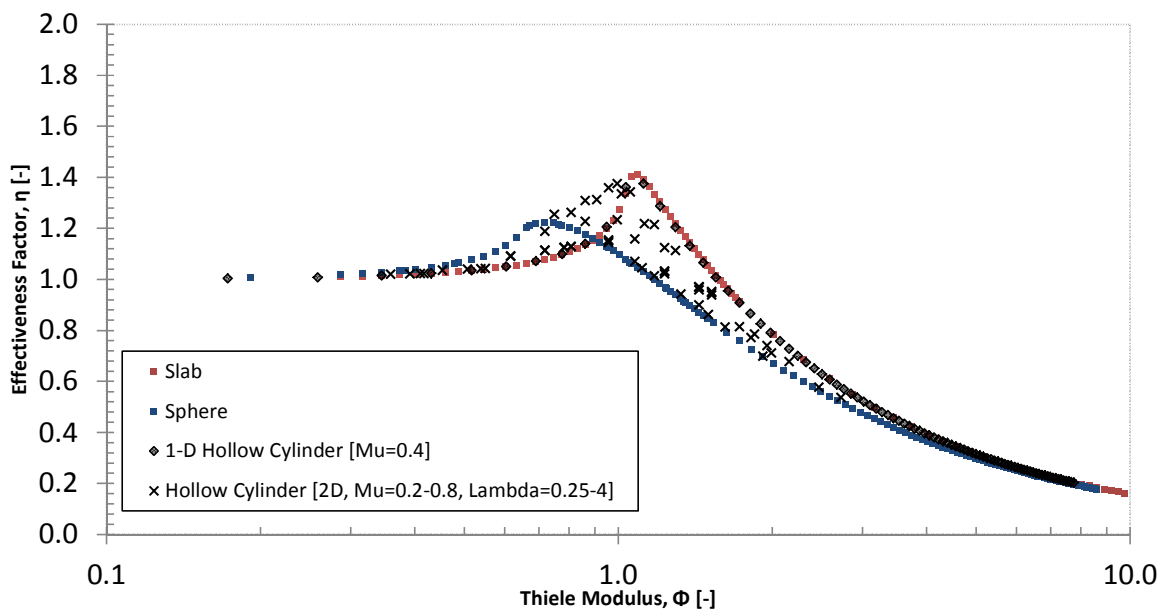


Figure 6.10. Effectiveness factor versus Thiele modulus for the 2-D hollow cylinder, 1-D hollow cylinder, slab and sphere shapes. Simulated reaction conditions of 493 K, 20 bara, $\text{H}_2/\text{CO} = 2$.

It appears that the behaviour of a 1-D hollow cylinder is well approximated by a slab model. Recently, Mandic *et al.* (2017) compared the behaviour of 1-D cylinders, slabs and spheres for the Fischer-Tropsch process, reporting that the hollow cylinder provided an improved effectiveness factor relative to a slab and sphere of similar length scale. However the comparison made in their study compared hollow cylinders and slab of the same thickness, and thus different V_p/S_p ratios, since the infinite hollow cylinder has two faces exposed to the reactant gases, rather than the single face in their 1-D slab model.

Figure 6.11 compares the differences between the assumption of a 1-D cylindrical geometry and the 2-D geometry for the hollow cylinder. Using the generalised Thiele modulus, as defined by equation (6.42), the effectiveness factors calculated for a 1-D hollow

cylinder almost overlap one another for radius ratios (μ) of 0.4 and 0.8. However, it is clear for practical hollow cylindrical pellets that the assumption of 1-D geometry may lead to significant error. The effectiveness factors for the 1-D and 2-D geometry pellets trend towards the same value at Thiele moduli above 3, however between Thiele moduli of ~0.6 and ~2.5, significant differences in the estimated effectiveness factor are apparent.

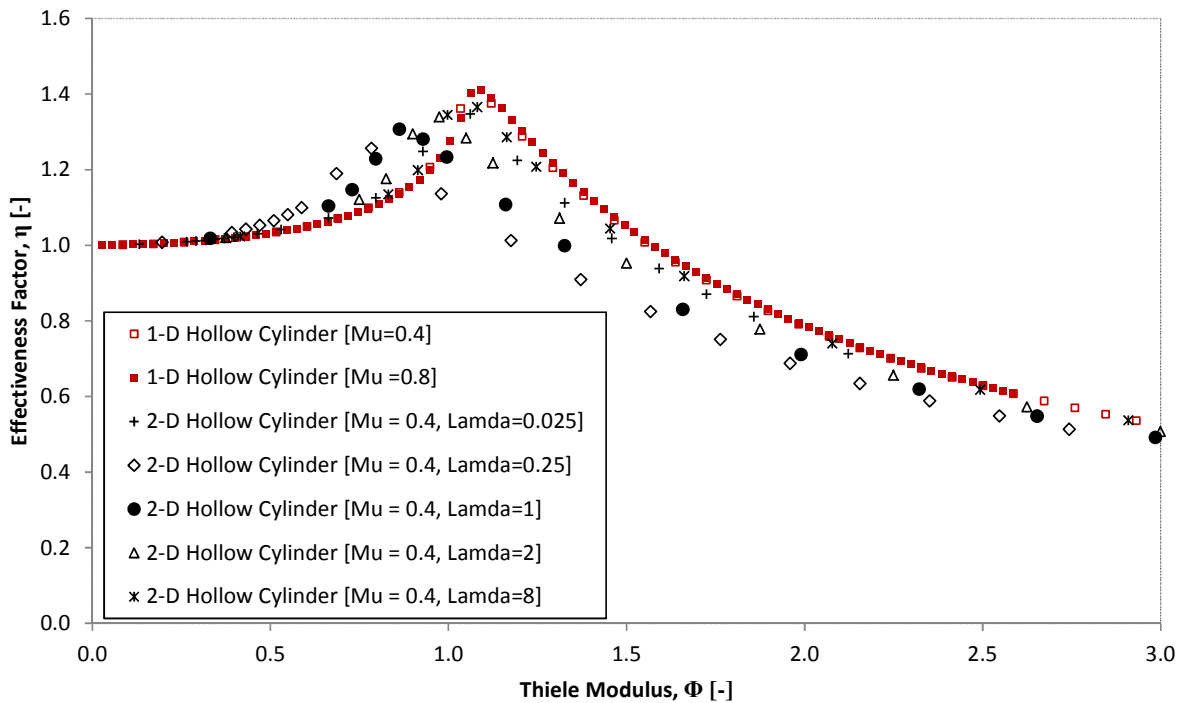


Figure 6.11. Effectiveness factor versus Thiele modulus for the hollow cylinder, slab and sphere shapes. Simulated reaction conditions of 493 K, 20 bara, H₂/CO ratio 2.

The influence of aspect ratio (λ), defined as length divided by the outer diameter, is clearly demonstrated in Figure 6.11. At both high and low aspect ratios the behaviour trends towards that of a slab/infinite cylinder. In the case of hollow cylinders of practicable aspect ratios (~1-2), the position of the peak in effectiveness factor is shifted to lower Thiele and shows a lower magnitude. The difference in hollow cylinder effectiveness factor through comparison of $\eta_{1D}/\eta_{2D,\lambda=1}$ ranged from -18% to 13% under the reaction conditions examined. The greatest deviation from the 1-D hollow cylinder model occurs where the pellet length is of comparable size to the radial thickness, $(1-\mu)R_{out}$. Under these conditions the ring-form catalyst behaviour may be more closely approximated by a sphere model.

For evaluation of pellets in fixed-bed reactor models, the means of comparison may be equivalent catalyst mass. In order to compare catalysts of similar mass, a series of equivalent (solid) volume catalysts were evaluated using the 2-D hollow cylinder model. Effectiveness factors for a hollow cylindrical, solid cylindrical and spherical particle at 5 equivalent sphere diameters are given in Table 6.7.

Table 6.7. Comparison of effectiveness factors at set sphere equivalent diameter (10 bar, 493 K, Yates and Satterfield (1991) kinetics).

d_{SE} [mm]	$\eta_{Hollow,2D}^{\dagger,\ddagger}$ [-]	$\eta_{Hollow,1D}^{\ddagger}$ [-]	$\eta_{Cylinder}^{\dagger}$ [-]	η_{Sphere} [-]	$\eta_{Sphere,Brunner}$ [Equation (6.44)]
0.5	1.00	1.01	1.01	1.01	0.98
1.0	1.01	1.08	1.05	1.08	0.94
2.0	1.06	0.85	0.95	0.86	0.80
3.0	1.11	0.61	0.72	0.63	0.65
5.0	0.73	0.38	0.48	0.41	0.44

\dagger Aspect ratio of 2, \ddagger Inner Radius/Outer Radius = 0.4.

It is apparent that comparisons of particles of equivalent volume might lead to significant differences in the effectiveness factor. By comparing particles of equivalent masses, the diffusion lengths differ between the particles, with the 2-D hollow cylinder showing a superior activity in comparison to the other shapes due to its greater surface area per unit volume. The 1-D hollow cylinder model however simulates particularly poor performance due to the neglect of the ends of the particle, with the equivalent volume comparison yielding a larger V_P/S_P ratio than the 2-D model.

The hollow cylinder shows the best performance for a given mass of catalyst material, however further investigation would be required in order to evaluate performance in an industrial fixed bed reactor. Changes in shape of the pellet may alter the catalyst bed's voidage, which will then impact the pressure drop across the bed itself. Changes may also affect the required reactor volume for a given mass of catalyst, and thus impact the associated capital costs.

6.7. Comparison with Simplified Effectiveness Factor Models

Fixed-bed reactor studies, *e.g.* Brunner *et al.* (2015), may require simplified models to evaluate catalyst effectiveness factor. The use of analytical models provides a means to estimate catalyst effectiveness factor without excessive computation. In their model of a 1-D fixed-bed, Brunner *et al.* (2015) compared uniformly active spheres, cylinders, trilobes and hollow cylinders on the basis of equivalent catalyst masses. In order to characterise the catalyst's effectiveness factor, the authors employed an n^{th} order Thiele modulus description. This approach for a slab, consisted of calculating the catalyst effectiveness factors using

equations (6.44) and (6.45).

$$\Phi_{n^{th}} = L \sqrt{\frac{(-R_{CO}^s)(n+1)(C_{CO}^s)^n}{2D_{CO,eff}C_{CO}^s}} \quad (6.44)$$

$$\eta = \frac{\tanh(\Phi)}{\Phi} \quad (6.45)$$

Here L is the diffusion length scale and n is a modifier to approximate non-first order behaviour, taken as -0.1 by Brunner *et al.* (2015) for their kinetics. The n^{th} order Thiele method was compared with the 2-D hollow pellet model to evaluate the differences in effectiveness factor between the methods, with the comparison shown in Figure 6.12 for $\Phi_{n^{th}}$ values between ~0.2 and ~7. For the Yates and Satterfield (1991) kinetics under the considered conditions, $n = -0.18$ was found to provide the best agreement at high Thiele values.

The validity of the n^{th} order slab approximation was found to provide an approximation of the kinetic behaviour for Langmuir-Hinshelwood expressions of the Yates and Satterfield form. The degree of error in the effectiveness factor for the sphere varies across the equivalent pellet volumes, with the greatest error occurring where the predicted effectiveness factor is greater than 1. Significant differences in effectiveness factor between the n^{th} order slab model and the 2-D hollow pellet model were noted for values of n^{th} order Thiele modulus between ~0.5 and ~1.5. It appears for pellet effectiveness factors >0.6 , the magnitude of error between the models may exceed 5%, with the greatest error reaching 30.8% based on $\eta_{n^{th}}/\eta_{2D}$. Accurate prediction further required fitting of the n parameter to suit the kinetics at a high Φ value.

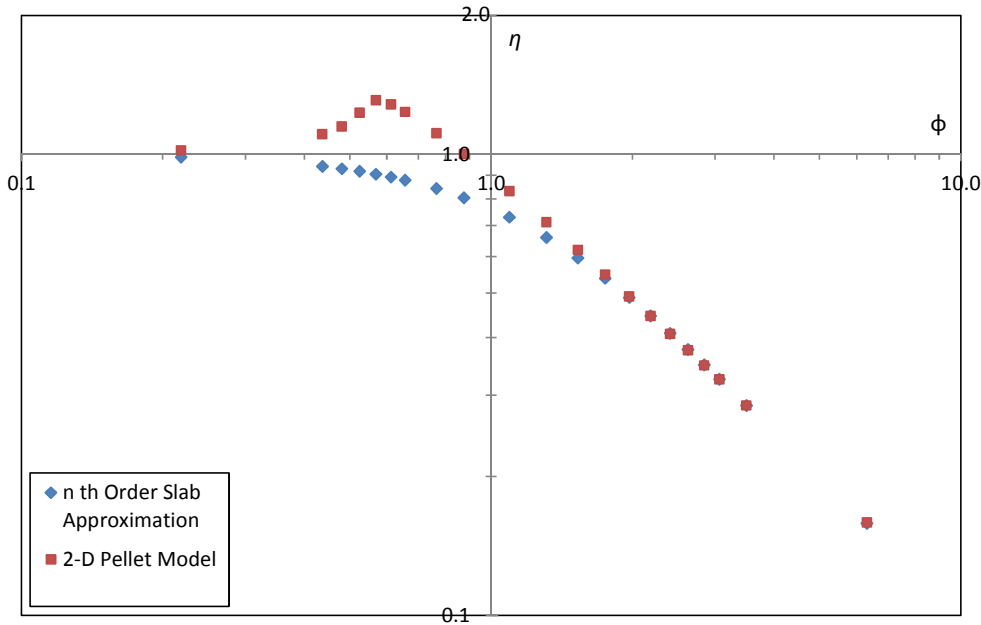


Figure 6.12. Comparison of the 2-D Hollow Cylinder against 1-D n -th order slab approximation. Simulation conditions $T=493$ K, $P=20$ bar, H_2/CO ratio = 2, $\mu=0.4$, $\lambda=1$.

6.8. Evaluation of α under Different Geometries

The alpha model of Vervloet *et al.* (2012) was used to examine the influence of the pellet shape on selectivity towards higher value hydrocarbons. The reaction-weighted average of the chain growth (α) parameter for a hollow cylinder was determined to evaluate the performance of the 2-D pellet using the integral in (6.46). Analogous reaction weighted integrals for slab, sphere and 1-D hollow cylinder geometries, equations (6.47)-(6.49), were also calculated for the purpose of comparison.

$$\alpha_{avg,2D\ Cylinder} = \frac{\int_0^1 \int_{\bar{r}_{in}}^1 \bar{r} \propto (\bar{r}, \bar{z}) \overline{R_{CO}}(\bar{r}, \bar{z}) d\bar{r} d\bar{z}}{\int_0^1 \int_{\bar{r}_{in}}^1 \bar{r} \overline{R_{CO}}(\bar{r}, \bar{z}) d\bar{r} d\bar{z}} \quad (6.46)$$

$$\alpha_{avg,Slab} = \frac{\int_0^1 \propto (\bar{z}) \overline{R_{CO}}(\bar{z}) d\bar{z}}{\int_0^1 \overline{R_{CO}}(\bar{z}) d\bar{z}} \quad (6.47)$$

$$\alpha_{avg,Sphere} = \frac{\int_0^1 \bar{r}^2 \propto (\bar{r}) \overline{R_{CO}}(\bar{r}) d\bar{r}}{\int_0^1 \bar{r}^2 \overline{R_{CO}}(\bar{r}) d\bar{r}} \quad (6.48)$$

$$\alpha_{avg,1D\ Cylinder} = \frac{\int_{\bar{r}_{in}}^1 \bar{r} \propto (\bar{r}, \bar{z}) \overline{R_{CO}}(\bar{r}, \bar{z}) d\bar{r}}{\int_{\bar{r}_{in}}^1 \bar{r} \overline{R_{CO}}(\bar{r}, \bar{z}) d\bar{r}} \quad (6.49)$$

Figure 6.13 compares the reaction-weighted α for slab, sphere and 2-D hollow cylinders. The α values for the different geometries show a similar behaviour to the

effectiveness factor plots. At low values of Φ , below 0.5, the selectivity essentially equals that at surface conditions. Above this, the selectivity begins to decrease due to increasing intra-particle mass transfer resistances. The intra-particle H₂/CO ratios increase, leading to a reduction in the overall alpha. As Φ further increases, the α value tends to a steady average.

The selectivity for the 2-D hollow cylinder is bounded by the behaviour of the sphere below $\Phi = 0.75$ and above $\Phi = 1.15$, with the hollow cylinder displaying the lowest α values in the transition region. The lower average α values are coincident with the Thiele modulus range in which the effectiveness factor peaks. Significant differences between the average α parameter are apparent at a fixed Thiele modulus, with a maximum difference of ~32% between the hollow cylinder and analogous slab at fixed Thiele modulus.

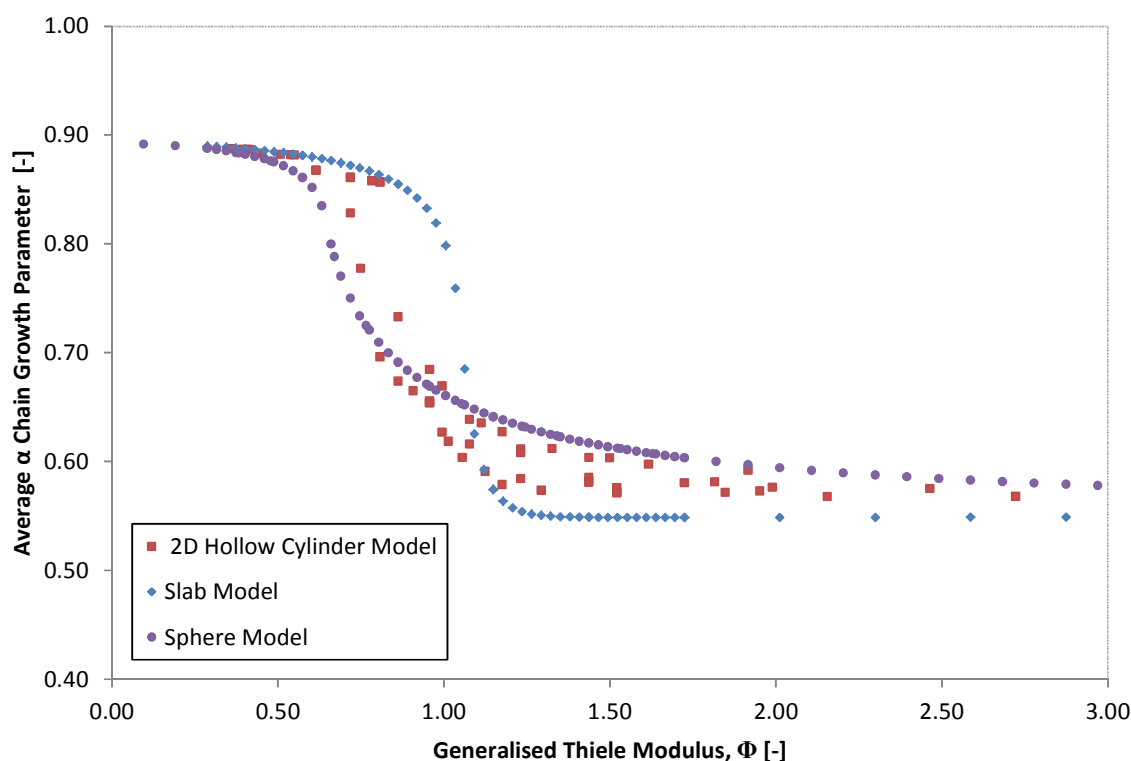


Figure 6.13. Comparison reaction-weighted chain growth parameter for sphere, slab and 2D hollow cylinder models (20 bar, 493 K, H₂/CO=2). For the hollow cylinder, r_{out}=1.5, 2.0, 3.0 mm, μ = 0.2-0.8, λ = 0.25-3.

Figure 6.14 displays the influence of aspect ratio on the plot of chain growth parameter *versus* the generalised Thiele modulus. Further results points were simulated at aspect ratios between 0.025 to 8 for generalised Thiele between 0 and 3. The selectivity behaviour of the 2-D hollow cylinder shifts between slab behaviour (or 1-D hollow cylinder) and sphere behaviour. The hollow cylinder displays slab-like behaviour at both high (1-D cylinder) and low aspect (flat disk) ratio ($\lambda=L/D_{out}$), with varying degrees of intermediate behaviour between these two limits. The greatest deviation from the slab behaviour occurs as

the length of the hollow cylinder tends towards values $\approx (1-\mu)r_{\text{out}}$, and thus having a square toroidal shape. Under these conditions, the behaviour tends towards that of a sphere.

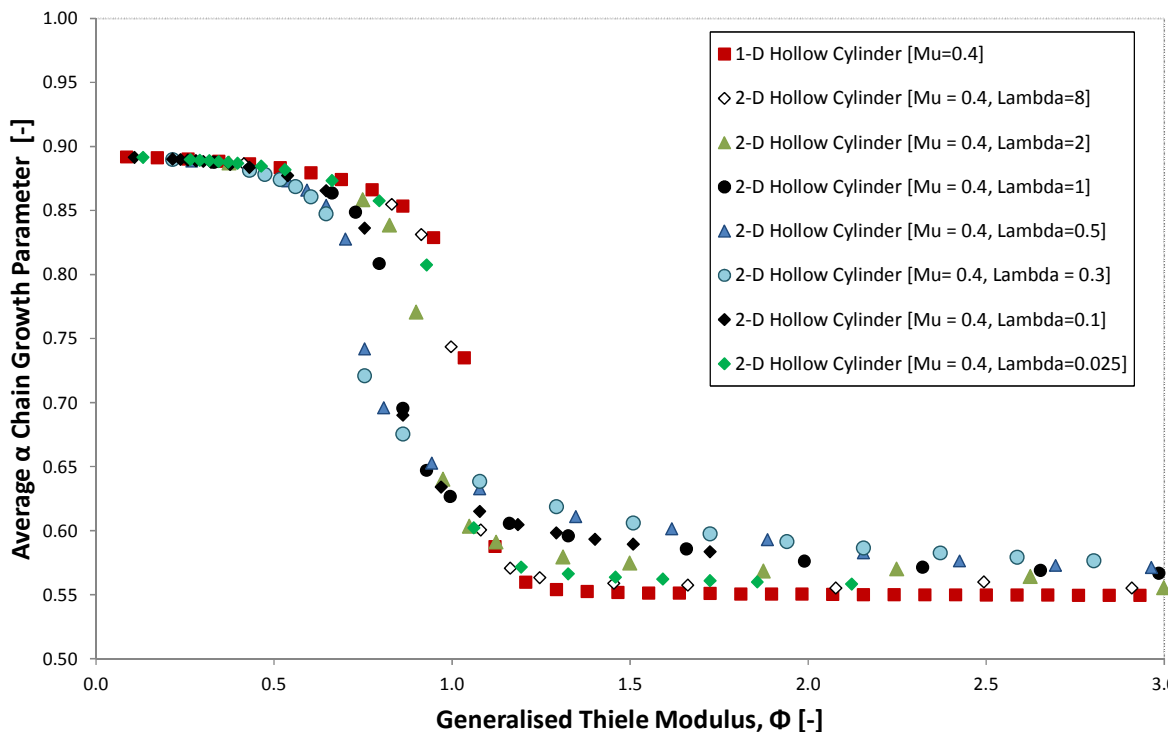


Figure 6.14. Influence of hollow cylinder aspect ratio on α parameter. Reaction conditions T=493 K, P= 20 bar, H₂/CO ratio=2. Thiele modulus varied through length/radius modification.

Table 6.8 shows the reaction-weighted average alpha parameter for solid ($\lambda = 2$) and hollow ($\mu = 0.4, \lambda = 2$) cylinders at equivalent volumes. It is clear that the sphere provides the lowest α value, and thus the highest selectivity towards undesirable methane production. As the volume of the pellet increases, the degree of mass transfer increases, leading to higher intra-particle H₂/CO ratios, and thus greater methane selectivity. The hollow cylinder however provides a greater efficiency in use of catalyst mass. This trend mirrors that noted for the effectiveness factor, with the lowered diffusion lengths for the solid and hollow cylinders relative to the sphere yielding reduced mass transfer limitations and thus less significant changes to the intra-particle H₂/CO ratio.

Table 6.8 Comparison of reaction-weighted selectivities at fixed equivalent sphere diameters (d_{SE})

d_{SE} [mm]	Sphere	Solid Cylinder †	Hollow Cylinder † ‡
1.36	0.81	0.87	0.88
3.00	0.62	0.64	0.84
3.54	0.60	0.62	0.64
3.80	0.60	0.61	0.60
5.44	0.58	0.58	0.57

† Aspect ratio of 2, ‡ Inner Radius/Outer Radius = 0.4.

The decline in the selectivity parameter commences at a Thiele modulus of ~0.5. This corresponds to the point at which the effectiveness factor begins to rise. Hence, catalyst operating at the peak effectiveness factor will display a much poorer selectivity for heavy hydrocarbons than a kinetically controlled system. This behaviour is expected since the rise in effectiveness factor is due to an increase in intra-pellet H₂/CO ratio, and thus reduced inhibition by CO. The increased intra-pellet H₂/CO ratios also results in a lighter product distribution, favouring methane.

6.9. Discussion

The influence of shape on the observed behaviour depends significantly on the intrinsic kinetics. At low rates, and thus low Thiele moduli, the reaction is kinetically controlled and uninfluenced by the particle's shape. At high reaction rates, and thus high Φ values, the reaction becomes limited to a thin surface layer in the particle, and thus depends mainly on the surface area of the particle. The model developed in this Dissertation has demonstrated that at intermediate Φ values, the Fischer-Tropsch reactions effectiveness factor and selectivity may be significantly influenced by shape, and the evaluation of simpler one-dimensional models has highlighted the cases where the catalyst performance is insufficiently described.

The form of the Langmuir-Hinshelwood kinetics, in combination with the selectivity equation of Vervloet *et al.* (2012), gives rise to effectiveness factors > 1, with differences between the particle shapes most prominent between generalised Thiele moduli of ~0.5 and ~1.5. The intrinsic kinetics available in the literature for the Fischer-Tropsch process have been reported over a significant range, with rates of CO consumption spanning orders of

magnitude from 0.1 to 10s of mmol/kg_{cat} s, *e.g.* Bruce *et al.* (1995), Keyser *et al.* (2000), Atashi *et al.* (2012), Lögdberg *et al.* (2011). The magnitude of the value depends on the catalyst formulation, conversion, pressure, H₂/CO ratio and with a significant dependence on temperature. The Yates and Satterfield (1991) kinetic model selected yielded intrinsic rates consistent within this range, with rates of ~0.2 - 5.3 mmol/kg_{cat} s for the modelled conditions.

Due to the exothermic nature of the reaction, and the larger reactor tube dimensions in industrial reactors, operation of catalysts with the highest intrinsic activities may lead to undesirable temperature gradients and the potential for runaway reaction. Indeed, the fixed-bed modelling study of Jess and Kern (2009) simulated the temperature profiles within a multi-tubular reactor for 2.7 mm diameter cobalt catalyst cylinders within a 46 mm diameter tube. The authors predicted that exothermic runaway could occur where the reactor inlet and wall cooling temperatures were both 215°C, which corresponded to an intrinsic reaction rate at the inlet of ~3.2 mmol/kg_{cat} s for their kinetic model.

The performance of the geometries simulated were determined under an isothermal pellet assumption to reduce the computational requirements. Under the simulated conditions, the assumption was determined to be reasonable, in agreement with one-dimensional studies. The boundary conditions assumed a fixed surface and thus pellet temperature, consistent with previous modelling studies, *e.g.* Vervloet *et al.* (2012), Gardezi and Joseph (2015). Within a fixed-bed, the external temperature of a pellet will depend on its position within its bed, the diameter of the tube, the diameter of the pellet, and the heat transfer coefficients between the wall, coolant and pellets. Since the temperature gradients within the pellet were not noted to be significant, the pellet temperature was considered constant. A fixed surface temperature was necessary to avoid the need for fixed-bed modelling and to allow clearer comparison of the behaviour of different pellet geometries. The lack of significant thermal gradients within the simulated pellet suggest this is reasonable, however integration of the pellet model into a fixed-bed model may require consideration of reactor-scale temperature gradients.

The model assumed that the pores are entirely and uniformly filled with wax. The wax within the pores is generated internally at the catalyst sites and it is likely that removal of long chain hydrocarbons from within the pore network will be frustrated by mass transport limitations. The assumption of filled pores has been applied in prior pellet models, with Pohlman and Jess (2016) recently investigating the degree of filling within Fischer-Tropsch pellets experimentally. Their examination of pore filling found carbon species to be deposited evenly throughout the pellet, in a contrast to the core-shell approach adopted by Gardezi and Joseph (2015) to model partially filled particles. Pohlman and Jess (2016) determined the degree of filling *via* thermogravimetric analysis of used catalyst particles, reporting a filling

degree of 1 (100%) at 200°C, with the degree subsequently decreasing with temperature. Pohlman and Jess (2016) found that a homogenous approach adequately described the mass transfer phenomena within partially-filled pellets, determining the effective diffusivity through combination of gas and liquid phase diffusivities in proportions determined by the experimentally-determined liquid filled fraction. In this Dissertation, a fully-filled particle was assumed, and whilst this condition may not hold true under certain operating conditions, with the pore filling degree dependent on temperature, liquid composition and pore size, the work of Pohlman and Jess (2016) demonstrates that a homogenous approach can provide agreement with experimental results. Hence the conclusions on the influence of pellet shape developed within this chapter remain applicable, and may be extended to partially-filled pellets by modifying the effective diffusivity, and thus the generalised Thiele modulus.

The extent of mass transfer limitation observed within a Fischer-Tropsch pellet of practical scale (\sim millimetre) depends significantly on the selected catalyst activity. By using a generalised Thiele modulus, the model developed permits evaluation of the influence of shape on the observed selectivity and effectiveness. It is evident the catalyst performance is sensitive to shape at Thiele moduli between 0.5 and 3, or effectiveness factors greater than ~ 0.55 . Comparing different geometries at equivalent V_p/S_p , the selectivity for the hollow cylinder was noted to reach values below that of the slab or sphere geometry between Thiele values of 0.75-1.15. Despite the region indicating lower selectivity, hollow cylinders compared to spherical pellets of equivalent volume demonstrate improved selectivity, which may be attributed to their lower V_p/S_p value at equivalent volume.

Other pellet-scale investigations have neglected the axial dimension in their considerations of hollow cylindrical pellets. However it has been demonstrated here to have a noticeable influence on catalyst performance at practical aspect ratios. Mandic *et al.* (2017) considered an infinite hollow cylinder, employing a simplified reaction scheme with fixed H₂/CO stoichiometry, modelling methane selectivity through consideration of a secondary reaction path solely for methane formation. The authors comparison of slab, spherical egg-shell and infinite hollow cylinders at fixed thickness led them to conclude that diffusional resistance decreased in the order hollow cylinder<egg-shell sphere<slab, with the difference attributed to the changes in diffusional length (V_p/S_p). The present research has shown that the 1-D hollow cylinder model appears well approximated by the slab assumption at equivalent V_p/S_p , however consideration of the axial dimension is necessary at aspect ratios below 8 for an inner/outer radius ratio of 0.4. The greatest deviation from slab behaviour occurred where the radial and axial length scales were comparable, with catalyst of square toroidal form behaving more similarly to the spherical particle model.

Shaped extrudates and hollow cylinders have been simulated in the literature to show superior fixed-bed performance in comparison to spherical particles in terms of both pressure drop and catalyst mass requirements. Here, the effectiveness factors and selectivities of different geometries have been evaluated in detail at both fixed volume to surface area ratio and fixed mass. At constant catalyst mass, the hollow cylindrical pellets provide significantly greater surface area than solid cylinders or spheres of equivalent mass, and thus a reduced effective diffusion length leading to an improved effectiveness factor and selectivity.

Due to the computational complexity of pellet scale models, literature investigations have adopted a number of simplifying assumptions when investigating the influence of shape on fixed-bed reactors, *e.g.* Nanduri and Mills (2015) assumed purely radial diffusion in their multi-hole pellet model, and Brunner *et al.* (2015) assumed a simplified n^{th} order effectiveness factor model. Whilst the scope of this chapter does not extend to multi-hole pellets, it has been demonstrated that the neglect of axial contributions for a single-hole pellet may result in significant error under certain conditions. In order to evaluate the validity of a simplified n^{th} order effectiveness factor model, a comparison was developed between the output from the 2-D model and the analytical approach. It was found to provide reasonable agreement (within 5%) to the detailed models at Thiele moduli below 0.5 and above 2, provided the effective order of the modulus was fitted to the pellet models at high Thiele values. The use of a simplified model significantly reduces the complexity and duration of calculation, however, as shown earlier; the asymptote for the η - Φ plot shifts with reaction conditions, and thus the effective reaction order will change with conversion along the length of the reactor. Hence, assuming a constant reaction order across the length of a reactor could well result in significant error.

Industrially, the operation of the reactor in the $\eta > 1$ peak region would be unfavourable. Despite the increased reaction rate, the changes in the intraparticle H₂/CO ratio decrease the yield of the valuable heavier products, and result in the production of greater quantities of methane. Similarly operation at a high Thiele modulus leads to excessive methane production and inefficient utilisation of the catalyst material. In order to avoid extensive mass transport issues whilst maintaining acceptable selectivities, an egg-shell distribution may need to be adopted. However, as with alterations to the catalyst shape, detailed consideration would be required to balance the overall catalyst and thus reactor volume with any gains in selectivity and effectiveness from the egg shell distribution.

6.10. Conclusions

In this chapter a reaction-diffusion model for a 2-D hollow cylinder has been developed. The model has been analysed across a range of Thiele moduli and the extents of error in both effectiveness factor and α parameter have been quantified relative to one-dimensional sphere and slab geometries. The application of 2-D modelling was noted to result in errors between slab, sphere and 1-D hollow cylinder geometries between Thiele moduli of ~0.25 to ~3.

Effectiveness factors were bounded by those of sphere and slab above and below Thiele moduli of ~0.75 and ~1.15 respectively for the conditions examined, with the effectiveness factors exceeding those of both sphere and slab models between these moduli. Concurrently, the α parameters between these values were lower than both those of sphere and slab geometry, and thus under these conditions hollow cylinders provide the greatest methane selectivity.

The model was evaluated against a simplified n^{th} order effectiveness factor model employed in fixed-bed modelling and found to differ over the Thiele range ~0.5 to ~1.5, with the greatest errors arising where the effectiveness factor exceeded 1. The use of the simplified model further required fitting at high Thiele in order to provide a reasonable representation of catalyst behaviour. However, the effective order of the reaction was noted to be dependent on the reaction conditions and thus selection of an appropriate reaction order represents a further source of error in fixed-bed modelling where the surface conditions of a pellet are a function of bed-length. A comparison of the hollow cylindrical pellets against spheres of equivalent volume demonstrated the hollow cylinder provided improved performance, with greater effectiveness factors and selectivities due to the lowered diffusion lengths for the hollow cylindrical geometry. In the context of industrial operation, it was noted the $\eta > 1$ region was not favourable for the production of valuable heavy hydrocarbons, with the product distribution shifting towards methane as the reaction became diffusion limited.

7 Conclusions

This Dissertation has examined the rates of methanation of CO₂ on both a Co/ZrO₂ catalyst and a Ni/γ-Al₂O₃ catalyst. These reactions have an important role in the production of synthetic fuels, with the methanation reaction providing a means to generate natural gas from captured carbon dioxide or that derived from biomass *via* combustion or gasification. Synthetic natural gas has further been highlighted as an efficient means of storing renewable energy and may be used in the existing natural gas distribution and storage networks. The methanation reaction was examined using a nickel catalyst under batch conditions at temperatures between 443 K and 483 K, pressures up to 16 bar, and initial H₂/CO₂ ratios between ~1.1 and ~5.5. The kinetics of the reaction in the batch reactor were compared to experimental results obtained under differential conditions at steady state within a fixed-bed reactor. A second study examined the methanation behaviour of a Co/ZrO₂ catalyst within the fixed-bed reactor under differential reaction conditions. Aside from natural gas, liquid fuels constitute a significant proportion of global fossil fuel demands, and this Dissertation has examined the influence of catalyst shape on the rate and selectivity of the Fischer-Tropsch process.

The apparatus used for batch and continuous reaction was described in Chapter 2. The use of the Carberry spinning basket batch reactor and the fixed-bed (BTRS) reactor allowed for the investigation of the CO₂ methanation reaction at both high and low conversions. The pressurised fixed-bed reactor, commissioned during this project, was applied as a means of comparing the reaction under transient and steady state reaction conditions. Prior to this Dissertation, no CO₂ methanation study has sought to examine and compare the reaction within both types of reactor system.

The two catalysts used for methanation studies were developed and characterised in Chapter 3. The 12 wt% Ni/γ-Al₂O₃ catalyst and the 4.5 wt% Co/ZrO₂ were both made by incipient wetness impregnation of an Al₂O₃ and a ZrO₂ support with nickel and cobalt nitrate solutions respectively. The impregnated γ-Al₂O₃ and ZrO₂ supports were then calcined and reduced to activate the materials. In the case of the nickel material, a passivation and re-reduction step was required to obtain a material of sufficient activity. The catalytic materials and their supports were examined for their structural properties using gas adsorption analysis and XRD, with the reducibility of the materials probed using temperature programmed reduction studies. In the case of the nickel catalyst, the reduction and passivation process was found to produce a metallic nickel catalyst upon reduction at 250°C, a requirement for use

within the Carberry batch reactor. The catalytic activity was compared to the material developed by Lim (2014) and was found to have a lower activity upon testing within the Carberry batch reactor. Comparison between the rate of mass loss under thermogravimetric analysis and the TPR profiles revealed significant differences in the peak positions despite an identical ramp rate, and highlighted the sensitivity of the catalyst reduction to the traces of oxygen present in the thermogravimetric analyser.

The Co/ZrO₂ catalyst was characterised similarly. Gas adsorption analysis characterised the changes in the pore structure of the support with calcination temperature. The preparation conditions finally used were noted to decrease slightly the pore surface area; however, significant losses were avoided by selecting 450°C as the calcination temperature. The cobalt loading of the catalyst was confirmed using thermogravimetric analysis, with the reducibility of the material observed to be influenced, similar to nickel catalyst, by the traces of oxygen present within the analyser. The reduction of the Co₃O₄ phase under TPR conditions was observed to rapidly occur about 250°C; however, in the TGA, some Co₃O₄ was thought to remain. The X-ray diffraction analysis confirmed the support was solely the tetragonal phase of zirconia; however the cobalt phase was not identifiable at the low loading used in the catalyst.

In Chapter 4, the methanation of CO₂ was investigated experimentally over a wide range of partial pressures of reactants for the 12 wt% Ni/γ-Al₂O₃ within both the gradientless, Carberry reactor operated in batch mode and the pressurised fixed-bed reactor operating at steady state. The behaviour observed in the batch reactor indicated that the rate increased with increasing partial pressures of H₂ at low H₂ partial pressures. However, the rate of reaction was found to be insensitive to changes in the partial pressures of H₂ and CO₂ at higher partial pressures. The fixed-bed reactor behaviour exhibited positive order behaviour in both H₂ and CO₂ with the core differences between the fixed-bed and batch reactor systems noted to be the differences in water partial pressure and conversion. By quantifying the reaction rates, experimental measurements were modelled with different kinetic equations. The expression derived from the batch results appeared consistent with the proposed mechanism of Lim (2014), in which adsorbed CO₂ dissociated to CO and O surface species, where the rate-limiting step was the subsequent dissociation of adsorbed CO. The ability of this expression to predict the fixed-bed results was then explored and this comparison noted that the kinetic expressions did not optimally represent the results from the fixed-bed experiments, with a C hydrogenation rate-limiting step providing the lowest error descriptor at differential conversion.

The research has indicated a difference in the kinetics of methanation on Ni/ γ -Al₂O₃ between the fixed-bed and Carberry reactors, and suggests that a Langmuir approach using a single rate-determining step might not be representative over a full range of conversions. Mass transfer phenomena were eliminated as a possible cause and the semi-empirical nature of the Langmuir-Hinshelwood description was ascribed as a potential reason for the discrepancy. It was noted that the quality of the fit of the Langmuir expression might be mathematical in basis rather than mechanistic, with the Langmuir approach an oversimplification of the complex reaction set.

In Chapter 5, the kinetics of methane formation were studied over the Co/ZrO₂ catalyst across a range of reactant partial pressures, total pressures between 5 and 15 barg, and temperatures between 433 K and 503 K. The rate of methanation on the Co/ZrO₂ catalyst displayed sensitivity to both hydrogen partial pressure and temperature, with the methanation rate increasing with both. The rate was noted to be very weakly dependent on carbon dioxide, with a near zero reaction order at the conditions investigated. In comparison with the Ni/ γ -Al₂O₃ catalyst, the Co/ZrO₂ catalyst displayed similar kinetics, with fair agreement between the hydrogen partial pressure dependences and apparent activation energies. In order to model the system, kinetic equations were developed and fitted to the experimental results, with a Langmuir-Hinshelwood approach found to most accurately represent the measured kinetics. The best fitting expression was based on a carbide pathway based reaction scheme, with a rate-determining step of CH hydrogenation. A literature review revealed uncertainty in the apparent activation energy for the reaction, with some authors indicating pressure sensitivity. However, the apparent activation energy observed at four pressures between 5 and 15 barg appeared to be insensitive to pressure. The values of the apparent activation energy were found to be consistent with those reported over the nickel catalysts, and in line with the expectation for CO hydrogenation on cobalt.

The influence of mass transport within a Fischer-Tropsch catalyst pellet typical of that used commercially was examined in Chapter 6. A reaction-diffusion model for a 2-D hollow cylinder was developed and the catalyst selectivity and its effectiveness factor were analysed across a range of Thiele moduli. The extents of error in both performance metrics were quantified relative to simpler one-dimensional sphere and slab approximations often adopted in the literature. By applying 2-D modelling, it was noted that significant errors existed between the 2D hollow cylinder and the equivalent slab, sphere or 1-D hollow model between generalised Thiele moduli of ~0.25 and ~3. The effectiveness factors of the 2-D system were bounded by those of sphere and slab above and below Thiele moduli of ~0.75 and ~1.15

respectively for the conditions examined, with model effectiveness factors exceeding those of both sphere and slab models between these moduli. Concurrently, the chain growth parameter, a measure of selectivity, was lower than those of both sphere and slab geometries. Hence under those conditions, use of hollow cylinders resulted in the greatest methane selectivity. The numerical model was evaluated against a simplified n^{th} order effectiveness factor model from the literature and was found to differ over the Thiele range ~ 0.5 to ~ 1.5 , with the greatest errors arising where the effectiveness factor exceeded 1. However, the use of the simplified model required fitting the models reaction order at high Thiele to obtain a reasonable representation of catalyst behaviour. The effective order of the reaction was also dependent on the reaction conditions and thus selection of an appropriate reaction order was noted to represent a further source of error in fixed-bed modelling. A comparison of the hollow cylindrical pellets against spheres of equivalent volume demonstrated that the hollow cylinder provided improved fixed-bed performance, with greater effectiveness factors and selectivities due to the lowered diffusion lengths of the hollow cylindrical geometry.

In summary, the kinetics of CO₂ methanation have been explored for both a nickel and a cobalt catalyst. The Ni/ γ -Al₂O₃ catalyst was examined using both a batch reactor and a fixed-bed system. The application of both types of reactor offered a means to study the kinetics of methanation under a wide range of conversions, and reactant partial pressures. A number of kinetic models were derived and compared to the observed behaviour in both regimes of operation and the best fitting models were identified. A comparison of the models was reported and the differences were attributed to the oversimplification through use of the assumptions upon which Langmuir-Hinshelwood equations are based. A second study investigated the rates of methanation over a Co/ZrO₂ catalyst, with the reaction order and activation energy identified across a range of reaction pressures and temperatures. The behaviour of the cobalt differed from that of the nickel. The cobalt catalyst showed a dependence on hydrogen partial pressure, and a very minor influence of carbon dioxide partial pressure, whereas the nickel catalyst showed a stronger dependence on carbon dioxide partial pressure, and a lesser influence of hydrogen partial pressure. It is clear the methanation behaviour may differ between catalysts, with the active metal, operating conditions and catalyst support all playing a role in the observed kinetics. A numerical modelling study was also presented, in which the significance of hollow cylinder shapes on the performance of Fischer-Tropsch catalyst pellets was investigated. The study provided insights into where lower dimensional approximations can lead to unacceptable levels of error, which is particularly important in the development of accurate industrial reactor models. The study identified where 1-D and 2-D models are necessary and through use of a generalised Thiele

modulus allows its applicability to be expanded to a generalised Fischer-Tropsch kinetic model. The changes in selectivity with Thiele modulus were examined and it was noted the methane selectivity was increased upon entering a mass transfer limited regime. The implications for this on industrial reactors and the effect of pellet geometry on these selectivity changes were discussed, with the hollow cylindrical pellet selectivity mainly bounded by the sphere and slab selectivities, and showing significantly higher methane selectivities for values of Thiele modulus between ~0.75-1.25, coinciding with the observed effectiveness factor peak.

8 Future Work

This Dissertation has investigated a Ni/ γ -Al₂O₃ catalyst in both a gradientless, spinning basket reactor, operated in batch mode, and a fixed-bed reactor operated differentially. The work has highlighted differences between the two systems, with water partial pressure a significant difference between the high-conversion Carberry reactor and the differential fixed-bed reactor. The Carberry reactor has indicated that water acts as an inhibitor, and may warrant further investigation. In order to characterise further the influence of water on the kinetics, it is suggested that steam is co-fed into the fixed-bed reactor, as this would permit easier control over the partial pressure of water than is afforded by Carberry reactor. Further results at higher conversions may also provide useful kinetic information from the fixed-bed reactor, however the system would require modification to reach larger conversions without significant residence times or heat transfer issues due to the reactions exothermic nature.

The Carberry reactor provides a means to determine the rates of reaction for gas-solid reactions. The technique may be used to investigate other gas-solid reactions, which may be operated within the operational temperature and pressure ranges. However it is recommended that potential upgrades for online measurements or switching between steady-state and batch operation are investigated, due to the time-intensive nature of the Carberry experiments. Where liquids are likely to form, *e.g.* in the Fischer-Tropsch process, it is recommended these are operated in the fixed-bed reactor instead, since the limited inventory in each Carberry batch reaction makes liquid collection and sampling infeasible.

The CO₂ methanation reaction has been characterised for both nickel and cobalt catalysts within the reactor systems outlined within the dissertation. As has been noted earlier, the identified kinetic equations may give an indication of the kinetic pathways in operation, however further studies may be useful to confirm such conclusions. The use of surface science techniques, such as DRIFTS, may give an indication of the most abundant surface intermediates and thus allow greater insight into the surface reaction. This technique may be particularly useful if the catalyst can be investigated at both high and low conversions to determine how the presence of water influences the identities and proportions of the adsorbed surface species during reaction.

The reaction kinetics on cobalt have not been studied to as significant a level as those on nickel and thus further studies on the kinetics of the reaction for cobalt on different supports may yield useful results. The literature concerning supported nickel catalysts show significant differences between studies and supports, hence testing CO₂ methanation across

different supported cobalt catalysts may yield additional insight into the reaction. The application of density functional theory (DFT) computational modelling, as has been applied for nickel catalysts, could identify likely surface reactions. Any further insight into the simpler CO₂ methanation reaction may then translate into a greater insight into the more complex CO hydrogenation (Fischer-Tropsch) reaction.

The research presented in Chapter 6 demonstrated the influence of hollow cylindrical pellet geometry on a Fischer-Tropsch catalyst's effectiveness factor and its selectivity towards more valuable heavy hydrocarbons. The reaction-diffusion system was explored under the assumption of a stationary wax phase of fixed composition entirely filling the pellet. This assumption is commonplace in lower dimensional Fischer-Tropsch pellet models, the scope remains to expand current modelling efforts to include transience in wax composition and the potential for the existences of gas/liquid interfaces within pellets. The main difficulties in expanding beyond this assumption lie in the computational complexity of simulating additional components, and difficulties obtaining results to accurately simulate the diffusivities and vapour pressures of heavy compounds within the porous networks. Furthermore, in real catalyst materials, the pore sizes will be distributed across a range and hence the influence of the pore curvature on the component vapour pressures may differ spatially throughout the pellet.

9 References

- Abate, S., Barbera, K., Giglio, E., Deorsola, F., Bensaid, S., Perathoner, S., Pirone, R., Centi, G., 2016. Synthesis, characterisation and activity pattern of Ni-Al hydrotalcite catalysts in CO₂ methanation *Industrial and Engineering Chemistry Research*, **55**, pp.8299-8308.
- Abelló, S., Berrueco, C., Montané, D., 2013. High-loaded nickel–alumina catalyst for direct CO₂ hydrogenation into synthetic natural gas (SNG). *Fuel*, **113**, pp.598-609.
- Adesina, A.A., 1996. Hydrocarbon synthesis via Fischer-Tropsch reaction: travails and triumphs. *Applied Catalysis A: General*, **138**(2), pp.345–367.
- Agilent, 2011. Agilent 7890A Extended Refinery Gas Analysis Manual.
- Akamaru, S., Shimazaki, T., Kubo, M., Abe, T., 2014. Density functional theory analysis of methanation reaction of CO₂ on Ru nanoparticle supported on TiO₂ (101). *Applied Catalysis A: General*. **470**, pp.405-411.
- Akgerman, A. 1984. Diffusivities of Synthesis Gas and Fischer-Tropsch Products in Slurry Media. Final Report. DOE Report-DOE/PC/70032-T2.
- Akgerman, A., 1987. Diffusivities of Synthesis Gas and Fischer-Tropsch Products in Slurry Media. In Proceedings of the Indirect Liquefaction Contractors' Review Meeting, Pittsburgh, PA, Federal Energy Technology Center (FETC), U.S. Department of Energy: Washington, D.C., pp. 354.
- Akin, A.N., Ataman, M., Aksoylu, A.E., Onsan, Z.I., 2002, CO₂ fixation by hydrogenation over coprecipitated Co/Al₂O₃. *Reaction Kinetics and Catalysis Letters*, **76**(2), pp.265-270.
- Aldana, P.A. U., Ocampo, F., Kobl, K., Louis, B., Thibault-Starzyk, F., Daturi, M., Bazin, P., Thomas, S., Roger, A. C., 2013. Catalytic valorization into CH₄ on Ni-based ceria-zirconia. Reaction mechanism by *operando* IR spectroscopy. *Catalysis Today*, **215**, pp.201-207.
- All, S., Chen, B., Goodwin, J.G., 1995. Zr Promotion of Co/SiO₂ for Fischer-Tropsch Synthesis. *Journal of Catalysis*, **157**(1), pp.35-41.
- Anderson, R.B., Seligman, B., Shultz, J.F., Kelly, R., Elliott, M.A., 1952. Fischer-Tropsch Synthesis. Some Important Variables of the Synthesis on Iron Catalysts. *Industrial & Engineering Chemistry*, **44**(2), pp.391-397
- Anderson, J. B., 1963. A criterion for isothermal behaviour of a catalyst pellet. *Chemical Engineering Science*, **18**(2), pp.143-148.

- Andersson, M.P., Abild-Peterson, F., Remediakis, L.N., Bligaard, T., Jones, G., Engbaek, J., Lytken, O., Horsch, S., Nielsen, J.H., Sehested, J., Rostrup-Nielsen, J.R., Norskov, J.K., Chorkendorff, J., 2008. Structure sensitivity of the methanation reaction: H₂-induced CO dissociation on nickel surfaces. *Journal of Catalysis*, **255**, pp.6-19.
- Aris, R., 1957. On shape factors for irregular particles—I: The steady state problem. Diffusion and reaction. *Chemical Engineering Science*, **6**, pp.262–268.
- Ashok, J., Ang M. L., Kawi, S., 2016. Enhanced activity of CO₂ methanation over Ni/CeO₂-ZrO₂ catalysts: Influence of preparation methods. *Catalysis Today*, **281**(2), pp.304-311.
- Atashi, H., Siami, F., Mirzaei, A.A. and Sarkari, M., 2010. Kinetic study of Fischer–Tropsch process on titania-supported cobalt–manganese catalyst. *Journal of Industrial and Engineering Chemistry*, **16**(6), pp.952–961.
- Audi, 2017. Power from gas: The new Audi A4 Avant g-tron [online]. Available at: <https://www.audi-mediacenter.com/en/press-releases/power-from-gas-the-new-audi-a4-avant-g-tron-4966> [Accessed 26th September 2017]
- Bae, J.W., Park, S.-J., Lee, Y.-J., Park, H.-G., Kim, Y.-B., Lee, D.H., Kim, B.-W. and Park, M.-J., 2011. Effects of Reaction Variables on Fischer–Tropsch Synthesis with Co-Precipitated K/FeCuAlO_x Catalysts. *Catalysis Letters*, **141**(6), pp.799–807.
- Barrett, E.P., Joyner, L.G., Halenda, P.P., 1951, The Determination of Pore Volume and Area Distribution in Porous Substances. Computations from Nitrogen Isotherms. *Journal of the American Chemical Society*, **73**, pp. 373-380.
- Bartholomew, C.H., 2001. Mechanisms of catalyst deactivation. *Applied Catalysis A: General*, **212**, pp.17-60.
- Bartholomew, C.H., Pannell, R.B., 1980. The Stoichiometry of Hydrogen and Carbon Monoxide Chemisorption on Alumina and Silica-Supported Nickel. *Journal of Catalysis*, **65**, pp.390-401.
- Bartholomew, C.H., Farrauto, R.J., 1976. Chemistry of Nickel-Alumina Catalysts. *Journal of Catalysis*, **45**, pp.41-53.
- Beaumont, S.K., Alayoglu, S., Specht, C., Kruse, N., Somorjai, G. A., 2014. A nanoscale demonstration of hydrogen atom spillover and surface diffusion across silica using the kinetics of CO₂ methanation catalysed on spatially separate Pt and Co nanoparticles. *Nanoletters*, **14**, pp.4792-4796.

- Becker, H., Gütterl, R., Turek, T., 2014. Optimization of Catalysts for Fischer-Tropsch Synthesis by Introduction of Transport Pores. *Chemie Ingenieur Technik*, **86**(4), pp.544-549.
- Berger, R.J., Pérez-Ramírez, J., Kapteijn, F., Moulijn, J.A., 2002. Catalyst performance testing: bed dilution revisited. *Chemical Engineering Science*, **57**, pp.4921-4932.
- Bessell, S., 1993. Support effects in cobalt based Fischer-Tropsch catalysis. *Applied Catalysis A: General*, **96**(2), pp.253-268.
- Binder, G.G., White, R.R., 1950. Synthesis of Methane from Carbon Dioxide and Hydrogen. *Chemical Engineering Progress*, **46**, pp.563-574.
- Bird, R.B., Stewart, W.E., Lightfoot, E.N., 1960. *Transport Phenomena*, John Wiley and Sons Inc
- Borg, Ø., Eri, S., Blekkan, E.A., Storsæter, S., Wigum, H., Rytter, E., Holmen, A., 2007. Fischer-Tropsch synthesis over γ -alumina-supported cobalt catalysts: Effect of support variables. *Journal of Catalysis*, **248**, pp.89-100.
- Bruce, L.A., Hoang, M., Hughes, A.E., Turney, T.W., 1993. Ruthenium promotion of Fischer-Tropsch synthesis over coprecipitated cobalt / ceria catalysts. *Applied Catalysis A: General*, **100**, pp.51–67.
- Brunnauer, S., Emmett, P.H., Teller, E., 1938. Adsorption of Gases in Multi-molecular Layers. *Journal of the American Chemical Society*. **60**(2), pp. 309-319.
- Brunner, K.M., Perez, H.D., Peguin, R.P.S., Duncan, J.C., Harrison, L.D., Bartholomew, C.H., Hecker, W.C., 2015. Effects of Particle Size and Shape on the Performance of a Trickle Fixed-Bed Recycle Reactor for Fischer-Tropsch Synthesis. *Industrial and Engineering Chemical Research*, **54**, pp.2902-2909.
- Cairns, R. W., Ott, E., 1933. X-Ray Studies of the System Nickel-Oxygen-Water. I. Nickelous Oxide and Hydroxide. *Journal of the American Chemical Society*, **55**, pp.527–533.
- Campbell, T.K., Falconer, J., 1989, Carbon dioxide hydrogenation on potassium-promoted nickel catalysts, *Applied Catalysis*, **50**(1), pp.189-197.
- Campelo, J.M., Garcia, A., Gutirrez, J.M., Luna, D., Marinas, J.M., 1983. AlPO₄-supported nickel catalysts. V. Effects of carrier, nickel precursor and nickel loading on particle size and 1-hexene hydrogenation activity. *Applied Catalysis*, **7**, pp.307-315.
- Carey, G.F., Finlayson, B.A., 1975. Orthogonal Collocation on Finite Elements. *Chemical Engineering Science*, **30**, pp.587-589.

Carmello, D., Fatutto, P., Marsella, A., 1999. Catalyst and oxychlorination process using it. EP1053789A1

Chang, F.W. , Kuo, M.S., Tsay, M.T., Hsieh, M.C., 2003. Hydrogenation of CO₂ over nickel catalysts on rice husk ash-alumina prepared by incipient wetness impregnation. *Applied Catalysis: A*, **247**(2), pp.309-320.

Chase Jr., M.W., 1998. NIST-JANAF Thermochemical Tables, Fourth Edition, Journal of Physical Chemistry Reference Data Monograph 9, pp.1-1951.

Chen, J.G., Sun, Y.H., 2004. The structure and reactivity of coprecipitated Co-ZrO₂ catalysts for Fischer-Tropsch synthesis. *Studies in Surface Science and Catalysis*, **147**, pp.277-282.

Chiang, J.H., Hopper, J.R., 1983. Kinetics of the Hydrogenation of Carbon Dioxide over Supported Nickel. *Industrial and Engineering Chemistry Product Research and Development*, **22**, pp.225-228.

Chintpong, N., Praserthdam, P., Jongsomjit, B., 2009. A study on characteristics and catalytic properties of Co/ZrO₂-B catalysts towards methanation. *Catalysis Letters*, **128**, pp.119-126.

Chu, C.F., Ng, K.M., 1989, Flow in packed tubes with a small tube to particle diameter ratio, AIChE Journal, **35**, pp.148-158.

Coenen, J.W.E., van Nisselrooy, P.F.M.T., de Croon, M.H.J.M, van Dooren, P.F.H.A., van Meerten, R.Z.C., 1986. The Dynamics of Methanation of Carbon Monoxide on Nickel Catalysts. *Applied Catalysis*, **25**, pp.1-8.

Coenen, J.W.E., 1979. Reduction of Silica Supported Nickel Catalysts. *Studies in Surface Science and Catalysis*, **3**, pp.89-111.

Dalmon, J.A., Martin, G.A., 1983. The Kinetics and Mechanism of Carbon Monoxide Methanation over Silica-Supported Nickel Catalysts. *Journal of Catalysis*, **84**, pp.45-54.

Das, T., Deo, G., 2012. Effects of metal loading and support for supported cobalt catalyst. *Catalysis Today*, **198**, pp.116-124.

De Deugd, R.M. Chougule, R.B. Kreutzer, M.T. Meeuse, F.M., Grievink, J., Kapteijn, F., Moulijn, J.A., 2003. Is a monolithic loop reactor a viable option for Fischer-Tropsch synthesis? *Chemical Engineering Science*, **58**, pp.583-591.

Delgado, J.M.P.Q., 2005. A critical review of dispersion in packed beds. *Heat and Mass Transfer*, **42**(4), pp.279–310.

Deller, K., Krause, H., Schmidhammer, L, Dafinger, W., 1990. Cylindrically formed catalyst

for the oxychlorination of ethylene. US5166120A.

Department for Business, Energy & Industrial Strategy, 2017. Digest of UK Energy Statistics (DUKES): foreign trade statistics: Imports and exports of fuels (DUKES G.1). Available at: <https://www.gov.uk/government/statistics/dukes-foreign-trade-statistics> [Accessed 26th September 2017]

Dew, J.N., White, R.R., Sliepcevich, C.M., 1955. Hydrogenation of Carbon Dioxide on Nickel-Kieselguhr Catalyst. *Industrial and Engineering Chemistry*, **47**, pp.140-146.

Díaz, J.A., Martínez-Fernández, M., Romero, A., Valverde, J.L., 2013. Synthesis of carbon nanofibers supported cobalt catalysts for Fischer-Tropsch process. *Fuel*, **111**, pp.422-429.

Dorner, R.W., Hardy, D.R., Williams, F.W., Davis, B.H. and Willauer, H.D., 2009. Influence of Gas Feed Composition and Pressure on the Catalytic Conversion of CO₂ to Hydrocarbons Using a Traditional Cobalt-Based Fischer-Tropsch Catalyst. *Energy & Fuels*, **23**(8), pp.4190–4195.

Downs, R.T., Hall-Wallace, M., 2003. The American Mineralogist Crystal Structure Database. *American Mineralogist*, **88**, pp.247-250.

Dry, M.E., 2002. The Fischer–Tropsch process: 1950–2000. *Catalysis Today*, **71**, pp.227–241.

Eckle, S., Anfang, H.-G., Behm, R. J., 2011. Reaction Intermediates and Side Products in the Methanation of CO and CO₂ over Supported Ru Catalysts in H₂-Rich Reformate Gases. *Journal of Physical Chemistry C*, **115**, pp.1361-1367.

Eichhorn, H.-D., Schneehage, H., Cordenmans, L., Hebgen, W., Jaeckh, C., Mross, W. D., 1986. Preparation of 1,2-dichloroethane by oxychlorination of ethylene over a copper-containing supported catalyst. US4740644A.

Enache, D.I., Roy-Auberger, M., Revel, R., 2004. Differences in the characteristics and catalytic properties of cobalt-based Fischer-Tropsch catalysts supported on zirconia and alumina. *Applied Catalysis A: General*, **268**(1-2), pp.51-60.

Erkey, C., Rodden, J. B., Akgerman, A., 1990. Diffusivities of synthesis gas and *n*-alkanes in Fischer-Tropsch wax. *Energy & Fuels*, 1990, **4**, pp.275-276.

Fan, L., Yokota, K. and Fujimoto, K., 1995. Characterization of mass transfer in supercritical-phase Fischer-Tropsch synthesis reaction. *Topics in Catalysis*, **2**(1-4), pp.267–283.

Feng, Y., Yang, W., Chen, S., Chu, W., 2014. Cerium promoted nano nickel catalysts Ni-Ce/CNTs and Ni-Ce/Al₂O₃ for CO₂ methanation. *Integrated Ferroelectrics*, **151**, pp.116-125.

Fujita, S.I., Nakamura, M., Doi, T., Takezawa, N., 1993. Mechanisms of methanation of CO and CO₂ over nickel/alumina catalysts. *Applied Catalysis A: General*, **104**(1), pp.87-100.

Fujita, S., Terunuma, H., Nakamura, N., Takezawa, N., 1991. Mechanisms of methanation of CO and CO₂ over nickel. *Industrial Engineering and Chemistry Research*, **30**(6), pp.1146-1151.

Fuller, E.N., Schettler, P.D. and Giddings, J.C., 1966. A new method for prediction of binary gas-phase diffusion coefficients. *Industrial and Engineering Chemistry*, **58**(5), pp.19–27.

Gardner, D.C., Bartholomew, C.H., 1981. Kinetics of Carbon Deposition during Methanation of CO. *Industrial Engineering and Chemistry Process Research and Development*, **20**(1), pp.80-87.

Gardezi, S.A., Joseph, B., 2015. Performance Characteristics of Eggshell Co/SiO₂ Fischer-Tropsch Catalysts: A Modelling Study. *Industrial and Engineering Chemical Research*, **54**, pp.8080-8092.

Gaube, J. and Klein, H.-F., 2008. Studies on the reaction mechanism of the Fischer–Tropsch synthesis on iron and cobalt. *Journal of Molecular Catalysis A: Chemical*, **283**(1–2), pp.60–68.

Girardon, J., Lermontov, A., Gengembre, L., Chernavskii, P., Gribovalconstant, A., Khodakov, A., 2005. Effect of cobalt precursor and pre-treatment conditions on the structure and catalytic performance of cobalt silica-supported Fischer-Tropsch catalysts. *Journal of Catalysis*, **230**(2), pp.339–352.

Gnanamani, M.K., Shafer, W.D., Sparks, D.E., Davis, B.H., 2011. Fischer–Tropsch synthesis: Effect of CO₂ containing syngas over Pt promoted Co/γ-Al₂O₃ and K-promoted Fe catalysts. *Catalysis Communications*, **12**(11), pp.936–939.

Gnanamani, M.K., Jacobs, G., Keogh, R.A. and Davis, B.H., Shafer, W.D., Sparks, D.E., Hopps, S.D., Thomas, G.A., Davis, B.H., 2015. Fischer-Tropsch synthesis: Effect of pretreatment conditions of cobalt on activity and selectivity for hydrogenation of carbon dioxide. *Applied Catalysis A: General*, **499**, pp.39-46.

Gnanamani, M.K., Jacobs, G., Hamdeh, H.H., Shafer, W.D., Liu, F., Hopps, S.D., Thomas, G.A., Davis, B.H., 2016. Hydrogenation of Carbon Dioxide over Co-Fe Bimetallic Catalysts. *ACS Catalysis*, **6**, pp.913-927.

GoGreenGas, 2016. First Project Process Report. <http://gogreengas.com/wp->

content/uploads/2015/11/BioSNG-Demonstration-Plant-June-2016-Project-Progress-Report.pdf [Accessed 27th September 2017].

Grazulis, S., Chateigner, D., Downs, R.T., Yokochi, A.T., Quiros, M., Lutterotti, L., Manakova, E., Butkus, J., Moeck, P., Le Bail, A., 2009. Crystallography Open Database – an open-access collection of crystal structures". *Journal of Applied Crystallography*. **42**, pp.726-729.

Gražulis, S., Daškevič, A., Merkys, A., Chateigner, D., Lutterotti, L., Quirós, M., Serebryanaya, N.R., Moeck, P., Downs, R.T., LeBail, A., 2012. Crystallography Open Database (COD): an open-access collection of crystal structures and platform for world-wide collaboration. *Nucleic Acids Research* **40**, pp.420-427.

Gražulis, S., Merkys, A., Vaitkus, A. & Okulič-Kazarinas, M., 2015. Computing stoichiometric molecular composition from crystal structures. *Journal of Applied Crystallography*, **48**, pp.85-91.

Habazaki, H., Yamasaki, M., Zhang, B.-P., Kawashima, A., Kohno, S., Takai, T., Hashimoto, K., 1998. Co-methanation of carbon monoxide and carbon dioxide on supported nickel catalysts prepared from amorphous alloys. *Applied Catalysis A: General*, **172**, pp.131-140.

Hallac, B.B., Keyvanloo, K., Hedengren, J.D., Hecker, W.C., Argyle, M.D., 2015. An optimisation simulation model for iron-based Fischer-Tropsch catalyst design: transfer limitations as function of operating and design conditions. *Chemical Engineering Journal*, **263**, pp.268-279.

He, F., Niu, N., Qu, F., Wei, S., Chen, Y., Gai, S., Gao, P., Wang, Y., Yang, P., 2013. Synthesis of three-dimensional reduced graphene oxide layer supported cobalt nanocrystals and their high catalytic activity in F-T CO₂ hydrogenation. *Nanoscale*, **5**, pp.8507-8516.

Hischfelder, J.O., Bird, R.B., Curtiss, C.F., 1954, Molecular theory of gases and liquids, Wiley, New York.

Hofmann, F., Krabetz, R., Schwarzmüller, M., 1984. Molded catalyst for reactions carried out under heterogenous catalysis. US4656157A

Holladay, J.D., Brooks, K.P., Wegeng, R., Hu, J., Sanders, J., Baird, S., 2007. Microreactor Development for *in-situ* Propellant Production. *Catalysis Today*, **120**(1), pp.35-44.

Hong, J., Chu, W., Chernavskii, P.A., Khodakov, A.Y., 2010. Effects of zirconia promotion on the structure and performance of smaller and larger pore silica-supported cobalt catalysts for

Fischer-Tropsch synthesis. *Applied Catalysis A: General*, **382** (1), pp.28–35.

Huff, G.A. and Satterfield, C.N., 1984. Evidence for two chain growth probabilities on iron catalysts in the Fischer-Tropsch synthesis. *Journal of Catalysis*, **85**(2), pp.370–379.

Huff, G.A. and Satterfield, C.N., 1985. Liquid accumulation in catalyst pores in a Fischer-Tropsch fixed-bed reactor. *Industrial & Engineering Chemistry Research*, **24**, pp.986–995.

Hwang, S., Lee, J., Hong, U.G., Seo, J.G., Jung, J.C., Koh, D.J., Lim, H., Byun, C., Song, I.K., 2011. Methane production from carbon monoxide and hydrogen over nickel-alumina xerogel catalyst: Effect of nickel content. *Journal of Industrial and Engineering Chemistry*, **17**, pp.154-157.

Iablokov, V., Beaumont, S.K., Alagoyu, S., Pushkarev, V.V., Specht, C., Gao, J., Alivisatos, P., Kruse, N., Somorjai, G.A., 2012. Size-Controlled Model Co Nanoparticle Catalysts for CO₂ Hydrogenation Synthesis, Characterization, and Catalytic Reactions. *Nano Letters*, **12**, pp.3091-3096.

Ibraeva, Z.A., Nekrasov, N.V., Gudkov, B.S., Yakerson, V.I., Beisembaeva, Z.T., Golosman, E.Z., Kiperman, S.L., 1991. Kinetics of methanation of carbon dioxide on a nickel catalyst. *Theoretical and Experimental Chemistry*, **26**(5), pp.584-588.

Ido, T., Kohmura, T., Goto, S., 1984. Reactions of Methanol to Methane on Nickel Catalyst. *Kagaku Kogaku Ronbunshu*, **10**, pp.82-88.

Iglesia, E., Reyes, S.C. and Madon, R.J., 1991. Transport-Enhanced α-Olefin Readsorption Pathways in Ru-Catalyzed Hydrocarbon Synthesis. *Journal of Catalysis*, **129**, pp.238–256.

Iglesia, E., Soled, S.L., Baumgartner, J.E., Reyes, S. C., 1995. Synthesis and catalytic properties of eggshell cobalt catalysts for the Fischer-Tropsch synthesis. *Topics in Catalysis*, **2**(1), pp.17-27.

Incropera, F.P., DeWitt, D.P., Bergman, T.L., Lavine, A.S., 2006. Fundamentals of Heat and Mass Transfer. John Wiley and Sons.

Inoue, H., Funakoshi, M., 1984. Kinetics of Methanation of Carbon Monoxide and Carbon Dioxide. *Journal of Chemical Engineering of Japan*. **17**(8), pp.602-610.

International Energy Agency, 2017. World Energy Balance: Overview (2017 edition). Available at: <https://www.iea.org/publications/freepublications/publication/WorldEnergyBalances2017Overview.pdf>. [Accessed 26th September 2017]

- Jacquemin, M., Beuls, A., Ruiz, P., 2009. Catalytic production of methane from CO₂ and H₂ at low temperature: Insight on the reaction mechanism. *Catalysis Today*, **157**(1-4), pp.462-466.
- Jess, A. and Kern, C., 2009. Modelling of Multi-Tubular Reactors for Fischer-Tropsch Synthesis. *Chemical Engineering & Technology*, **32**(8), pp.1164–1175.
- Ji, Y., Zhao, Z., Duan, A., Jiang, G., Liu, J., 2009. Comparative Study in the Formation and Reduction of Bulk and Al₂O₃-Supported Cobalt Oxides by H₂-TPR Technique. *Journal of Physical Chemistry C*, **113**(17), pp.7186-7199.
- Jia, C., Gao, J., Li, J., Gu, F., Xu, G., Zhong, Z., Su, F., 2013. Nickel catalysts supported on calcium titanate for enhanced CO methanation. *Catalysis Science and Technology*, **3**, pp.490-499.
- Kai, T., Takahashi, T., Furusaki, S., 1988. Kinetics of the methanation of carbon dioxide over a supported Ni-La₂O₃ catalyst. *The Canadian Journal of Chemical Engineering*, **66**(2), pp.343-347.
- Kaiser, P., Pöhlmann, F. and Jess, A., 2014. Intrinsic and Effective Kinetics of Cobalt-Catalyzed Fischer-Tropsch Synthesis in View of a Power-to-Liquid Process Based on Renewable Energy. *Chemical Engineering & Technology*, **37**(6), pp.964–972.
- Kangvansura, P., Schulz, H., Suramitr, A., Poo-arporn, Y., Viravathana, P., Worayizingyong, A., 2014. Reduced cobalt phases of ZrO₂ and Ru/ZrO₂ promoted cobalt catalysts and product distributions from Fischer-Tropsch synthesis. *Material Science and Engineering B*, **190**, pp.82-89.
- Karelovic, A., Ruiz, P., 2012. CO₂ hydrogenation at low temperature over Rh/γ-Al₂O₃ catalysts: Effect of the metal particle size on catalytic performances and reaction mechanism. *Applied Catalysis B: Environmental*, **113-114**, pp.237-249.
- Kaskes, B., Vervloet, D., Kapteijn, F., van Ommen, J.R., 2016. Numerical optimisation of a structured tubular reactor for Fischer-Tropsch synthesis. *Chemical Engineering Journal*, **283**, pp.1465-1483.
- Keely, W.M., Maynor, H.W., 1963. Thermal Studies of Nickel, Cobalt, Iron and Copper Oxides and Nitrates. *Journal of Chemical & Engineering Data*, **8**(3), pp.297-300.
- Keyser, M.J., Everson, R.C., Espinoza, R.L., 2000. Fischer-Tropsch kinetic studies with cobalt-manganese oxide catalysts. *Industrial & engineering chemistry research*, **39**(1), pp.48–54.

Kim, H.Y., Lee, H.M., Park, J.N., 2010. Bifunctional mechanism of CO₂ methanation on Pd-MgO/SiO₂ catalyst: independent roles of MgO and Pd on CO₂ methanation. *Journal of Physical Chemistry C*, 2010, **114**(15), pp.7128-7131.

King, D., 1978. A Fischer-Tropsch study of supported ruthenium catalysts. *Journal of Catalysis*, **51**, pp.386–397.

Klemens, P.G., 1996, Thermal Conductivity of Zirconia. In: Wilkes, K.E., Dinwiddie, R.B., Greaves, R.S. ed., *Thermal Conductivity 23: International Conference Proceedings 23*. CRC Press pp. 209-216.

Klose, J., Baerns, M., 1984. Kinetics of Methantion of Carbon Monoxide on an Alumina-Supported Nickel Catalyst. *Journal of Catalysis*, **85**, pp.105-116.

Kopyscinski, J., Schildhauer, T.J., Biollaz, S., 2010. Production of synthetic natural gas (SNG) from coal and dry biomass – A technology review from 1950 to 2009. *Fuel*, **89**(8), pp.1763-1783.

Koschany, F., Schlereth, D., Hinrichsen, O., 2016. On the kinetics of the methanation of carbon dioxide on coprecipitated NiAl(O)_x. *Applied Catalysis B: Environmental*, **181**, pp.504-516.

Kraum, M., Baerns, M., 1999. Fischer-Tropsch synthesis: the influence of various cobalt compounds applied in the preparation of supported cobalt catalysts on their performance. *Applied Catalysis A: General*, **186**(1-2), pp.189-200.

Kruissink, E., van Reijen, L.L., Ross, J.R.H., 1981. Co-precipitated nickel-alumina catalysts for methanation at high temperature. Part I. – Chemical composition and structure of the precipitates. *Journal of the Chemical Society, Faraday Transactions I*, **77**, pp.649-663.

Kuipers, E., Schaper, C., Wilson, J., Vinkenburg, I. and Oosterbeek, H., 1996. Non-ASF product distributions due to secondary reactions during Fischer-Tropsch synthesis. *Journal of Catalysis*, **158**(1), pp.288–300.

Kuipers, E.W., Vinkenburg, I.H. and Oosterbeek, H., 1995. Chain Length Dependence of alpha-Olefin Readsorption in Fischer-Tropsch Synthesis. *Journal of Catalysis*, **152**, pp.137–146.

Laarson, A.,Hedenskong, M., Thunman, H., 2015. Monitoring the Bed Material Activation in the GoBiGas- Gasifier. Nordic Flame Days 2015, Copenhagen. Available online at: http://publications.lib.chalmers.se/records/fulltext/225499/local_225499.pdf [Accessed 27th

September 2017]

- Lahitnen, J., Anraku, T., Somorjai, G.A., 1994. C, CO, and CO₂ hydrogenation on cobalt foil model catalysts: evidence for the need of CoO reduction. *Catalysis Letters*, **25**, pp.241-255.
- Lamas, D.G., Walsoe de Reca, N.E., 2000. X-ray diffraction study of compositionally homogeneous, nanocrystalline yttria-doped zirconia powders. *Journal of Materials Science*, **35**, pp.5563-5567.
- Laurer, P., R., Krome, G., Cordemans, L., Seifert, R., Danz, E., 1980. Supported Catalyst containing copper and alkali metals. US4382021A
- Leckel, D., 2009. Diesel Production from Fischer-Tropsch: The Past, the Present, and New Concepts. *Energy & Fuels*, **23**(5), pp.2342–2358.
- Lejaeghere, K., Van Speybroeck, V., Van Oost, G., Cottenier, S, 2014. Error Estimates for Solid-State Density-Functional Theory Predictions: An Overview by Means of the Ground-State Elemental Crystals. *Critical Reviews in Solid State and Materials Sciences*, **39**(1), pp.1-27.
- Lee, S., Lee, B., Seifert, S., Winans, R.E., Vadja, S., 2015. Fischer-Tropsch Synthesis at a Low Pressure on Subnanometer Cobalt Oxide Clusters: The Effect of Cluster Size and Support on Activity and Selectivity. *Journal of Physical Chemistry C*, **119**, pp.11210-11216.
- Li, C., Chen, Y.-W., 1995. Temperature-Programmed-Reduction Studies of Nickel Oxide/Alumina Catalysts: Effect of the Preparation Method. *Thermochimica Acta*, **256**, pp.457-465.
- Lin, H.-Y., Chen, Y.-W., 2004. The mechanism of reduction of cobalt by hydrogen. *Material Chemistry and Physics*, **85**, pp.171-175.
- Lim, J.Y., 2014, Fundamental Studies of Methanation and Related Reactions in Porous Catalysts, PhD Thesis, University of Cambridge.
- Lim, J.Y., McGregor, J., Sederman, A.J., Dennis, J.S., 2016. Kinetic studies of CO₂ methanation over a Ni/γ-Al₂O₃ catalyst using a batch reactor. *Chemical Engineering Science*, **141**, pp.28-45.
- Liu Q., Gu, F., Lu, X., Liu, Y., Li, H., Zhong, Z., Xu, G., Su, F., 2014. Enhanced catalytic performances of Ni/Al₂O₃ catalyst *via* addition of V₂O₃ for CO methanation. *Applied Catalysis A: General*, **488**, pp.37-47.
- Lögdberg, S., Boutonnet, M., Walmsley, J.C., Järås, S., Holmen, A. and Blekkan, E. a., 2011.

Effect of water on the space-time yield of different supported cobalt catalysts during Fischer-Tropsch synthesis. *Applied Catalysis A: General*, **393**(1–2), pp.109–121.

Lu, H., Yang, X., Gao, G., Wang, J., Han, C., Liang, X., Li, C., Li, Y., Zhang, W., Chen, X., 2016. Metal (Fe, Co, Ce or La) doped nickel catalyst supported on ZrO₂ modified mesoporous clays for CO and CO₂ methanation. *Fuel*, **183**, pp.335-344.

Lu, X., Gu, F., Liu, Q., Gao, J., Liu, Y., Li, H., Jia, L., Xu, G., Zhong, Z., Su, F., 2015. VO_x promoted Ni catalysts supported on the modified bentonite for CO and CO₂ methanation. *Fuel Processing Technology*, **135**, 34-36.

Lunde, P.J., Kester, F.L., 1974. Carbon Dioxide Methanation on a Ruthenium Catalyst. *Industrial and Engineering Chemistry Process Design and Development*, **13**(1), pp.27-33.

MacLaren, J.M., Vvedensky, D.D., Pendry, J.B., Joyner, R.W., 1987. Catalytic implications of local electronic interactions between carbon monoxide and coadsorbed promoters on nickel surfaces. *Journal of the Chemical Society, Faraday Transactions I*, **83**, pp.1945-1962.

Madon, R. and Iglesia, E., 1994. Hydrogen and CO intrapellet diffusion effects in ruthenium-catalyzed hydrocarbon synthesis. *Journal of Catalysis*, **149**, pp.428–437.

Makrodimitri, Z.A., Unruh, D.J.M., Economou, I.G., 2011. Molecular simulation of diffusion of hydrogen, carbon monoxide, and water in heavy *n*-alkanes. *Journal of Physical Chemistry B*, **115**, pp.1429-1439.

Mandić, M., Todić, B., Živanić, L., Nikalčević, N., Bukur, D.B., 2017. Effects of Catalyst Activity, Particle Size and Shape, and Process Conditions on Catalyst Effectiveness and Methane Selectivity for Fischer-Tropsch Reaction: A Modelling Study. *Industrial and Engineering Chemistry Research*, **56**, pp.2733-2745.

Marano, J.J., Holder, G.D., 1997b. A General Equation for Correlating the Thermophysical Properties of *n*-Paraffins, *n*-Olefins, and Other Homologous Series. 3. Asymptotic Behaviour Correlations for Thermal and Transport Properties. *Industrial and Engineering Chemical Research*, **36**, pp.2399-2408.

Marano, J.J., Holder, G.D., 1997a. Prediction of Bulk Properties of Fischer-Tropsch Derived Liquids. *Industrial and Engineering Chemical Research*, **36**, pp.2409-2420.

Marano, J.J., Holder, G.D., 1997c. Characterization of Fischer-Tropsch liquids for vapor-liquid equilibria calculations. *Fluid Phase Equilibria*, **138**, pp.1-21.

Maretto, C. and Krishna, R., 1999. Modelling of a bubble column slurry reactor for Fischer-

- Tropsch synthesis. *Catalysis Today*, **52**(2-3), pp.279–289.
- Marwood, M., van Vyve, F., Doepper, R., Renken, A., 1994. Periodic operation applied to the kinetic study of CO₂ methanation. *Catalysis Today*, **20**, pp.437-448.
- Masuku, C., Hildebrandt, D. and Glasser, D., 2011. The role of vapour–liquid equilibrium in Fischer–Tropsch product distribution. *Chemical Engineering Science*, **66**(23), pp.6254–6263.
- McCarthy, J.J., Canziani, O.F., Leary, N.A., Dokken, D.J., White, K.S. 2001. Climate Change 2001: Impacts, Adaption and Vulnerability. Cambridge University Press, Cambridge.
- McLennan, F., Bruce R. Kowalski, B.R. (1995). Process Analytical Chemistry. Springer Netherlands
- McGlade, C., Ekins, P., 2015. The geographical distribution of fossil fuels unused when limiting global warming to 2 °C. *Nature*, **517**, pp.187-190.
- McNair, H.M., Miller, J. M., (2011). Basic Gas Chromatography. John Wiley and Sons.
- Mears, D.E., 1971. Diagnostic criteria for heat transport limitations in fixed-bed reactors. *Journal of Catalysis*, **20**(2), pp.127-131.
- Meleat, G., Ralston, W., Li, C.-S., Alagoyu, S., An, K., Musselwhite, N., Kalkan, B., Somorjai, G. A., 2014. Evidence of Highly Active Cobalt Oxide Catalyst for the Fischer-Tropsch synthesis and CO₂ Hydrogenation. *Journal of the American Chemical Society*, **136**, pp.2260-2263.
- Mercera, P.D.L., van Ommen, J.G., Doesburg, F.B.M., Burggraaf, A.J., Ross, J.R.H., 1990. Evolution of Texture and Structure on Calcination in Air. *Applied Catalysis*, **57**, pp.127-148.
- Merkys, A., Vaitkus, A., Butkus, J., Okulič-Kazarinas, M., Kairys, V. & Gražulis, S. (2016) "COD::CIF::Parser: an error-correcting CIF parser for the Perl language". *Journal of Applied Crystallography*, **49**, pp. 292-301.
- Methivier, A., Pijolat, M., 1993. Thermal Stability of Zirconia as a Catalyst Support: Kinetics and Modelling. *Journal of Catalysis*, **139**, pp.329-337.
- Miao, B., Ma, S.S.K., Wang, X., Su, H., Chan, S.H., 2016. Catalysis Mechanisms of CO₂ and CO Methanation. *Catalysis Science & Technology*, **12**, 2016.
- Mile, B., Stirling, D., Zammitt, M.A., Lovell, A., Webb, M., 1990. TPR Studies on the Effects of Preparation Conditions on Supported Nickel Catalysts. *Journal of Molecular Catalysis*, **62**, pp.179-198.

Mu, S., Li, D., Hou, B., Jia, L., Chen, J., Sun, Y., 2010. Influence of ZrO₂ Loading on SBA-15-Supported Cobalt Catalysts for Fischer–Tropsch Synthesis. *Energy and Fuels*, **24**(7), pp.3715-3718.

Munnik, P., de Jongh, P.E., de Jong, K.P., 2014. Control and impact of the nanoscale distribution of supported cobalt particles used in the Fischer-Tropsch catalysis. *Journal of the American Chemical Society*, **136**, pp.7333-7340.

Nanduri, A., 2014. Catalyst-scale modeling and simulation of a fixed-bed reactor for Fischer-Tropsch synthesis. Master's Thesis. Texas A&M University.

Nanduri, A., Mills, P.L., 2015. Comparison of diffusion flux models for Fischer-Tropsch synthesis. Excerpt from the Proceedings of the 2015 COMSOL Conference, Boston.

NASA, 2011. The Sabatier System: Producing Water on the Space Station [online]. Available at: https://www.nasa.gov/mission_pages/station/research/news/sabatier.html. [Accessed 26th September 2017]

NASA, 2017. Global Climate Change – Vital Signs of the Planet: Evidence. [online] Available at <https://climate.nasa.gov/evidence/> [Accessed 26th September 2017].

Neslen, A. (2016). BA blames UK government for scrapping of £340m green fuels project. *The Guardian*. [online] Available at:

<https://www.theguardian.com/environment/2016/jan/06/ba-blames-uk-government-for-scrapping-of-340m-green-fuels-project> [Accessed 26th September 2017].

Newman, J.A., Schmitt, P.D., Toth, S.J., Deng, F., Zhang, S., Simpson, G.J., 2016. Parts per Million Powder X-Ray Diffraction. *Analytical Chemistry*, **87**(21), pp.10950-10955.

Novak, S., Madon, R.J. and Suhl, H., 1981. Models of hydrocarbon product distributions in Fischer–Tropsch synthesis. I. *The Journal of Chemical Physics*, **74**(11), pp.6083–6091.

Okabe, K., Murata, K., Nakanishi, M., Ogi, T., Nurunnabi, M. and Liu, Y., 2008. Fischer–Tropsch Synthesis over Ru Catalysts by Using Syngas Derived from Woody Biomass. *Catalysis Letters*, **128**(1–2), pp.171–176.

Olajire, A.A., 2013. Valorization of greenhouse carbon dioxide emissions into value-added products by catalytic processes. *Journal of CO₂ Utilisation*, **3**-**4**, pp.74-92

Owen, R.E., Plucinski, P., Mattia, D., Torrente-Murciano, L., Ting, V.P., Jones, M.D., 2016. Effect of support of Co-Na-Mo catalysts on the direct conversion of CO₂ to hydrocarbons. *Journal of CO₂ Utilization*, **16**, pp.97-103.

- Pan, Q., Peng, J., Sun, T., Wang, S., Wang, S., 2014. Insight into the reaction route of CO₂ methanation: Promotion effect of medium basic sites. *Catalysis Communications*, **45**, pp.74-78.
- Peebles, D.E., Goodman, D.W., White, J.M., 1983. Methanation of Carbon Dioxide on Ni(100) and the Effects of Surface Modifiers. *Journal of Physical Chemistry*, **87**, pp.4378-4387.
- Perego, C., Villa, P., 1997, Chapter 3: Catalyst preparation methods. *Catalysis Today*, **34**, pp. 281-305.
- Pohlmann, F., Jess, A., 2016. Interplay of reaction and pore diffusion during cobalt-catalyzed Fischer-Tropsch synthesis with CO₂-rich syngas. *Catalysis Today*, pp.172-182.
- Poole, C. (2012). Gas Chromatography, Elsevier.
- Porosoff, M.D., Chen, J.G., 2013. Trends in the catalytic reduction of CO₂ by hydrogen over supported monometallic and bimetallic catalysts. *Journal of Catalysis*, **301**, pp.30-37.
- Post, M.F.M., Van't Hoog, a. C., Minderhoud, J.K. and Sie, S.T., 1989. Diffusion limitations in fischer-tropsch catalysts. *AIChE Journal*, **35**(7), pp.1107–1114.
- Pour, V., 1969. Hydrogenation of carbon dioxide on nickel catalysts. I. Kinetics of hydrogenation on nickel-chromia catalysts. *Collections of Czechoslovak Chemical Communications*, **34**, pp.45-56.
- Rahmani, S., Rezaei, M., Meshkani, F., 2014. Preparation of promoted nickel catalysts supported on mesoporous nanocrystalline gamma alumina for carbon dioxide methanation reaction. *Journal of Industrial and Engineering Chemistry*, **20**, pp.4176-4182.
- Raje, A., Inga, J. and Davis, B., 1997. Fischer-Tropsch synthesis: process considerations based on performance of iron-based catalysts. *Fuel*, **76**(3), pp.273–280.
- Razzaq, R., Li, C., Usman, M., Suzuki, K., Zhang, S., 2015. A highly active and stable Co₄N/γ-Al₂O₃ catalyst for CO and CO₂ methanation to produce synthetic natural gas (SNG). *Chemical Engineering Journal*, **262**, pp1090-1098.
- Reinalda, D., Derking, A., Blankenstein, P., Meuris, T., Gerard, J., Decleer, M., 1990. Process for the preparation of extrudates. EP0428223A1.
- Richardson, J.T., Scates, R., Twigg, M.V., 2003. X-ray diffraction study of nickel oxide reduction by hydrogen. *Applied Catalysis A: General*, **246**, pp.137-150.
- Ren, J., Guo, H., Yang, J., Qin, Z., Lin, J., Li, Z., 2015. Insights into the mechanisms of CO₂

methanation on Ni(111) surfaces by density functional theory. *Applied Surface Science*, **351**, pp.504-516.

Riedel, T., Claeys, M., Schulz, H., Schaub, G., Nam, S.-S., Jun, K.-W., Choi, M.-J., Kishan, G., Lee, K.-W., 1999. Comparative study of Fischer-Tropsch synthesis with H₂/CO and H₂/CO₂ syngas using Fe- and Co-based catalysts. *Applied Catalysis A: General*, **186**, pp.201-213.

Rodden, J.B., Erkey, C., Akgerman, A., 1988. High-Temperature Diffusion, Viscosity and Density Measurements in *n*-Eicosane. *Journal of Chemical and Engineering Data*, **33**(3), pp.344-347.

Rostrup-Nielsen, J., 1993. Reaction Kinetics and Industrial Catalysts. In: Joyner, R.W., van Santen, R.A., Elementary Reaction Steps in Heterogeneous Catalysis. Springer, pp.441-461.

Rynkowski, J.M., Paryjczak, T., Lenik, M., 1993. On the nature of oxidic nickel phases in NiO/ γ -Al₂O₃ catalysts, **106**, pp.73-82.

Sabatier, P.; Senderens, J.B. Nouvelles syntheses du methane, 1902. *C. R. Acad. Sci.* , **134**, pp.514–516

Sai-Prasad, P.S., Bae, J.W., Jun, K.-W. and Lee, K.-W., 2008. Fischer-Tropsch Synthesis by Carbon Dioxide Hydrogenation on Fe-Based Catalysts. *Catalysis Surveys from Asia*, **12**(3), pp.170–183.

Sánchez-López, J.R.G., Martínez-Hernández, A., Hernández-Ramírez, A., 2016. Modelling of transport phenomena in fixed-bed reactors for the Fischer-Tropsch reaction; a brief literature review. *Reviews in Chemical Engineering*, **33**(2), pp.1-33.

Sasaki, S., Fujino, K., Takéuchi, Y., 1979. X-Ray Determination of Electron-Density Distributions in Oxides, MgO, MnO, CoO, and NiO, and Atomic Scattering Factors of their Constituent Atoms. *Proceedings of the Japan Academy, Series B: Physical and Biological Sciences*, **55**(2), pp.43-48.

Schaaf, T., Grünig, J, Schuster, M.R., Rothenfluh, T., Orth, A., 2014. Methanation of CO₂: Storage of renewable energy in a gas distribution system. *Energy, Sustainability and Society*, **4**(2), <https://doi.org/10.1186/s13705-014-0029-1>.

Schaper, H., Doesburg, E.B.M., van Reijen, L.L., 1983. The Influence of Lanthanum Oxide on the Thermal Stability of γ -Alumina Supports. *Applied Catalysis*, **7**, pp.211-220.

Schild, C., Wokaun, A., Koppel, R.A., Balken, A., 1991. Carbon dioxide hydrogenation over

- nickel/zirconia catalysts from amorphous precursors: on the mechanism of methane formation. *Journal of Physical Chemistry*, **95**(16), pp.6341-6346.
- Schlereth, D., 2015. Kinetic and Reactor Modelling for the Methanation of Carbon Dioxide. PhD Thesis. Technische Universitat Munchen.
- Schlichting, K.W., Padture, N.P. and Klemens, P.G., 2001. Thermal conductivity of dense and porous yttria-stabilized zirconia. *Journal of Materials Science*, **36**(12), pp.3003–3010.
- Schulz, H., 1999. Short history and present trends of Fischer-Tropsch synthesis. *Applied Catalysis A: General*, **186**, pp.3–12.
- Schulz, H., 2003. Major and minor reactions in Fischer – Tropsch synthesis on cobalt catalysts. *Topics in Catalysis*, **26** (1–4), pp.73–85.
- Sehabigue, L., 2012. Modelling, Scale-Up and Optimization of Slurry Bubble Column Reactors for Fischer-Tropsch Synthesis. PhD Thesis, University of Pittsburgh.
- Sehested, J., Dahl, S., Jacobsen, J., Rostrup-Nielsen, J.R., 2005. Methanation of CO over Nickel: Mechanism and Kinetics at High H₂/CO Ratios. *Journal of Physical Chemistry B*, **109**(6), pp.2432-2438.
- Shi, B. and Davis, B.H., 2005. Fischer-Tropsch synthesis: The paraffin to olefin ratio as a function of carbon number. *Catalysis Today*, **106**(1–4), pp.129–131.
- Shin, H.H., Lu, L., Yang, Z., Kiely, C.J., McIntosh, S., 2016. Cobalt catalysts with platinum atoms supported on barium zirconate provide enhanced activity and selectivity for CO₂ methanation. *ACS Catalysis*, **6**, pp.2811-2818.
- Shiozaki, K., Kazunori, T., Ohnishi, A., 1981, Cylindrical molded catalyst. US4366093A
- Sing, K.S.W., 1982. Reporting Physisorption Data for Gas/Solid Systems with Special Reference to the Determination of Surface Area and Porosity [online]. Available at: <https://www.iupac.org/publications/pac-2007/1982/pdf/5411x2201.pdf> [Date Accessed: 27th September 2017].
- Smith, D.S., Alzina, A., Bourret, J., Nait-Ali, B., Pennec, F., Tessier-Doyen, N., Otsu, K., Matsubara, H., Elser, P., Gonzenbach, U.T., 2013. Thermal conductivity of porous materials. *Journal of Materials Research*, **28**(17), pp.2260-2272.
- Smrčok, L., Langer, V., Krestan, J., 2006. γ -Alumina: a single-crystal X-ray diffraction study, *Acta Crystallographica Section C*, **62**(9), pp.83-84.

- Snel, R., 1987. Olefins from Syngas. *Catalysis Reviews*, **29**(4), pp.361–445.
- Solc, M., 1962. Kinetik der Hydrierung des Kohlendioxyds zu Methan an einem Nickel-Chrom(III)-Oxyd-Katalysator. *Collection of Czechoslovak Chemical Communications*.**27**(11), pp. 2621-2627.
- Soled, S.L., Iglesia, E., Fiato, R.A., Baumgartner, J.E., Vroman, H., Miseo, S., 2003. Control of metal dispersion and structure by changes in the solid-state chemistry of supported cobalt Fischer-Tropsch catalysts. *Topics in Catalysis*, **26**, pp.101-109.
- Soled, S.L., Iglesia, E., Miseo, S., DeRites, B.A. and Fiato, R.A., 1995. Selective synthesis of alpha-olefins on Fe-Zn Fischer-Tropsch catalysts. *Topics in Catalysis*, **2**, pp.193–205.
- Soomro, M. and Hughes, R., 1976. The Thermal Conductivity of Porous Catalyst Pellets. *The Canadian Journal of Chemical Engineering*, **57**, pp.358–363.
- Urasaki, K., Tanpo, Y., Nagashima, Y., Kikuchi, R., Satokawa, S., 2013. Effects of preparation conditions of Ni/TiO₂ catalysts for selective CO methanation in the reformate gas. *Applied Catalysis A: General*, pp.174-178.
- Van de Loosdrecht, J., Barradas, S., Caricato, E.A., Ngwenya, N.G., Nkwanyana, P.S., Rawat, M.A.S., Sigwebela, B.H., van Berge, P.J., Visagie, J.L., 2003. Calcination of Co-based Fischer-Tropsch synthesis catalysts. *Topics in Catalysis*, **26**(1-4), pp.121-127.
- Van de Loosdrecht, J., van der Haar, M., van der Kraan, A.M., van Dillen, A.J., Geus, J.W., 1997. Preparation and properties of supported cobalt catalysts for Fischer-Tropsch synthesis. *Applied Catalysis A: General*, **150**, pp.365-376.
- van der Laan, G.P. and Beenackers, A.A.C.M., 1999. Kinetics and Selectivity of the Fischer-Tropsch Synthesis: A Literature Review. *Catalysis Reviews*, **41**(3&4), pp.255–318.
- van Dijk, W., Niemantsverdriet, J., van der Kraan, A. and van der Baan, H.S., 1982. Effects of Manganese Oxide and Sulphate on the Olefin Selectivity of Iron Catalyst in the Fischer Tropsch Reaction. *Applied Catalysis*, **2**, pp.273–288.
- van Herwijnen, T., Van Doesburg, H., De Jong, W.A., 1973. Kinetics of the methanation of CO and CO₂ on a nickel catalyst. *Journal of Catalysis*, **28**(3), pp.391-402.
- van Meerten, R.Z.C., Vollenbroek, J.G., de Croon, M.H.J.M., van Nisselrooy, P.F.M.T., Coenen, J.W.E., 1982. The Kinetics and Mechanism of the Methanation of Carbon Monoxide on a Nickel-Silica Catalyst. *Applied Catalysis*, **3**(1), pp.29-56.
- Vance, C.K., Bartholomew, C.H., 1983. Hydrogenation of carbon dioxide on group VIII

metals: III, Effects of support on activity/selectivity and adsorption properties of nickel. *Applied Catalysis*, **7**(2), pp.167-177.

Varma, R.L., Bakhshi, N.N. and Mathews, J.F., 1990. Selective synthesis of hydrocarbons from syngas using nickel/ZSM-5 catalysts. *Industrial & Engineering Chemistry Research*, **29**(9), pp.1753–1757.

Velocys, 2017. Our Biorefineries [online]. Available at:<https://www.velocys.com/our-biorefineries/> [Date Accessed 27th September 2017].

Vervloet, D., Kapteijn, F., Nijenhuis, J. and van Ommen, J.R., 2012. Fischer-Tropsch reaction–diffusion in a cobalt catalyst particle: aspects of activity and selectivity for a variable chain growth probability. *Catalysis Science & Technology*, **2**(6), p.1221.

Visconti, C.G., Lietti, L., Tronconi, E., Forzatti, P., Zennaro, R. and Finocchio, E., 2009. Fischer–Tropsch synthesis on a Co/Al₂O₃ catalyst with CO₂ containing syngas. *Applied Catalysis A: General*, **355**(1–2), pp.61–68.

Vlasenko, V.M., Yuzefovich, G.E., 1969. Mechanism of the Catalytic Hydrogenation of Oxides of Carbon to Methane. *Russian Chemical Reviews*, **38**(9), pp.728-739.

Wakao, N. and Funazkri, T., 1978. Effect of fluid dispersion coefficients on particle-to-fluid mass transfer coefficients in packed beds. *Chemical Engineering*

Wang, G., Xu, S., Jiang, L., Wang, C., 2016. Nickel supported on iron-bearing olivine for CO₂ methanation. *International Journal of Hydrogen Energy*, **41**, pp.12910-12919.

Wang, W., Wang, S., Ma, X., Gong, J., 2011. Recent advances in catalytic hydrogenation of carbon dioxide. *Chemical Society reviews*, **40**(7), pp.3703–3727.

Wang, Y.-N., Xu, Y.-Y., Xiang, H.-W., Li, Y.-W. and Zhang, B.-J., 2001. Modelling of Catalyst Pellets for Fischer–Tropsch Synthesis. *Industrial & Engineering Chemistry Research*, **40**(20), pp.4324–4335.

Weatherbee, G.D., Bartholomew, C.H., 1982. Hydrogenation of CO₂ on group VIII metals. II. Kinetics and mechanism of CO₂ hydrogenation on nickel. *Journal of Catalysis*, **77**(2), pp.460-472.

Weatherbee, G.D. and Bartholomew, C.H., 1984. Hydrogenation of CO₂ on group VIII metals: IV. Specific activities and selectivities of silica-supported Co, Fe, and Ru. *Journal of Catalysis*, **87**(2), pp.352–362.

Westermann, A., Azambre, B., Bacariza, M.C., Graça, I., Ribiero, M.F., Lopes, J.M.,

- Henriques, C., 2015. Insight into CO₂ methanation mechanisms over NiUSY zeolites: An *operando* IR study. *Applied Catalysis B: Environmental.* **174**, pp.120-125.
- Wijngaarden, R.J., Kronberg, A., Westerterp, K.R., 1998. Industrial Catalysis: Optimizing Catalysts and Processes., Weinheim, Germany: Wiley-VCH Verlag.
- Wilke, C.R., Chang, P., 1955. Correlation of diffusion coefficients in dilute solutions. *AIChE Journal*, **1**(2), pp.264-270.
- Withers, H.P., Eliezer, K.F. and Mitchell, J.W., 1990. Slurry-phase Fischer-Tropsch synthesis and kinetic studies over supported cobalt carbonyl derived catalysts. *Industrial & Engineering Chemistry Research*, **29**(9), pp.1807–1814.
- Yan, Z., Wang, Z., Bukur, D.B., Goodman, D.W., 2009. Fischer-Tropsch synthesis on a model Co/SiO₂ catalyst. *Journal of Catalysis*, **268**, pp.196-200.
- Yao, Y., 2011. *Fischer-Tropsch Synthesis Using CO₂-Containing Syngas Mixtures Over Cobalt and Iron Based Catalysts*. University of the Witwatersrand, Johannesburg.
- Yao, Y., Hildebrandt, D., Glasser, D. and Liu, X., 2010. Fischer-Tropsch Synthesis Using H₂/CO/CO₂ Syngas Mixtures over a Cobalt Catalyst. *Industrial & Engineering Chemistry Research*, **49**, pp.11061–11066.
- Yates, J.T., Gates, S.M., Russel Jr, J.N., 1985. Chemisorbed Methyl as an Intermediate Surface Species in the Methanation Reaction on Nickel. *Surface Science*, **164**, pp.839-847.
- Yates, I.C. and Satterfield, C.N., 1991. Intrinsic kinetics of the Fischer-Tropsch synthesis on a Cobalt Catalyst. *Energy & Fuels*, **5**, pp.168–173.
- Zagli, E., Falconer, J.L., 1981. Carbon dioxide adsorption and methanation on ruthenium. *Journal of Catalysis*, **69**(1), pp.1-8.
- Zhang, Y., Jacobs, G., Sparks, D.E., Dry, M.E. and Davis, B.H., 2002. CO and CO₂ hydrogenation study on supported cobalt Fischer-Tropsch synthesis catalysts. *Catalysis today*, **71**(3–4), pp.411–418.
- Zhou, G., Wu, T., Xie, H., Zheng, X., 2013. Effects of structure on the carbon dioxide methanation performance of Co-based catalysts. *International Journal of Hydrogen Energy*, **38**(24), pp.10012-10018.
- Zielinski, J., 1982. Morphology of Nickel/Alumina catalysts. *Journal of Catalysis*, **76**(1), pp.157-163.

10 Nomenclature

10.1 Abbreviations

Abbreviations followed by a # indicate they may be followed by a number as an identifier for the abbreviated part.

(ads)	Adsorbed, indicating surface species.
AOV#	Air Operated Valve
ASF	Anderson-Schulz-Flory
BET	Brunauer Emmett Teller
BJH	Barrett Joyner Halenda
BPR#	Back Pressure Regulator
BTRS	Bench Top Reactor System
cat	Catalyst
CNT	Carbon nanotube
CV#	Check Valve
DFT	Density Functional Theory
DRIFTS	Diffuse-reflectance infrared spectroscopy
FID	Flame Ionisation Detector
FT	Fischer-Tropsch
FTIR	Fourier Transform Infra-Red
GC	Gas Chromatograph
GHSV	Gas Hourly Space Velocity
ID	Internal Diameter
IR	Infra-red
IWI	Incipient Wetness Impregnation
LC#	Level Controller
LHHW	Langmuir Hinshelwood Hougan Watson
MASI	Most abundant surface intermediate
MFC	Mass Flow Controller
NIST	National Institute of Standards and Technology
NV	Needle Valve
OD	Outer Diameter
ODE	Ordinary Differential Equation

PID	Proportional Integral Derivative
PG#	Pressure Gauge
RG#	Regulator
SEM	Scanning Electron Microscopy
SSITKA	Steady-State Isotopic Transient Kinetic Analysis
SL#	Sample Loop
SNG	Synthetic Natural Gas
STP	Standard Temperature and Pressure (25°C and 1 bar)
SV#	Solenoid Valve
TC#	Thermocouple
TCD	Thermal Conductivity Detector
TEM	Transmission Electron Microscopy
TGA	Thermogravimetric Analysis/Analyser
TI#	Temperature Indicator
TIC	Temperature Indicator Controller
TPR	Temperature Programmed Reduction
WGS	Water-gas shift reaction
V#	Valve
XRD	X-ray Diffraction

10.2 Symbols

A	Pre-exponential Arrhenius constant	[Varies]
a_I	Kinetic parameter for model I	[Varies]
b_I	Kinetic parameter for model I	[Varies]
c_I	Kinetic parameter for model I	[Varies]
C_j	Concentration of species j	[mol m ⁻³]
\bar{C}_j	Dimensionless concentration of species j	[-]
$C_{j,0}$	Surface concentration of species j	[mol m ⁻³]
d_I	Kinetic parameter for model I	[Varies]
D_{eff}	Effective diffusivity	[m ² s ⁻¹]
D_{bulk}	Bulk diffusivity	[m ² s ⁻¹]
D_j	Diffusivity of species j in wax medium	[m ² s ⁻¹]
D_{12}	Diffusivity of species 1 in species 2	[m ² s ⁻¹]
E_A	Activation energy	[kJ/mol]
F	Volumetric flowrate of gas under standard conditions (25°C and 1 bar)	[cm ³ min ⁻¹]
\bar{G}_j	Molar Gibbs energy of pure species j	
GHSV	Gas Hourly Space Velocity. The ratio of volumetric flow under standard conditions (25°C and 1 atm) to the volume of the catalyst bed.	[h ⁻¹]
\bar{H}	Molar Enthalpy	[J mol ⁻¹]
H_i	Henry Constant	[bar ⁻¹]
k	Thermal conductivity	[W/m K]
k_p	Chain propagation rate constant	[mol s ⁻¹]
k_t	Chain termination rate constant	[mol s ⁻¹]
K_{Eq}	Equilibrium Constant	[-]
L	Cylindrical pellet half-length or Slab half-thickness	[-]
m_{cat}	Catalyst mass	[g]
M_j	Molecular mass of species j	[g mol ⁻¹]
n	Power law exponent	[-]
n_j	Moles of species j	[mole]
N	Carbon number	[-]
N_A	Avagadro's constant	[mol ⁻¹]

NE	Number of elements	[$-$]
obj	Objective function	[$-$]
P	Pressure	[bar]
P_j	Partial pressure of species j	[bar]
R_{Gas}	Ideal gas constant	[J mol $^{-1}$ K $^{-1}$]
r	Radial position within spherical/cylindrical pellet	[m]
\bar{r}	Dimensionless radius	[$-$]
r_p or r_0	Particle radius	[m]
R_j	Rate of formation of species j	[mol g $_{\text{cat}}^{-1}$ s $^{-1}$]
\bar{R}_j	Dimensionless rate of reaction	[$-$]
$R_{i,0}$	Surface rate of reaction	[$-$]
RF_j	TCD or FID response factor of species j	[%/Area]
\bar{S}	Molar Entropy	[J mol $^{-1}$ K $^{-1}$]
S_P	Particle surface area	[m 2]
t	Time	[s]
T	Temperature	[K]
\bar{T}	Dimensionless temperature	[$-$]
T_0	Reference temperature	[K]
v_i	Stoichiometric coefficient	[$-$]
\dot{V}	Volumetric flowrate	[m 3 s $^{-1}$]
V_{Reactor}	Reactor volume	[m 3]
\bar{V}	Molar volume	[m 3 mol $^{-1}$]
\bar{V}_0	Molar volume of solvent	[m 3 mol $^{-1}$]
V_P	Particle volume	[m 3]
x_j	Mole fraction of species j	[$-$]
y_j	Mole fraction of species j in wax phase	[$-$]
W_N	Weight fraction of product of carbon number N	[$-$]
z	Axial direction within cylindrical catalyst pellet	[m]
\bar{z}	Dimensionless axial position	[$-$]
*	Asterisk appended to chemical species, representing surface adsorption.	[$-$]

10.3 Greek Symbols

α	Anderson-Schulz-Flory chain growth parameter	[$-$]
β	Pellet aspect ratio (radius/half-length)	[$-$]
γ	Dimensionless parameter $\left(\frac{kT_0}{\Delta H_0 R_{CO,0} r_0^2} \right)$	[$-$]
ΔH_j	Enthalpy change of formation of species j	[kJ/mol]
ΔH_{Rxn}	Enthalpy change of reaction	[kJ/mol]
ε	Voidage	[$-$]
η	Effectiveness factor	[$-$]
θ	X-ray Diffraction Angle	[$^\circ$]
κ_i	Dimensionless parameter $\left(\frac{D_i C_{i,0}}{R_{i,0} r_0^2} \right)$	[$-$]
λ	Aspect ratio	[$-$]
μ_s	Solvent viscosity	[cP]
μ	Radius ratio	[$-$]
ρ_m	Molar density	[mol m $^{-3}$]
ρ_{cat}	Catalyst mass density	[g m $^{-3}$]
σ_1	Hard sphere diameter of species 1	[\AA]
τ	Tortuosity	[$-$]
χ	Simulation time	[s]
Φ	Thiele Modulus	[$-$]
φ	Association parameter	[$-$]

A1. Appendix A. Derivation of Langmuir-Hinshelwood Expressions for CO₂ Methanation.

A1.1. Introduction

The kinetic equations for CO₂ methanation have been derived using a methodology analogous to that of Weatherbee and Bartholomew (1982). This method has been applied in the derivation of carbon oxide hydrogenation kinetics by Kopyscinsky *et al.* (2010), Schlereth (2015) and Lim (2014).

The form of Langmuir-Hinshelwood type kinetic expressions depend on (i) the assumed mechanism and its underlying reaction set, (ii) the rate-limiting step (RLS) and (iii) the most abundant surface intermediates. The assumption of the mechanism permits a rate-limiting step to be selected and tested, whilst the identity of the most abundant surface intermediates (MASI) are determined through assumptions of equilibrium positions.

The following section provides the reaction sets examined, a sample derivation and tables of possible Langmuir-Hinshelwood expressions. The following symbols P_i , R_x , θ_i , k_x and k_{-x} are defined as the partial pressure of species i , the net forward reaction rate of step x , the site occupancy fraction of species i , the forward reaction constant for step x , and the reverse reaction constant for step x respectively. The equilibrium constant for step x is expressed as $K_x = k_x/k_{-x}$. Vacant sites in the reaction set are indicated by a * with the vacancies indicated by θ_* . An intermediate bound to the catalyst surface is indicated as X*, where X is the bound species.

As noted in Chapter 4, the mechanism for CO₂ methanation is typically discussed in terms of a surface carbon intermediate (carbide-type mechanism) or in terms of a formyl intermediate (formyl-type mechanism). The elementary steps for these reactions are set forth in the following tables alongside Langmuir expressions derived on the basis of various rate-determining steps and assumptions. Elementary steps highlighted in **bold** are considered as potential rate-limiting steps.

A1.2. Carbide-Type Mechanism

A1.2.1. Carbide Mechanism: Carbon Monoxide Dissociation Rate-Limiting Step

The dissociation of carbon monoxide to surface carbon and oxygen (A1.8) has been reported to be the rate-limiting step in this reaction scheme by Weatherbee and Bartholomew (1982). Under this assumption, the rate of methanation is described as (A1.1).

$$R_{CH_4} = k_3 \theta_{CO} \theta_* \quad (A1.1)$$

The elementary steps of the reaction are given in Table A1.1. The reaction was assumed to be irreversible and thus the recombination of surface carbon and oxygen negligible. Under this scheme, the adsorption of carbon dioxide and hydrogen were assumed to be at quasi-equilibrium, *i.e.* the rates of adsorption and desorption are significantly greater than the rate of CO consumption. Hence, the coverages of CO, H₂O and H may be expressed as (A1.2)-(A1.4).

$$K_2 P_{CO_2} \theta_*^2 = \theta_{CO} \theta_O \quad (A1.2)$$

$$\theta_{H_2O} = \frac{P_{H_2O} \theta_*}{K_{11}} \quad (A1.3)$$

$$\theta_H = \sqrt{K_1 P_{H_2}} \theta_* \quad (A1.4)$$

If the adsorbed water dissociates to form hydroxyl groups and hydrogen, the site occupancy may be expressed as:

$$\theta_{OH} = \frac{\theta_{H_2O} \theta_*}{K_{10} \theta_H} = \frac{P_{H_2O} \theta_*}{K_{10} K_{11} \sqrt{K_1 P_{H_2}}} \quad (A1.5)$$

The carbon monoxide site occupancy may be determined from (A1.2) upon determination of θ_O . In the derivation of the Langmuir-Hinshelwood expressions for this rate-limiting step, the form of the oxygen removal reaction selected influences the final equation. In their work, Lim (2014) set reaction (A1.14) as quasi-equilibrium and (A1.15) as irreversible. Schlereth (2015) however selected (A1.14) to be irreversible, *i.e.* the equilibrium was assumed to favour products to an extent that the reverse reaction could be ignored. If (A1.15) is set as irreversible, the oxygen occupancy is expressed by rearrangement of (A1.18) and insertion of the (A1.14) equilibrium relationship, since the oxygen generation rate is twice the rate of methanation at steady state.

Table A1.1. Kinetic scheme for CO₂ methanation *via* a surface carbon intermediate.

#	Reaction Step	Forward Reaction	Reverse Reaction	Surface Equilibrium Relationship
(A1.6)	H ₂ (g)+2*=2H*	R ₁ = k ₁ P _{H₂} θ* ²	R ₁ ' = k ₋₁ θ _H ²	θ _H = √K ₁ P _{H₂} θ*
(A1.7)	CO ₂ (g)+2*=CO*+O*	R ₂ = k ₂ P _{CO₂} θ* ²	R ₂ ' = k ₋₂ θ _{CO} θ _O	K ₂ P _{CO₂} θ* ² = θ _{CO} θ _O
(A1.8)	CO*+*=C*+O*	R ₃ = k ₃ θ _{CO} θ*	R ₃ ' = k ₋₃ θ _C θ _O	K ₃ θ _{CO} θ* = θ _C θ _O
(A1.9)	C*+H*=CH*+*	R ₄ = k ₄ θ _C θ _H	R ₄ ' = k ₋₄ θ _{CH} θ*	K ₄ θ _C θ _H = θ _{CH} θ*
(A1.10)	CH*+H*=CH ₂ *+*	R ₅ = k ₅ θ _{CH} θ _H	R ₅ ' = k ₋₅ θ _{CH₂} θ*	K ₅ θ _{CH} θ _H = θ _{CH₂} θ*
(A1.11)	CH ₂ *+H*=CH ₃ *+*	R ₆ = k ₆ θ _{CH₂} θ _H	R ₆ ' = k ₋₆ θ _{CH₃} θ*	K ₆ θ _{CH₂} θ _H = θ _{CH₃} θ*
(A1.12)	CH ₃ *+H*=CH ₄ *+*	R ₇ = k ₇ θ _{CH₃} θ _H	R ₇ ' = k ₋₇ θ _{CH₄} θ*	K ₇ θ _{CH₃} θ _H = θ _{CH₄} θ*
(A1.13)	CH ₄ *=CH ₄ (g)+*	R ₈ = k ₈ θ _{CH₄}	R ₈ ' = k ₋₈ P _{CH₄} θ*	θ _{CH₄} = $\frac{P_{CH_4}\theta_*}{K_8}$
(A1.14)	O*+H*=OH*+*	R ₉ = k ₉ θ _O θ _H	R ₉ ' = k ₋₉ θ _{OH} θ*	K ₉ θ _O θ _H = θ _{OH} θ*
(A1.15)	OH*+H*=H ₂ O*+*	R ₁₀ = k ₁₀ θ _{OH} θ _H	R ₁₀ ' = k ₋₁₀ θ _{H₂O} θ*	K ₁₀ θ _{OH} θ _H = θ _{H₂O} θ*
(A1.16)	H ₂ O*=H ₂ O(g)+*	R ₁₁ = k ₁₁ θ _{H₂O}	R ₁₁ ' = k ₋₁₁ P _{H₂O} θ*	θ _{H₂O} = $\frac{P_{H_2O}\theta_*}{K_{11}}$
(A1.17)	CO*=CO(g)+*	R ₁₂ = k ₁₂ θ _{CO}	R ₁₂ ' = k ₋₁₂ P _{CO} θ*	θ _{CO} = $\frac{P_{CO}\theta_*}{K_{12}}$

$$R_{10} = k_{10}\theta_{OH}\theta_H = 2k_3\theta_{CO}\theta_* \quad (\text{A1.18})$$

$$k_{10}\left(\frac{K_9\theta_O\theta_H}{\theta_*}\right)\theta_H = 2k_3\theta_{CO}\theta_* \quad (\text{A1.19})$$

$$\theta_O = \frac{2k_3\theta_{CO}\theta_*^2}{k_{10}K_9\theta_H^2} \quad (\text{A1.20})$$

This may be combined with the equilibrium relationship for CO₂ adsorption (A1.21).

$$K_2 P_{CO_2} \theta_*^2 = \theta_{CO} \theta_O \quad (\text{A1.21})$$

$$\theta_{CO}\theta_O = \frac{2k_3\theta_{CO}^2\theta_*^2}{k_{10}K_9\theta_H^2} = K_2 P_{CO_2} \theta_*^2 \quad (\text{A1.22})$$

Hence

$$\theta_{CO}^2 = \frac{K_2 P_{CO_2} k_{10} K_9 \theta_H^2}{2k_3} \quad (\text{A1.23})$$

$$\theta_{CO} = \sqrt{\left(\frac{K_2 k_{10} K_9 K_1}{2k_3}\right) P_{CO_2} P_{H_2} \theta_*} \quad (\text{A1.24})$$

This yields a rate of methanation of

$$R_{CH_4} = k_3 \sqrt{\left(\frac{K_2 k_{10} K_9 K_1}{2k_3}\right) P_{CO_2} P_{H_2} \theta_*^2} \quad (\text{A1.25})$$

The fraction of empty sites may be determined from the site balance given (A1.26).

$$\theta_* + \theta_{CO} + \theta_H + \theta_{H_2O} + \theta_{OH} + \theta_O = 1 \quad (\text{A1.26})$$

In the case of Lim's derivation, the most abundant surface intermediates (MASI) were assumed to be H, CO and H₂O, or O, CO and H₂O in a separate derivation. The first results in the vacancy expression (A1.27) and the latter in expression (A1.28).

$$\theta_* = \frac{1}{\left(1 + \sqrt{K_1 P_{H_2}} + \sqrt{\left(\frac{K_2 k_{10} K_9 K_1}{2k_3}\right) P_{CO_2} P_{H_2}} + \frac{P_{H_2O}}{K_{11}}\right)} \quad (\text{A1.27})$$

$$\theta_* = \frac{1}{\left(1 + \sqrt{\left(\frac{2k_3 K_2}{k_{10} K_9 K_1}\right)} \sqrt{\left(\frac{P_{CO_2}}{P_{H_2}}\right)} + \sqrt{\left(\frac{K_2 k_{10} K_9 K_1}{2k_3}\right) P_{CO_2} P_{H_2}} + \frac{P_{H_2O}}{K_{11}}\right)} \quad (\text{A1.28})$$

The resultant rate expressions are given by (A1.29) and (A1.30) respectively.

$$R_{CH_4} = \frac{k_3 \sqrt{\left(\frac{K_2 k_{10} K_9 K_1}{2k_3}\right) P_{CO_2} P_{H_2}}}{\left(1 + \sqrt{K_1 P_{H_2}} + \sqrt{\left(\frac{K_2 k_{10} K_9 K_1}{2k_3}\right) P_{CO_2} P_{H_2}} + \frac{P_{H_2O}}{K_{11}}\right)^2} \quad (\text{A1.29})$$

$$R_{CH_4} = \frac{k_3 \sqrt{\left(\frac{K_2 k_{10} K_9 K_1}{2k_3}\right) P_{CO_2}^{0.5} P_{H_2}^{0.5}}}{\left(1 + \sqrt{\left(\frac{2k_3 K_2}{k_{10} K_9 K_1}\right)} \left(\frac{P_{CO_2}^{0.5}}{P_{H_2}^{0.5}}\right) + \sqrt{\left(\frac{K_2 k_{10} K_9 K_1}{2k_3}\right) P_{CO_2}^{0.5} P_{H_2}^{0.5}} + \frac{P_{H_2O}}{K_{11}}\right)^2} \quad (\text{A1.30})$$

The alternative assumption of Schlereth (2015) alters the expression for the oxygen occupancy.

$$R_9 = k_9 \theta_O \theta_H = 2k_3 \theta_{CO} \theta_* \quad (\text{A1.31})$$

$$\theta_O = \frac{2k_3 \theta_{CO}}{k_9 \sqrt{K_1 P_{H_2}}} \quad (\text{A1.32})$$

Substituting this expression into (A1.21) yields (A1.33).

$$\frac{2k_3 \theta_{CO}^2}{k_9 \sqrt{K_1 P_{H_2}}} = K_2 P_{CO_2} \theta_*^2 \quad (\text{A1.33})$$

$$\theta_{CO} = \sqrt{\frac{k_9 K_2 \sqrt{K_1}}{2k_3}} P_{CO_2}^{0.5} P_{H_2}^{0.25} \theta_* \quad (\text{A1.34})$$

The rate of methanation is then expressed as (A1.35) under the assumption of CO, H and H₂O MASI:

$$R_{CH_4} = \frac{k_3 \sqrt{\frac{k_9 K_2 \sqrt{K_1}}{2k_3}} P_{CO_2}^{0.5} P_{H_2}^{0.25}}{\left(1 + \sqrt{\frac{k_9 K_2 \sqrt{K_1}}{2k_3}} P_{CO_2}^{0.5} P_{H_2}^{0.25} + \sqrt{K_1 P_{H_2}} + \frac{P_{H_2 O}}{K_{11}}\right)^2} \quad (\text{A1.35})$$

Under the assumption of full reversibility for reactions (A1.14) and (A1.15), the oxygen site occupancy may be expressed as (A1.36).

$$\theta_O = \frac{\theta_{OH} \theta_*}{K_9 \theta_H} = \frac{P_{H_2 O} \theta_*}{K_9 K_{10} K_{11} K_1 P_{H_2}} \quad (\text{A1.36})$$

This yields a CO site occupancy expressed by

$$\theta_{CO} = \frac{K_9 K_{10} K_{11} K_1 P_{H_2} K_2 P_{CO_2} \theta_*}{P_{H_2 O}} \quad (\text{A1.37})$$

Consequently, the methanation rate is expressed by (A1.38) for H, OH, O and CO MASI.

$$R_{CH_4} = \frac{k_3 K_9 K_{10} K_{11} K_1 P_{H_2} K_2 P_{CO_2}}{P_{H_2 O} \left(1 + \sqrt{K_1 P_{H_2}} + \frac{K_9 K_{10} K_{11} K_1 K_2 P_{H_2} P_{CO_2}}{P_{H_2 O}} + \frac{P_{H_2 O}}{K_9 K_{10} K_{11} K_1 P_{H_2}} + \frac{P_{H_2 O}}{K_{10} K_{11} \sqrt{K_1 P_{H_2}}}\right)^2} \quad (\text{A1.38})$$

Here gas phase water is assumed to dissociate to hydrogen and hydroxyl groups upon adsorption to the catalyst surface. The identities of the MASI depend on the positions of the water formation equilibria.

A1.2.2. Carbide Mechanism: Other Rate-Limiting Steps

Table A1.2 provides a summary of alternative kinetic equations and statements of the assumed rate-limiting steps and other assumptions on the basis of the carbide mechanism. Mechanisms based on a formyl type intermediate are examined in §A1.3.

Table A1.2. A summary of the Langmuir-Hinshelwood models developed, their assumed reaction scheme, and the most abundant surface intermediates.

	Methanation Kinetic Equation	MASI	Rate-limiting Step [Additional Assumptions]
C2a	$R_{CH_4} = \frac{k_2 P_{CO_2}}{\left(1 + \sqrt{K_1 P_{H_2}} + \frac{P_{H_2O}}{K_{11}}\right)^2}$	H and H ₂ O	CO ₂ Adsorption (A1.7) [Quasi-equilibrium adsorption in H and H ₂ O]
C2b	$R_{CH_4} = \frac{k_2 P_{CO_2}}{\left(1 + \sqrt{K_1 P_{H_2}} + \frac{P_{H_2O}}{K_{10} K_{11} \sqrt{K_1 P_{H_2}}}\right)^2}$	H and OH	CO ₂ Adsorption (A1.7) [Quasi-equilibrium adsorption in H and H ₂ O]
C3a	$R_{CH_4} = \frac{k_3 \sqrt{\left(\frac{K_2 k_{10} K_9 K_1}{2k_3}\right)} P_{CO_2}^{0.5} P_{H_2}^{0.5}}{\left(1 + \sqrt{K_1 P_{H_2}} + \sqrt{\left(\frac{K_2 k_{10} K_9 K_1}{2k_3}\right)} P_{CO_2}^{0.5} P_{H_2}^{0.5} + \frac{P_{H_2O}}{K_{11}}\right)^2}$	H, H ₂ O, CO	CO dissociation (A1.8) / (A1.15) assumed irreversible.]
C3b	$R_{CH_4} = \frac{k_3 \sqrt{\left(\frac{K_2 k_{10} K_9 K_1}{2k_3}\right)} P_{CO_2}^{0.5} P_{H_2}^{0.5}}{\left(1 + \sqrt{\left(\frac{2k_3 K_2}{k_{10} K_9 K_1}\right)} \left(\frac{P_{CO_2}^{0.5}}{P_{H_2}^{0.5}}\right) + \sqrt{\left(\frac{K_2 k_{10} K_9 K_1}{2k_3}\right)} P_{CO_2}^{0.5} P_{H_2}^{0.5} + \frac{P_{H_2O}}{K_{11}}\right)^2}$	O, CO and H ₂ O	CO dissociation (A1.8) / (A1.15) assumed irreversible.]
C3c	$R_{CH_4} = \frac{k_3 \sqrt{\frac{k_9 K_2 \sqrt{K_1}}{2k_3}} P_{CO_2}^{0.5} P_{H_2}^{0.25}}{\left(1 + \sqrt{\frac{k_9 K_2 \sqrt{K_1}}{2k_3}} P_{CO_2}^{0.5} P_{H_2}^{0.25} + \sqrt{K_1 P_{H_2}} + \frac{P_{H_2O}}{K_{11}}\right)^2}$	H, H ₂ O, CO	CO dissociation (A1.8) / (A1.14) assumed irreversible.]
C3d	$R_{CH_4} = \frac{k_3 K_9 K_{10} K_{11} K_1 P_{H_2} K_2 P_{CO_2}}{P_{H_2O} \left(1 + \sqrt{K_1 P_{H_2}} + \frac{K_9 K_{10} K_{11} K_1 K_2 P_{H_2} P_{CO_2}}{P_{H_2O}} + \frac{P_{H_2O}}{K_9 K_{10} K_{11} K_1 P_{H_2}} + \frac{P_{H_2O}}{K_{10} K_{11} \sqrt{K_1 P_{H_2}}}\right)^2}$	H, O, CO, OH	CO dissociation (A1.8) / (A1.14) assumed irreversible.]

C4a	$R_{CH_4} = \frac{k_4 \sqrt[3]{\left(\frac{k_9}{2k_4}\right)^2 K_2 K_3 P_{CO_2}}^{0.33} \sqrt{K_1} P_{H_2}^{0.5}}{\left(1 + \sqrt{K_1 P_{H_2}} + \sqrt[3]{\left(\frac{k_9}{2k_4}\right)^2 K_2 K_3 P_{CO_2}}^{0.33} + \frac{P_{H_2O}}{K_{11}}\right)^2}$	H, C and H ₂ O	C Hydrogenation (A1.9) [<i>(A1.14) assumed irreversible</i>]
C4b	$R_{CH_4} = \frac{k_4 \sqrt[3]{\left(\frac{K_9 k_{10}}{2k_4}\right)^2 K_1 K_2 K_3 P_{CO_2}}^{0.33} \sqrt{K_1} P_{H_2}^{0.833}}{\left(1 + \sqrt{K_1 P_{H_2}} + \sqrt[3]{\left(\frac{K_9 k_{10}}{2k_4}\right)^2 K_1 K_2 K_3 P_{CO_2}}^{0.33} P_{H_2}^{0.33} + \frac{P_{H_2O}}{K_{11}}\right)^2}$	H, C, H ₂ O	C Hydrogenation (A1.9) [<i>(A1.15) assumed irreversible</i>]
C4c	$R_{CH_4} = \frac{k_4 K_2 K_3 K_1^{2.5} (K_9 K_{10} K_{11})^2 P_{CO_2} P_{H_2}^{2.5}}{P_{H_2O}^2 \left(1 + \sqrt{K_1 P_{H_2}} + K_2 K_3 (K_1 K_9 K_{10} K_{11})^2 \frac{P_{CO_2} P_{H_2}^{2.5}}{P_{H_2O}^2} + \frac{P_{H_2O}}{K_{11}}\right)^2}$	H, C, H ₂ O	C Hydrogenation (A1.9) [<i>Quasi-equilibrium gas adsorption</i>]
C5a	$R_{CH_4} = \frac{k_5 \sqrt[3]{\left(\frac{k_9}{2k_5}\right)^2 \sqrt{K_1} K_2 K_3 K_4 P_{CO_2}}^{0.33} \sqrt{K_1} P_{H_2}^{0.66}}{\left(1 + \sqrt{K_1 P_{H_2}} + \sqrt[3]{\left(\frac{k_9}{2k_5}\right)^2 \sqrt{K_1} K_2 K_3 K_4 P_{CO_2}}^{0.33} P_{H_2}^{0.16} + \frac{P_{H_2O}}{K_{11}}\right)^2}$	H, CH, H ₂ O	CH Hydrogenation (A1.10) [<i>(A1.14) assumed irreversible</i>]
C5b	$R_{CH_4} = \frac{k_5 \sqrt[3]{\left(\frac{k_{10} K_9}{2k_5}\right)^2 K_1^{1.5} K_2 K_3 K_4 P_{CO_2}}^{0.33} \sqrt{K_1} P_{H_2}}{\left(1 + \sqrt{K_1 P_{H_2}} + \sqrt[3]{\left(\frac{k_{10} K_9}{2k_5}\right)^2 K_1^{1.5} K_2 K_3 K_4 P_{CO_2}}^{0.33} P_{H_2}^{0.5} + \frac{P_{H_2O}}{K_{11}}\right)^2}$	H, CH, H ₂ O	CH Hydrogenation (A1.10) [<i>(A1.15) assumed irreversible</i>]
C5c	$R_{CH_4} = \frac{k_5 (K_1^2 K_2 K_3 K_4) (K_9 K_{10} K_{11})^2 P_{CO_2} P_{H_2}^{2.5}}{P_{H_2O}^2 \left(1 + \sqrt{K_1 P_{H_2}} + (K_1^{1.5} K_2 K_3 K_4) (K_9 K_{10} K_{11})^2 \frac{P_{CO_2} P_{H_2}^{1.5}}{P_{H_2O}^2} + \frac{P_{H_2O}}{K_{11}}\right)^2}$	H, CH, H ₂ O	CH Hydrogenation (A1.10) [<i>Quasi-equilibrium gas adsorption</i>]

C6	$R_{CH_4} = \frac{k_9 \sqrt{(K_1^3 K_2 K_3 K_4 K_5 K_6 K_7 K_8)} P_{CO_2}^{0.5} P_{H_2}^{1.5}}{P_{CH_4}^{0.5} \left(1 + \sqrt{K_1 P_{H_2}} + \sqrt{(K_1^2 K_2 K_3 K_4 K_5 K_6 K_7 K_8)} \frac{P_{CO_2}^{0.5} P_{H_2}}{P_{CH_4}^{0.5}} + \frac{P_{H_2 O}}{K_{11}} \right)^2}$	O, H, H ₂ O	O Hydrogenation (A1.14) [Quasi-equilibrium gas adsorption]
C7	$R_{CH_4} = \frac{k_{10} K_9 \sqrt{(K_1^4 K_2 K_3 K_4 K_5 K_6 K_7 K_8)} P_{CO_2}^{0.5} P_{H_2}^2}{P_{CH_4}^{0.5} \left(1 + \sqrt{K_1 P_{H_2}} + K_9 \sqrt{(K_1^4 K_2 K_3 K_4 K_5 K_6 K_7 K_8)} \frac{P_{CO_2}^{0.5} P_{H_2}^{1.5}}{P_{CH_4}^{0.5}} + \frac{P_{H_2 O}}{K_{11}} \right)^2}$	H, OH, H ₂ O	OH Hydrogenation (A1.15) [Quasi-equilibrium gas adsorption]

A1.3. Formyl Intermediate Mechanism

The development of rate equations for reaction *via* a CHO intermediate for the methanation of carbon monoxide was discussed by Kopyinski (2010). This reaction set was expanded for the methanation of carbon dioxide here in Table A1.3. The elementary reactions within the table do not follow sequentially; rather they represent a collection of possible reactions. Since it is not possible to develop a simple Langmuir relationship for the parallel pathways proceeding at once, the considered mechanisms have been split into 5 separate pathways. Under analysis of each pathway the rate-determining step is assumed irreversible, and that the possible alternate reactions of the intermediate species are far slower than those of selected pathway.

The five pathways examined in this section are:

- Pathway 1: CO* hydrogenated to COH₂*, prior to hydrogenation into CH* and H₂O*.
- Pathway 2: CO* hydrogenated to COH*, prior to hydrogenation to CH* and OH*.
- Pathway 3: CO* hydrogenated to COH*, prior to decomposition into CH* and O*.
- Pathway 4: CO* hydrogenated to COH*, prior to hydrogenation to C* and H₂O*.
- Pathway 5: CO* hydrogenated to COH₃*, prior to hydrogenation to CH₂* and H₂O*.

As identified in the derivation of the carbide route equations, the mechanism of oxygen removal from the surface can impact the form of the reaction, and thus three potential mechanisms are considered for each rate-determining step. These are quasi-equilibrium of all oxygen species with H₂O partial pressure, irreversible hydrogenation of O* to OH*, with quasi-equilibrium of OH* and H₂O*, and finally irreversible hydrogenation of OH* to H₂O*, as assumed by Lim (2014).

Table A1.3. Reaction set for CO₂ methanation via a formyl intermediate.

#	Reaction Step	Forward Reaction	Reverse Reaction	Surface Equilibrium Relationship
(A1.39)	H ₂ (g)+2*=2H*	$R_{13} = k_{13}P_{H_2}\theta_*^2$	$R_{13}' = k_{-13}\theta_H^2$	$\theta_H = \sqrt{K_{13}P_{H_2}\theta_*}$
(A1.40)	CO ₂ (g)+2*=CO*+O*	$R_{14} = k_{14}P_{CO_2}\theta_*^2$	$R_{14}' = k_{-14}\theta_{CO}\theta_O$	$K_{14}P_{CO_2}\theta_*^2 = \theta_{CO}\theta_O$
(A1.41)	CO*+H*=COH*+*	$R_{15} = k_{15}\theta_{CO}\theta_H$	$R_{15}' = k_{-15}\theta_{COH}\theta_*$	$K_{15}\theta_{CO}\theta_H = \theta_{COH}\theta_*$
(A1.42)	COH*+H*=COH ₂ *+*	$R_{16} = k_{16}\theta_{COH}\theta_H$	$R_{16}' = k_{-16}\theta_{COH_2}\theta_*$	$K_{16}\theta_{COH}\theta_H = \theta_{COH_2}\theta_*$
(A1.43)	COH*+H*=CH*+OH*	$R_{17} = k_{17}\theta_{COH}\theta_H$	$R_{17}' = k_{-17}\theta_{CH}\theta_{OH}$	$K_{17}\theta_{COH}\theta_H = \theta_{CH}\theta_{OH}$
(A1.44)	COH ₂ *+H*=CH*+H ₂ O*	$R_{18} = k_{18}\theta_{COH_2}\theta_H$	$R_{18}' = k_{-18}\theta_{CH}\theta_{H_2O}$	$K_{18}\theta_{COH_2}\theta_H = \theta_{CH}\theta_{H_2O}$
(A1.45)	COH*+H*=C*+H ₂ O*	$R_{19} = k_{19}\theta_{COH}\theta_H$	$R_{19}' = k_{-19}\theta_C\theta_{H_2O}$	$K_{19}\theta_{COH}\theta_H = \theta_C\theta_{H_2O}$
(A1.46)	COH ₂ *+H*=COH ₃ *+*	$R_{20} = k_{20}\theta_{COH_2}\theta_H$	$R_{20}' = k_{-20}\theta_{COH_3}\theta_H$	$K_{20}\theta_{COH_2}\theta_H = \theta_{COH_3}\theta_*$
(A1.47)	COH ₃ *+H*=H ₂ O*+CH ₂ *	$R_{21} = k_{21}\theta_{COH_3}\theta_H$	$R_{21}' = k_{-21}\theta_{CH_2}\theta_{H_2O}$	$K_{21}\theta_{COH_2}\theta_H = \theta_{CH_2}\theta_{H_2O}$
(A1.48)	COH*+*=CH*+O*	$R_{22} = k_{22}\theta_{COH}\theta_H$	$R_{22}' = k_{-22}\theta_{CH}\theta_O$	$K_{22}\theta_{COH}\theta_H = \theta_{CH}\theta_O$
(A1.49)	C*+H*=CH*+*	$R_{23} = k_{23}\theta_C\theta_H$	$R_{23}' = k_{-23}\theta_{CH}\theta_*$	$K_{23}\theta_C\theta_H = \theta_{CH}\theta_*$
(A1.50)	CH*+H*=CH ₂ *+*	$R_{24} = k_{24}\theta_{CH}\theta_H$	$R_{24}' = k_{-24}\theta_{CH_2}\theta_*$	$K_{24}\theta_{CH}\theta_H = \theta_{CH_2}\theta_*$
(A1.51)	CH ₂ *+H*=CH ₃ *+*	$R_{25} = k_{25}\theta_{CH_2}\theta_H$	$R_{25}' = k_{-25}\theta_{CH_3}\theta_*$	$K_{25}\theta_{CH_2}\theta_H = \theta_{CH_3}\theta_*$
(A1.52)	CH ₃ *+H*=CH ₄ *+*	$R_{26} = k_{26}\theta_{CH_3}\theta_H$	$R_{26}' = k_{-26}\theta_{CH_4}\theta_*$	$K_{26}\theta_{CH_3}\theta_H = \theta_{CH_4}\theta_*$

(A1.53)	$O^* + H^* = OH^* + *$	$R_{27} = k_{27}\theta_O\theta_H$	$R_{27}' = k_{-27}\theta_{OH}\theta_*$	$K_{27}\theta_O\theta_H = \theta_{OH}\theta_*$
(A1.54)	$OH^* + H^* = H_2O^* + *$	$R_{28} = k_{28}\theta_{OH}\theta_H$	$R_{28}' = k_{-28}\theta_{H_2O}\theta_*$	$K_{28}\theta_{OH}\theta_H = \theta_{H_2O}\theta_*$
(A1.55)	$H_2O^* = H_2O(g) + *$	$R_{29} = k_{29}\theta_{H_2O}$	$R_{29}' = k_{-17}P_{H_2O}\theta_*$	$K_{29}\theta_{H_2O} = P_{H_2O}\theta_*$
(A1.56)	$CH_4^* = CH_4(g) + *$	$R_{30} = k_{30}\theta_{CH_4}$	$R_{30}' = k_{-30}P_{CH_4}\theta_*$	$K_{30}\theta_{CH_4} = P_{CH_4}\theta_*$

A1.3.1. Pathway 1: CO*→COH*→COH₂*→CH*

Table A1.4. Reaction set for CO₂ methanation *via* pathway 1.

#	Reaction Step	Forward Reaction	Reverse Reaction	Surface Equilibrium Relationship
(A1.57)	H ₂ (g)+2*=2H*	$R_{13} = k_{13}P_{H_2}\theta_*^2$	$R_{13}' = k_{-13}\theta_H^2$	$\theta_H = \sqrt{K_{13}P_{H_2}\theta_*}$
(A1.58)	CO ₂ (g)+2*=CO* + O*	$R_{14} = k_{14}P_{CO_2}\theta_*^2$	$R_{14}' = k_{-14}\theta_{CO}\theta_O$	$K_{14}P_{CO_2}\theta_*^2 = \theta_{CO}\theta_O$
(A1.59)	CO*+H*=COH* + *	$R_{15} = k_{15}\theta_{CO}\theta_H$	$R_{15}' = k_{-15}\theta_{COH}\theta_*$	$K_{15}\theta_{CO}\theta_H = \theta_{COH}\theta_*$
(A1.60)	COH*+H*=COH ₂ *+*	$R_{16} = k_{16}\theta_{COH}\theta_H$	$R_{16}' = k_{-16}\theta_{COH_2}\theta_*$	$K_{16}\theta_{COH}\theta_H = \theta_{COH_2}\theta_*$
(A1.61)	COH ₂ *+H*=CH*+H ₂ O*	$R_{18} = k_{18}\theta_{COH_2}\theta_H$	$R_{18}' = k_{-18}\theta_{CH}\theta_{H_2O}$	$K_{18}\theta_{COH_2}\theta_H = \theta_{CH}\theta_{H_2O}$
(A1.62)	CH*+H*=CH ₂ *+*	$R_{24} = k_{24}\theta_{CH}\theta_H$	$R_{24}' = k_{-24}\theta_{CH_2}\theta_*$	$K_{24}\theta_{CH}\theta_H = \theta_{CH_2}\theta_*$
(A1.63)	CH ₂ *+H*=CH ₃ *+*	$R_{25} = k_{25}\theta_{CH_2}\theta_H$	$R_{25}' = k_{-25}\theta_{CH_3}\theta_*$	$K_{25}\theta_{CH_2}\theta_H = \theta_{CH_3}\theta_*$
(A1.64)	CH ₃ *+H*=CH ₄ *+*	$R_{26} = k_{26}\theta_{CH_3}\theta_H$	$R_{26}' = k_{-26}\theta_{CH_4}\theta_*$	$K_{26}\theta_{CH_3}\theta_H = \theta_{CH_4}\theta_*$
(A1.65)	O*+H*=OH*+*	$R_{27} = k_{27}\theta_O\theta_H$	$R_{27}' = k_{-27}\theta_{OH}\theta_*$	$K_{27}\theta_O\theta_H = \theta_{OH}\theta_*$
(A1.66)	OH*+H*=H ₂ O*+*	$R_{28} = k_{28}\theta_{OH}\theta_H$	$R_{28}' = k_{-28}\theta_{H_2O}\theta_*$	$K_{28}\theta_{OH}\theta_H = \theta_{H_2O}\theta_*$
(A1.67)	H ₂ O*=H ₂ O(g)+*	$R_{29} = k_{29}\theta_{H_2O}$	$R_{29}' = k_{-29}P_{H_2O}\theta_*$	$K_{29}\theta_{H_2O} = P_{H_2O}\theta_*$
(A1.68)	CH ₄ * = CH ₄ (g) + *	$R_{30} = k_{30}\theta_{CH_4}$	$R_{30}' = k_{-30}P_{CH_4}\theta_*$	$K_{30}\theta_{CH_4} = P_{CH_4}\theta_*$

Table A1.5. A summary of Langmuir-Hinshelwood models developed, the assumed reaction scheme, and the most abundant surface intermediates.

	Methanation Kinetic Equation	MASI	Rate-Limiting Step <i>[Additional Assumptions]</i>
F1A	$R_{CH_4} = \frac{k_{15} K_{13}^{1.5} K_{14} (K_{27} K_{28} K_{29}) P_{CO_2} P_{H_2}^{1.5}}{P_{H_2O} \left(1 + \sqrt{K_{13} P_{H_2}} + K_{13} K_{14} (K_{27} K_{28} K_{29}) \frac{P_{CO_2} P_{H_2}}{P_{H_2O}} + \frac{P_{H_2O}}{K_{29}} \right)^2}$	CO, H and H ₂ O	CO Hydrogenation to CHO [Quasi-equilibrium in all other steps]
F1B	$R_{CH_4} = \frac{k_{15} \sqrt{\left(\frac{k_{27}}{k_{15}}\right)} K_{14} K_{13} P_{CO_2}^{0.5} P_{H_2}^{0.5}}{\left(1 + \sqrt{K_{13} P_{H_2}} + \sqrt{\left(\frac{k_{27}}{k_{15}}\right)} K_{14} P_{CO_2}^{0.5} + \frac{P_{H_2O}}{K_{29}} \right)^2}$	CO, H and H ₂ O	CO Hydrogenation to CHO <i>[A1.65) assumed irreversible.]</i>
F1C	$R_{CH_4} = \frac{k_{15} \sqrt{\left(\frac{k_{28}}{k_{15}}\right)} K_{27} K_{14} K_{13}^{1.5} P_{CO_2}^{0.5} P_{H_2}^{0.75}}{\left(1 + \sqrt{K_{13} P_{H_2}} + \sqrt{\left(\frac{k_{28}}{k_{15}}\right)} K_{27} K_{14} K_{13}^{0.5} P_{CO_2}^{0.5} P_{H_2}^{0.25} + \frac{P_{H_2O}}{K_{29}} \right)^2}$	H, H ₂ O, CO	CO Hydrogenation to CHO <i>[A1.66) assumed irreversible.]</i>
F2A	$R_{CH_4} = \frac{(K_{13}^2 K_{14} K_{15} k_{16} (K_{27} K_{28} K_{29}) P_{CO_2} P_{H_2}^2)}{P_{H_2O} \left(1 + \sqrt{K_{13} P_{H_2}} + K_{13}^{1.5} K_{14} K_{15} (K_{27} K_{28} K_{29}) \frac{P_{CO_2} P_{H_2}^{1.5}}{P_{H_2O}} + \frac{P_{H_2O}}{K_{29}} \right)^2}$	H, CHO and H ₂ O	CHO Hydrogenation [Quasi-equilibrium in all other steps]
F2B	$R_{CH_4} = \frac{k_{16} \sqrt{\left(\frac{k_{27}}{k_{16}}\right)} K_{15} K_{14} P_{CO_2}^{0.5} (K_{13} P_{H_2})^{0.75}}{\left(1 + \sqrt{K_{13} P_{H_2}} + \sqrt{\left(\frac{k_{27}}{k_{16}}\right)} K_{15} K_{14} P_{CO_2}^{0.5} (K_{13} P_{H_2})^{0.25} + \frac{P_{H_2O}}{K_{29}} \right)^2}$	H, CHO and H ₂ O	CHO Hydrogenation <i>[A1.65) assumed irreversible.]</i>
F2C	$R_{CH_4} = \frac{k_{16} \sqrt{\left(\frac{k_{28}}{k_{16}}\right)} K_{27} K_{15} K_{14} P_{CO_2}^{0.5} (K_{13} P_{H_2})}{\left(1 + \sqrt{K_{13} P_{H_2}} + \sqrt{\left(\frac{k_{28}}{k_{16}}\right)} K_{27} K_{15} K_{14} P_{CO_2}^{0.5} (K_{13} P_{H_2})^{0.5} + \frac{P_{H_2O}}{K_{29}} \right)^2}$	H, CHO and H ₂ O	CHO Hydrogenation <i>[A1.66) assumed irreversible.]</i>

F3A	$R_{CH_4} = \frac{k_{18}(K_{13}^{2.5} K_{14} K_{15} K_{16} (K_{27} K_{28} K_{29}) P_{CO_2} P_{H_2}^{2.5})}{P_{H_2O} \left(1 + \sqrt{K_{13} P_{H_2}} + K_{13}^2 K_{14} K_{15} K_{16} (K_{27} K_{28} K_{29}) \frac{P_{CO_2} P_{H_2}^{2.5}}{P_{H_2O}^2} + \frac{P_{H_2O}}{K_{29}} \right)^2}$	H, CH ₂ O, H ₂ O	CH ₂ O Hydrogenation [Quasi-equilibrium in all other steps]
F3B	$R_{CH_4} = \frac{k_{18} \sqrt{\left(\frac{k_{27}}{k_{18}}\right)} K_{16} K_{15} K_{14} P_{CO_2}^{0.5} (K_{13} P_{H_2})}{\left(1 + \sqrt{K_{13} P_{H_2}} + \sqrt{\left(\frac{k_{27}}{k_{18}}\right)} K_{16} K_{15} K_{14} P_{CO_2}^{0.5} (K_{13} P_{H_2})^{0.5} + \frac{P_{H_2O}}{K_{29}} \right)^2}$	H, CH ₂ O, H ₂ O	CH ₂ O Hydrogenation [(A1.65) assumed irreversible.]
F3C	$R_{CH_4} = \frac{k_{16} \sqrt{\left(\frac{k_{28}}{k_{18}}\right)} K_{27} K_{16} K_{15} K_{14} P_{CO_2}^{0.5} (K_{13} P_{H_2})^{1.5}}{\left(1 + \sqrt{K_{13} P_{H_2}} + \sqrt{\left(\frac{k_{28}}{k_{18}}\right)} K_{27} K_{16} K_{15} K_{14} P_{CO_2}^{0.5} (K_{13} P_{H_2}) + \frac{P_{H_2O}}{K_{29}} \right)^2}$	H, CH ₂ O, H ₂ O	CH ₂ O Hydrogenation [(A1.66) assumed irreversible.]
F4A	$R_{CH_4} = \frac{k_{24} (K_{13}^3 K_{14} K_{15} K_{16} K_{18} (K_{27} K_{28} K_{29}^2) P_{CO_2} P_{H_2}^3)}{P_{H_2O}^2 \left(1 + \sqrt{K_{13} P_{H_2}} + K_{13}^{2.5} K_{14} K_{15} K_{16} K_{18} (K_{27} K_{28} K_{29}) \frac{P_{CO_2} P_{H_2}^{2.5}}{P_{H_2O}^2} + \frac{P_{H_2O}}{K_{29}} \right)^2}$	H, CH, H ₂ O	CH Hydrogenation [Quasi-equilibrium in all other steps]
F4B	$R_{CH_4} = \frac{k_{24} \sqrt{\left(K_{13}^{2.5} K_{14} K_{15} K_{16} K_{18} \left(\frac{k_{27}}{k_{24}}\right) K_{29}\right)} P_{CO_2}^{0.5} P_{H_2}^{1.25}}{P_{H_2O}^{0.5} \left(1 + \sqrt{K_{13} P_{H_2}} + \sqrt{\left(K_{13}^{1.5} K_{14} K_{15} K_{16} K_{18} \left(\frac{k_{27}}{k_{24}}\right) K_{29}\right)} \frac{P_{CO_2}^{0.5} P_{H_2}^{0.75}}{P_{H_2O}^{0.5}} + \frac{P_{H_2O}}{K_{29}} \right)^2}$	H, CH, H ₂ O	CH Hydrogenation [(A1.65) assumed irreversible.]
F4C	$R_{CH_4} = \frac{k_{24} \sqrt{\left(K_{13}^3 K_{14} K_{15} K_{16} K_{18} \left(\frac{k_{28}}{k_{24}}\right) K_{27} K_{29}\right)} P_{CO_2}^{0.5} P_{H_2}^{1.5}}{P_{H_2O}^{0.5} \left(1 + \sqrt{K_{13} P_{H_2}} + \sqrt{\left(K_{13}^2 K_{14} K_{15} K_{16} K_{18} \left(\frac{k_{28}}{k_{24}}\right) K_{27} K_{29}\right)} \frac{P_{CO_2}^{0.5} P_{H_2}^{0.5}}{P_{H_2O}^{0.5}} + \frac{P_{H_2O}}{K_{29}} \right)^2}$	H, CH, H ₂ O	CH Hydrogenation [(A1.66) assumed irreversible.]

A1.3.2. Pathway 2: CO* → COH* → CH* + OH*

Table A1.6. Reaction set for CO₂ methanation *via* pathway 2.

#	Reaction Step	Forward Reaction	Reverse Reaction	Surface Equilibrium Relationship
(A1.69)	H ₂ (g)+2*=2H*	$R_{13} = k_{13}P_{H_2}\theta_*^2$	$R_{13}' = k_{-13}\theta_H^2$	$\theta_H = \sqrt{K_{13}P_{H_2}\theta_*}$
(A1.70)	CO ₂ (g)+2*=CO* + O*	$R_{14} = k_{14}P_{CO_2}\theta_*^2$	$R_{14}' = k_{-14}\theta_{CO}\theta_O$	$K_{14}P_{CO_2}\theta_*^2 = \theta_{CO}\theta_O$
(A1.71)	CO*+H*=COH* + *	$R_{15} = k_{15}\theta_{CO}\theta_H$	$R_{15}' = k_{-15}\theta_{COH}\theta_*$	$K_{15}\theta_{CO}\theta_H = \theta_{COH}\theta_*$
(A1.72)	COH*+H*=CH* + OH*	$R_{17} = k_{17}\theta_{COH}\theta_H$	$R_{17}' = k_{-17}\theta_{CH}\theta_{OH}$	$K_{17}\theta_{COH}\theta_H = \theta_{CH}\theta_{OH}$
(A1.73)	CH*+H*=CH ₂ * + *	$R_{24} = k_{24}\theta_{CH}\theta_H$	$R_{24}' = k_{-24}\theta_{CH_2}\theta_*$	$K_{24}\theta_{CH}\theta_H = \theta_{CH_2}\theta_*$
(A1.74)	CH ₂ *+H*=CH ₃ * + *	$R_{25} = k_{25}\theta_{CH_2}\theta_H$	$R_{25}' = k_{-25}\theta_{CH_3}\theta_*$	$K_{25}\theta_{CH_2}\theta_H = \theta_{CH_3}\theta_*$
(A1.75)	CH ₃ *+H*=CH ₄ * + *	$R_{26} = k_{26}\theta_{CH_3}\theta_H$	$R_{14}' = k_{-26}\theta_{CH_4}\theta_*$	$K_{26}\theta_{CH_3}\theta_H = \theta_{CH_4}\theta_*$
(A1.76)	O*+H*=OH* + *	$R_{27} = k_{27}\theta_O\theta_H$	$R_{27}' = k_{-27}\theta_{OH}\theta_*$	$K_{27}\theta_O\theta_H = \theta_{OH}\theta_*$
(A1.77)	OH*+H*=H ₂ O*+*	$R_{28} = k_{28}\theta_{OH}\theta_H$	$R_{28}' = k_{-28}\theta_{H_2O}\theta_*$	$K_{28}\theta_{OH}\theta_H = \theta_{H_2O}\theta_*$
(A1.78)	H ₂ O*=H ₂ O(g)+*	$R_{29} = k_{29}\theta_{H_2O}$	$R_{29}' = k_{-29}P_{H_2O}\theta_*$	$K_{29}\theta_{H_2O} = P_{H_2O}\theta_*$
(A1.79)	CH ₄ *=CH ₄ (g) + *	$R_{30} = k_{30}\theta_{CH_4}$	$R_{30}' = k_{-30}P_{CH_4}\theta_*$	$K_{30}\theta_{CH_4} = P_{CH_4}\theta_*$

Table A1.7. A summary of Langmuir-Hinshelwood models developed, the assumed reaction scheme, and the most abundant surface intermediates (Pathway 2).

	Methanation Kinetic Equation	MASI	Rate-limiting Step <i>[Additional Assumptions]</i>
F5A	$R_{CH_4} = \frac{K_{13}^{1.5} K_{14} k_{15} (K_{27} K_{28} K_{29}) P_{CO_2} P_{H_2}^{1.5}}{P_{H_2O} \left(1 + \sqrt{K_{13} P_{H_2}} + K_{13} K_{14} (K_{27} K_{28} K_{29}) \frac{P_{CO_2} P_{H_2}}{P_{H_2O}} + \frac{P_{H_2O}}{K_{29}} \right)^2}$	CO, H and H ₂ O	CO Hydrogenation to CHO [Quasi-equilibrium in all other steps]
F5B	$R_{CH_4} = \frac{k_{15} \sqrt{\left(\frac{k_{27}}{k_{15}}\right) K_{14} K_{13}} P_{CO_2}^{0.5} P_{H_2}^{0.5}}{\left(1 + \sqrt{K_{13} P_{H_2}} + \sqrt{\left(\frac{k_{27}}{k_{15}}\right) K_2} P_{CO_2}^{0.5} + \frac{P_{H_2O}}{K_{29}} \right)^2}$	CO, H and H ₂ O	CO Hydrogenation to CHO <i>[A1.76) assumed irreversible.]</i>
F5C	$R_{CH_4} = \frac{k_{15} \sqrt{\left(\frac{k_{28}}{2k_{15}}\right) K_{27} K_{14} K_{13}^{1.5}} P_{CO_2}^{0.5} P_{H_2}^{0.75}}{\left(1 + \sqrt{K_{13} P_{H_2}} + \sqrt{\left(\frac{k_{28}}{2k_{15}}\right) K_{27} K_{14} K_{13}^{0.5}} P_{CO_2}^{0.5} P_{H_2}^{0.25} + \frac{P_{H_2O}}{K_{29}} \right)^2}$	H, H ₂ O, CO	CO Hydrogenation to CHO <i>[A1.77) assumed irreversible.]</i>
F6A	$R_{CH_4} = \frac{(K_{13}^2 K_{14} K_{15} k_{17} (K_{27} K_{28} K_{29}) P_{CO_2} P_{H_2}^2)}{P_{H_2O} \left(1 + \sqrt{K_{13} P_{H_2}} + K_{13}^{1.5} K_{14} K_{15} (K_{27} K_{28} K_{29}) \frac{P_{CO_2} P_{H_2}^{1.5}}{P_{H_2O}} + \frac{P_{H_2O}}{K_{29}} \right)^2}$	H, CHO and H ₂ O	CHO Hydrogenation [Quasi-equilibrium in all other steps]
F6B	$R_{CH_4} = \frac{k_{17} \sqrt{\left(\frac{k_{27}}{k_{17}}\right) K_{15} K_{14}} P_{CO_2}^{0.5} (K_{13} P_{H_2})^{0.75}}{\left(1 + \sqrt{K_{13} P_{H_2}} + \sqrt{\left(\frac{k_{27}}{k_{17}}\right) K_{15} K_{14}} P_{CO_2}^{0.5} (K_{13} P_{H_2})^{0.25} + \frac{P_{H_2O}}{K_{29}} \right)^2}$	H, CHO and H ₂ O	CHO Hydrogenation <i>[A1.76) assumed irreversible.]</i>
F6C	$R_{CH_4} = \frac{k_{17} \sqrt{\left(\frac{k_{28}}{2k_{17}}\right) K_{27} K_{15} K_{14}} P_{CO_2}^{0.5} (K_{13} P_{H_2})}{\left(1 + \sqrt{K_{13} P_{H_2}} + \sqrt{\left(\frac{k_{28}}{2k_{17}}\right) K_{27} K_{15} K_{14}} P_{CO_2}^{0.5} (K_{13} P_{H_2})^{0.5} + \frac{P_{H_2O}}{K_{29}} \right)^2}$	H, CHO and H ₂ O	CHO Hydrogenation <i>[A1.77) assumed irreversible.]</i>

F7A	$R_{CH_4} = \frac{k_{24}(K_{13}^3 K_{14} K_{15} K_{17} (K_{27} K_{28}^2 K_{29}^2) P_{CO_2} P_{H_2}^3)}{P_{H_2O}^2 \left(1 + \sqrt{K_{13} P_{H_2}} + K_{13}^{2.5} K_{14} K_{15} K_{17} (K_{27} K_{28}^2 K_{29}^2) \frac{P_{CO_2} P_{H_2}^{2.5}}{P_{H_2O}^2} + \frac{P_{H_2O}}{K_{29}} \right)^2}$	H, CH, H ₂ O	CH Hydrogenation [Quasi-equilibrium in all other steps]
F7B	$R_{CH_4} = \frac{k_{24} \sqrt{\left(K_{13}^{2.5} K_{14} K_{15} K_{16} K_{17} \left(\frac{k_{27}}{k_{24}} \right) K_{29} \right)} P_{CO_2}^{0.5} P_{H_2}^{1.25}}{P_{H_2O}^{0.5} \left(1 + \sqrt{K_{13} P_{H_2}} + \sqrt{\left(K_{13}^{1.5} K_{14} K_{15} K_{17} \left(\frac{k_{27}}{k_{24}} \right) K_{29} \right)} \frac{P_{CO_2}^{0.5} P_{H_2}^{0.75}}{P_{H_2O}^{0.5}} + \frac{P_{H_2O}}{K_{29}} \right)^2}$	H, CH, H ₂ O	CH Hydrogenation <i>[A1.76) assumed irreversible.]</i>
F7C	$R_{CH_4} = \frac{K_{13} \sqrt[3]{\left(K_{14} K_{15} K_{17} k_{24} K_{27} k_{28}^2 \right)} P_{CO_2}^{0.33} P_{H_2}}{\left(1 + \sqrt{K_{13} P_{H_2}} + \frac{K_{13}^{0.5}}{k_{24}^{0.66}} \sqrt[3]{\left(K_{14} K_{15} K_{17} K_{27} k_{28}^2 \right)} P_{CO_2}^{0.33} P_{H_2}^{0.5} + \frac{P_{H_2O}}{K_{29}} \right)^2}$	H, CH, H ₂ O	CH Hydrogenation <i>[A1.77) assumed irreversible.]</i>

A1.3.3. Pathway 3: CO* → COH* → CH* + O*

Table A1.8. Reaction set for CO₂ methanation *via* pathway 3.

#	Reaction Step	Forward Reaction	Reverse Reaction	Surface Equilibrium Relationship
(A1.80)	H ₂ (g) + 2* = 2H*	$R_{13} = k_{13}P_{H_2}\theta_*^2$	$R_{13}' = k_{-13}\theta_H^2$	$\theta_H = \sqrt{K_{13}P_{H_2}\theta_*}$
(A1.81)	CO ₂ (g) + 2* = CO* + O*	$R_{14} = k_{14}P_{CO_2}\theta_*^2$	$R_{14}' = k_{-14}\theta_{CO}\theta_O$	$K_{14}P_{CO_2}\theta_*^2 = \theta_{CO}\theta_O$
(A1.82)	CO* + H* = COH* + *	$R_{15} = k_{15}\theta_{CO}\theta_H$	$R_3' = k_{-15}\theta_{COH}\theta_*$	$K_{15}\theta_{CO}\theta_H = \theta_{COH}\theta_*$
(A1.83)	COH* + * = CH* + O*	$R_{22} = k_{22}\theta_{COH}\theta_*$	$R_{22}' = k_{-22}\theta_{CH}\theta_O$	$K_{22}\theta_{COH}\theta_* = \theta_{CH}\theta_O$
(A1.84)	CH* + H* = CH ₂ * + *	$R_{24} = k_{24}\theta_{CH}\theta_H$	$R_{24}' = k_{-24}\theta_{CH_2}\theta_*$	$K_{24}\theta_{CH}\theta_H = \theta_{CH_2}\theta_*$
(A1.85)	CH ₂ * + H* = CH ₃ * + *	$R_{25} = k_{25}\theta_{CH_2}\theta_H$	$R_{25}' = k_{-25}\theta_{CH_3}\theta_*$	$K_{25}\theta_{CH_2}\theta_H = \theta_{CH_3}\theta_*$
(A1.86)	CH ₃ * + H* = CH ₄ * + *	$R_{26} = k_{26}\theta_{CH_3}\theta_H$	$R_{26}' = k_{-26}\theta_{CH_4}\theta_*$	$K_{26}\theta_{CH_3}\theta_H = \theta_{CH_4}\theta_*$
(A1.87)	O* + H* = OH* + *	$R_{27} = k_{27}\theta_O\theta_H$	$R_{27}' = k_{-27}\theta_{OH}\theta_*$	$K_{27}\theta_O\theta_H = \theta_{OH}\theta_*$
(A1.88)	OH* + H* = H ₂ O* + *	$R_{28} = k_{28}\theta_{OH}\theta_H$	$R_{28}' = k_{-28}\theta_{H_2O}\theta_*$	$K_{28}\theta_{OH}\theta_H = \theta_{H_2O}\theta_*$
(A1.89)	H ₂ O* = H ₂ O(g) + *	$R_{29} = k_{29}\theta_{H_2O}$	$R_{29}' = k_{-29}P_{H_2O}\theta_*$	$K_{29}\theta_{H_2O} = P_{H_2O}\theta_*$
(A1.90)	CH ₄ * = CH ₄ (g) + *	$R_{30} = k_{30}\theta_{CH_4}$	$R_{30}' = k_{-30}P_{CH_4}\theta_*$	$K_{30}\theta_{CH_4} = P_{CH_4}\theta_*$

Table A1.9. A summary of Langmuir-Hinshelwood models developed, the assumed reaction scheme, and the most abundant surface intermediates (Pathway 3).

	Methanation Kinetic Equation	MASI	Rate-limiting Step [Additional Assumptions]
F8A	$R_{CH_4} = \frac{k_{15}K_{14}(K_{27}K_{28}K_{29})P_{CO_2}K_{13}^{1.5}P_{H_2}^{1.5}}{P_{H_2O} \left(1 + \sqrt{K_{13}P_{H_2}} + K_{13}K_{14}(K_{27}K_{28}K_{29}) \frac{P_{CO_2}P_{H_2}}{P_{H_2O}} + \frac{P_{H_2O}}{K_{29}} \right)^2}$	CO, H and H ₂ O	CO Hydrogenation to CHO [Quasi-equilibrium in all other steps]
F8B	$R_{CH_4} = \frac{k_{15}\sqrt{\left(\frac{k_{27}}{k_{15}}\right)K_{14}K_{13}}P_{CO_2}^{0.5}P_{H_2}^{0.5}}{\left(1 + \sqrt{K_{13}P_{H_2}} + \sqrt{\left(\frac{k_{27}}{k_{15}}\right)K_2}P_{CO_2}^{0.5} + \frac{P_{H_2O}}{K_{29}} \right)^2}$	CO, H and H ₂ O	CO Hydrogenation to CHO [(A1.87) assumed irreversible.]
F8C	$R_{CH_4} = \frac{k_{15}\sqrt{\left(\frac{k_{28}}{2k_{15}}\right)K_{27}K_{14}K_{13}^{1.5}}P_{CO_2}^{0.5}P_{H_2}^{0.75}}{\left(1 + \sqrt{K_{13}P_{H_2}} + \sqrt{\left(\frac{k_{28}}{2k_{15}}\right)K_{27}K_{14}K_{13}^{0.5}}P_{CO_2}^{0.5}P_{H_2}^{0.25} + \frac{P_{H_2O}}{K_{29}} \right)^2}$	H, H ₂ O, CO	CO Hydrogenation to CHO [(A1.88) assumed irreversible.]
F9A	$R_{CH_4} = \frac{k_{22}K_{14}K_{15}(K_{27}K_{28}K_{29})P_{CO_2}K_{13}^{1.5}P_{H_2}^{1.5}}{P_{H_2O} \left(1 + \sqrt{K_{13}P_{H_2}} + K_{13}^{1.5}K_{14}K_{15}(K_{27}K_{28}K_{29}) \frac{P_{CO_2}P_{H_2}^{1.5}}{P_{H_2O}} + \frac{P_{H_2O}}{K_{29}} \right)^2}$	H, CHO and H ₂ O	CHO Dissociation [Quasi-equilibrium in all other steps]
F9B	$R_{CH_4} = \frac{k_{22}\sqrt{\left(\frac{k_{27}}{2k_{22}}\right)K_{13}K_{14}K_{15}}P_{CO_2}^{0.5}P_{H_2}^{0.5}}{\left(1 + \sqrt{K_{13}P_{H_2}} + \sqrt{\left(\frac{k_{27}}{2k_{22}}\right)K_{13}K_{14}K_{15}}P_{CO_2}^{0.5}P_{H_2}^{0.5} + \frac{P_{H_2O}}{K_{29}} \right)^2}$	H, CHO and H ₂ O	CHO Dissociation [(A1.87) assumed irreversible.]
F9C	$R_{CH_4} = \frac{k_{22}\sqrt{\left(\frac{k_{28}}{2k_{22}}\right)K_{27}K_{15}K_{14}K_{13}^{1.5}}P_{CO_2}^{0.5}P_{H_2}^{0.75}}{\left(1 + \sqrt{K_{13}P_{H_2}} + \sqrt{\left(\frac{k_{28}}{2k_{22}}\right)K_{27}K_{15}K_{14}K_{13}^{1.5}}P_{CO_2}^{0.5}P_{H_2}^{0.75} + \frac{P_{H_2O}}{K_{29}} \right)^2}$	H, CHO and H ₂ O	CHO Dissociation [(A1.88) assumed irreversible.]

F10A	$R_{CH_4} = \frac{k_{24}(K_{13}^{3.5} K_{14} K_{15} K_{22} (K_{27} K_{28} K_{29})^2 P_{CO_2} P_{H_2}^{3.5})}{P_{H_2O}^2 \left(1 + \sqrt{K_{13} P_{H_2}} + K_{13}^3 K_{14} K_{15} K_{22} (K_{27} K_{28} K_{29})^2 \frac{P_{CO_2} P_{H_2}^{3.5}}{P_{H_2O}^2} + \frac{P_{H_2O}}{K_{29}} \right)^2}$	H, CH, H ₂ O	CH Hydrogenation [Quasi-equilibrium in all other steps]
F10B	$R_{CH_4} = \frac{\sqrt[3]{\frac{1}{4} K_{13}^{2.5} K_{14} K_{15} K_{22} k_{24} k_{27}^2 P_{CO_2} P_{H_2}^{2.5}}}{\left(1 + \sqrt{K_{13} P_{H_2}} + \frac{\sqrt[3]{\frac{1}{4} K_{13}^{2.5} K_{14} K_{15} K_{22} k_{24} k_{27}^2 P_{CO_2} P_{H_2}^{2.5}}}{k_{24} \sqrt{K_{13} P_{H_2}}} + \frac{P_{H_2O}}{K_{29}} \right)^2}$	H, CH, H ₂ O	CH Hydrogenation <i>[A1.87) assumed irreversible.]</i>
F10C	$R_{CH_4} = \frac{\sqrt[3]{\frac{1}{4} K_{13}^{3.5} K_{14} K_{15} K_{22} k_{24} k_{27}^2 K_{28}^2 P_{CO_2} P_{H_2}^{3.5}}}{\left(1 + \sqrt{K_{13} P_{H_2}} + \frac{\sqrt[3]{\frac{1}{4} K_{13}^{3.5} K_{14} K_{15} K_{22} k_{24} k_{27}^2 K_{28}^2 P_{CO_2} P_{H_2}^{3.5}}}{k_{24} \sqrt{K_{13} P_{H_2}}} + \frac{P_{H_2O}}{K_{29}} \right)^2}$	H, CH, H ₂ O	CH Hydrogenation <i>[A1.88) assumed irreversible.]</i>

A1.3.4. Pathway 4: CO* → COH* → C* → CH*

Table A1.10. Reaction set for CO₂ methanation *via* pathway 4.

#	Reaction Step	Forward Reaction	Reverse Reaction	Surface Equilibrium Relationship
(A1.91)	H ₂ (g)+2*=2H*	$R_{13} = k_{13}P_{H_2}\theta_*^2$	$R_{13}' = k_{-13}\theta_H^2$	$\theta_H = \sqrt{K_{13}P_{H_2}\theta_*}$
(A1.92)	CO ₂ (g)+2*=CO*+O*	$R_{14} = k_{14}P_{CO_2}\theta_*^2$	$R_{14}' = k_{-14}\theta_{CO}\theta_O$	$K_{14}P_{CO_2}\theta_*^2 = \theta_{CO}\theta_O$
(A1.93)	CO*+H*=COH*+*	$R_{15} = k_{15}\theta_{CO}\theta_H$	$R_{15}' = k_{-15}\theta_{COH}\theta_*$	$K_{15}\theta_{CO}\theta_H = \theta_{COH}\theta_*$
(A1.94)	COH*+H*=C*+H ₂ O*	$R_{19} = k_{19}\theta_{COH}\theta_H$	$R_{19}' = k_{-19}\theta_C\theta_{H_2O}$	$K_{19}\theta_{COH}\theta_H = \theta_C\theta_{H_2O}$
(A1.95)	C*+H*=CH*+*	$R_{23} = k_{23}\theta_C\theta_H$	$R_{23}' = k_{-23}\theta_{CH}\theta_*$	$K_{23}\theta_C\theta_H = \theta_{CH}\theta_*$
(A1.96)	CH*+H*=CH ₂ *+*	$R_{24} = k_{24}\theta_{CH}\theta_H$	$R_{24}' = k_{-24}\theta_{CH_2}\theta_*$	$K_{24}\theta_{CH}\theta_H = \theta_{CH_2}\theta_*$
(A1.97)	CH ₂ *+H*=CH ₃ *+*	$R_{25} = k_{25}\theta_{CH_2}\theta_H$	$R_{25}' = k_{-25}\theta_{CH_3}\theta_*$	$K_{25}\theta_{CH_2}\theta_H = \theta_{CH_3}\theta_*$
(A1.98)	CH ₃ *+H*=CH ₄ *+*	$R_{26} = k_{26}\theta_{CH_3}\theta_H$	$R_{26}' = k_{-26}\theta_{CH_4}\theta_*$	$K_{26}\theta_{CH_3}\theta_H = \theta_{CH_4}\theta_*$
(A1.99)	O*+H*=OH*+*	$R_{27} = k_{27}\theta_O\theta_H$	$R_{27}' = k_{-27}\theta_{OH}\theta_*$	$K_{27}\theta_O\theta_H = \theta_{OH}\theta_*$
(A1.100)	OH*+H*=H ₂ O*+*	$R_{28} = k_{28}\theta_{OH}\theta_H$	$R_{28}' = k_{-28}\theta_{H_2O}\theta_*$	$K_{28}\theta_{OH}\theta_H = \theta_{H_2O}\theta_*$
(A1.101)	H ₂ O*=H ₂ O(g)+*	$R_{29} = k_{29}\theta_{H_2O}$	$R_{29}' = k_{-29}P_{H_2O}\theta_*$	$K_{29}\theta_{H_2O} = P_{H_2O}\theta_*$
(A1.102)	CH ₄ *=CH ₄ (g)+*	$R_{30} = k_{30}\theta_{CH_4}$	$R_{30}' = k_{-30}P_{CH_4}\theta_*$	$K_{30}\theta_{CH_4} = P_{CH_4}\theta_*$

Table A1.11. A summary of Langmuir-Hinshelwood models developed, the assumed reaction scheme, and the most abundant surface intermediates (Pathway 4).

	Methanation Kinetic Equation	MASI	Rate-limiting Step [Additional Assumptions]
F11A	$R_{CH_4} = \frac{k_{15}K_{14}(K_{27}K_{28}K_{29})P_{CO_2}K_{13}^{1.5}P_{H_2}^{1.5}}{P_{H_2O} \left(1 + \sqrt{K_{13}P_{H_2}} + K_{13}K_{14}(K_{27}K_{28}K_{29}) \frac{P_{CO_2}P_{H_2}}{P_{H_2O}} + \frac{P_{H_2O}}{K_{29}} \right)^2}$	CO, H and H ₂ O	CO Hydrogenation to CHO [Quasi-equilibrium in all other steps]
F11B	$R_{CH_4} = \frac{k_{15}\sqrt{\left(\frac{k_{27}}{k_{15}}\right)K_{14}K_{13}}P_{CO_2}^{0.5}P_{H_2}^{0.5}}{\left(1 + \sqrt{K_{13}P_{H_2}} + \sqrt{\left(\frac{k_{27}}{k_{15}}\right)K_{14}}P_{CO_2}^{0.5} + \frac{P_{H_2O}}{K_{29}} \right)^2}$	CO, H and H ₂ O	CO Hydrogenation to CHO [(A1.99) assumed irreversible.]
F11C	$R_{CH_4} = \frac{k_{15}\sqrt{\left(\frac{k_{28}}{k_{15}}\right)K_{27}K_{14}K_{13}}P_{CO_2}^{0.5}P_{H_2}^{0.75}}{\left(1 + \sqrt{K_{13}P_{H_2}} + \sqrt{\left(\frac{k_{28}}{k_{15}}\right)K_{27}K_{14}K_{13}}P_{CO_2}^{0.5}P_{H_2}^{0.25} + \frac{P_{H_2O}}{K_{29}} \right)^2}$	H, H ₂ O, CO	CO Hydrogenation to CHO [(A1.100) assumed irreversible.]
F12A	$R_{CH_4} = \frac{k_{19}K_{14}K_{15}(K_{27}K_{28}K_{29})P_{CO_2}K_{13}^2P_{H_2}^2}{P_{H_2O} \left(1 + \sqrt{K_{13}P_{H_2}} + K_{14}K_{15}(K_{27}K_{28}K_{29})K_{13}^{1.5} \frac{P_{CO_2}P_{H_2}^{1.5}}{P_{H_2O}} + \frac{P_{H_2O}}{K_{29}} \right)^2}$	H, CHO and H ₂ O	CHO Hydrogenation [Quasi-equilibrium in all other steps]
F12B	$R_{CH_4} = \frac{k_{19}\sqrt{\left(\frac{k_{27}}{k_{19}}\right)K_{14}K_{15}}P_{CO_2}^{0.5}(K_{13}P_{H_2})^{0.75}}{\left(1 + \sqrt{K_{13}P_{H_2}} + \sqrt{\left(\frac{k_{27}}{k_{19}}\right)K_{14}K_{15}}P_{CO_2}^{0.5}(K_{13}P_{H_2})^{0.25} + \frac{P_{H_2O}}{K_{29}} \right)^2}$	H, CHO and H ₂ O	CHO Hydrogenation [(A1.99) assumed irreversible.]
F12C	$R_{CH_4} = \frac{k_{19}\sqrt{\left(\frac{k_{28}}{k_{19}}\right)K_{14}K_{15}K_{27}}P_{CO_2}^{0.5}(K_{13}P_{H_2})}{\left(1 + \sqrt{K_{13}P_{H_2}} + \sqrt{\left(\frac{k_{28}}{k_{19}}\right)K_{14}K_{15}K_{27}}P_{CO_2}^{0.5}(K_{13}P_{H_2})^{0.5} + \frac{P_{H_2O}}{K_{29}} \right)^2}$	H, CHO and H ₂ O	CHO Hydrogenation [(A1.100) assumed irreversible.]

F13A	$R_{CH_4} = \frac{k_{23}K_{14}K_{15}K_{19}(K_{27}K_{28}K_{29}^2)P_{CO_2}K_1^{2.5}P_{H_2}^{2.5}}{P_{H_2O}^2 \left(1 + \sqrt{K_{13}P_{H_2}} + K_{14}K_{15}K_{19}(K_{27}K_{28}K_{29}^2)K_{13}^2 \frac{P_{CO_2}P_{H_2}^2}{P_{H_2O}^2} + \frac{P_{H_2O}}{K_{29}} \right)^2}$	H, C, H ₂ O	C Hydrogenation [Quasi-equilibrium in all other steps]
F13B	$R_{CH_4} = \frac{k_{23}\sqrt{\left(\frac{k_{27}}{k_{23}}\right)}K_{14}K_{15}K_{19}K_{29}P_{CO_2}^{0.5}(K_{13}P_{H_2})}{P_{H_2O}^{0.5} \left(1 + \sqrt{K_{13}P_{H_2}} + \sqrt{\left(\frac{k_{27}}{k_{23}}\right)}K_{14}K_{15}K_{19}K_{29} \frac{P_{CO_2}^{0.5}(K_{13}P_{H_2})^{0.5}}{P_{H_2O}^{0.5}} + \frac{P_{H_2O}}{K_{29}} \right)^2}$	H, C, H ₂ O	C Hydrogenation [(A1.99) assumed irreversible.]
F13C	$R_{CH_4} = \frac{k_{23}\sqrt{\left(\frac{k_{28}}{k_{23}}\right)}K_{14}K_{15}K_{19}K_{27}K_{29}P_{CO_2}^{0.5}(K_{13}P_{H_2})^{1.25}}{P_{H_2O}^{0.5} \left(1 + \sqrt{K_{13}P_{H_2}} + \sqrt{\left(\frac{k_{28}}{k_{23}}\right)}K_{14}K_{15}K_{19}K_{27}K_{29} \frac{P_{CO_2}^{0.5}(K_{13}P_{H_2})^{0.5}}{P_{H_2O}^{0.5}} + \frac{P_{H_2O}}{K_{29}} \right)^2}$	H, C, H ₂ O	C Hydrogenation [(A1.100) assumed irreversible.]
F14A	$R_{CH_4} = \frac{k_{24}K_{14}K_{15}K_{19}K_{23}(K_{27}K_{28}K_{29}^2)P_{CO_2}K_{13}^3P_{H_2}^3}{P_{H_2O}^2 \left(1 + \sqrt{K_{13}P_{H_2}} + K_{14}K_{15}K_{19}K_{23}(K_{27}K_{28}K_{29}^2)K_{13}^{2.5} \frac{P_{CO_2}P_{H_2}^{2.5}}{P_{H_2O}^2} + \frac{P_{H_2O}}{K_{29}} \right)^2}$	H, CH, H ₂ O	CH Hydrogenation [Quasi-equilibrium in all other steps]
F14B	$R_{CH_4} = \frac{k_{24}\sqrt{\left(\frac{k_{27}}{k_{24}}\right)}K_{14}K_{15}K_{19}K_{23}K_{29}P_{CO_2}^{0.5}(K_{13}P_{H_2})^{1.25}}{P_{H_2O}^{0.5} \left(1 + \sqrt{K_{13}P_{H_2}} + \sqrt{\left(\frac{k_{27}}{k_{24}}\right)}K_{14}K_{15}K_{19}K_{23}K_{29} \frac{P_{CO_2}^{0.5}(K_{13}P_{H_2})^{0.75}}{P_{H_2O}^{0.5}} + \frac{P_{H_2O}}{K_{29}} \right)^2}$	H, CH, H ₂ O	CH Hydrogenation [(A1.99) assumed irreversible.]
F14C	$R_{CH_4} = \frac{k_{24}\sqrt{\left(\frac{k_{28}}{k_{24}}\right)}K_{14}K_{15}K_{19}K_{23}K_{27}K_{29}P_{CO_2}^{0.5}(K_{13}P_{H_2})^{1.5}}{P_{H_2O}^{0.5} \left(1 + \sqrt{K_{13}P_{H_2}} + \sqrt{\left(\frac{k_{28}}{k_{24}}\right)}K_{14}K_{15}K_{19}K_{23}K_{27}K_{29} \frac{P_{CO_2}^{0.5}(K_{13}P_{H_2})}{P_{H_2O}^{0.5}} + \frac{P_{H_2O}}{K_{29}} \right)^2}$	H, CH, H ₂ O	CH Hydrogenation [(A1.100) assumed irreversible.]

A1.3.5. Pathway 5: CO* → COH* → COH₂* → COH₃ → CH₂

Table A1.12. Reaction set for CO₂ methanation *via* pathway 5.

#	Reaction Step	Forward Reaction	Reverse Reaction	Surface Equilibrium Relationship
(A1.103)	H ₂ (g)+2*=2H*	$R_{13} = k_{13}P_{H_2}\theta_*^2$	$R_{13}' = k_{-13}\theta_H^2$	$\theta_H = \sqrt{K_{13}P_{H_2}}\theta_*$
(A1.104)	CO ₂ (g)+2*=CO*+O*	$R_{14} = k_{14}P_{CO_2}\theta_*^2$	$R_{14}' = k_{-14}\theta_{CO}\theta_O$	$K_{14}P_{CO_2}\theta_*^2 = \theta_{CO}\theta_O$
(A1.105)	CO*+H*=COH*+*	$R_{15} = k_{15}\theta_{CO}\theta_H$	$R_{15}' = k_{-15}\theta_{COH}\theta_*$	$K_{15}\theta_{CO}\theta_H = \theta_{COH}\theta_*$
(A1.106)	COH*+H*=COH ₂ *+*	$R_{16} = k_{16}\theta_{COH}\theta_H$	$R_{16}' = k_{-16}\theta_{COH_2}\theta_*$	$K_{16}\theta_{COH}\theta_H = \theta_{COH_2}\theta_*$
(A1.107)	COH ₂ *+H*=COH ₃ *+*	$R_{20} = k_{20}\theta_{COH_2}\theta_H$	$R_{20}' = k_{-20}\theta_{COH_3}\theta_H$	$K_{20}\theta_{COH_2}\theta_H = \theta_{COH_3}\theta_*$
(A1.108)	COH ₃ *+H*=H ₂ O*+CH ₂ *	$R_{21} = k_{21}\theta_{COH_3}\theta_H$	$R_{21}' = k_{-21}\theta_{CH_2}\theta_{H_2O}$	$K_{21}\theta_{COH_2}\theta_H = \theta_{CH_2}\theta_{H_2O}$
(A1.109)	CH ₂ *+H*=CH ₃ *+*	$R_{25} = k_{25}\theta_{CH_2}\theta_H$	$R_{25}' = k_{-25}\theta_{CH_3}\theta_*$	$K_{25}\theta_{CH_2}\theta_H = \theta_{CH_3}\theta_*$
(A1.110)	CH ₃ *+H*=CH ₄ *+*	$R_{26} = k_{26}\theta_{CH_3}\theta_H$	$R_{26}' = k_{-26}\theta_{CH_4}\theta_*$	$K_{26}\theta_{CH_3}\theta_H = \theta_{CH_4}\theta_*$
(A1.111)	O*+H*=OH*+*	$R_{27} = k_{27}\theta_O\theta_H$	$R_{27}' = k_{-27}\theta_{OH}\theta_*$	$K_{27}\theta_O\theta_H = \theta_{OH}\theta_*$
(A1.112)	OH*+H*=H ₂ O*+*	$R_{28} = k_{28}\theta_{OH}\theta_H$	$R_{28}' = k_{-28}\theta_{H_2O}\theta_*$	$K_{28}\theta_{OH}\theta_H = \theta_{H_2O}\theta_*$
(A1.113)	H ₂ O*=H ₂ O(g)+*	$R_{29} = k_{29}\theta_{H_2O}$	$R_{29}' = k_{-29}P_{H_2O}\theta_*$	$K_{29}\theta_{H_2O} = P_{H_2O}\theta_*$
(A1.114)	CH ₄ *=CH ₄ (g)+*	$R_{30} = k_{30}\theta_{CH_4}$	$R_{30}' = k_{-18}P_{CH_4}\theta_*$	$K_{30}\theta_{CH_4} = P_{CH_4}\theta_*$

Table A4.13. A summary of Langmuir-Hinshelwood models developed, the assumed reaction scheme, and the most abundant surface intermediates (Pathway 5).

	Methanation Kinetic Equation	MASI	Rate-limiting Step [Additional Assumptions]
F15A	$R_{CH_4} = \frac{k_{15}K_{14}(K_{27}K_{28}K_{29})P_{CO_2}K_{13}^{1.5}P_{H_2}^{1.5}}{P_{H_2O}\left(1 + \sqrt{K_{13}P_{H_2}} + K_{13}K_{14}(K_{27}K_{28}K_{29})\frac{P_{CO_2}P_{H_2}}{P_{H_2O}} + \frac{P_{H_2O}}{K_{29}}\right)^2}$	CO, H and H ₂ O	CO Hydrogenation to CHO [Quasi-equilibrium in all other steps]
F15B	$R_{CH_4} = \frac{k_{15}\sqrt{\left(\frac{k_{27}}{k_{15}}\right)K_{14}K_{13}}P_{CO_2}^{0.5}P_{H_2}^{0.5}}{\left(1 + \sqrt{K_{13}P_{H_2}} + \sqrt{\left(\frac{k_{27}}{k_{15}}\right)K_{14}}P_{CO_2}^{0.5} + \frac{P_{H_2O}}{K_{29}}\right)^2}$	CO, H and H ₂ O	CO Hydrogenation to CHO [(A1.111) assumed irreversible.]
F15C	$R_{CH_4} = \frac{k_{15}\sqrt{\left(\frac{k_{28}}{k_{15}}\right)K_{27}K_{14}K_{13}}P_{CO_2}^{0.5}P_{H_2}^{0.75}}{\left(1 + \sqrt{K_{13}P_{H_2}} + \sqrt{\left(\frac{k_{28}}{k_{15}}\right)K_{27}K_{14}K_{13}}P_{CO_2}^{0.5}P_{H_2}^{0.25} + \frac{P_{H_2O}}{K_{29}}\right)^2}$	H, H ₂ O, CO	CO Hydrogenation to CHO [(A1.112) assumed irreversible.]
F16A	$R_{CH_4} = \frac{k_{16}K_{14}K_{15}(K_{27}K_{28}K_{29})P_{CO_2}K_{13}^2P_{H_2}^2}{P_{H_2O}\left(1 + \sqrt{K_{13}P_{H_2}} + K_{14}K_{15}(K_{27}K_{28}K_{29})K_1^{1.5}\frac{P_{CO_2}P_{H_2}}{P_{H_2O}} + \frac{P_{H_2O}}{K_{29}}\right)^2}$	H, CHO and H ₂ O	CHO Hydrogenation [Quasi-equilibrium in all other steps]
F16B	$R_{CH_4} = \frac{k_{16}\sqrt{\left(\frac{k_{27}}{k_{16}}\right)K_{14}K_{15}}P_{CO_2}^{0.5}(K_{13}P_{H_2})^{0.75}}{\left(1 + \sqrt{K_{13}P_{H_2}} + \sqrt{\left(\frac{k_{27}}{k_{16}}\right)K_{14}K_{15}}P_{CO_2}^{0.5}(K_{13}P_{H_2})^{0.25} + \frac{P_{H_2O}}{K_{29}}\right)^2}$	H, CHO and H ₂ O	CHO Hydrogenation [(A1.111) assumed irreversible.]
F16C	$R_{CH_4} = \frac{k_{16}\sqrt{\left(\frac{k_{28}}{k_{16}}\right)K_{14}K_{15}K_{27}}P_{CO_2}^{0.5}(K_{13}P_{H_2})}{\left(1 + \sqrt{K_{13}P_{H_2}} + \sqrt{\left(\frac{k_{28}}{k_{16}}\right)K_{14}K_{15}K_{27}}P_{CO_2}^{0.5}(K_{13}P_{H_2})^{0.5} + \frac{P_{H_2O}}{K_{29}}\right)^2}$	H, CHO and H ₂ O	CHO Hydrogenation [(A1.112) assumed irreversible.]

F17A	$R_{CH_4} = \frac{k_{20}K_{14}K_{15}K_{16}(K_{27}K_{28}K_{29})P_{CO_2}K_{13}^{2.5}P_{H_2}^{2.5}}{P_{H_2O} \left(1 + \sqrt{K_{13}P_{H_2}} + K_{14}K_{15}K_{16}(K_{27}K_{28}K_{29})P_{CO_2}K_{13}^2 \frac{P_{CO_2}P_{H_2}^{2.5}}{P_{H_2O}} + \frac{P_{H_2O}}{K_{29}} \right)^2}$	H, COH ₂ , H ₂ O	COH ₂ Hydrogenation [Quasi-equilibrium in all other steps]
F17B	$R_{CH_4} = \frac{k_{20}\sqrt{\left(\frac{k_{27}}{k_{20}}\right)}K_{14}K_{15}K_{16}P_{CO_2}^{0.5}(K_{13}P_{H_2})}{\left(1 + \sqrt{K_{13}P_{H_2}} + \sqrt{\left(\frac{k_{27}}{k_{20}}\right)}K_{14}K_{15}K_{16}P_{CO_2}^{0.5}(K_{13}P_{H_2})^{0.5} + \frac{P_{H_2O}}{K_{29}} \right)^2}$	H, COH ₂ , H ₂ O	COH ₂ Hydrogenation [(A1.111) assumed irreversible.]
F17C	$R_{CH_4} = \frac{k_{20}\sqrt{\left(\frac{k_{28}}{k_{20}}\right)}K_{14}K_{15}K_{16}K_{27}P_{CO_2}^{0.5}(K_{13}P_{H_2})^{1.25}}{\left(1 + \sqrt{K_{13}P_{H_2}} + \sqrt{\left(\frac{k_{28}}{k_{20}}\right)}K_{14}K_{15}K_{16}K_{27}P_{CO_2}^{0.5}(K_{13}P_{H_2})^{0.75} + \frac{P_{H_2O}}{K_{29}} \right)^2}$	H, COH ₂ , H ₂ O	COH ₂ Hydrogenation [(A1.112) assumed irreversible.]
F18A	$R_{CH_4} = \frac{k_{21}K_{14}K_{15}K_{16}K_{20}(K_{27}K_{28}K_{29})P_{CO_2}K_{13}^{3.5}P_{H_2}^3}{P_{H_2O} \left(1 + \sqrt{K_{13}P_{H_2}} + K_{14}K_{15}K_{16}K_{20}(K_{27}K_{28}K_{29})P_{CO_2}K_{13}^{2.5} \frac{P_{CO_2}P_{H_2}^{2.5}}{P_{H_2O}} + \frac{P_{H_2O}}{K_{29}} \right)^2}$	H, COH ₃ , H ₂ O	COH ₃ Hydrogenation [Quasi-equilibrium in all other steps]
F18B	$R_{CH_4} = \frac{k_{21}\sqrt{\left(\frac{k_{27}}{k_{21}}\right)}K_{14}K_{15}K_{16}K_{20}P_{CO_2}^{0.5}(K_{13}P_{H_2})^{1.25}}{\left(1 + \sqrt{K_{13}P_{H_2}} + \sqrt{\left(\frac{k_{27}}{k_{21}}\right)}K_{14}K_{15}K_{16}K_{20}P_{CO_2}^{0.5}(K_{13}P_{H_2})^{0.75} + \frac{P_{H_2O}}{K_{29}} \right)^2}$	H, COH ₃ , H ₂ O	COH ₃ Hydrogenation [(A1.111) assumed irreversible.]
F18C	$R_{CH_4} = \frac{k_{21}\sqrt{\left(\frac{k_{28}}{k_{21}}\right)}K_{14}K_{15}K_{16}K_{20}K_{27}P_{CO_2}^{0.5}(K_{13}P_{H_2})^{1.5}}{\left(1 + \sqrt{K_{13}P_{H_2}} + \sqrt{\left(\frac{k_{28}}{k_{21}}\right)}K_{14}K_{15}K_{16}K_{20}K_{27}P_{CO_2}^{0.5}(K_{13}P_{H_2}) + \frac{P_{H_2O}}{K_{29}} \right)^2}$	H, COH ₃ , H ₂ O	COH ₃ Hydrogenation [(A1.112) assumed irreversible.]

A2. Appendix B: Consideration of Heat and Mass Transfer Effects

A2.1. Introduction

The presence of heat and mass transfer resistances can obfuscate the measurements of chemical kinetics. These resistances may arise in systems with fast chemical kinetics, where the rates of heat and mass transport within a particle or between the surface of a catalyst particles and the bulk gas are insufficient to meet the demands of the reaction. If intra-particle mass transfer limitations are present, a significant concentration gradient may exist within the pellet, and therefore the measured bulk composition will not be representative of the concentrations. Equally, interphase heat and mass transfer resistances will result in the measured temperatures and pressures of the bulk fluid differing from those within the catalyst particle. Hence in the event of significant heat and mass transfer resistances, any results obtained would not be representative of the intrinsic kinetics.

For fixed-bed reaction studies, the significance of heat and mass transfer may be elucidated through calculation of the Weisz-Prater, Mears and Anderson criteria. Given estimates of the chemical and transport properties of a reaction system, these criteria provide a simple metric to determine whether the observed rate will differ from the intrinsic rate by greater than 5% due to transport resistances.

A2.2. Estimation of Transport and Thermodynamic Properties

A2.2.1. Viscosity

The viscosity of a gas species at reaction conditions was calculated to first approximation using the equation given by Hirschfelder *et al.* (1954) based on Chapman-Enskog theory of gases (Bird *et al.*, 2002). The equation is reported to be a good approximation for both monatomic and polyatomic gases, despite its derivation being based the assumption of a monatomic gas.

$$\mu = \frac{5}{16} \frac{\sqrt{\pi m k T}}{\pi \sigma^2 \Omega_\mu} \quad (\text{A2.1})$$

Here, μ is the kinematic viscosity, T is the gas temperature in K, k is the Boltzmann constant, m is the molecular mass in g/mol, σ is the collision diameter in Å, and Ω_μ is the Lennard-Jones parameter. The required parameters were extracted from Bird *et al.* (2002) and collated in a look-up table. Once the pure gas viscosities were calculated, the Wilke mixing rule was applied to determine the mixture viscosity.

$$\mu_{mix} = \sum_{i=1}^N \frac{x_i \mu_i}{\sum_j x_j \psi_{ij}} \quad (\text{A2.2})$$

Here x_i is the mole fraction of species i , μ_i and μ_{mix} are the viscosities of species i and the mixture respectively, and ψ_{ij} is defined as

$$\psi_{ij} = \frac{\left(1 + \left(\frac{\mu_i}{\mu_j}\right)^{0.5} \left(\frac{MW_j}{MW_i}\right)^{0.25}\right)^2}{\sqrt{8 \left(1 + \frac{MW_i}{MW_j}\right)}} \quad (\text{A2.3})$$

Here, MW_i is the molecular weight of species i . According to the kinetic theory of gases, the viscosity and thermal conductivity of a gas may be considered invariant with pressure. Hence the viscosities determined by equations (A2.1) and (A2.2) may be applied at any reactor pressure.

A2.2.2. Specific Heat

The specific heat (C_P) of each species at 50 K intervals from 300-1000 K were extracted from a UniSim® simulation, assuming the Peng-Robinson equation of state. The results were then used to form a look-up table, permitting the interpolation of the specific heat over a range of reaction temperatures.

A2.2.3. Thermal Conductivity

Gas thermal conductivities were calculated by applying the Eucken equation. The thermal conductivity, k , for each component was estimated using equation (A2.4), with the overall mixture thermal conductivity calculated from the individual species conductivities using the Wilke mixing rule, (A2.2).

$$k = \left(C_P + \frac{5}{4} \frac{R}{M}\right) \mu \quad (\text{A2.4})$$

Here, k is the thermal conductivity in W/m K, C_P is the specific heat in J/kg K, R is the ideal gas constant in J/mol K, and M is the species molecular mass with units of kg/mol. The species viscosity term, μ , has units of N/m² s.

In order to quantify intraparticle heat transfer, the thermal conductivity of the catalyst support is required. The thermal conductivities of the support materials were determined from the literature. In porous catalysts, the porosity of the catalyst has a strong influence on the effective thermal conductivity. The simplest means of calculating the thermal conductivity for a porous material was applied by Lim (2014), and is given by equation (A2.5).

$$k_{eff} = \varepsilon k_{gas} + (1 - \varepsilon)k_{solid} \quad (\text{A2.5})$$

Whilst this may provide a reasonable first order estimate for low porosity materials, Smith *et al.* (2013) note that its estimations are only reasonable below porosities of 0.10 and conversely at porosities above 0.90. The Landauer equation is suggested by Smith *et al.* (2013) as a more accurate means of estimation, whilst Schlichting *et al.* (2001) suggest the Maxwell-Eucken equation (A2.6). Whilst the equations are similar in form, the Landauer equation (A2.7) estimates were lower; hence these were taken to be the effective values of the catalysts.

$$k_{eff} = k_s \frac{\left(1 + 2\frac{k_s}{k_g} - 2\varepsilon\left(\frac{k_s}{k_g} - 1\right)\right)}{\left(1 + 2\frac{k_s}{k_g} + \varepsilon\left(\frac{k_s}{k_g} - 1\right)\right)} \quad (\text{A2.6})$$

$$k_{eff} = \frac{1}{4} \left\{ k_s(3\varepsilon - 1) + k_g(2 - 3\varepsilon) + \sqrt{\left(k_s(3\varepsilon - 1) + k_g(2 - 3\varepsilon)\right)^2 + 8k_s k_g} \right\} \quad (\text{A2.7})$$

Here, k_{eff} is the effective thermal conductivity, k_s is the thermal conductivity of the solid were it non-porous, and k_g is the gas thermal conductivity. The particle void fraction is expressed as ε . The solid thermal conductivity is assumed to be invariant over the range of reaction temperatures in this dissertation. The thermal conductivities of bulk zirconia and alumina were estimated to be 2.5 W/m K and 28 W/m K respectively, which yielded thermal conductivities of 0.8 W/m K and 8.7 W/m K respectively for the zirconia and alumina catalysts. Klemens (1996) reported that the intrinsic thermal conductivity of non-porous zirconia may be approximated as $1700/T$ W/m K, where the temperature (T) is given in kelvin. This equation yields a fair agreement with the experimental results of Schlichting *et al.* (2001) and indicates that the thermal conductivity of zirconia is unlikely to vary significantly over the temperature ranges within this thesis.

Metal impregnation of catalysts can improve the thermal conductivities of a porous material, with Soomro and Hughes (1979) reporting a ~50% increase in thermal conductivity upon impregnation of 5 wt% nickel onto their alumina support. However, due to the complexity in estimating the effect of metal loadings, the catalysts were assumed to have the thermal conductivity of their respective support material.

A2.2.4. Density

The catalyst densities were taken to be those of the catalyst support as communicated by the support manufacturer. These were 1000 kg/m³ and 2000 kg/m³ for the alumina and zirconia catalysts respectively. Gas densities were calculated using the ideal gas law.

A2.2.5. Diffusivity

The bulk diffusivities and Knudsen diffusivities were calculated using equations (A2.8)(Fuller *et al.*, 1966) and (A2.9) respectively. The diffusion volumes for the reactants were taken from Bird *et al.* (2002) and the pore diameters (d_{pore}) were taken from the BJH analysis of the prepared catalyst.

$$D_{AB} = \frac{10^{-3}T^{1.75} \left(\frac{1}{M_A} + \frac{1}{M_B} \right)^{\frac{1}{2}}}{P \left[(\sum V_A)^{\frac{1}{3}} + (\sum V_B)^{\frac{1}{3}} \right]} \quad (\text{A2.8})$$

$$D_{A,Kn} = \frac{\varepsilon d_{pore}}{3\tau} \sqrt{\frac{8RT}{\pi M_A}} \quad (\text{A2.9})$$

Here D_{AB} and $D_{A,Kn}$ are the bulk diffusivity of species A in B and the Knudsen diffusivity of species A respectively. The molecular masses of A and B are given by M_A and M_B and the molecular volumes of species A and B are given by V_A and V_B . The Knudsen diffusion equation considers the impact of tortuosity (τ) and voidage (ε) of the catalyst through the inclusion of the ε/τ factor. This factor may be employed to transform a bulk diffusivity to an effective diffusivity ($D_{AB,eff}$) for application within a porous media, as in equation (A2.10).

$$D_{AB,eff} = \frac{\varepsilon}{\tau} D_{AB} \quad (\text{A2.10})$$

For mesoporous support material, such as those used in these studies, it is probable that diffusion will be in the Knudsen regime. The Knudsen number, the ratio between mean free path and the characteristic length scale, was calculated to be 1.42 for carbon dioxide

under typical reaction (200°C, 10 bar) conditions within the zirconia support. The bulk diffusivities of CO₂ in H₂ and CO₂ in CH₄ were found to be greater than the CO₂ Knudsen diffusivity. The net diffusivity was estimated using the Bosanquet approximation. The Bosanquet approximation combines the resistances posed by molecule-wall and molecule-molecule collisions, leading to a lower effective diffusivity than that of bulk or Knudsen diffusivities.

$$\frac{1}{D_{A,eff}} = \frac{1}{D_{A,Kn}} + \frac{1}{D_{AB,eff}} \quad (\text{A2.11})$$

A2.3. Heat and Mass Transfer Considerations in the Batch Reactor Experiments

Each experiment was checked for limitations due to intraparticle mass transport, intraparticle heat transport, external mass transport and external heat transport using the Weisz-Prater criterion, the Anderson criterion and the Mears criteria respectively.

A2.3.1. Intraparticle Mass Transfer

Intra-particle mass transfer limitations may be considered negligible in the case of the Weisz-Prater criterion (A2.12) having a value < 0.3.

$$N_{WP} = \frac{\hat{r}\rho_{cat}R_p^2}{C_s D_{eff}} \quad (\text{A2.12})$$

The values of the Weisz-Prater criterion (N_{WP}) for the batch experiments for CO₂ hydrogenation were calculated at the reaction conditions under which the reaction was most rapid. Here \hat{r} is the reaction rate per m³ of catalyst, ρ_{cat} the density in kg/m³, R_p the particle radius in m, C_s the surface concentration of the limiting reagent in mol/m³ and D_{eff} the effective diffusivity in m²/s. For the Carberry experiments, the Weisz-Prater criterion did not exceed 0.3 for the conditions tested. The largest value obtained for the nickel alumina catalyst was ~0.12.

A2.3.2. Intraparticle Heat Transfer

Anderson's criterion determines whether the deviation of the observed rate from the isothermal rate is less than 5% (Mears, 1971). For a spherical catalyst this is stated as equation (A2.13).

$$\frac{\hat{r}\rho_{cat}R_p^2|\Delta H|}{k_{eff}T} < 0.75 \frac{RT}{E_a} \quad (\text{A2.13})$$

Here \hat{r} is the reaction rate per m^3 of catalyst, ρ_{cat} the density in kg/m^3 , R_p the particle radius in m , k_{eff} is the effective thermal conductivity of the pellet, T is the temperature in kelvin, and R represents the ideal gas constant. The reaction enthalpy ($|\Delta H|$) and activation energy (E_a) for carbon dioxide methanation were assumed to be 165 kJ/mol and 85 kJ/mol respectively.

The Anderson criterion may be rearranged to determine the maximum reaction rate above which thermal limitations are likely. The catalyst investigated did not exceed these rates; hence the batch experiments may be considered free of intra-particle heat transfer limitations.

A2.3.3. External Heat Transfer

The significance of external heat transfer was quantified through application of an energy balance across the surface of the pellet.

$$\rho_{cat}\hat{r}V_p\Delta H = hA_p\Delta T_p \quad (\text{A2.14})$$

Here \hat{r} is the specific reaction rate, ρ_{cat} the density in kg/m^3 , V_p the particle volume in m^3 , A_p is the pellet surface area in m^2 , ΔT_p is the film temperature difference in kelvin, and ΔH represents the enthalpy of reaction. For the spherical catalyst particles, the average Nusselt (Nu) number was estimated using the Whitaker correlation (Whitaker, 1972) (Incropera *et al.*, 2006). The terms Re , Pr , μ , and μ_s represent the Reynolds number, Prandtl number, viscosity (with units of Pa s), and the viscosity at the pellet surface respectively.

$$Nu = 2 + (0.4Re^{\frac{1}{2}} + 0.06Re^{\frac{2}{3}})Pr^{0.4} \left(\frac{\mu}{\mu_s} \right) \quad (\text{A2.15})$$

The gas velocity was assumed using the same methodology of Lim (2014). That is the gas velocity was assumed to be that of the basket at the half diameter of the basket, 1.6 cm from axis of rotation. The baskets' rotational rate used in all experiments was 600 rpm. The surface viscosity, μ_s , was assumed to be equal to that of the bulk. The Nusselt number was found to be only slightly dependent on the temperature and predicted temperature differences are summarised in Table A2.1.

Table A2.1. Predicted Nusselt numbers and corresponding temperature differences.

Catalyst	Condition	Nu	Temperature Difference [K]
12 wt% Ni/Al ₂ O ₃	483 K, 10 bara	~13.7	0.7 K
	473 K, 10 bara		0.4 K

The predicted external temperature differences are similar in size to typical thermal gradients which might occur across a fixed-bed reactor, hence the assumption of isothermality is reasonable for the purpose of comparison between the two systems. The influence of film heat transfer was determined to be negligible in each set of Carberry experiments through the variation of stirrer speed.

A2.3.4. External Mass Transfer

External mass transfer for the methanation reaction was quantified through a mass balance across a pellet's surface.

$$\rho_{cat} \hat{r} V_P = k A_P \Delta C_g \quad (\text{A2.16})$$

Here ρ_{cat} , \hat{r} , V_P , k , A_P and ΔC_g are defined as the catalyst density, specific reaction rate, particle volume, mass transfer coefficient, particle surface area and concentration difference between the bulk and the particle surface. The mass transfer coefficient was computed from the Sherwood number using the Chilton-Colburn analogy. The Chilton-Colburn analogy relates the Stanton numbers for heat (St_h) and mass (St_m) transfer to the friction factor.

$$\frac{C_f}{2} = St_h Pr^{\frac{2}{3}} = \left(\frac{Nu}{Re Pr} \right) Pr^{\frac{2}{3}} = St_m Sc^{\frac{2}{3}} = \left(\frac{Sh}{Re Sc} \right) Sc^{\frac{2}{3}} \quad (\text{A2.17})$$

Pr , Sh , Sc and Re represent the Prandtl, Sherwood, Scmidt and Reynolds numbers and C_f represent the friction factor. The concentration differences between the bulk and the particle surface were small, and therefore the measured concentration may be considered representative of the concentration at the external surface of the catalyst pellet. This conclusion was confirmed experimentally through the variation of stirrer speed for each experimental set in the Carberry reactor.

A2.4. Heat and Mass Transfer Considerations for the BTRS

A2.4.1. Intraparticle Heat and Mass Transport

Experiments in the Bench Top Reactor System were conducted within an 8 mm diameter fixed-bed reactor. In each experiment, catalyst particles between 100-200 micron were diluted within alumina particles, sieved to the same size fraction.

The fixed-bed experiments were carried out at conditions similar to those of the batch reactor, where 3 mm diameter particles were used, hence intra-particle heat and mass transfer will not be a concern for the far smaller <200 micron particles. The Anderson and Weisz-Prater criteria for these particles were certainly satisfied.

A2.4.2. Dilution in Fixed-Beds

Bed dilution is required in exothermic reactions to increase the volume over which reaction heat is generated. However, excessive dilution can result in lowered conversions due to local bypass effects (Berger *et al.*, 2002). Berger *et al.* (2002) note that the conversion can be considered unaffected by the use of inert diluent when the following criterion is satisfied.

$$\Delta = \left(\frac{b}{1-b} \right) \frac{X_{diluted} d_p}{2 h_{bed}} \quad (\text{A2.18})$$

Here, Δ is the error due to dilution, b is the volume fraction of diluent, d_p is the particle diameter, h_{bed} is the diluted bed height, and $X_{diluted}$ is the observed reactant conversion. The beds used in the carbon dioxide methanation experiments were diluted at ratios ~1:4 catalyst:inert by volume, and hence for a 5% conversion, the conversion error introduced by dilution is 0.02%.

A2.4.3. Axial Dispersion

The effect of axial dispersion was quantified through the computation of the criterion defined by Mears. Fulfilment of the criterion permits the neglection of axial dispersion, and thus the assumption of plug flow behaviour. The criterion is given by equation (A2.19).

$$\frac{h_{bed}}{d_p} > \frac{8}{Bo} n \ln \left(\frac{1}{1 - X_A} \right) \quad (\text{A2.19})$$

Where

$$Bo = 0.5 + \frac{\varepsilon_b}{\tau_b Re Sc} \quad (\text{A2.20})$$

Here Bo , ε_b , τ_b , Re , Sc , X_A , n , h_{bed} and d_p are the Bodenstein number, the bed voidage, the

bed tortuosity, Reynolds number, Schmidt number, maximum reaction conversion, reaction order, bed height and particle diameter respectively. Due to the large bed height to particle diameter ratio (~250), this inequality is satisfied for conversions significantly beyond those used within the experimental studies.

A2.4.4. Radial Dispersion

Radial dispersion occurs when the velocity profile within the tube cannot be considered flat. The effect of this however is only significant at low tube to particle diameter ratio, namely $d_{\text{tube}}/d_{\text{particle}} < 8$ (Chu and Ng, 1989). In the case of the bench top reactor system, the tube to particle diameter ratio is in excess of 38, and therefore plug flow may be assumed within the reactor tube.

A2.4.5. Pressure Drop

In order to characterise the intrinsic kinetics of a reaction in a fixed-bed, the pressure drop across the bed must be insignificant, such that the partial pressure of the reactants may be accurately quantified. The beds pressure drop (ΔP) was calculated using the Ergun equation, which is valid between $0.1 < \text{Re} < 1000$. The bed Reynolds number was ~ 0.1 . The pressure drop per unit length of bed is given by

$$\frac{\Delta P}{h_{\text{Bed}}} = \frac{C_f \rho_g u^2}{d_p} \quad (\text{A2.21})$$

Where C_f is the friction factor given by

$$C_f = \frac{(1 - \varepsilon_b)}{\varepsilon_b} \left(1.75 + 150 \frac{\mu_g (1 - \varepsilon_b)}{\rho_g u d_p} \right) \quad (\text{A2.22})$$

Here ε_b , μ_g , ρ_g , d_p , h_{Bed} and u are the bed voidage, gas viscosity, gas density, particle diameter, bed height and gas velocity respectively. The pressure drop through the catalyst bed under the typical reaction conditions is ~ 0.02 bar, and hence poses no significant influence on the calculation of the intrinsic kinetics. The pressure drop across the reactor tube was generally higher than this due to the sand packing above and below the diluted catalyst plug, however the pressure drop across the entire reactor system was experimentally determined to be less than 0.2 bar from measurements of the upstream pressure under the highest flow conditions at atmospheric pressure and reaction temperatures.

A2.4.6. Heat Transport in a Fixed-Bed Reactor

A criterion, defined by Mears (1971) was used to determine whether radial heat transport within the fixed-bed was negligible.

$$\frac{q\bar{R}r_{bed}^2}{k_{eff}T_w} < 0.4 \frac{RT_w}{E_A} \quad (\text{A2.23})$$

Here q , \bar{R} , r_{bed} , k_{eff} , T_w , R and E_A are the enthalpy of reaction in J/mol, the reaction rate per unit volume, the bed radius, the effective thermal conductivity, the wall temperature, the ideal gas constant and the activation energy respectively. This criterion ensures less than 5% deviation in the measured reaction rate and was found to be satisfied below a ~20% CO₂ conversion for 3:1 H₂:CO₂ synthesis gas fed at 206 cm³/min (at STP). This conversion level is above those obtained in the differential bed experiments, and hence radial heat transfer limitation may be ruled out.

A2.4.7. Mass Transport in a Fixed-Bed Reactor

For fixed-beds, the Sherwood number (Sh) may be correlated by the correlation of Wakao and Funazkri (1978). The terms k_g , d_p , D_{eff} , Re and Sc are defined as the convective mass transfer coefficient, the particle diameter, the effective diffusivity, the Reynolds number and the Schmidt number respectively.

$$Sh = \frac{k_g d_p}{D_{eff}} = 2 + 1.1 Re^{0.6} Sc^{0.33} \quad (\text{A2.24})$$

The Sherwood number under typical reaction conditions (473 K, 10 barg, 150:50: 6 H₂:CO₂:Ar) was calculated to be 2.4, with only a weak dependence on the temperature. Through calculation of the Sherwood number, the mass transfer coefficient and the Carberry number could be determined. The Carberry number, Ca , is defined as below (Mears, 1971).

$$Ca = \frac{\ddot{R}_{obs}}{k_g a C_{CO_2}} \quad (\text{A2.25})$$

Here C_{CO_2} , a , and \ddot{R}_{obs} are the surface carbon dioxide concentration, the catalyst external surface area per m³ of catalyst and the observed volumetric reaction rate respectively. A reaction may be considered free of external mass transfer when the Carberry number is below 0.05/n for an nth order reaction. For the bench top reactor experiments, the Carberry number was found to be of order 10⁻⁶, hence it is evident the reaction should not be limited by external mass transfer.

A2.5. Summary

The influence of transport phenomena has been evaluated for the Carberry and BTRS reactor systems for the carbon dioxide methanation reaction. The BTRS experiments were found to be clearly free of heat and mass transport limitations. The Carberry experiments are noted to be closer to the limit for heat and mass transport limits, which is due to the limit on the particle size which can safely be used within the spinning basket reactor. However the Carberry experiments are noted to only approach these limits when operating at the highest temperature studied.

A3. Appendix C: Literature Review of Carbon Dioxide Methanation Kinetics and Thermodynamics

A3.1. Mechanisms

Despite the apparent simplicity of the methanation reaction, the mechanism remains subject to debate, with the main point of contention found in the identity of the surface intermediate. The reaction mechanisms proposed within the literature may be divided into two categories. The first proposes that the reaction proceeds *via* direct hydrogenation of carbon dioxide to methane, whilst the latter proposes the reaction proceeds *via* a carbon monoxide surface intermediate. In forming a carbon monoxide surface intermediate, the reaction is then proposed to follow an analogous mechanism to carbon monoxide hydrogenation.

The route of formation for the carbon monoxide intermediate has been suggested to occur either directly *via* dissociation of CO₂ to CO(ads) and O(ads) on the surface (Eckle *et al.*, 2011). Indirect formation *via* the partial reduction of carbonate or formate surface species has also been proposed (Westerman *et al.*, 2015). Using infrared spectroscopy, the surface species during methanation can be determined; however, it is often the case that both formate and carbonyl species are present on the surface of a catalyst. Eckle *et al.* (2011) employed DRIFTS to observe the state of a Ru/Al₂O₃ catalyst surface during CO₂ methanation, reporting both carbonyl and formate adsorption bands. In switching between ¹²CO₂ to ¹³CO₂, a rapid shift in the intensity of carbonyl bands between ¹²CO(ads) and ¹³CO(ads) was observed, with a slower response observed for the formate bands. The differing responses indicated that the formate species acted as spectators, with the carbonyl species representing the primary intermediate for the formation of methane.

Falconer and Zagli (1980) examined the adsorption and methanation of CO₂ on a supported Ni/SiO₂ catalyst using temperature programmed desorption and reaction. The adsorption of carbon dioxide on to nickel was reported to be activated, with carbon dioxide noted to dissociate upon adsorption to yield CO and O atoms. Fujita *et al.* (1991) switched the feed gases from CO₂/H₂ to He/H₂ and from CO₂/H₂ to He and interpreted the observed transients by invoking a two-path mechanism for water formation. The first mode of generation was through the hydrogenation of O(ads) formed by CO₂ dissociation, the second

through hydrogenation of O(ads) formed by the dissociation of CO to C(ads) and O(ads). The resulting kinetic model agreed well with the transient behaviour, and thus provided support for a directly-formed CO intermediate. The dissociation of CO₂ has also been reported on rhodium by Jacquemin *et al.* (2010) and Karelovic and Ruiz (2013).

Formate has been reported to act as a precursor for the formation of CO surface species. Westermann *et al.* (2015) investigated CO₂ methanation over a Y-type zeolite (USY) supported nickel catalyst using FTIR spectroscopy between 150°C and 450°C. The intensity of the formate signal decreased with temperature, accompanied by a rise in carbonyl concentration. The formate species were noted to have formed *via* hydrogenation of adsorbed CO₂ on the support and their subsequent decrease was attributed to decomposition into carbonyls. The carbonyl groups were rationalised to form *via* formate decomposition rather than direct dissociation, since carbonyl groups were found to form at lower temperatures in atmospheres of CO₂/H₂ than CO₂ alone. The formation of CO from formate species was also proposed by Marwood *et al.* (1994), who developed a kinetic model suggesting the formation of formate from CO₂ and its subsequent decomposition to CO occurred at similar rates.

Distinguishing between the formation of CO *via* formate or *via* direct dissociation is complicated due to the adsorption behaviour of the support. Marwood *et al.* (1997) suggested a mechanism where only the formate formed at the metal-support interface is active for the formation of CO, and hence observations of ‘spectator’ formate species, such as those of Eckle *et al.* (2011), might be due to the adsorption of inactive formate species away from the metal support interface. Karelovic and Ruiz (2013), however, considered that direct dissociation of CO₂ occurs, with the observed formate species formed simply through combination of surface hydroxyl groups with the formed CO.

Density functional theory (DFT) has been used to examine the energy landscape of the CO₂ methanation reaction. Ren *et al.* (2015) compared the different mechanisms for CO₂ methanation on a Ni(111) surface with and without a CO intermediate. Of the three pathways identified, the lowest energy path was determined to be CO₂ dissociation to CO, followed by further dissociation of CO to C(ads) and O (ads), which are then hydrogenated to methane and water respectively. Akamura *et al.* (2013) simulated CO₂ methanation on a TiO₂-supported ruthenium nanoparticle, reporting direct CO₂ dissociation was favoured on sites atop the Ru nanoparticle, whereas sites nearer the metal support interface favoured formate decomposition, with both pathways having similar activation energies.

The subsequent reaction of the adsorbed CO has been proposed to occur *via* dissociation to surface carbon and surface oxygen, as prescribed by Weatherbee and Bartholomew (1982) in equation (A3.3) in Table A3.1, or associatively *via* partial hydrogenation of the adsorbed CO species to COH, CHO or CHO intermediates prior to CO bond scission (Miao *et al.*, 2016). The hydrogenation of CO on nickel and other transition metal surfaces has been more extensively investigated in the literature than that of CO₂, with significant bodies of work focussed on the hydrogenation of CO over cobalt and iron, otherwise known as the Fischer-Tropsch process. Despite extensive experimental and theoretical investigations, there is no agreement on the mechanism.

Table A3.1. Mechanism reaction *via* CO and surface carbon intermediates, adapted from Weatherbee and Bartholomew (1982). The * represent surface sites.

Reaction Step	
$H_2(g) + 2* \rightleftharpoons 2H^*$	(A3.1)
$CO_2(g) + 2* \rightleftharpoons CO^* + O^*$	(A3.2)
$CO^* + * \rightleftharpoons C^* + O^*$	(A3.3)
$C^* + H^* \rightleftharpoons CH^* + *$	(A3.4)
$CH^* + H^* \rightleftharpoons CH_2^* + *$	(A3.5)
$CH_2^* + H^* \rightleftharpoons CH_3^* + *$	(A3.6)
$CH_3^* + H^* \rightleftharpoons CH_4^* + *$	(A3.7)
$CH_4^* \rightleftharpoons CH_4(g) + *$	(A3.8)
$O^* + H^* \rightleftharpoons OH^* + *$	(A3.9)
$OH^* + H^* \rightleftharpoons H_2O^* + *$	(A3.10)
$H_2O^* \rightleftharpoons H_2O(g) + *$	(A3.11)
$CO^* \rightleftharpoons CO(g) + *$	(A3.12)

Knowledge of the rate-limiting step is important in the determination of reaction kinetics. For carbon dioxide methanation *via* the carbonyl surface species, a number of rate-limiting steps have been proposed. In their study on the methanation of mixed carbon oxides on nickel, van Herwien *et al.* (1973) proposed the rate-limiting step for carbon dioxide methanation was the adsorption of carbon dioxide. Peebles *et al.* (1983) suggested that a path analogous to that of carbon monoxide hydrogenation appears more probable, suggesting the rate is determined by a ‘delicate balance’ between surface carbon formation and hydrogenation. Weatherbee and Bartholomew (1982) (Table A3.1) proposed that the rate-

limiting step (A3.3) was the dissociation of adsorbed CO to surface carbon and oxygen species, in agreement with Falconer and Zagli (1980), who reported CO bond breakage to be the rate-limiting step on their Ni/SiO₂ catalyst. Where carbon dioxide adsorption and CO formation are not the limiting step, the mechanism might proceed in a manner akin to CO methanation. Coenen *et al.* (1986) in their study of the CO methanation behaviour of a Ni/SiO₂ catalyst indicated CO dissociation under methanation conditions might occur *via* a COH intermediate. In methanating a mixture of ¹³C¹⁶O and ¹²C¹⁸O, the authors reported only a small quantity of isotopic scrambling, which indicated that little dissociated CO recombined to form CO, and thus proposed CO dissociated *via* equations (A3.13)-(A3.14).



The dissociation of the CO on nickel with the assistance of hydrogen has found support with computational studies indicating that the unassisted dissociation of CO is less favourable (Andersson *et al.*, 2008). The DFT study of CO dissociation on nickel surfaces indicated that, without hydrogen, the activation energy for dissociation exceeded that of desorption. In the presence of hydrogen, however, Andersson *et al.* (2008) reported an activation energy of 1.08 eV for dissociation *via* adsorbed carbon-hydroxyl COH*, consistent with the activation energy of the methanation reaction (1.01 eV on supported nickel and 1.08 eV on single crystal nickel).

Hydrogenation of surface carbon has also been proposed to be rate-limiting. Atomic carbon can react with hydrogen and the presence of hydrogen inhibits growth into unreactive polymeric carbon. Gardner and Bartholomew (1981) found that ratios of H₂/CO below ~0.5 resulted in the initiation of the formation of carbon filaments, with growth then possible at higher ratios, but at values unlikely to occur during CO₂ methanation. Van Meerten *et al.* (1982) proposed hydrogenation of CO occurred *via* dissociation of CO on the surface of their Ni/SiO₂ catalyst, because the assumption that hydrogenation of CH surface species was the rate-limiting step providing the best fit to their kinetic measurements. This proposal was supported by the work of Dalmon and Martin (1983), with Klose and Baerns (1984) reporting the reaction of surface carbon with hydrogen to form CH₂ as the most probable rate-limiting step for CO methanation on a Ni/Al₂O₃ catalyst. Further investigation by Yates *et al.* (1985) reported the hydrogenation of CH₃ species to methane to be faster than methanation on Ni(111), and thus the rate-limiting step must occur prior to this reaction.

It is clear the mechanisms for both CO and CO₂ methanation are complicated. Indeed, Sughrue and Bartholomew (1982) proposed three rate-controlling steps dependent on temperature for CO methanation on nickel (H₂ adsorption between 475-525 K, CO dissociation and carbon hydrogenation between 525-575 K and carbon hydrogenation above 575 K). A significant literature base favours carbon dioxide methanation *via* a carbonyl intermediate; however, it is evident there is disagreement on the means of CO formation as well as the rate-limiting step in the methanation of carbon dioxide. Given the delicate interplay between the rates of CO formation, dissociation and hydrogenation, as noted by Peebles *et al.* (1983), it is not unexpected for mechanistic differences to arise due to differences in catalyst support, metal or even reaction temperature.

Aside from methanation *via* a carbonyl intermediate, hydrogenation has been proposed to proceed *via* the direct hydrogenation of formate or carbonate species. Liu *et al.* (2016) examined the methanation of CO₂ on Mg/Al mixed oxide supported catalyst using steady state isotopic transient kinetic analysis (SSITKA). By switching ¹²CO₂ to ¹³CO₂, ¹²C carbonate and hydrocarbonate species were observed to decrease with a corresponding increase in ¹³C carbonate and hydrocarbonate. The authors attributed this decrease to indicate these species acted as intermediates in the methanation reaction, and noted the basic sites on the Mg/Al mixed oxide could support enhanced CO₂ adsorption and result in superior activity, relative to a carbon nanotube (CNT) supported nickel catalyst without basic sites. The reaction was proposed to occur at the metal/support interface, with dissociated H on the metal reacting with adsorbed carbonate species. Interestingly the authors did not report IR peaks due to carbonyl adsorption during the reaction.

Further support for a direct hydrogenation mechanism *via* a carbonate/formate type intermediate is given by Aldana *et al.* (2013). These authors determined the surface species of CO₂ methanation on a ceria/zirconia supported nickel catalyst using IR spectroscopy, concluding that CO might not necessarily act as an intermediate. At a temperature of 150°C, initially mono- and bi-dentate carbonate species were observed, followed by hydrogen carbonates after 1 minute, with their concentration decreasing over time. Formate species were observed after 30 minutes, and were supposed to be formed by the reduction of the hydro-carbonates species. The surface concentrations of formates increased with temperature up to 250°C, above which the concentration rapidly decreased, with a coincident appearance of and rise in methane. The disappearance of formate and the appearance of CH₄ could either indicate that formate acts as an intermediate or that it acts as an inhibitor to CO₂ methanation,

with the decrease in formate resulting in increased availability of reactive sites for CH₄ formation.

Aldana *et al.* (2013) investigated the reaction further using *in operando* transient experiments, switching the inlet feed of a CO₂/H₂ mixture to either H₂ or CO₂. In ceasing the H₂ supply, a rapid decline in methane was observed, which Aldana *et al.* (2013) took to indicate a low hydrogen adsorption capacity. The CO formation continued for a greater period of time, which led the authors to conclude that CO is not an intermediate, but a side product. When CO₂ was removed from the feed, the CO on the surface rapidly diminished as well as the CO in the offgas. The carbonates and formates diminished at a slower rate. The authors concluded that CO formation was not necessary for the methanation reaction, with redox reaction between CO₂ and Ce³⁺ responsible for the production of CO.

In summary, two main pathways for CO₂ methanation have been proposed in the literature. The first proceeds *via* a CO intermediate with a pathway similar to that of CO methanation. The second proceeds *via* a formate intermediate. The determination of the rate-determining step and indeed the true intermediate is complicated, with some IR studies showing the presence of carbonyl and formate species on the surface of the catalyst. The rate-determining step for CO₂ methanation *via* a carbonyl intermediate has been proposed to consist of either CO₂ adsorption, CO₂ dissociation to CO, dissociation of CO or indeed the hydrogenation of a surface carbon intermediate. The true role of formate in the reaction is also unknown, with some authors proposing it is simply a side product, whilst others suggesting that it is a key intermediate, which may either decompose to CO or be hydrogenated directly. The investigations in support of a formate intermediate have employed reducible supports or those with basic sites, which has been noted to enhance CO₂ adsorption, and thus it appears support differences might provide a reason for the observed differences in behaviour.

A3.2. Thermodynamics of CO₂ Methanation

The equilibrium conversions in the hydrogenation of carbon dioxide are near complete conversion to methane under the conditions explored within this Dissertation. The equilibrium conversions were computed using Gibbs energy minimisation with the constraint of an atomic balance. The species considered in the minimisation routine were H₂, CO₂, CH₄, H₂O and CO.

The total Gibbs energy of the system was minimised with the systems Gibbs energy represented by equation (A3.15).

$$G(P, T) = \sum_{i=1}^5 n_i \left(\bar{G}_i^\circ(1 \text{ bar}, T) + RT \ln \left(\frac{P_i}{P_{ref}} \right) \right) \quad (\text{A3.15})$$

Here, \bar{G}_i° is the molar Gibbs energy of pure species i at 1 bara pressure, and temperature T . The Gibbs energy of formation for the pure species were computed using the standard expression for Gibbs energy (A3.16).

$$\bar{G}(1 \text{ bar}, T) = \bar{H}(1 \text{ bar}, T) - TS(1 \text{ bar}, T) \quad (\text{A3.16})$$

The enthalpies and entropies of the pure species over the temperature range of interest were obtained from the NIST chemical database (Chase, 1998). The Gibbs energy was then minimised using the *fmincon* MATLAB® solver at intervals of 25 K. The resulting equilibrium mole fractions are displayed in Figure A3.1 for a 3:1 H₂:CO₂ ratio at 10 bara reaction pressure.

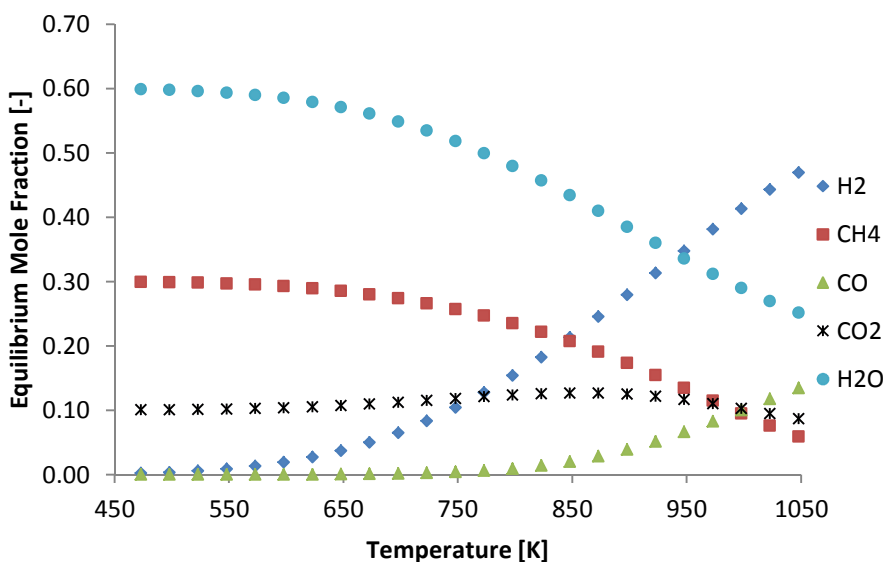


Figure A3.1. Equilibrium mole fractions determined through Gibbs energy minimisation of a 3:1 H₂:CO₂ mixture at 10 bar.

It is clear the production of CO is less thermodynamically favourable than the formation of methane in the region of interest ($T < 523\text{K}$). The point at which CO is formed in the equilibrium product is a function of the H₂:CO₂ ratio, as well as the reaction pressure. Increases in the CO₂ content favour the appearance of CO in the equilibrium product; however, the concentration remains insignificant below 523 K. These observations agree with those made by Lunde and Kester (1974) who computed the equilibrium conversions at H₂/CO₂ ratios between 2 and 4. The authors noted that methane is the thermodynamically-

favoured product below 584 K (at a H₂/CO₂ ratio of 2), with carbon monoxide only being formed above this.

A3.3. Published Kinetics Investigations

A summary of the published kinetic equations for nickel based CO₂ methanation catalysts are given below in Table A3.2. The kinetics of carbon dioxide hydrogenation has been investigated over a number of decades, with the majority of studies characterising the rate of methanation by a Langmuir-Hinshelwood type expression.

The earliest of the studies into the kinetics of carbon dioxide methanation was performed by Binder and White (1950) at atmospheric pressure between 533-673 K, and later extended by Dew *et al.* (1955) at pressures between 2-30 bar. In developing their kinetic equation, Binder and White (1950) assumed a rate-limiting step being the surface reaction between adsorbed carbon dioxide and with either two or four hydrogen molecules (Vlasenko *et al.*, 1969). The investigation by Dew *et al.* on the same catalyst developed a kinetic equation of similar form to that of Binder and White (1950) under the assumption of non-dissociative surface reaction. However, despite the agreement between the data and the equation, the mechanism has been reported to be unlikely (Vlasenko *et al.*, 1969). The experimental results are suspected to be biased by transport phenomena, with Dew *et al.* (1955) themselves noting the effects of diffusion, if present, have been included in their model constants, reasoning that diffusion is an inherent property of their catalyst pellets. The low apparent activation energy of 54.8-58.1 kJ/mol obtained in their study indicates diffusional limitations may have been present, with more recent studies typically observing activation energies in the range of 80-100 kJ/mol.

Table A3.2. Kinetic equations for the methanation of carbon dioxide on Nickel.

Kinetic Equation		Catalyst [Metal/Support]	Apparent E_A [kJ/mol]
Binder and White (1950)	$R_{CH_4} = \frac{a \left(P_{CO_2} P_{H_2}^4 - \frac{P_{CH_4} P_{H_2O}^2}{K_{Eq} P_{H_2}^2} \right)}{(1 + b P_{H_2}^{0.5} + c P_{CO_2})^5}$	Ni/Kieselguhr	-
Dew <i>et al.</i> (1955)	$R_{CH_4} = \frac{a P_{CO_2}^{0.5} P_{H_2}^2}{(1 + b P_{H_2})^3}$	Ni/Kieselguhr	54.8-58.1
Šolc (1962)	$-R_{CO_2} = a P_{CO_2}^{0.66}$	Ni/Cr ₂ O ₃	85.6
Van Herwijnen <i>et al.</i> (1973)	$-R_{CO_2} = \frac{a P_{CO_2}}{(1 + b P_{CO_2})}$	Ni/ γ -Al ₂ O ₃ (33.6 wt% NiO)	105.8
Weatherbee and Bartholomew (1982)	$R_{CH_4} = \frac{a P_{CO_2}^{0.5} P_{H_2}^{0.5}}{\left(1 + b \sqrt{\frac{P_{CO_2}}{P_{H_2}}} + c \sqrt{P_{H_2} P_{CO_2}} + d P_{CO_2} \right)^2}$	Ni/SiO ₂	94
Chiang and Hopper (1983)	$-R_{CO_2} = \frac{a P_{H_2} P_{CO_2}}{(1 + b P_{CO_2} + c P_{H_2})}$	Ni/Kieselguhr (58 wt% Ni)	61.1
Ido <i>et al.</i> (1984)	$-R_{CO_2} = \frac{a P_{H_2}^{0.5} P_{CO_2}}{(1 + b P_{CO_2})}$	Ni/Al ₂ O ₃	-
Inoue <i>et al.</i> (1984)	$-R_{CO_2} = \frac{a P_{H_2} P_{CO_2}}{(1 + b P_{CO_2} + c P_{H_2} + d P_{H_2O})}$	Ni deposited on reactor tube wall.	-
Kai <i>et al.</i> (1988)	$-R_{CO_2} = \frac{a P_{H_2}^{0.5} P_{CO_2}^{0.33}}{(1 + b P_{H_2}^{0.5} + c P_{CO_2}^{0.5} + d P_{H_2O})^2}$	Ni/La ₂ O ₃	72.5
Ibraeva <i>et al.</i> (1991)	$-R_{CO_2} = \frac{a P_{H_2}^{0.5} P_{CO_2}}{(b P_{CO_2} + P_{H_2}^{0.5})}$	Ni/NKM-4A catalyst	78.6
Koschany <i>et al.</i> (2016)	$R_{CH_4} = \frac{a P_{H_2}^{0.5} P_{CO_2}^{0.5}}{\left(1 + b \left(\frac{P_{H_2O}}{P_{H_2}^{0.5}} \right) + c P_{H_2}^{0.5} + d P_{CO_2}^{0.5} \right)^2}$	Ni/Al ₂ O ₃ (Co-precipitated)	77.5
Lim <i>et al.</i> (2016)	$R_{CH_4} = \frac{a P_{CO_2}^{0.5} P_{H_2}^{0.5}}{\left(1 + b \sqrt{\frac{P_{CO_2}}{P_{H_2}}} + c \sqrt{P_{H_2} P_{CO_2}} + d P_{H_2O} \right)^2}$	Ni/ γ -Al ₂ O ₃ (Impregnation)	92.0

Later work by Vlasenko *et al.* (1962), Šolc (1962), Pour (1969) and van Herwijnen *et al.* (1973) investigated the kinetics of methanation for high H₂/CO₂ feeds. Both Pour (1969) and Šolc (1962) reported a half order dependence of carbon dioxide on nickel chromium catalysts, which indicated dissociative adsorption of carbon dioxide in the rate-limiting step. In contrast with these, Vlasenko *et al.* (1962) observed a first-order dependence of rate on carbon dioxide and zeroth order in hydrogen in their study at low CO₂ concentrations between 0.05-0.4% at 1 atm and temperatures between 125°C and 300°C. The first order dependence was proposed to indicate an Eley-Rideal type mechanism, where the rate of methanation was determined by the collision of gas phase carbon dioxide with adsorbed hydrogen atoms.

Weatherbee and Bartholomew (1982) investigated the reaction on their 3 wt% Ni/SiO₂ catalyst between 500-600 K under differential conditions (<10% CO₂ conversion), at H₂ pressures between 2.8 and 13.8 kPa, CO₂ partial pressures between 0.276 and 2.76 kPa and nitrogen dilution to bring the total pressure to 1.4 bar. The dependence of methane formation echoed van Herwijnen *et al.* (1973), with a diminishing dependence on carbon dioxide partial pressure upon increasing carbon dioxide partial pressure. The dependence of methanation rate on hydrogen was noted to follow a similar trend, with the rate being most sensitive at low hydrogen partial pressures, with the influence decreasing with rising hydrogen partial pressure. Weatherbee and Bartholomew (1982) found that a Langmuir-Hinshelwood expression was found to provide an adequate fit across the full range of experimental results. The Langmuir-Hinshelwood assumed dissociative adsorption of both carbon dioxide and hydrogen. Over 30 separate kinetic expressions were developed from their proposed CO intermediate reaction mechanism (shown in Table A3.1) assuming various surface coverages and rate-limiting steps. Of these, the assumption of a CO dissociation rate-limiting step produced the lowest residuals between theory and experiment. The adsorption of carbon dioxide was excluded as a mechanism since a negative hydrogen order was not observed. The authors rationalised a reaction limited by CO₂ adsorption would be inhibited by H₂ competing for sites, and thus leading to an apparent negative reaction order through site blocking.

Chiang and Hopper (1983) examined the hydrogenation kinetics of carbon dioxide over kieselguhr-supported nickel, and varied the volume percentages of CO₂ and H₂ between 20-30 % and 67-80% respectively. The pressure and temperature were varied between 6.9 to 17.2 bar and 550 K to 590 K. In fitting a power law equation to their experimental results, orders of 0.21 for H₂ and 0.66 for CO₂ were determined, with an average deviation of 6.93%. A Langmuir-Hinshelwood model was also applied, providing a fit with an average deviation

of 4.3%. Despite the better agreement between the data and the Langmuir model, the authors favoured the power law model because of its simplicity.

The kinetic study of Kai *et al.* (1988) investigated methanation on a Ni/La₂O₃ catalyst under both differential and integral reaction. The molar ratio of H₂ to CO₂ was varied between 0.6 and 30 and rates were measured up to 90% conversion, with the temperatures being varied between 513 K and 593 K. A Langmuir-Hinshelwood expression was found to aptly describe the results, with dissociative H₂ and CO₂ adsorption assumed. However, surface carbon hydrogenation was proposed by Kai *et al.* (1988) to be the rate-limiting step. The suitability of the developed kinetic equations was investigated at high CO₂ conversion and it was found the addition of a H₂O inhibition term was requisite to represent accurately the results at high conversions. An activation energy of 72.5 kJ/mol was reported and appears to demonstrate the absence of diffusional limitations.

Ibraeva *et al.* (1989) examined a NKM-4A nickel-containing catalyst at atmospheric pressure and CO₂ conversions between 0.18 and 0.90. A range of hydrogen (12-98 kPa) and carbon dioxide (0.03-4.5 kPa) partial pressures with a helium balance gas were investigated at temperatures of 498 to 543 K. The kinetics were derived assuming the involvement of oxygen-containing intermediates but without the preliminary dissociation of carbon dioxide. A rate-limiting step of adsorbed CO₂ hydrogenation to form a COOH species was reported to provide a good fit to the experiments. Interestingly, the authors did not observe any change in the reaction rate when methane and water were added, contrary to the findings of others that water inhibits the reaction. Further support for hydrogen being involved in the rate-limiting step was demonstrated *via* an isotopic switching experiment. On changing the feed from H₂ to D₂, a kinetic isotope effect was observed, indicating hydrogens involvement in the rate-limiting step. This observation is counter to the proposed rate-limiting step of Weatherbee and Bartholomew (1982), with carbonyl dissociation not involving hydrogen in their study.

Most recently, Lim *et al.* (2016) and Koschany *et al.* (2016) examined the kinetics of methanation on a Ni/Al₂O₃ catalyst. Lim *et al.* (2016) undertook the reaction in the Carberry batch reactor used in this thesis. The reaction was assumed to be limited by CO dissociation, with the reaction insensitive to the partial pressure of hydrogen and carbon dioxide at low batch conversions. As observed in the first experimental section of chapter 4, the rate displayed dependence on hydrogen only at high conversions, and was inhibited by water. These observations appear comparable to those of van Herwijnen *et al.* (1973) and Weatherbee and Bartholomew (1982), with their apparent reaction order for carbon dioxide

approaching zero at high carbon dioxide partial pressures. In their fixed-bed reactor study, Koschany *et al.* (2016) examined power law and Langmuir-Hinshelwood kinetic expressions, reporting a Langmuir-Hinshelwood expression based on a formyl formation rate-limiting step provided the best fit for their data.

In summary, the literature is discordant on the best form for kinetic representation, reflecting the uncertainty in the underlying kinetic mechanisms. The majority of studies favour a CO dissociation based mechanism, with a rate-limiting step of either CO dissociation or hydrogenation of the resultant carbon species. The role of hydrogen in the rate-limiting step is uncertain, with the apparent order of reaction positive but variable between zeroth and first order depending on the study in question. Similarly the apparent order of reaction with respect to P_{CO_2} varies between studies; with some authors reporting zeroth order behaviour and others predicting orders between 0 and 1.

A4. Appendix D: Method of Numerical Solution

A4.1. Background

In reaction-diffusion problems, where no analytical solution exists, numerical methods are commonly applied to generate approximations of concentration and temperature profiles within catalyst pellets. The necessity to solve these equations accurately has resulted in the development of numerous numerical solution techniques, e.g. the collocation method, the finite difference (FD) method, the finite element (FE) method and the orthogonal collocation on finite elements method (OCFE). Of these methods, the OCFE method provides a reliable means of solution.

The OCFE method has been the subject of numerous publications, with a good account of the method being given in the works of Finlayson, *e.g.* Carey and Finlayson (1975). The OCFE method is a combination of the finite element and orthogonal collocation method. In the orthogonal collocation method, the zeroes of orthogonal polynomials, such as the Legendre polynomials, are chosen to be the collocation points. By approximating the concentration or temperature profile as a combination of orthogonal polynomials, the gradient can be numerically approximated through minimising the residual at each collocation point. The OCFE method applies the orthogonal collocation method within an element, with the continuity of gradients and numerical values ensured between elements.

Under certain operating regimes, the rate of reaction is expected to be rapid, which may result in significant intra-particle concentration gradients. The stiffness of this problem may be handled using the orthogonal collocation on finite elements method. The method is well suited to problems of this nature as the ability to shrink elements in regions of steep process variable gradients and expand in regions of shallower gradients reduces the memory requirements for the simulation. The orthogonal collocation method allows for quicker convergence in comparison to simpler finite difference schemes, with significantly fewer nodes, and thus a lower memory overhead.

In this study, five collocation points were used within each spatial element. The use of five collocation points allows for a 4th order polynomial fit within the finite element. Applying the collocation method across a finite element, rather than the whole domain, allows for nodes to be selectively placed, such that node density is greater in regions of steep gradients and vice versa. This selective placement of nodes reduces the total number of nodes used,

minimising memory usage without significant sacrifice to solution accuracy.

In order, to determine a near optimum number of collocation elements for the system, a sensitivity analysis was conducted. Here, the number of elements in each region was increased until the output values became insensitive to the addition of further elements. Whilst the number of elements was used to balance accuracy and computation time, altering the number of collocation points per element can produce a similar effect. Details of the sensitivity of the solution to the number of elements are given in §6.4.2.

A4.2. Discretisation of the System

Discretisation of the system is required to solve the concentration profiles over a cylindrical pellet. This process uses fixed points to represent regions within the pellet. Due to the symmetry of the cylindrical pellet, a point on the annulus should have an identical concentration to all other points on the annulus, provided the structure of the pellet is isotropic. This use of symmetry allows the concentration within the pellet to be characterised as a plane, significantly decreasing computation time and memory requirements.

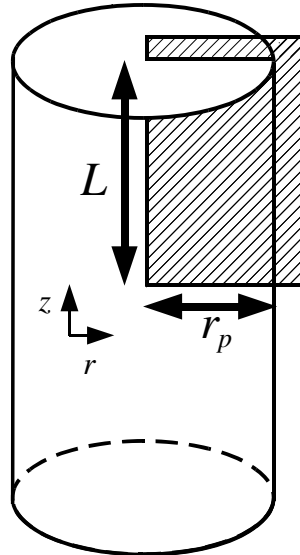


Figure A4.1 This plane through the cylindrical catalyst pellet was selected over which the nodes are overlaid. The rotational symmetry about the axis and the mirror symmetry about the centre of the particle allow the problem to be reduced to this slice.

This plane within the pellet may then be discretised into rectangular elements. These elements contain the collocation points, with the position of the points in each axis determined by roots of the Legendre polynomials.

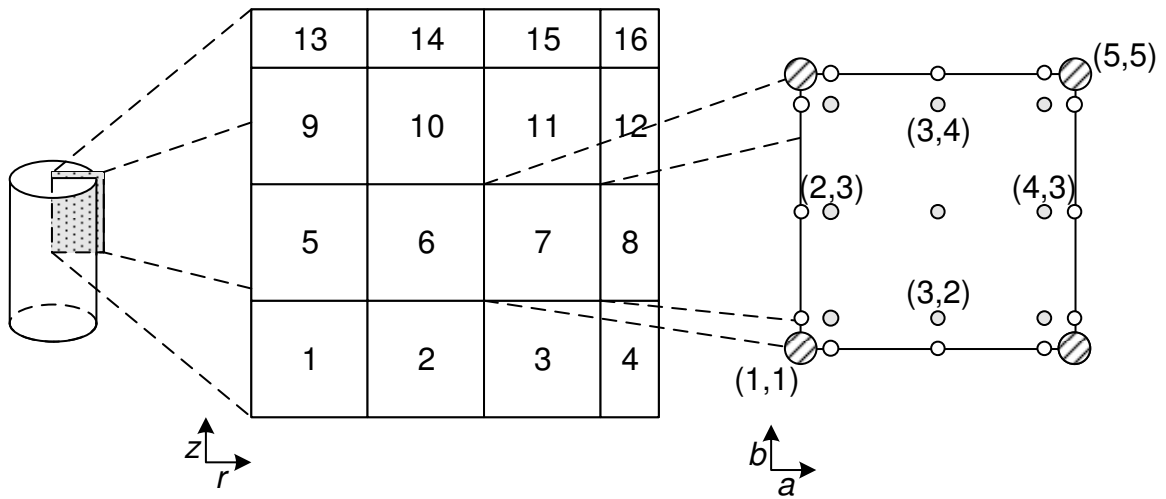


Figure A4.2 The slice through the catalyst particle is broken up into a number of elements. The diagram shows a typical layout with a small number of elements for simplicity. The outer boundary elements are set to be narrower than the inner elements in order to approximate adequately steeper concentration gradients in these regions.

Figure A4.2 shows the structure of the grid over which the concentration gradients were computed. The coordinates identify the node number within each axis, *i.e.* reference (3,2) is the 3rd node along the a axis and the 2nd node along the b axis. Within an element of unit edge length, the nodes are spaced at the roots of the Legendre polynomials, *viz.* (0,0.11,0.50,0.89,1), in both axes a and b .

The solution was found by minimising the residual equations calculated at each node. The form of the residual equations depends on both the position of the node within its rectangular element and its location within the overall system. However they can be broken down into 3 groups. These are internal node residuals, elemental boundary residuals, and system boundary residuals. Figure A4.3 shows how each node may be classified into one of these groups.

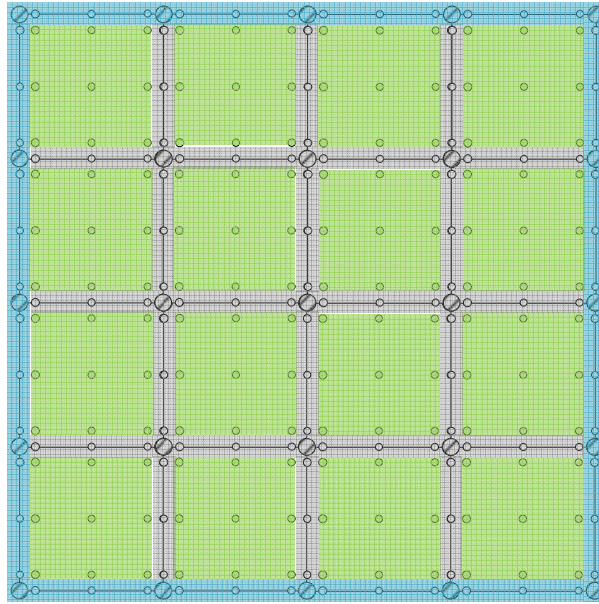


Figure A4.3 The classification of the residual equation based on node location based on a 4×4 element grid. The green sections are internal nodes, the grey sections are the elemental boundary nodes and the blue sections are system boundary nodes. The residual calculation method at each of these nodes is described in sections A4.2.1, A4.2.2 and A4.2.3 respectively.

A4.2.1. Specification of Internal Node Residuals

The internal nodes are used to solve the transport equations for both concentration and temperature within the pellet. The residuals at these nodes are derived from equations (6.9) and (6.10) through linearization of the derivatives using the orthogonal collocation method.

In order to approximate the derivatives, the A and B collocation matrices were generated from the roots of the Legendre polynomials, given by equations (A4.1) and (A4.2) respectively.

$$A = \begin{bmatrix} -13.00 & 14.79 & -2.67 & 1.88 & -1.00 \\ -5.32 & 3.87 & 2.06 & -1.29 & 0.67 \\ 1.50 & -3.23 & 0 & 3.23 & -1.50 \\ -0.67 & 1.29 & -2.06 & -3.87 & 5.32 \\ 1.00 & -1.88 & 2.67 & -14.79 & 13.00 \end{bmatrix} \quad (\text{A4.1})$$

$$B = \begin{bmatrix} 84.00 & -122.06 & 58.67 & -44.60 & 24.00 \\ 53.24 & -73.33 & 26.67 & -13.33 & 6.76 \\ -6.00 & 16.67 & -21.33 & 16.67 & -6.00 \\ 6.76 & -13.33 & 26.67 & -73.33 & 53.24 \\ 24.00 & -44.60 & 58.67 & -122.06 & 84.00 \end{bmatrix} \quad (\text{A4.2})$$

The locations of the nodes are described by $\bar{r} = \Delta r_e u + \bar{r}_e$ and $\bar{z} = \Delta z_e f + \bar{z}_e$, where Δr_e and Δz_e are the dimensionless lengths of each element in the radial and axial direction respectively. The \bar{r}_e and \bar{z}_e terms describe the radial and axial co-ordinates of the start of each

element, with u and f representing the local node position within an element. With the development of this co-ordinate system, the equations describing the system may be reformed.

Forming the problem in this manner allows for the derivatives to be expressed as a linear equation, though use of the collocation matrixes. The derivatives at node with coordinates (a,b) within element e are expressed as

$$\frac{\partial \bar{T}_{e,(a,b)}}{\partial f} = \sum_{j=1}^5 A_{b,j} T_{e,(a,j)}, \quad \frac{\partial^2 \bar{T}_{e,(a,b)}}{\partial f^2} = \sum_{j=1}^5 B_{b,j} T_{e,(a,j)} \quad (\text{A4.3})$$

$$\frac{\partial \bar{T}_{e,(a,b)}}{\partial u} = \sum_{j=1}^5 A_{a,j} T_{e,(j,b)}, \quad \frac{\partial^2 \bar{T}_{e,(a,b)}}{\partial u^2} = \sum_{j=1}^5 B_{a,j} T_{e,(j,b)} \quad (\text{A4.4})$$

Hence, for the mass transport equation for the cylindrical system:

$$-\alpha \left(\frac{1}{(\Delta r_e u + \bar{r}_e) \Delta r_e^2} \frac{\partial}{\partial u} \left((\Delta r_e u + \bar{r}_e) \frac{\partial \bar{C}}{\partial u} \right) + \frac{\beta}{\Delta z_e^2} \left(\frac{\partial^2 \bar{C}}{\partial f^2} \right) \right) = \bar{R} \quad (\text{A4.5})$$

The equation is transformed into a linear system of simultaneous equations:

$$\begin{aligned} & -\alpha \left(\frac{1}{(\Delta r_e u + \bar{r}_e) \Delta r_e^2} \left(\left(\Delta r_e \sum_{j=1}^5 A_{a,j} C_{e,(j,b)} \right) \right. \right. \\ & \quad \left. \left. + \left((\Delta r_e u + \bar{r}_e) \sum_{j=1}^5 B_{a,j} C_{e,(j,b)} \right) \right) + \frac{\beta}{\Delta z_e^2} \sum_{j=1}^5 B_{b,j} C_{e,(a,j)} \right) \\ & = \bar{R}(e, a, b) \end{aligned} \quad (\text{A4.6})$$

Transforming the thermal transport equations for the cylindrical system

$$-\gamma \left(\frac{1}{(\Delta r_e u + \bar{r}_e) \Delta r_e^2} \frac{\partial}{\partial u} \left((\Delta r_e u + \bar{r}_e) \frac{\partial \bar{T}}{\partial u} \right) + \frac{\beta}{\Delta z_e^2} \left(\frac{\partial^2 \bar{T}}{\partial f^2} \right) \right) = \bar{R} \quad (\text{A4.7})$$

$$\begin{aligned} & -\gamma \left(\frac{1}{(\Delta r_e u + \bar{r}_e) \Delta r_e^2} \left(\left(\Delta r_e \sum_{j=1}^5 A_{a,j} T_{e,(j,b)} \right) \right. \right. \\ & \quad \left. \left. + \left((\Delta r_e u + \bar{r}_e) \sum_{j=1}^5 B_{a,j} T_{e,(j,b)} \right) \right) + \frac{\beta}{\Delta z_e^2} \sum_{j=1}^5 B_{b,j} T_{e,(a,j)} \right) \\ & = \bar{R}(e, a, b) \end{aligned} \quad (\text{A4.8})$$

Once the equations are cast in a linear form, they are solved using the MATLAB® *fsolve* solver function through minimisation of the equation residuals at each collocation point.

A4.2.2. Treatment of Elemental Boundaries

For an internal rectangular element, there are 3 types of elemental boundary conditions. Figure A4.4 shows cross-hatched and white nodes, representing the corner and edge nodes of the element. At corner nodes, continuity between both z and r derivatives between neighbouring elements is ensured. For nodes on the edges, continuity is only ensured for the first derivative in the axis orthogonal to the face. That is, the left and right edges are continuous in value and in first derivatives of r ; and the top and bottom edges are continuous in value and in first derivatives of z .

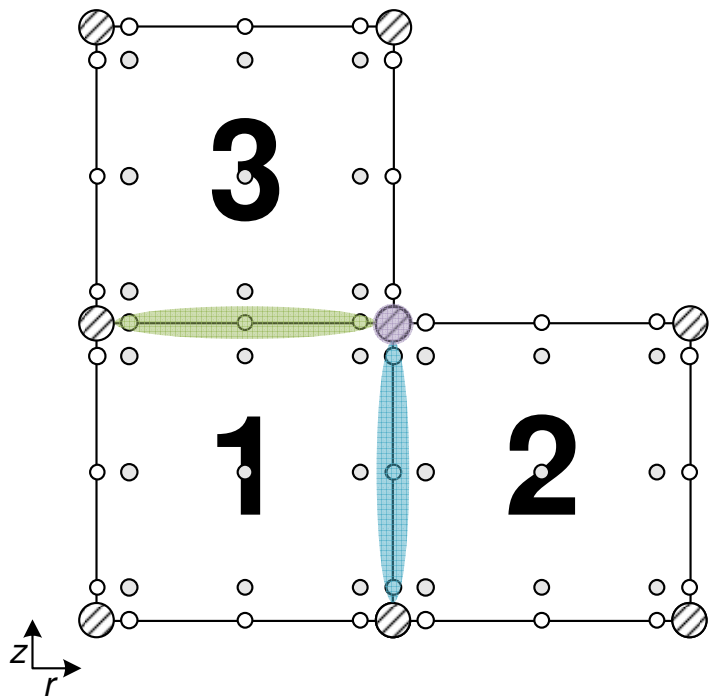


Figure A4.4. A depiction of the treatment of internal element boundary conditions. Nodes in the blue region require radial gradient continuity, nodes in the green region requires axial gradient continuity. At the purple shaded corner node, both radial and axial gradient continuity is required between elements.

The equations used to represent the boundary conditions are given below in equations (A4.9)-(A4.11). The coordinate system set out in Figure A4.2 is used to describe the locations of the relevant nodes.

Right Edge Node of Axial Coordinate b :

$$Residual = \frac{1}{\Delta r_{e=2}} \sum_{k=1}^5 A_{1,k} C_{e=2,(k,b)} - \frac{1}{\Delta r_{e=1}} \sum_{j=1}^5 A_{5,j} C_{e=1,(j,b)} \quad (\text{A4.9})$$

Top Edge Node of Radial Coordinate a :

$$Residual = \frac{1}{\Delta z_{e=3}} \sum_{k=1}^5 A_{1,k} C_{e=3,(a,k)} - \frac{1}{\Delta z_{e=1}} \sum_{j=1}^5 A_{5,j} C_{e=1,(a,j)} \quad (\text{A4.10})$$

Corner Node:

$$\begin{aligned} Residual &= \frac{1}{\Delta r_{e=2}} \sum_{k=1}^5 A_{1,k} C_{e=2,(k,5)} - \frac{1}{\Delta r_{e=1}} \sum_{j=1}^5 A_{5,j} C_{e=1,(j,5)} \\ &\quad + \frac{1}{\Delta z_{e=3}} \sum_{k=1}^5 A_{1,k} C_{e=3,(5,k)} - \frac{1}{\Delta z_{e=1}} \sum_{j=1}^5 A_{5,j} C_{e=1,(5,j)} \end{aligned} \quad (\text{A4.11})$$

A4.2.3. Specification of System Boundaries

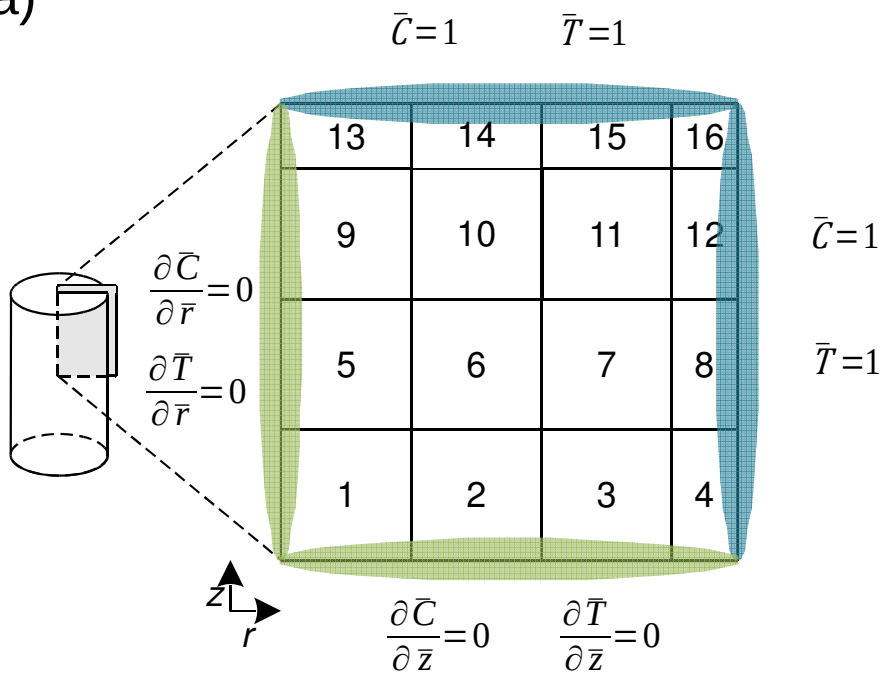
At the system boundaries, the nodes must meet the system boundary conditions stated in §6.3.4. Hence the residual equations for a node at the surface of the pellet, where the concentration and temperature are fixed values, are given in equations (A4.12) and (A4.13).

$$Residual = \bar{T}_{node} - 1 \quad (\text{A4.12})$$

$$Residual = \bar{C}_{node} - 1 \quad (\text{A4.13})$$

These surface nodes are shown within the blue regions in Figure A4.5. The surface boundary conditions are applied at 3 of the 4 corners of the systems domain in the full cylinder case, with the forth corner having both the axial and radial symmetry condition applied. The residuals for the symmetry conditions set out in Figure A4.5 and Figure A4.6 and are demonstrated in equations (A4.14)-(A4.18).

a)



b)

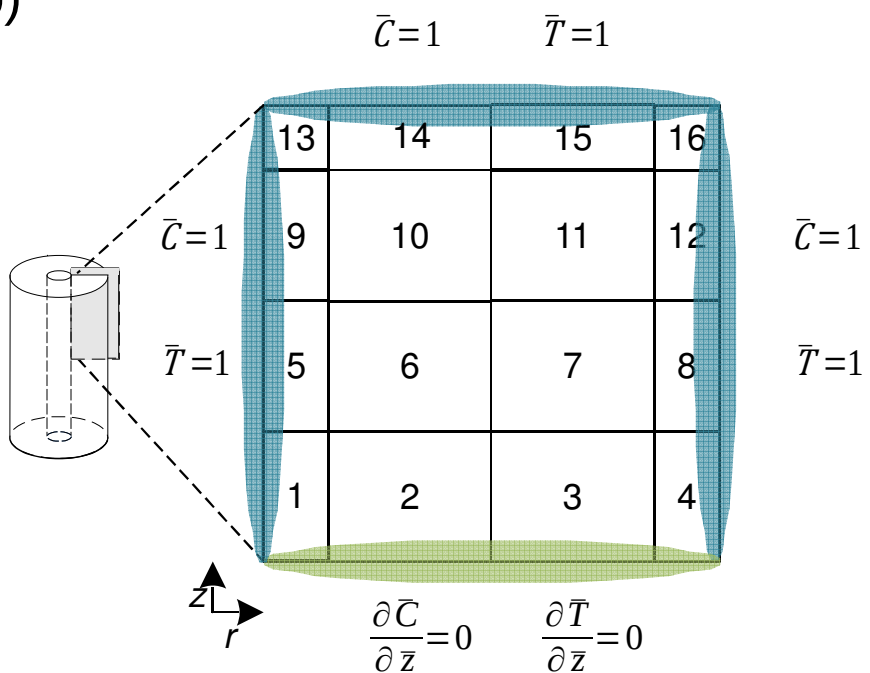


Figure A4.5. The boundary conditions for the pellet and their locations. The blue shaded edges represent the surface boundary conditions, that is a concentration and temperature equal to that of the bulk, whereas the green shaded edges represent symmetry conditions, that is gradients perpendicular to the edges face equalling zero.

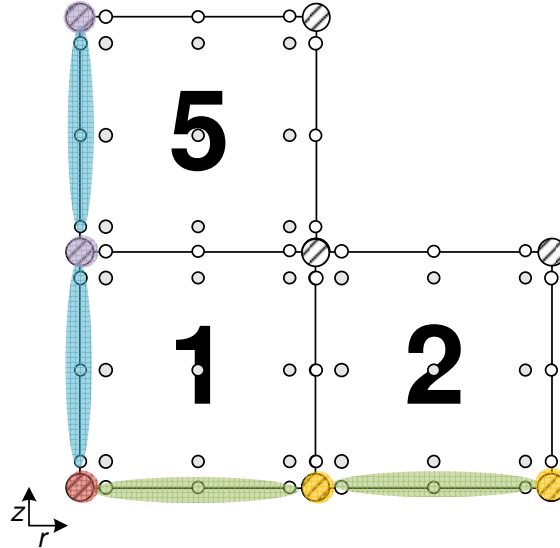


Figure A4.6. Corner boundary node and treatment of the symmetry conditions.

The residual at the red corner node in Figure A4.6 is given by equation (A4.16). The residuals of the blue shaded edge nodes are given for element 1 by equation (A4.14) however their form applies to all elements on this boundary. The green shaded edge node residuals are similarly described by equation (A4.15). The residuals for the yellow and purple shaded corner nodes are demonstrated for element 1 in equations (A4.17) and (A4.18) respectively.

$$\text{Residual} = \frac{1}{\Delta r_{e=1}} \sum_{k=1}^5 A_{1,k} C_{e=1,(k,b)} \quad (\text{A4.14})$$

$$\text{Residual} = \frac{1}{\Delta Z_{e=1}} \sum_{k=1}^5 A_{1,k} C_{e=1,(a,k)} \quad (\text{A4.15})$$

$$\text{Residual} = \frac{1}{\Delta Z_{e=1}} \sum_{k=1}^5 A_{1,k} C_{e=1,(1,k)} + \frac{1}{\Delta r_{e=1}} \sum_{k=1}^5 A_{1,k} C_{e=1,(k,1)} \quad (\text{A4.16})$$

$$\begin{aligned} \text{Residual} = & \frac{1}{\Delta Z_{e=1}} \sum_{k=1}^5 A_{1,k} C_{e=1,(5,k)} + \frac{1}{\Delta r_{e=2}} \sum_{k=1}^5 A_{1,k} C_{e=2,(k,1)} \\ & - \frac{1}{\Delta r_{e=1}} \sum_{k=1}^5 A_{5,k} C_{e=1,(k,1)} \end{aligned} \quad (\text{A4.17})$$

$$\begin{aligned} \text{Residual} = & \frac{1}{\Delta r_{e=1}} \sum_{k=1}^5 A_{1,k} C_{e=1,(k,5)} + \frac{1}{\Delta Z_{e=3}} \sum_{k=1}^5 A_{1,k} C_{e=3,(1,k)} \\ & - \frac{1}{\Delta Z_{e=1}} \sum_{k=1}^5 A_{5,k} C_{e=1,(1,k)} \end{aligned} \quad (\text{A4.18})$$